THE KINETICS OF FLOWING DISPERSIONS

A Thesis

by

AKIO OKAGAWA
B.Eng. (Shibaura Institute of Technology)
M.Sc. (Tokyo College of Science)

Submitted to the Faculty of Graduate Studies
and Research of McGill University in partial
fulfilment of the requirements for the
degree of Doctor of Philosophy

Department of Chemistry,
McGill University,
Montreal, Canada

March 1973

ACKNOWLEDGEMENTS

The author wishes to express his sincere thanks to

Dr. Stanley G. Mason

for his invaluable guidance, patience and encouragement in this work.

Grateful acknowledgement is also made to:

Dr. R.G. Cox for assistance in theoretical derivations in Chapters II and IV, particularly for his contribution to Section 5 of Chapter II, and for many valuable discussions and suggestions;

Kimberly-Clark of Canada Limited for awarding Scholarships during the sessions 1967-68, 1971-72 and 1972-73;

Hercules Incorporated for a Fellowship during the session 1968-69;

The National Research Council of Canada for a Bursary during the session 1969-70;

The Pulp and Paper Research Institute of Canada for awarding the Otto Maass Memorial Fellowship during the session 1970-71, for provision of laboratory accommodation and equipment, and for the co-operation of the machine-shop and photographic department;

Messrs. C.P. Henry and W.S. Paor for their assistance in designing experimental set-ups;

Miss P. Manning and Messrs. A. Kamath and A. Broadway for their assistance in the film analysis;

Miss G. von Chamier for her assistance in typing the thesis.

ABSTRACT

Theoretical equations of probability distributions of orientations, orbit constants and phase angles of rods and discs in dilute suspensions subjected to shear, electric and combined shear and electric fields in non-equilibrium states have been derived, and used to calculate various mean particle orientation parameters and macroscopic rheological properties.

The spread in axis ratios among particles and interactions between particles are examined in some detail and shown to be two most likely causes of establishment of equilibrium distributions of orientations and orbits.

Oscillatory changes in the orientation distributions of rods and discs of various axis ratios and concentrations were measured in shear flow and used to calculate distributions of orbits and phase angles, mean projections and rheological properties. Transient orientation distributions of particles were also measured in various combinations of shear and electric fields. In general, measured transient and equilibrium orientation distributions were in good agreement with the theory, from which a number of interesting and unusual non-Newtonian rheological effects are predicted.

The fading memory effect in suspensions when the flow is cyclically reversed was examined briefly.

RESUME

Les équations théoriques de la probabilité des distributions d'orientations, des constantes d'orbites et des angles de phase des bâtonnets et des disques en suspensions diluées, soumises à un champ de cisaillement, à un champ électrique ou aux champs combinés, ont été dérivées. Ces équations ont servies à calculer les différents paramètres des orientations moyennes des particules et les propriétés macroscopiques rhéologiques.

La répartition des rapports d'axes parmis les particules, et les interactions entre les particules sont examinées en détail et se sont montrées comme étant vraisemblablement les deux causes de l'établissement des distributions équilibrées des orientations et des orbites.

Les changements oscillatoire dans les distributions d'orientation des bâtonnets et des disques de divers rapports d'axes et de concentrations ont été mesurés dans un écoulement de cisaillement et utilisés pour calculer les distributions d'orbites et d'angles de phase, les projections moyennes et les propriétés rhéologiques. Les distributions d'orientation transitoires des particules ont aussi été mesurées en différentes combinations de champs de cisaillement et électriques. En général, les distributions d'orientation équilibrées et transitoires étaient en accord avec la théorie pour laquelle un nombre d'effets rhéologiques non-Newtonien, intérressants et rares, sont prédits.

L'effet d'estompement dans les suspensions, lorsque l'écoulement est renversé d'une façon cyclique, a été étudié brièvement.

TABLE OF CONTENTS

page

CHAPTER III

OSCILLATORY BEHAVIOR OF RODS AND DISCS IN SHEAR FLOW

CHAPTER IV

THE MICRORHEOLOGY OF RIGID SPHEROIDS IN SHEAR AND ELECTRIC FIELDS

page

CHAPTER V

ORIENTATION DISTRIBUTIONS OF CYLINDERS IN SHEAR AND ELECTRIC FIELDS

page

CHAPTER VI

GENERAL CONCLUSION

APPENDICES

page

LIST OF FIGURES

CHAPTER II

CHAPTER III

LIST OF TABLES

MASTER LIST OF SYMBOLS

To avoid confusion the master list of symbols is given here since, due to the limited number of letters available, certain symbols designated different quantities between one Chapter and another. A list of symbols is also given at the beginning of each Chapter.

The following notations are used. An equation number followed by a Roman numeral indicates the Chapter in which it appears; thus [20]-II designates Equation [20] of Chapter II. Prime superscripts designate quantities given relative to the x_i'-axes with a few exceptions which are clearly identified. A bar over a symbol designates its average value; a wavy underline designates a vector quantity.

ROMAN SYMBOLS

a, b	= major and minor semi-axes of a particle.
a_1, a_2, a_3	= constants used in [83]-II.
	= semi-axes of an ellipsoid (Chapter IV).
A	= function of r_e defined in [17]-IV.
$A(n_1\bar{T}/4)$, $A(t)$	= amplitude of oscillation.
A_i, A_{ij}, B_{ij}	= first and second order tensor.
A_n, B_n	= Fourier coefficients.
b_1, b_2	= constant defined in [31]-III.
$\underset{\sim}{B}$	= magnetic induction.
c	= volume fraction of particles ($m\ell/m\ell$).
C	= spherical elliptical orbit constant.
C_1, C_2, C_3, C_4	= constants in rheological equations.
C_o, C_E	= integration constant used in Chapter IV.
d	= diameter of a cylinder.
d_{23}	= minor axis of the projected ellipse of the face of a disc on x_2x_3-plane.
D	= relative amplitude of oscillation
D_1	$= \sqrt{A_1^2 + B_1^2}$
D_r	= rotary diffusion constant.
$\underset{\sim}{E}_o$, $\underset{\sim}{E}_+$	= electric field outside and inside a particle.
$E_{crit.}$	= critical electric field
f	= dimensionless parameter defined in [30]-IV.
$f_n(\bar{r}_e)$	= function of $\bar{r}_e$, defined in [86]-II.
$f_{\alpha-\beta}$	= frequency of class (α-β) interactions (per particles per unit time).

$F(\theta_1,\phi_1)$ = arbitrary function of θ_1, ϕ_1.

$\mathcal{F}_i$ = force per unit length on the particle along the particle axis.

$g(r_e)$, $g(r_p)$ = probability distribution of axis ratio.

g_{ij} = force doublet per unit length on a particle.

G = velocity gradient.

$\underset{\sim}{H}_o$, $\underset{\sim}{H}_+$ = magnetic field outside and inside a particle.

I_i = various integrals.

$J(C,\kappa/\theta_1,\phi_1)$ = Jacobian.

k_o = integration constant used in Chapter III.

k_i = modulus of elliptic integrals.

K_1,K_{ij}; K_2 = dielectric constant of isotropic and anisotropic particles; that of the suspending liquid.

$K(k_i)$, $E(k_i)$, $\Pi(\alpha_i^2,k_i)$ = complete elliptic integrals of the first, second and third kinds.

ℓ = length of cylinder.

ℓ_{23} = projected length of a rod on the x_2x_3-plane.

m = permanent dipole moment per unit volume.

m', m'' = function defined in [26]-II and [28]-II. (not relative to x_i'-axis).

m_i = function of t,r_e,θ_1 defined in [21]-II and Table I-II.

= function defined in [55]-IV, [68]-IV and [71]-IV.

$\underset{\approx}{M}$ = magnetic moment of a particle

n = integer

N = number of particles per unit volume of suspension.

p = pressure of fluid

$\underset{\sim}{P}_1$, $\underset{\sim}{P}_2$ = permanent and induced polarization per unit volume of particle.

p_{ij}, P_{ij} = stress tensor for fluid and for a suspension.

$\underset{\sim}{P}$, $\underset{\sim}{P}_1$, $\underset{\sim}{P}_2$ = total, permanent and induced dipole moment of a particle.

$[^{H}P_{ij}]$, $[^{E}P_{ij}]$ = intrinsic viscous and electric stresses.

$p_t(n)$, $P_t(n)$ = probability and cumulative distributions of $n = \theta_1, \phi_1, C, \kappa, \phi_{2m}, \phi_{3m}$.

$p_t(n,\ell)$ = probability distribution functions of $n,\ell = \theta_1,\phi_1;\ C,\kappa\ ;\ C_o,\kappa_1;\ \phi_{im},\kappa_1$ etc.

$P(q,r_e)$ = function of q and r_e defined in [19b]-IV.

$P(r_{eE})$ = function defined in [14]-V.

Pé = rotary Péclet number.

q, q_{ij} = dielectric and permeability ratios.

$q_t(\theta_1)$ = probability function defined in [21]-III.

$Q(r_e)$ = function of r_e defined in [19a]-IV.

r, r_o = distance from the center of a particle.

r_e, r_{eH} = hydrodynamically equivalent ellipsoidal (spheroidal) axis ratio.

r_{eE} = electrostatically equivalent ellipsoidal (spheroidal) axis ratio.

r_p = particle axis ratio (= a/b)

r_i = projection length of unit axis length of prolate spheroids and rods.

R = particular value of r_e.

s = x_1'/a.

s_{ij} = function defined in [35]-II.

= component of the rate of strain used in Chapter IV.

S_{ij} = projection area of unit equatorial area of oblate spheroid and discs.

t = time

T, T_1, T_2, T_3 = period of rotation at $f = 0$, $f^2 < 1$, $f^2 > 1$ and $G = 0$.

T_{κ_1} = period of oscillation for $p_{\sigma,t}(\kappa)$.

u_i, v_i = fluid velocity and disturbance velocity.

V = volume of a particle.

x_i; x_i' = Cartesian coordinate axes for space; for a particle.

Y = $(r_e - \bar{r}_e)/\sigma$.

Y = function defined in [40]-II.

Y_1, Y_2, Y_3 = function defined in [85e-d]-IV and [87e]-IV.

$Z(\beta,k)$ = Jacobian Zeta function.

GREEK SYMBOLS

$\alpha_i, \beta_i, \gamma_i$ = elliptic integrals given by [6]-IV, [73c-d]-IV.

α_i = parameter of complete elliptic integrals of the third kind.

$\alpha_o', \alpha_o'', \beta_o', \beta_o''$ = spheroidal integrals defined in [40]-II.

β = parameter of Jacobian Zeta function.

$\underset{\sim}{\Gamma}, \underset{\sim}{\Gamma}_H, \underset{\sim}{\Gamma}_E, \underset{\sim}{\Gamma}_M$ = total, hydrodynamic, electric and magnetic torques.

δ_{ij} = Kronecker delta.

$\delta(n)$ = Dirac delta function of n = θ_1, ϕ_1 etc.

ε_{ijk} = permutation symbol

ζ_i = fluid vorticity

η_o, η = viscosity of fluid and suspension.

$[\eta]$ = intrinsic viscosity

θ_1, ϕ_1, ψ_1 = Eulerian angles of the particle axis.

κ = phase angle of ϕ_1 of a rotating particle.

κ_1 = relative phase angle defined in [17]-III.

$\kappa_c, \kappa_E, \kappa_1, \kappa_2$ = integration constant used in Chapter IV.

λ = cross-sectional radius of the particle at the point s (Chapter II).

Λ = integral defined in [61b]-II.

$\Lambda_o(\Phi_i, k)$ = Heuman Lambda function

μ_2; μ_{ij} = magnetic permeability of fluid; of particle.

ν = function defined in [49]-IV.

ν, $\bar{\nu}$ = $2G/(r_e + r_e^{-1})$, $2G/(\bar{r}_e + \bar{r}_e^{-1})$ used in Chapter II.

ν_{ij} = polarizability tensor used in Chapter V.

$[\xi_{ij}]$ = $(P_{ii} - P_{jj})/\eta_o Gc$, the intrinsic normal stress difference of a suspension.

ξ_i = induced magnetic dipole moment per unit volume.

$\sigma_e, \sigma_p, \sigma_m, \sigma_2$ = various standard deviations.

$\tau, \tau_\sigma, \tau_{1n}, \tau_2, \tau_3, \tau_4, \tau_5$ = various relaxation times.

ϕ_{im} = orbit parameters (i = 2,3).

ϕ_{crit} = critical orientation angle at $f^2 = 1$.

$\phi_{1\infty}$; $\phi'_{1\infty}, \phi''_{1\infty}$ = steady orientation at $f^2 > 1$; stable and unstable values.

Φ = function given by [2b]-V.

Φ_i = parameter of Heuman Lambda function.

χ; χ_1, χ_2, χ_3 = function defined in [17]-II, and [50]-IV and Table II-IV.

Ψ_1, Ψ_2 = function defined in [47]-IV and [58c]-IV.

ω_i = spins of particle about x_i.

$\omega(\phi_1)$ = angular velocity of ϕ_1.

CHAPTER I

GENERAL INTRODUCTION

Rheology is the science of deformation and flow of matter. Because it deals with the composition and structure of flowing and deformed materials, it is highly interdisciplinary with an appeal to the physical, biological, medical and earth sciences, and to various associated technologies. It can be conveniently subdivided into two related parts: (i) macrorheology which deals with macroscopic and hence measurable stresses (the external forces applied per unit area of the boundary of a body) and strains (changes of shape and volume resulting from the stresses) of materials, and (ii) microrheology which is concerned with predicting the macrorheological behavior of a body from a detailed description of its elementary units.

This thesis deals theoretically and experimentally with certain aspects of the rheology of dilute suspensions of rigid particles in Newtonian liquids for simple shear strains, including those occurring in the presence of externally applied electric fields. From descriptions of the microrheological behavior of single particles, the elementary units of our systems, and of the collective behavior of populations of particles in dilute suspensions, reasonably complete theories of macrorheology have been developed.

In a dilute suspension of rigid spheroidal particles subjected to a simple shear flow, each particle rotates,

translates and interacts with others. The rotational motion of each isolated particle is governed by Jeffery's equations[1] (which we will consider in detail in later Chapters, and especially Chapter II), and the macrorheological properties of suspensions are determined by the orientation distributions at any given instant. A series of experimental investigations conducted in this laboratory have confirmed Jeffery's equation for rigid cylindrical particles[2,3,4]; it was shown that single particles rotated in fixed orbits, and that, in dilute suspensions, the equilibrium distributions of orbits[5,6] fell between those predicted from considerations of minimum energy dissipation (the so-called Jeffery's hypothesis[1]) and from a random orientation of particles (the so-called Eisenschitz assumption[7]); the equilibrium distribution of orbit constants, which is essential to a complete rheological description (including the intrinsic viscosity, the simplest rheological property), is thus theoretically indeterminate. It was observed experimentally that when a shear is suddenly applied to an initially isotropic suspension, the orbit distributions of rods gradually changed toward equilibrium[8]. Several attempts have been made to remove the indeterminacy of orbit distributions; the orbit distributions following from the Eisenschitz assumption[7] are valid with very intense rotary Brownian motion (or, in the notation we employ in Chapter III, at Pé = 0); others deal with the effect of weak rotary Brownian motion of particles[9,10] and inertial and non-

Newtonian properties of the suspending medium[11]. As discussed in the Historical Survey given in Appendix V, none of these theories can account for the experimental observations[5,6,8], a critical review of which has been made by Goldsmith and Mason[12]. This indeterminacy of particle orbits has led us to the investigation of the microrheological behavior of particles in the transient states of flowing suspensions described in this thesis. We have not, let us hasten to admit, removed this indeterminacy, but we have established unambiguously the important role of particle interactions which has hitherto been ignored in theoretical treatments. In the course of the studies we have discovered a number of other interesting effects.

Specifically, the present studies were undertaken to examine, both theoretically and experimentally, transient properties such as orientation distributions of suspensions of rods and discs when a shear is suddenly applied to a non-equilibrium state, including states existing in externally applied electric fields, and to study mechanisms for establishing equilibrium distributions of particle orientations and particle orbits. In the course of the investigation we found it necessary to study the transient microrheological behavior until equilibrium in particle orientations in the plane normal to the vorticity axis (see Chapter II) is established; this equilibrium was established much more rapidly than that of particle orbits and as will be seen proved to be amenable to theoretical analysis. Thus our studies in shear flow are limited

to the transient orientation distributions of particles over the period of time in which orbit distributions remained constant.

The term "kinetics" is used in the title of this thesis because of the close parallel between the equations describing molecular behavior (especially collisions) in the kinetic theory of gases and those describing particle behavior in sheared suspensions in which, we believe, particle interaction (or collision) is the primary mechanism for establishing equilibrium state.

In Chapter II, transient orientation probability functions for initially isotropic suspensions of spheroids in simple shear flow are derived from Jeffery's equations[1] of motion of a single particle assuming that no particle interactions occur. The various mean orientation parameters such as projection lengths and area of particles are derived from the orientation probability function for convient description of the experimental results. The results are also used to calculate instantaneous macrorheological properties (e.g. the intrinsic viscosity and intrinsic normal stress differences) of suspensions. Two possible mechanisms for establishing equilibrium orientation distributions are then considered: the variations in particle shape, and particle interactions. Each mechanism has its own relaxation time, that of the first being independent of particle concentration, and that of the second varying inversely with it. Comparison with experimental results for suspensions of various cylindrical particles is given in Chapter III.

A generalized theory of the motion of ellipsoidal particles in combined shear and electric fields is derived in Chapter IV. From the equations of motion of single particles with no permanent dipole, the probability functions of particle orientations and rheological properties are given for suspensions in transient states using the method of analysis employed in Chapter II. Experimental confirmation of the equations for shear and electric fields in both transient and steady states is presented in Chapter V.

Chapter VI presents the general findings and conclusions and suggestions for further work.

The Appendices include (I) detailed mathematical derivations for equations given in Chapters II and III, (II) memory fading in suspensions arising from the predicted and observed effects of reversing the direction of shear, (III) application of the theory given in Chapter IV when the electric field is replaced by a magnetic fields, (IV) detailed description of the experimental devices used, and (V) a historical survey included for the benefit of the general reader.

REFERENCES

1. Jeffery, G.B., Proc. Roy. Soc. (London), A102, 161 (1922).
2. Trevelyan, B.J. and Mason, S.G., J. Colloid Sci., 6, 354 (1951).
3. Bartok, W. and Mason, S.G., ibid, 12, 243 (1957).
4. Goldsmith, H.L. and Mason, S.G., J. Fluid Mech., 12, 88 (1962).
5. Mason, S.G. and Manley, R.St.J., Proc. Roy. Soc. (London), A238, 117 (1956).
6. Anczurowski, E. and Mason, S.G., J. Colloid Interface Sci., 23, 533 (1967).
7. Eisenschitz, R., Z. Phys. Chem., A158, 85 (1932).
8. Anczurowski, E., Cox, R.G. and Mason, S.G., J. Colloid Interface Sci., 23, 547 (1967).
9. Brenner, H., ibid, 34, 103 (1970).
10. Leal, L.G. and Hinch, E.J., J. Fluid Mech., 46, 685 (1971).
11. Saffman, P.G., ibid, 1, 540 (1957).
12. Goldsmith, H.L. and Mason, S.G., Rheology: Theory and Applications (F.R. Eirich, ed.) Vol. 4, 85, Academic Press, New York (1967).

CHAPTER II

TRANSIENT ORIENTATION AND RHEOLOGICAL PHENOMENA OF RODS AND DISCS IN SHEAR FLOW

ABSTRACT

The non-equilibrium state of the probability distribution of orientations of non-spherical axisymmetric rigid particles is derived for a dilute suspension subjected to a simple shear flow assuming no particle interactions and negligible Brownian motion. If the particles in the suspension are initially oriented randomly, the orientation distribution function undergoes undamped oscillations of frequency twice that of a particle rotation about the vorticity axis. Thus the instantaneous rheological properties of the suspension,such as the intrinsic normal stress differences and the intrinsic viscosity which are obtained as averages with respect to orientation, should also oscillate with time. Experiments on sheared suspensions of rigid rods and discs have shown that the orientation distribution does oscillate but is damped, dying away to an equilibrium distribution which may then proceed to change slowly with time.

Two possible causes for this damping are considered, the first being the slight variation in shape between particles and the second, the changes in orientations resulting from 2-body interactions. In both cases, the rotating particles experience changes in rotational phase which lead eventually to the equilibrium distribution of orientation and of the associated rheological properties. It is predicted that the systems are non-Newtonian in the non-equilibrium state

except when the equivalent axis ratio is unity (corresponding to spheres), but Newtonian in the equilibrium state. Each mechanism has its own relaxation time for which approximate equations are derived.

LIST OF SYMBOLS

a, b	=	semi-axes of a particle
a_1, a_2, a_3	=	defined in Eq. [84]
$A_i, A_{ij}, A'_i, A'_{ij}$	=	first and second order tensors relative to x_i and x'_i.
A_n, B_n	=	Fourier coefficients
B'_{ij}	=	second order tensor relative to x'_i
c	=	volume concentration (ml./ml.)
C	=	orbit constant
C_1, C_2, C_3	=	constants in viscosity and normal stress equations
D_1	=	$\sqrt{A_1^2 + B_1^2}$
$f_n(\bar{r}_e)$	=	function of $\bar{r}_e$ defined in Eq. [86]
$f_{\alpha-\beta}$	=	frequency of class $(\alpha-\beta)$ interactions per particle per unit time
$\mathcal{F}'_i$	=	force per unit length on the particle along the particle axis
$g(r_e)$	=	probability distribution of axis ratio
g'_{ij}	=	force doublet per unit length on the particle
G	=	velocity gradient
$J\left(\frac{C,\kappa}{\theta_1,\phi_1}\right)$	=	Jacobian defined by Eq. [10]
k_i	=	moduli of elliptic integrals
K	=	defined in Eq. [56]
$K(k_i), E(k_i) \Pi(\alpha_i^2, k_i)$	=	complete elliptic integrals of the first, second and third kinds.
ℓ	=	$2a$, length of cylinder

m', m''	=	functions of C and r_e defined in Eq. [26] and [28]
m_i	=	functions of t, r_e, θ_1 defined in Eq.[21] and Table I (i = 1,2,3,4,5)
M_{ij}	=	transformation tensor
n	=	integer
N	=	number of particles per unit volume
p	=	isotropic pressure of fluid
p_{ij}, P_{ij}	=	stress tensor for fluid and for a suspension
$\underline{p}(\zeta)$	=	probability distribution of $\zeta = \kappa$, C, θ_1, ϕ_1
$P(\zeta)$	=	cumulative distribution of $\zeta = \kappa$, C, θ_1, ϕ_1
$p(C,\kappa)$, $p_t(\theta_1,\phi_1)$	=	two dimensional probability distribution of κ, C and θ_1, ϕ_1
$p_\infty(\kappa)$, $p_\infty(\phi_1)$	=	equilibrium distribution of κ and ϕ_1
r, r_o	=	distance from the center of particle
r_e	=	equivalent axis ratio
r_p	=	particle axis ratio = a/b
r_i, $\bar{r}_i$, $\bar{r}_{i\sigma}$	=	projection length of rod (i = 1,2,3) and mean values
R	=	particular value of r_e
s	=	x_1'/a
s_{ij}	=	function defined in Eq. [35].
S_{ij}, $\bar{S}_{ij}$, $\bar{S}_{ij\sigma}$	=	projection area of disc (i,j = 1,2,3, $i \neq j$) and its mean value
t	=	time
T	=	period of rotation

u_i = velocity components of the fluid ($i = 1,2,3$)

u_i', u_{io}', v_i' = velocity components of total flow, undisturbed flow and disturbance flow along x_i'-axis

X_i, X_i' = Cartesian coordinate axis for a space and for a particle

y = $(r_e - \bar{r}_e)/\sigma$

Y = function defined in Eq. [40]

$Z(\beta,k)$ = Jacobian Zeta function

α_o', α_o'', β_o', β_o'' = spheroid integrals

α_i = parameter of complete elliptic integral of the third kind ($i = 0,1,3,4,5$)

β = parameter of Jacobian Zeta function

δ_{ij} = Kronecker's delta

η, η_o = viscosity of suspension and medium

$[\eta]$ = intrinsic viscosity of a suspension

θ_1, ϕ_1, θ_{10}, ϕ_{10} = spherical polar coordinate for axis of revolution

κ = initial phase angle

λ; Λ = cross-sectional radius of the particle at the point s; integral defined by [61b]

$\Lambda_o(\Phi_i,k)$ = Heuman's Lambda function

ν, $\bar{\nu}$ = $2G/(r_e + r_e^{-1})$, $2G/(\bar{r}_e + \bar{r}_e^{-1})$

$[\xi_{ij}]$ = $(P_{ii} - P_{jj})/\eta_o Gc$, the intrinsic normal stress difference of a suspension

σ = standard deviation of axis ratio

τ_{1n}, τ_2, τ_3 = relaxation times

Φ_i = parameter of Heuman's Lambda function ($i = 1,2,3,4$)

χ, χ_1, χ_2, χ_3 = function defined in Eq. [17]

1. INTRODUCTION

In a suspension of rigid anisometric particles undergoing viscometric flow each particle rotates and interacts with others as it travels along with the suspending medium. As a result of the variation in angular velocity of each particle, preferred orientations are adopted which give rise to anisotropies which have various consequences, for example the development of non-Newtonian behaviour and streaming birefringence. In previous papers from this laboratory[1,2,3] the steady state orientation distributions in dilute suspensions of rigid, non-sedimenting spheroids which are subjected to a simple shear field were calculated and experimentally confirmed for rods and discs. In the steady state, rods showed a most probable orientation with their axes oriented along the direction of flow[2,4], whereas discs showed a most probable orientation with their axis of revolution directed across the shear[2]. The transient phenomena involved in the process of establishing equilibrium were also considered[3]. When a shear is suddenly applied to a suspension which is isotropic (i.e. the particles are randomly oriented), it was predicted that the orientation distribution undergoes a damped oscillation initially, followed by a gradual monotonic change in orientations until equilibrium is attained. The experimental data of Anczurowski *et al*[3], however, fell largely within the latter period of slow monotonic change, while their theoretical analysis for the

orientation processes was incomplete.

In this Chapter we wish to extend the earlier calculations[3] to provide a more complete theoretical basis for further experimental studies of the oscillations in orientation distributions, the results of which are given in the following Chapter[5]. It is appropriate at this point to list the assumptions on which the present theory is based:

(1) the particles of the suspension are rigid, neutrally buoyant and of axisymmetric shape and do not possess rotary Brownian movement;

(2) the suspending medium is Newtonian;

(3) both particle and fluid inertia are negligible so that the fluid motion is determined by the Stokes equation;

(4) the suspension is monodisperse;

(5) there are no interactions (collisions) so that each particle may be considered as isolated.

From the equations of motion for a single axisymmetric particle in a simple shear flow, the two-dimensional orientation distribution function for the non-equilibrium state is derived, from which several mean orientation parameters (for example, projections of particle length and equatorial area) and the intrinsic viscosity and normal stresses are calculated. All of these quantities are shown to undergo undamped oscillations.

The restrictions of assumptions (4) and (5) are

then separately removed. In both circumstances, the oscillations are damped, with characteristic relaxation times, until equilibrium values are attained. These two mechanisms of damping, which have been confirmed experimentally[5], are discussed in some detail in Sections 4 and 5.

2. SINGLE PARTICLES

Jeffery[6] has calculated the rotation of a single spheroidal particle immersed in a viscous fluid undergoing a simple shear flow whose undisturbed velocity components (i.e. components along the Cartesian coordiante axes in the absence of a particle) are described by

$$u_1 = u_2 = 0 \quad , \qquad u_3 = Gx_2 \quad , \tag{1}$$

where G is the velocity gradient. Throughout this Chapter we shall employ a notation similar to that previously defined[1-3] except for the use of the coordinate system $x_i (i = 1,2,3)$ in place of x,y,z (see the inset of Fig. 1), the components of vectors now being denoted by the use of subscripts 1,2,3. When a single neutrally buoyant rigid spheroid of axis ratio r_e is introduced into the shear flow, its axis of revolution assumes angular velocities given by Jeffery's equations[6]

$$\frac{d\theta_1}{dt} = \frac{G(r_e^2 - 1)}{4(r_e^2 + 1)} \sin 2\theta_1 \sin 2\phi_1 \quad , \tag{2}$$

$$\frac{d\phi_1}{dt} = \frac{G}{r_e^2 + 1}\,(r_e^2\cos^2\phi_1 + \sin^2\phi_1) \qquad [3]$$

where θ_1 and ϕ_1 are Eulerian angles* for the axis of revolution of the spheroid with respect to X_1 as a polar axis (see the center inset of Fig. 1). Integration of [2] and [3] yields

$$\tan\theta_1 = \frac{Cr_e}{(r_e^2\cos^2\phi_1 + \sin^2\phi_1)^{\frac{1}{2}}} \qquad [4]$$

$$\tan\phi_1 = r_e \tan\left(\frac{2\pi t}{T} + \kappa\right) \qquad [5]$$

where the integration constants C and κ denote the orbit constant and the initial phase angle respectively, and where T is the period of one complete rotation of the spheroid about the vorticity axis (X_1) between $\phi_1 = 0$ and 2π, given by

$$T = \frac{2\pi}{G}\,(r_e + r_e^{-1}) \quad . \qquad [6]$$

A single spheroid thus rotates in the periodic manner defined by [4] and [5] for a given orbit constant $C(-\infty \leq C \leq \infty)$, the trace of the particle end being a spherical ellipse (see the inset of Fig. 1).

It has been shown by Bretherton[7] that the rotation of a rigid axisymmetric body (for example a spheroid, a

*Since the treatment is restricted to axisymmetric particles, the third Eulerian angle, describing axial spin, is neglected in the present treatment.

circular cylinder or a cone) in a uniform simple shear flow is mathematically identical with that of a spheroid obtained by Jeffery[6]. The quantity r_e, which no longer represents the true axis ratio of the particle, is a function only of the particle shape and is then called the equivalent axis ratio ($r_e < 1$ for discs and oblate spheroids, and $r_e > 1$ for rods and prolate spheroids). It is calculated by means of [6] from the measured period of rotation T. This has been experimentally confirmed for rods[8] and discs[9], it being found that a cylindrical particle of axis ratio r_p (length to diameter) of 0.86 is equivalent to a sphere ($r_e = 1$) for rotation in shear flow.[10]

Recently Cox [11] has shown theoretically that for long slender particles the equivalent axis ratio is related to the actual axis ratio by r_e = const. r_p for sharp-ended bodies and r_e = constant. $r_p/\sqrt{\ell n\ r_p}$ for blunt-ended bodies. From a comparison with experiments, the value of constant in the latter formula is found to be 1.24 for cylindrical particles. The theory that follows will therefore not be restricted to spheroidal particles, but will deal with general axisymmetric particles. Distinction is therefore made between one end of the axis of revolution of a particle and the other.

3. MONODISPERSE AND COLLISION-FREE SUSPENSIONS

(a) Probability Distribution of θ_1 and ϕ_1*

(i) Arbitrary Initial Orientation

The orientation distribution $p_t(\phi_1)$ obtained in the previous papers for both transient and steady states[1,3] does not describe completely the resultant anisotropy of the flowing suspension since there is no consideration made for the distribution of particle orbits. Here the two-dimensional orientation distribution function will be considered for a collision-free suspension of axisymmetric particles of uniform size in a simple shear flow, defined by [1]. In a collision-free suspension each particle is assumed to be well isolated from the others so that it rotates in a fixed orbit as described in the previous section.

Particle orientations may be described by a distribution function $p_t(\theta_1,\phi_1)$ with $0 \leq \theta_1 \leq \pi$ and $0 \leq \phi_1 \leq 2\pi$ defined such that $p_t(\theta_1,\phi_1)\, d\theta_1 d\phi_1$ is the fraction of particles with axes directed in the intervals $(\theta_1,\theta_1 + d\theta_1)$ and $(\phi_1,\phi_1 + d\phi_1)$ (shown by the hatched area in the inset in the center of Fig. 1) where θ_1 and ϕ_1 are measured for one end of each particle axis. One may also consider a

* Since the probabilities must always be positive, all distribution functions should be taken as the absolute values in the equations which give them.

distribution function $p(C,\kappa)$ with $-\infty \leq C \leq \infty$ and $0 \leq \kappa \leq 2\pi$ defined as the fractions of particles with values of C, κ lying in the intervals $(C, C + dC)$ and $(\kappa, \kappa + d\kappa)$ respectively. It must be noted that the regions of θ_1, ϕ_1 used here are chosen to be the same as those used previously[3], where the normalization of the distribution function is made over the entire sphere

$$\int_0^{2\pi}\int_0^{\pi} p_t(\theta_1,\phi_1)d\theta_1 d\phi_1 = \int_0^{2\pi}\int_{-\infty}^{\infty} p(C,\kappa)dCd\kappa = 1 \quad . \qquad [7]$$

It immediately follows from the above definitions that

$$p_t(\theta_1,\phi_1)d\theta_1 d\phi_1 = p(C,\kappa)dCd\kappa \qquad [8]$$

where the increments dC and $d\kappa$ correspond to the increments $d\theta_1$ and $d\phi_1$. Thus

$$dCd\kappa = J\left(\frac{C,\kappa}{\theta_1,\phi_1}\right) d\theta_1 d\phi_1 \qquad [9]$$

where the Jacobian is defined by

$$J\left(\frac{C,\kappa}{\theta_1,\phi_1}\right) = \frac{\partial C}{\partial \theta_1} \cdot \frac{\partial \kappa}{\partial \phi_1} - \frac{\partial C}{\partial \phi_1} \cdot \frac{\partial \kappa}{\partial \theta_1} \quad . \qquad [10]$$

The partial derivatives in [10] are evaluated from [4] and [5] as

$$\frac{\partial C}{\partial \theta_1} = \frac{(r_e^2 \cos^2\phi_1 + \sin^2\phi_1)^{1/2}}{r_e \cos^2\theta_1} \quad ,$$

$$\frac{\partial \kappa}{\partial \phi_1} = \frac{r_e}{r_e^2 \cos^2\phi_1 + \sin^2\phi_1} \quad , \qquad [11]$$

$$\frac{\partial C}{\partial \phi_1} = \frac{(1 - r_e^2)\tan\theta_1 \sin\phi_1 \cos\phi_1}{r_e (r_e^2 \cos^2\phi_1 + \sin^2\phi_1)^{1/2}} \quad ,$$

$$\frac{\partial \kappa}{\partial \theta_1} = 0 \quad .$$

Substituting the resulting value for the Jacobian into [9] and making use of [8], the probability distribution $p_t(\theta_1, \phi_1)$ may be obtained as

$$p_t(\theta_1, \phi_1) = \frac{\sec^2\theta_1}{(r_e^2 \cos^2\phi_1 + \sin^2\phi_1)^{1/2}} p(C, \kappa) \qquad [12]$$

Since both C and κ are assumed to be constants for any given particle in a collision-free suspension, $p(C, \kappa)$ must also be a constant and be determined by the initial orientations of particles. If the probability orientation distribution of particles in a suspension at some initial instant t = 0 is given by $p_o(\theta_{10}, \phi_{10})$, then the corresponding distribution function $p(C, \kappa)$ is given by

$$p(C,\kappa) = \cos^2\theta_{10}(r_e^2\cos^2\phi_{10} + \sin^2\phi_{10})^{1/2}\, p_o(\theta_{10},\phi_{10}) \quad , \qquad [13]$$

where θ_{10},ϕ_{10} are the initial orientation angles of a particle also given by

$$\tan\theta_{10} = C(\cos^2\kappa + r_e^2\sin^2\kappa)^{1/2} \qquad [14]$$

$$\tan\phi_{10} = r_e\tan\kappa \quad .$$

Therefore [13] may be written as

$$p(C,\kappa) = \frac{r_e p_o[\tan^{-1}\{C(\cos^2\kappa + r_e^2\sin^2\kappa)^{1/2}\}, \tan^{-1}(r_e\tan\kappa)]}{(\cos^2\kappa + r_e^2\sin^2\kappa)^{1/2}\{1 + C^2(\cos^2\kappa + r_e^2\sin^2\kappa)\}} \quad . \qquad [15]$$

Substitution into [12] yields the distribution function $p_t(\theta_1,\phi_1)$ at a general time t as

$$p_t(\theta_1,\phi_1) = \frac{p_o\left[\tan^{-1}(\chi\tan\theta_1),\ \tan^{-1}\left(\dfrac{\tan\phi_1 - r_e\tan\frac{2\pi t}{T}}{1 + r_e^{-1}\tan\phi_1\tan\frac{2\pi t}{T}}\right)\right]}{\chi(\cos^2\theta_1 + \chi^2\sin^2\theta_1)} \quad . \qquad [16]$$

where $\chi^2 = \chi_1\sin^2\phi_1 + \chi_2\sin\phi_1\cos\phi_1 + \chi_3\cos^2\phi_1$

$$\chi_1 = \tfrac{1}{2}\{1 + r_e^{-2} + (1 - r_e^{-2})\cos\tfrac{4\pi t}{T}\} \quad ,$$

$$\chi_2 = (r_e^{-1} - r_e)\sin\tfrac{4\pi t}{T} \quad , \qquad [17]$$

$$\chi_3 = \tfrac{1}{2}\{1 + r_e^{2} + (1 - r_e^{2})\cos\tfrac{4\pi t}{T}\} \quad .$$

If the initial orientation distribution $p_o(\theta_{10},\phi_{10})$ of particles in a suspension is known, the instantaneous probability distribution $p_t(\theta_1,\phi_1)$ at time t can be evaluated from [16]. Inspection of the function χ^2 shows that $p_t(\theta_1,\phi_1)$ generally oscillates with a period T. If initially $p_o(\theta_{10},\phi_{10}) = p_o(\theta_{10},\phi_{10} + \pi)$, which includes the case where we do not distinguish between the ends of the particle axes, it oscillates with a period T/2.

(ii) Random Initial Orientation

For the special and interesting case where the particles are initially randomly (isotropically) oriented, the distribution function $p_o(\theta_{10},\phi_{10})$ is given by

$$p_o(\theta_{10},\phi_{10}) = \frac{1}{4\pi}\sin\theta_{10} \quad . \qquad [18]$$

If this suspension is sheared, the probability distribution $p_t(\theta_1,\phi_1)$ at a future t is obtained by substituting [18] into [16].

Thus

$$p_t(\theta_1,\phi_1) = \frac{\sin\theta_1}{4\pi(\cos^2\theta_1 + \chi^2\sin^2\theta_1)^{3/2}} \quad , \qquad [19]$$

while the corresponding distribution function $p(C,\kappa)$ is obtained from [15] as

$$p(C,\kappa) = \frac{Cr_e}{4\pi\{1 + C^2(\cos^2\kappa + r_e^2\sin^2\kappa)\}^{3/2}} \quad . \qquad [20]$$

The probability distributions of the individual orientation angles θ_1 and ϕ_1 can immediately be obtained by the integrations over the limit of ϕ_1 and θ_1 respectively. Thus

$$p_t(\theta_1) = \int_0^{2\pi} p_t(\theta_1,\phi_1)d\phi_1 = \frac{\sin\theta_1}{\pi m_1^{\frac{1}{2}} m_2} E(k_1) \quad , \qquad [21a]$$

where

$$m_1 = 1 + \tfrac{1}{4}\sin^2\theta_1\left[(r_e - r_e^{-1})^2(1 - \cos\tfrac{4\pi t}{T}) + \{(r_e - r_e^{-1})^4(1 - \cos\tfrac{4\pi t}{T})^2 + 8(r_e - r_e^{-1})^2(1 - \cos\tfrac{4\pi t}{T})\}^{\frac{1}{2}}\right] \qquad [21b]$$

$$m_2 = 1 + \tfrac{1}{4}\sin^2\theta_1\left[(r_e - r_e^{-1})^2(1 - \cos\tfrac{4\pi t}{T}) - \{(r_e - r_e^{-1})^4(1 - \cos\tfrac{4\pi t}{T})^2 + 8(r_e - r_e^{-1})^2(1 - \cos\tfrac{4\pi t}{T})\}^{\frac{1}{2}}\right] \qquad [21c]$$

and $E(k_1)$ is the complete elliptic integral of the second kind with modulus $k_1^2 = 1 - m_2/m_1$, and

$$p_t(\phi_1) = \int_o^{\pi} p_t(\theta_1,\phi_1)\, d\theta_1 = \frac{1}{2\pi\chi^2} \qquad [22]$$

which is equivalent to [11]-3*. The corresponding cumulative distributions are

$$P_t(\theta_1) = \frac{1}{\pi}\int_o^{\theta_1} \frac{\sin\theta_1}{m_1^{\frac{1}{2}}m_2} E(k_1)d\theta_1 \quad , \qquad [23]$$

and

$$P_t(\phi_1) = \frac{1}{2\pi}\tan^{-1}\left(\frac{4\chi_1\tan\phi_1}{2\chi_1\chi_2\tan\phi_1 + \chi_2^2 + 4}\right) \quad . \qquad [24]$$

As predicted previously[3], both $p_t(\theta_1)$ and $p_t(\phi_1)$ are oscillating functions of time with a period of T/2. The variations of $p_t(\phi_1)$ for suspensions of rods ($r_e = 5$) and discs ($r_e = 0.2$) are illustrated in Fig. 1(a) and (b). The value of $\sqrt{p_t(\phi_1)}$ plotted against ϕ_1 in polar coordinates gives a circle of radius $1/\sqrt{2\pi}$ (corresponding to $p_t(\phi_1) = 1/2\pi$) for $t = 0, T/2, T, 3T/2$, etc., which corresponds to the random distribution given by [18], whereas for $t = T/4$, $3T/4$, $5T/4$ etc., it gives an ellipse with semi-axes corresponding to $p_t(\phi_1)$ equalling $r_e^2/2\pi$ and $1/2\pi r_e^2$, the orientation distribution $p_t(\theta_1,\phi_1)$ at such times being

$$p_{T/4}(\theta_1,\phi_1) = \frac{\sin\theta_1}{4\pi\{\cos^2\theta_1 + (r_e^2\cos^2\phi_1 + r_e^{-2}\sin^2\phi_1)\sin^2\theta_1\}^{3/2}} \quad . \qquad [25]$$

* For convenience we adopt a convention whereby [11]-3 denotes Equation [11] of Reference (3).

FIGURE 1

Various probability functions for an initially isotropic and collision-free suspension of rods ($r_e = 5$) and discs ($r_e = 0.2$) which illustrate behaviour typical for all values of $r_e > 1$ and $r_e < 1$.

(a); $\sqrt{p_t(\phi_1)}$ for rods at various time periods (i) $t/T = 0$, (ii) 0.03, (iii) 0.25, (iv) 0.47 and (v) ∞, being calculated from [22] and [102].

(b); $\sqrt{p_t(\phi_1)}$ for discs at the same time periods as in (a).

(c); $p_E(C)$ for (i) rods and (ii) discs calculated from [26], the distribution at $-\infty < C < 0$ being the mirror image about $C = 0$, so that $P_E(\infty) = 1$.

(d); $\sqrt{p(\kappa)}$ for (i) rods and (ii) discs calculated from [27], and (iii) the equilibrium distribution $p_\infty(\kappa) = 1/\sqrt{2\pi}$ for both rods and discs from [103].

As explained in Section 3(b) when r_e's for rods and discs are reciprocals of one another, the curves in (a) become identical with those in (b) when rotated through $\pi/2$; the same applies to (i) and (ii) in (d).

The central inset shows the coordinate systems x_i and x_i', and Eulerian angles θ_1 and ϕ_1 of the particle axis with respect to the X_1-axis as a polar axis; the orbits of a rod and disc are shown by the heavy solid and broken lines respectively.

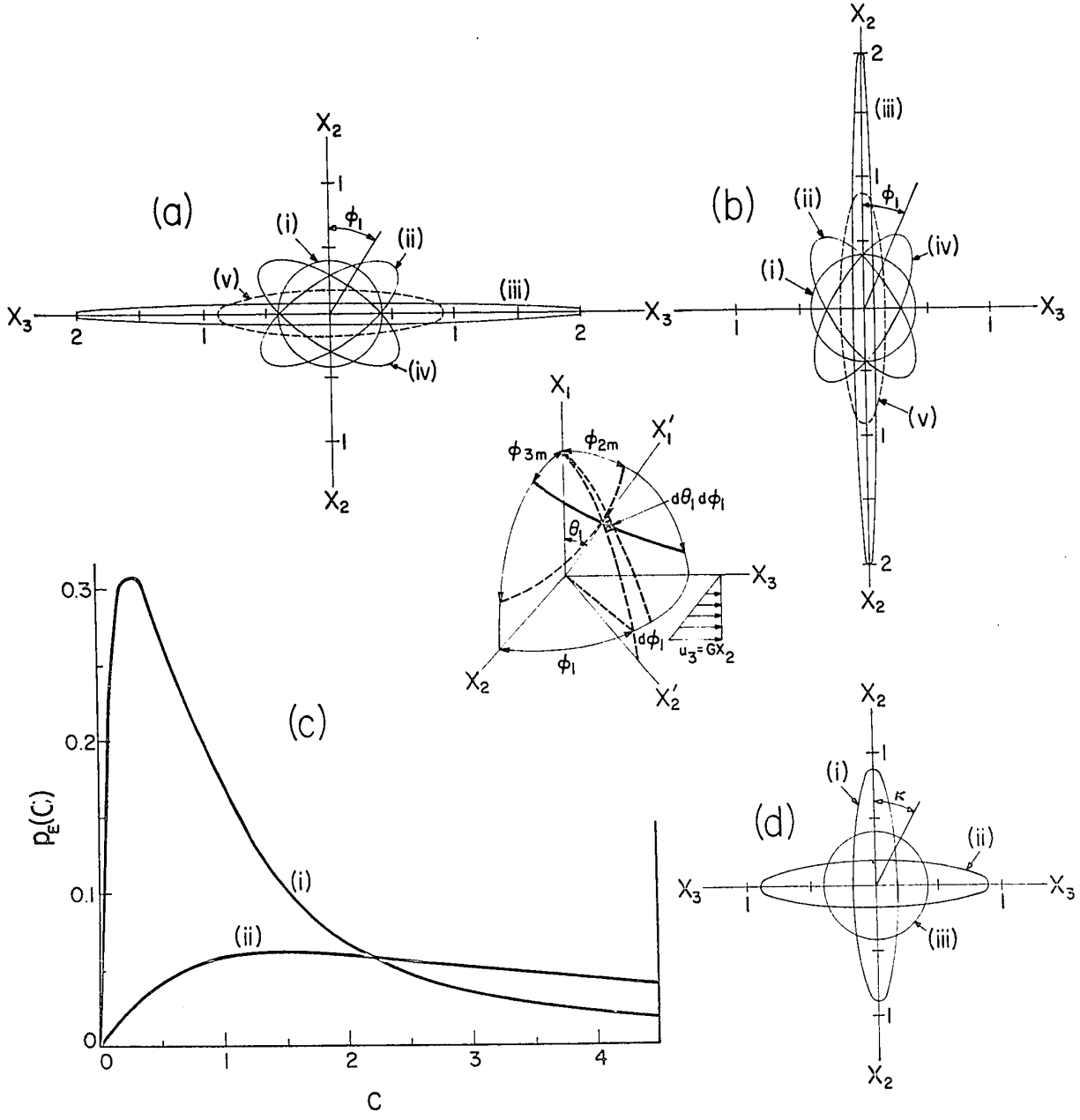
(a)
(b)
(c)
(d)
(i)
(ii)
(iii)
(iv)
(v)
X_1
X_2
X_3
X_1'
X_2'
ϕ_1
ϕ_{2m}
ϕ_{3m}
θ_1
$d\theta_1 d\phi_1$
$d\phi_1$
$u_3 = GX_2$
κ
$p_E(C)$
C
0
0.1
0.2
0.3
1
2
3
4

This corresponds to the situation in which, for $r_e > 1$, nearly all the particle axes lie approximately in the X_1X_3-plane, whilst for $r_e < 1$ most of the particles have the orientation $\phi_1 \simeq 0$.

Similarly the probability distributions $p_E(C)$ and $p(\kappa)$ can be obtained from [20]. Thus

$$p_E(C) = \int_0^{2\pi} p(C,\kappa)d\kappa = m'E(k_2) \quad , \qquad [26a]$$

where m' and k_2 are given by:

<u>for $r_e > 1$ (prolate spheroids and rods)</u>

$$m' = \frac{Cr_e}{\pi(1 + C^2)(1 + C^2r_e^2)^{1/2}} \quad , \quad k_2^2 = \frac{C^2(r_e^2 - 1)}{C^2r_e^2 + 1} \quad , \qquad [26b]$$

<u>and for $r_e < 1$ (oblate spheroids and discs)</u>

$$m' = \frac{Cr_e}{\pi(1 + C^2)^{1/2}(1 + C^2r_e^2)} \quad , \quad k_2^2 = \frac{C^2(1 - r_e^2)}{C^2 + 1} \quad , \qquad [26c]$$

and

$$p(\kappa) = \int_{-\infty}^{\infty} p(C,\kappa)dC = \frac{r_e}{2\pi(\cos^2\kappa + r_e^2\sin^2\kappa)} \quad . \qquad [27]$$

The orbit distribution $p_E(C)$ given by [26] is equivalent to [9]-3 and corresponds to the Eisenschitz[12] distribution for which orbit constant values

are assumed to be those of an initially random distribution of orientations. The corresponding cumulative distribution of orbit constants $P_E(C)$ is therefore the Eisenschitz cumulative distribution $P_E(C)$ given by [17]-1, which is

$$P_E(C) = \int_{-C}^{C} p_E(C)\,dC = 1 - \frac{2m''}{\pi}\,\Pi(\alpha_o^2, k_2) \qquad [28a]$$

where $\Pi(\alpha_o^2, k_2)$ is the complete elliptic integral of the third kind, m'' and α_o^2 are given by

<u>for $r_e > 1$,</u>

$$m'' = \frac{1}{r_e(C^2 r_e^2 + 1)^{\frac{1}{2}}}\,, \qquad \alpha_o^2 = \frac{r_e^2 - 1}{r_e^2}\,, \qquad [28b]$$

<u>and for $r_e < 1$,</u>

$$m'' = \frac{r_e}{(C^2 + 1)^{\frac{1}{2}}}\,, \qquad \alpha_o^2 = 1 - r_e^2\,, \qquad [28c]$$

and the modulus k_2 is given by [26]. The cumulative distribution $P(\kappa)$ derived from [27] is given by

$$P(\kappa) = \int_{o}^{\kappa} p(\kappa)\,d\kappa = \frac{1}{2\pi}\tan^{-1}(r_e \tan \kappa)\,. \qquad [29]$$

The values of $p_E(C)$ and $p(\kappa)$ for initially isotropic suspensions of rods ($r_e = 5$) and discs ($r_e = 0.2$) are shown in Fig. 1(c) and (d) respectively, and are representative of the experimental values of r_e used[5].

(b) Mean Projections

Although the orientation distribution $p_t(\theta_1,\phi_1)$ describes completely the resulting anisotropy of a flowing suspension, it is useful to calculate the mean values of the various particle projections used previously for the analysis of experimental results[2,3] as single measures of the mean particle orientation. Convenient choices are the projection of unit length r_i (i = 1,2,3) of a cylinder on each of the three Cartesian axes, and the projection of unit area S_{ij} (i,j = 1,2,3, i ≠ j) of the face of a cylinder on the three coordinate planes given by

$$\begin{aligned} r_1 &= S_{23} = |\cos\theta_1| \quad , \\ r_2 &= S_{13} = |\sin\theta_1\cos\phi_1| \quad , \\ r_3 &= S_{12} = |\sin\theta_1\sin\phi_1| \quad , \end{aligned} \tag{30}$$

the projections always being positive. The mean values of these projections are given by the integral

$$\bar{r}_i = \bar{S}_{jk} = \int_0^{2\pi}\int_0^{\pi} r_i \cdot p_t(\theta_1,\phi_1)\,d\theta_1 d\phi_1 \tag{31}$$

where, for a suspension of particles with initially random orientation, $p_t(\theta_1,\phi_1)$ is given by [19]. Solutions of these integrals are expressed in terms of the complete elliptic integrals and are summarized in Table I. For convenience

TABLE I

Equations for Mean Projected Lengths of Rods and Faces of Discs
for Initially Isotropic and Collision-free Suspensions

Quantity	Equations
$\bar{r}_1$ for $r_e > 1$	$\bar{r}_1 = \bar{S}_{23} = \frac{4}{\pi(m_1 + m_2)(1 - m_2)}\left[K(k_3) - \frac{2m_2}{1 + m_2}\Pi(\alpha_1^2, k_3)\right]$
$\bar{S}_{23}$ for $r_e < 1$	$k_3^2 = \frac{m_1 - m_2}{m_1 + m_2}$, $\alpha_1^2 = k_3^2\frac{1 - m_2}{1 + m_2}$
$\bar{r}_2$ for $r_e > 1$	$\bar{r}_2 = \bar{S}_{12} = \frac{2}{\pi}\left[\frac{k_4^2}{m_3^2}K(k_4) + \frac{1 - m_4k_4^2}{m_3\sqrt{m_3^2 + 4}}\Pi(\alpha_2^2, k_4) - \frac{1 - m_5k_4^2}{m_3\sqrt{m_3^2 + 4}}\Pi(\alpha_3^2, k_4)\right]$
$\bar{S}_{12}$ for $r_e < 1$	$k_4^2 = \frac{1}{2}(1 - r_e^2)(1 - \cos\frac{4\pi t}{T})$ for $r_e < 1$
	$k_4^2 = \frac{1}{2}(1 - r_e^{-2})(1 - \cos\frac{4\pi t}{T})$ for $r_e > 1$
	$\alpha_2^2 = 1/m_4$, $\alpha_3^2 = 1/m_5$
$\bar{r}_3$ for $r_e > 1$	$\bar{r}_3 = \bar{S}_{13} = \frac{2}{\pi m_3\sqrt{(m_3^2 + 4)(1 + k_5^2)}}\left[\Pi(\alpha_4, k_6) - \Pi(\alpha_5, k_6)\right]$
$\bar{S}_{13}$ for $r_e < 1$	$k_5^2 = \frac{1}{2}(r_e^{-2} - 1)(1 - \cos\frac{4\pi t}{T})$ for $r_e < 1$
	$k_5^2 = \frac{1}{2}(r_e^2 - 1)(1 - \cos\frac{4\pi t}{T})$ for $r_e > 1$
	$k_6^2 = \frac{k_5^2}{1 + k_5^2}$, $\alpha_4^2 = \frac{1 + m_4k_5^2}{m_4(1 + k_5^2)}$, $\alpha_5^2 = \frac{1 + m_5k_5^2}{m_5(1 + k_5^2)}$

m_1 and m_2 are given by [21b] and [21c] respectively; the other coefficients are $m_3^2 = \frac{1}{2}(r_e - r_e^{-1})^2(1 - \cos\frac{4\pi t}{T})$, $m_4^2 = \frac{1}{2}(1 + \sqrt{1 - 4/m_3^2})$, $m_5^2 = \frac{1}{2}(1 - \sqrt{1 - 4/m_3^2})$.

Note that the equalities shown for $\bar{r}_i$ of rods and $\bar{S}_{ij}$ of discs apply only for when their r_e's are reciprocals of one another. Details of the derivation of these equations are given in Reference (13).

TABLE II

Alternate Formulas to those in Table I for Mean Projections

Quantity	Equations
$\bar{r}_1$	$\bar{r}_1 = \bar{S}_{23} = \frac{4}{\pi}\left[\frac{1}{(m_1 + m_2)(1 + m_2)} K(k_3) - \frac{1}{\{(m_1^2 - 1)(1 - m_2^2)\}^{\frac{1}{2}}} K(k_3) Z(\beta , k_3) \right]$
$\bar{S}_{23}$	$\beta = \sin^{-1}\left[\frac{(m_1 + m_2)(1 - m_2)}{(m_1 - m_2)(1 + m_2)} \right]^{\frac{1}{2}}$
$\bar{r}_2$	$\bar{r}_2 = \bar{S}_{12} = \frac{1}{m_3\sqrt{m_3^2 + 4}}\left[\frac{2}{\pi} K(k_4) + \left(\frac{m_4(1 - m_4 k_4^2)}{m_4 - 1}\right)^{\frac{1}{2}} \{1 - \Lambda_o(\phi_1, k_4)\} - \left(\frac{m_5(1 - m_5 k_4^2)}{m_5 - 1}\right)^{\frac{1}{2}} \Lambda_o(\phi_2, k_4) \right]$
$\bar{S}_{12}$	$\phi_1 = \sin^{-1}\left(\frac{m_4 - 1}{m_4(1 - k_4^2)}\right)^{\frac{1}{2}}, \qquad \phi_2 = \sin^{-1}\left(\frac{1}{1 - m_5 k_4^2}\right)^{\frac{1}{2}}$
$\bar{r}_3$	$\bar{r}_3 = \bar{S}_{13} = \frac{1}{m_3\sqrt{m_3^2 + 4}}\left[\frac{2(1 + m_5 k_5^2)}{\pi\sqrt{1 + k_5^2}} K(k_6) + \left(\frac{m_4(1 + m_4 k_5^2)}{m_4 - 1}\right)^{\frac{1}{2}} \{1 - \Lambda_o(\phi_3, k_6)\} - \left(\frac{m_5(1 + m_5 k_5^2)}{m_5 - 1}\right)^{\frac{1}{2}} \Lambda_o(\phi_4, k_6) \right]$
$\bar{S}_{13}$	$\phi_3 = \sin^{-1}\left(\frac{m_4 - 1}{m_4}\right)^{\frac{1}{2}}, \qquad \phi_4 = \sin^{-1}\left(1 - m_5 k_5^2\right)^{\frac{1}{2}}$

As in Table I, equalities of $\bar{r}_i$ and $\bar{S}_{jk}$ appear only when $\bar{r}_e$'s of rods and discs are reciprocals.

in the numerical evaluation, Table II provides alternate formulas of the mean projections, where $\Lambda_o(\Phi_i,k)$ is Heuman's Lambda function and $Z(\beta,k)$ is the Jacobian Zeta function. The variation of $\bar{r}_i$ for $r_e = 10$ and $\bar{S}_{ij}$ for $r_e = 0.1$ with time is shown in Fig. 2 (a). All mean values at the initial time and at times $t = T/2, T, 3T/2$ etc., are 0.5 corresponding to random orientation, while for times $t = T/4$, $3T/4$, $5T/4$ etc., $\bar{r}_1$ and $\bar{r}_2$ (also $\bar{S}_{12}$ and $\bar{S}_{13}$) assume their minimum values and $\bar{r}_3$ (also $\bar{S}_{13}$) its maximum, corresponding to the orientation distribution $p_t(\theta_1,\phi_1)$ given by [25]. It is readily shown from the equations for $\bar{r}_i = \bar{S}_{jk}$ that $d\bar{r}_i/dt = 0$ at $t = 0, T/2, T, 3T/2$ etc., so that slopes of the curves in Fig. 2(a) are continuous at $\bar{r}_i = \bar{S}_{jk} = 0.5$.

Since the projections in [30] are the absolute values, the period of oscillation of $\bar{r}_i = \bar{S}_{jk}$ must always be $T/2$ no matter what the initial distribution of orientations.

The equalities $\bar{r}_1$ (rods $r_e = 10$) $= \bar{S}_{23}$ (discs $r_e = 1/10$), $\bar{r}_2 = \bar{S}_{12}$ and $\bar{r}_3 = \bar{S}_{13}$ illustrated in Fig. 2(a) result from the permutability of r_e and r_e^{-1} in a number of the relevant equations. Thus it is seen from [21] that the orientation distributions $p_t(\theta_1)$ for the initially isotropic case are identical for $r_e = R$ and $r_e = R^{-1}$, R being a specific value. Since, from [30], $\bar{r}_1$ and $\bar{S}_{23}$ depend only upon θ_1, the mean values $\bar{r}_1$ for rods R and $\bar{S}_{23}$ for discs R^{-1} are the same.

FIGURE 2

(a) Variations of mean orientation parameters for rods ($r_e = 10$) and discs ($r_e = 1/10$) with time; $\bar{r}_1$ and $\bar{S}_{23}$ (broken line), $\bar{r}_2$ and $\bar{S}_{12}$ (solid line), and $\bar{r}_3$ and $\bar{S}_{13}$ (broken and dotted line). For explanation of coincidences of $\bar{r}_i$ and $\bar{S}_{jk}$ for rods and discs where r_e's are reciprocals, see text. Since $(d\bar{r}_i/dt)_{t=o} = 0$, the peaks appearing at each half rotation are not singularities.

(b) Variations of the intrinsic viscosity $[\eta]$ for a suspension of prolate spheroids ($r_e = 10$) calculated from [48].

(c) Variations of three intrinsic normal stress differences for prolate spheroids ($r_e = 10$) calculated from [50]; $[\xi_{12}]$ is shown as the solid line, $[\xi_{23}]$ by the dashed line and $[\xi_{31}]$ by the dotted line.

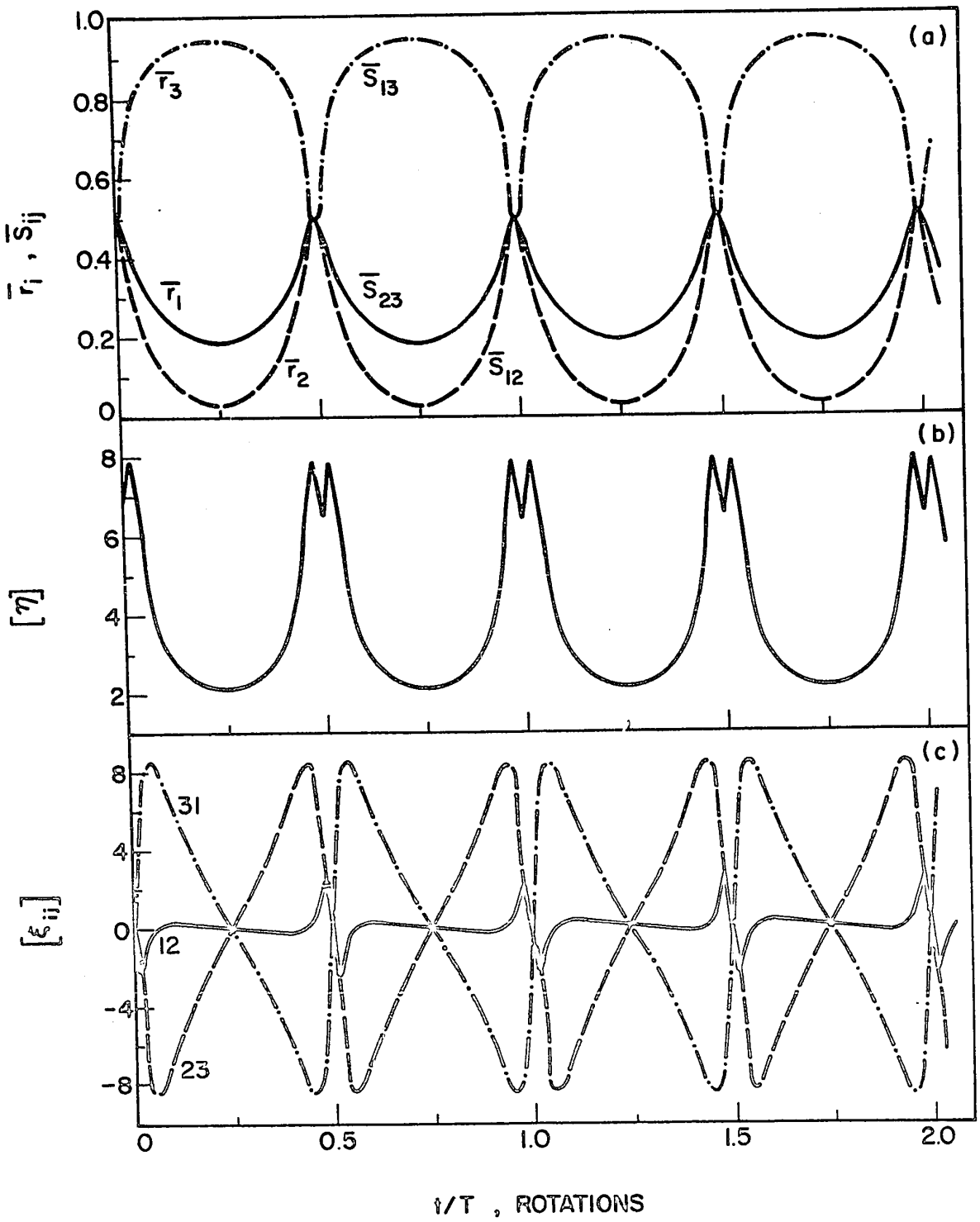
(a)
(b)
(c)
$\bar{r}_3$
$\bar{S}_{13}$
$\bar{r}_1$
$\bar{S}_{23}$
$\bar{r}_2$
$\bar{S}_{12}$
$\bar{r}_i$, $\bar{S}_{ij}$
$[\eta]$
$[\xi_{ij}]$
31
12
23
1.0
0.8
0.6
0.4
0.2
0
8
6
4
2
-4
-8
0.5
1.0
1.5
2.0
t/T , ROTATIONS

On the other hand, it is readily seen from [17] and [22] that $p_t(\phi_1)$ for rods R and $p_t(\phi_1 - \pi/2)$ for discs R^{-1} are equal. This is illustrated graphically in Fig.1(a) and (b) for another example in which the r_e's bear a reciprocal relationship, so that the polar diagrams become coincident when one on set is rotated through $\phi_1 = \pi/2$; similar behaviour is shown by the polar diagrams for $p(\kappa)$ in Fig. 1(d) as is readily shown from [27]. It follows that the products $p_t(\phi_1) \times |\sin\phi_1|$ and $p_t(\phi_1) \times |\cos\phi_1|$ for rods R are respectively equal to $p_t(\phi_1 - \pi/2) \times |\cos(\phi_1 - \pi/2)|$ and $p_t(\phi_1 - \pi/2) \times |\sin(\phi_1 - \pi/2)|$ for discs R^{-1}. Therefore, from the complete integration of [31], integration of which with respect to θ_1 is unaffected by the permutation for the reason stated above, $\bar{r}_2$ and $\bar{r}_3$ for rods R are equal to $\bar{S}_{12}$ and $\bar{S}_{13}$ respectively for discs R^{-1}.

Thus we have the following relations between $\bar{r}_i$ and $\bar{S}_{jk}$ for suspensions of initially random orientation

$$\bar{r}_1(r_e) = \bar{r}_1(r_e^{-1}) = \bar{S}_{23}(r_e) = \bar{S}_{23}(r_e^{-1}) \quad ,$$

$$\bar{r}_2(r_e) = \bar{r}_3(r_e^{-1}) = \bar{S}_{13}(r_e) = \bar{S}_{12}(r_e^{-1}) \quad ,$$

$$\bar{r}_3(r_e) = \bar{r}_2(r_e^{-1}) = \bar{S}_{12}(r_e) = \bar{S}_{13}(r_e^{-1})$$

for a given value of r_e.

(c) Viscosity and Normal Stresses

(i) Suspensions of Spheroids

The general theory of the rheological behaviour of a suspension in a Newtonian fluid developed by Cox and Brenner[14] may be applied to the present study of suspensions of spheroids and circular cylinders. We will now consider a suspension of spheroids, a suspension of long slender rods being examined separately in the following section. Application of the Cox and Brenner theory requires the introduction of the particle coordinate axes X_i' as shown in Figure 1. The flow field u_i when expressed relative to the x_i'-system of axes (and denoted by u_i') is given by

$$u_i = M_{ij}u_j' \qquad \text{or} \qquad u_i' = M_{ji}u_j \qquad [32]$$

where M_{ij} is the transformation tensor given by

$$M = \begin{pmatrix} \cos\theta_1 & -\sin\theta_1 & 0 \\ \cos\phi_1\sin\theta_1 & \cos\phi_1\cos\theta_1 & -\sin\phi_1 \\ \sin\phi_1\sin\theta_1 & \sin\phi_1\cos\theta_1 & \cos\phi_1 \end{pmatrix} \qquad [33]$$

Here any symbol with a 'prime' denotes its value given relative to the x_i'-system, its value relative to the x_i'-system being obtained by means of an equation of the form [32].

The disturbance flow v_i' caused by the presence of a spheroidal particle in a viscous flow field is given by Jeffery ([52]-6), as

$$v_i' = u_i' - u_{io}' = -\frac{4x_i'}{r^5} B_{jk}' x_j' x_k' \qquad [34]$$

where u_i' is the complete flow field, u_{io}' is the undisturbed fluid flow, and r is the distance from the particle center: $r = (x_1'^2 + x_2'^2 + x_3'^2)^{\frac{1}{2}}$. The term B_{ij}' is a function of particle shape and orientation and is given by [25]-6 and [39]-6.

On the other hand, the disturbance flow produced by a rigid particle of arbitrary shape in a viscous flow field was obtained[14] in the tensor form

$$v_i' = A_j' s_{ij} + A_{jk}' \frac{\partial s_{ij}}{\partial x_k'} \qquad [35]$$

where

$$s_{ij} = \frac{\delta_{ij}}{r} + \frac{x_i' x_j'}{r^3} \quad ,$$

the terms involving A_j' and A_{jk}' representing flow fields produced by a point force and a point force doublet respectively. Since there is no external force acting on the particle to balance the hydrodynamic force, A_j' must vanish. Also since no resultant couple acts on the particle, the tensor A_{ij}' must be symmetric, from which it follows that

$$v_i' = A_{jk}' \frac{\partial s_{ij}}{\partial x_k'} = \frac{1}{2} A_{jk}' \left(\frac{\partial s_{ij}}{\partial x_k'} + \frac{\partial s_{ik}}{\partial x_j'} \right) \qquad [36]$$

Furthermore A_{ii}' may be taken to be zero (i.e. $A_{11}' + A_{22}' + A_{33}' = 0$) since $\delta_{jk} \frac{\partial s_{ij}}{\partial x_k'} = 0$. Therefore, the disturbance flow v_i' may be written as

$$v_i' = \frac{3 x_i'}{r^5} A_{jk}' x_j' x_k' \qquad [37]$$

Comparing the two equations [34] and [37], the tensor A_{ij}' is obtained as

$$A_{ij}' = \frac{4}{3} B_{ij}' \qquad [38]$$

If the undisturbed flow is the plane shear flow defined by [1], the tensor A_{ij}' for a spheroidal particle,

obtained from Jeffery's values of B'_{ij}, is expressed in terms of the axis ratio and orientation as

$$A'_{11} = \frac{G}{9\beta''_o} \sin^2\theta_1 \sin 2\phi_1 \quad ,$$

$$A'_{22} = \frac{G}{9a^2\alpha'_o\beta''_o} \{(\tfrac{1}{2}\sin 2\phi_1 + \cos^2\theta_1 \sin 2\phi_1)\beta''_o - \frac{\alpha''_o}{2}\sin^2\theta_1 \sin 2\phi_1\} \quad ,$$

$$A'_{33} = \frac{-G}{9b^2\alpha'_o\beta''_o} \{(\sin 2\phi_1 + \tfrac{1}{2}\cos^2\theta_1 \sin 2\phi_1)\beta''_o + \frac{\alpha''_o}{2}\sin^2\theta_1 \sin 2\phi_1\} \quad ,$$

$$A'_{12} = A'_{21} = \frac{G}{6(a^2 + b^2)\beta'_o} \sin 2\theta_1 \sin 2\phi_1 \quad , \qquad [39]$$

$$A'_{23} = A'_{32} = \frac{G}{6b^2\alpha'_o} \cos\theta_1 \cos 2\phi_1 \quad ,$$

$$A'_{13} = A'_{31} = \frac{G}{3(a^2 + b^2)\beta'_o} \sin\theta_1 \cos 2\phi_1 \quad ,$$

where b and a are the cross sectional radius at center and semi-length of the spheroid respectively. The terms α'_o, β'_o, α''_o, β''_o in [39] are spheroidal integrals and are given as follows[12,15],

$$\alpha'_o = \frac{[2r_e^3 - 5r_e - 3Y]}{4b^5(r_e^2 - 1)^2} \quad ,$$

$$\beta'_o = \frac{[r_e + 2r_e^{-1} - 3Y]}{b^5(r_e^2 - 1)^2} \quad , \qquad [40]$$

$$\alpha''_o = \frac{[2r_e^3 + r_e - (4r_e^2 - 1)Y]}{4b^3(r_e^2 - 1)^2} \quad ,$$

$$\beta''_o = \frac{[-3r_e + (2r_e^2 + 1)Y]}{b^3(r_e^2 - 1)^2} \quad ,$$

where

$$Y = \frac{\cos^{-1} r_e}{(1 - r_e^2)^{1/2}} = \frac{\cosh^{-1} r_e}{(r_e^2 - 1)^{1/2}} \quad .$$

The value of A_{ij} may then be obtained using the transformation

$$A_{ij} = M_{ip} M_{jq} A'_{pq} \quad . \qquad [41]$$

If we assume that all particles in the suspension have the same size and shape and that there are no particle interactions so that at any particular time the orientation probability distribution is given by [19], then the macroscopic stress tensor P_{ij} for the suspension is related to the value of A_{ij} by

$$P_{ij} = p_{ij} + 8\pi\eta_o N\bar{A}_{ij} \qquad [42]$$

where N is the number of particles in unit volume and $\bar{A}_{ij}$ is the mean value of A_{ij} for particles of the suspension at every instant, being given by

$$\bar{A}_{ij} = \int_o^{2\pi} \int_o^{\pi} A_{ij} p_t(\theta_1, \phi_1) d\theta_1 d\phi_1 \quad . \qquad [43]$$

The term p_{ij} is the stress tensor for a suspending medium of viscosity η_o, which, for the given plane shear flow, is

given by

$$P_{ij} = \begin{pmatrix} -p & 0 & 0 \\ 0 & -p & \eta_o G \\ 0 & \eta_o G & -p \end{pmatrix} \qquad [44]$$

where p is the pressure. If the viscosity of the suspension has a value η, the shear stress $P_{23} = P_{32}$ may be written as

$$P_{23} = \eta G = \eta_o G + 8\pi\eta_o N\bar{A}_{23} \qquad [45]$$

so that the intrinsic viscosity $[\eta]$ defined by

$$\frac{\eta}{\eta_o} = 1 + [\eta]c \qquad [46]$$

where c is the volume fraction of spheroids ($= \frac{4}{3}\pi ab^2 N$), may be obtained as

$$[\eta] = \frac{6\bar{A}_{23}}{ab^2 G} \quad . \qquad [47]$$

Substituting $\bar{A}_{23}$ obtained from [39], [41] and [43], we obtain

$$[\eta] = C_1 \overline{\sin^4\theta_1 \sin^2 2\phi_1} + C_2 \overline{\cos^2\theta_1} + C_3 \overline{\sin^2\theta_1} \qquad [48]$$

$$C_1 = \frac{1}{2b^5 r_e}\left(\frac{\alpha_o''}{\alpha_o'\beta_o''} + \frac{1}{\alpha_o'} - \frac{4}{(r_e^2+1)\beta_o'}\right),$$

$$C_2 = \frac{1}{b^5 r_e \alpha_o'} \quad , \quad C_3 = \frac{2}{b^5 r_e (r_e^2+1)\beta_o'} \quad .$$

A bar over symbols indicates their mean values obtained by means of equations of the form [43]. Eq. [48] is equivalent to the result of Jeffery[6] who obtained the viscosity by calculating the rate of energy dissipation due to the presence of a spheroid in a viscous shear flow. The normal stress differences are, from [42],

$$P_{ii} - P_{jj} = 8\pi\eta_o N\ (\bar{A}_{ii} - \bar{A}_{jj}) \qquad [49]$$

without summation over i or j.

The evaluation of $\bar{A}_{11}$, $\bar{A}_{22}$ and $\bar{A}_{33}$ from [39] and [41] and subsequent substitution into [49] yields

$$[\xi_{12}] = C_1\ \{2\ \overline{\sin^2\theta_1 \sin 2\phi_1} - 3\ \overline{\sin^4\theta_1 \sin 2\phi_1} - \tfrac{1}{2}\ \overline{\sin^4\theta_1 \sin 4\phi_1}\}$$
$$+ (C_2 - C_3)\ \overline{\sin^2\theta_1 \sin 2\phi_1}$$

$$[\xi_{23}] = C_1\ \overline{\sin^4\theta_1 \sin 4\phi_1} \qquad [50]$$

$$[\xi_{31}] = C_1\ \{3\ \overline{\sin^4\theta_1 \sin 2\phi_1} - 2\ \overline{\sin^2\theta_1 \sin 2\phi_1} - \tfrac{1}{2}\ \overline{\sin^4\theta_1 \sin 4\phi_1}\}$$
$$- (C_2 - C_3)\ \overline{\sin^2\theta_1 \sin 2\phi_1}\ ,$$

where $[\xi_{ij}] = (P_{ii} - P_{jj})/\eta_o Gc$ is the intrinsic normal stress difference defined by analogy to the intrinsic viscosity $[\eta]$. It should be noted that the quantity usually discussed is $(P_{22} - P_{33})$, corresponding to $[\xi_{23}]$.

The other components of shear stress, $P_{12} = P_{21}$ and $P_{13} = P_{31}$ are

$$\frac{P_{12}}{\eta_o G c} = 4C_1 \overline{\sin^3\theta_1\cos\theta_1\sin\phi_1\cos^2\phi_1} + (C_3 - C_2) \overline{\sin\theta_1\cos\theta_1\sin\phi_1}$$

$$\frac{P_{13}}{\eta_o G c} = 4C_1 \overline{\sin^3\theta_1\cos\theta_1\sin^2\phi_1\cos\phi_1} + (C_3 - C_2) \overline{\sin\theta_1\cos\theta_1\cos\phi_1} \quad . \qquad [51]$$

The values of P_{12} and P_{13} are identically zero for an initially isotropic suspension for all time, but not equal to zero in general (for example when all particles are initially aligned in some direction with $\theta \neq 0$ or $\pi/2$).

The spheroidal integrals α_o', β_o' etc., can be approximated for an elongated spheroid ($r_e >> 1$) by

$$\alpha_o' \simeq \frac{1}{2b^5 r_e} \quad , \quad \alpha_o'' \simeq \frac{1}{2b^3 r_e} \quad ,$$

$$\beta_o' \simeq \frac{1}{b^5 r_e^3} \quad , \quad \beta_o'' \simeq \frac{2(\ell n 2r_e - 1.5)}{b^3 r_e^3} \qquad [52a]$$

and for a very flat oblate spheroid ($r_e << 1$) by

$$\alpha_o' \simeq \frac{3\pi}{8b^5} \quad , \quad \alpha_o'' \simeq \frac{\pi}{8b^3} \quad ,$$

$$\beta_o' \simeq \frac{2}{b^5 r_e} \quad , \quad \beta_o'' \simeq \frac{\pi}{2b^3} \quad . \qquad [52b]$$

The constants C_1, C_2, C_3 then take the values

<u>for $r_e >> 1$</u>,

$$C_1 = \frac{r_e^2}{4(\ell n 2r_e - 1.5)} \quad , \quad C_2 = C_3 = 2, \qquad [53a]$$

(ii) Suspension of Long Slender Particles

Although rotation of a long slender axisymmetric particle in a plane shear flow has been shown to be identical to that of a spheroid[7-9], its disturbance flow is generally different from that produced by a spheroid. Therefore, in this section, we consider a suspension of long slender axisymmetric particles of length 2a and cross-sectional radius b at its mid-point. Taking the X_i'-axes as before with the X_1'-axis lying along the particle's center-line, we define $s = x_1'/a$ as a dimensionless distance along particle axis and a function $\lambda(s)$ such that $b\lambda$ is the cross-sectional radius of the particle at the position $s[|s| \leq 1]$ on its axis. Following the analysis given by Cox[16], it is seen that, to the lowest order, the disturbance flow produced by such a particle is that produced by a line of force $-\mathcal{F}_i'$ per unit length acting at the particle axis. For the given plane shear flow, this is evaluated to be

$$\mathcal{F}_1' = \pi\eta_o G x_1' \left[\frac{1}{\ell n r_p} + \frac{\frac{3}{2} - \ell n 2 - \frac{1}{2}\ell n\left(\frac{1-s^2}{\lambda^2}\right)}{(\ell n r_p)^2}\right] \sin^2\theta_1 \sin 2\phi_1 \qquad [54]$$

$$\mathcal{F}_2' = \mathcal{F}_3' = 0$$

where $r_p = a/b$ is the axis ratio.

The tensor A_{ij}' has therefore only one component

and for $r_e << 1$,

$$C_1 = \frac{5}{3\pi r_e} \quad , \quad C_2 = \frac{8}{3\pi r_e} \quad , \quad C_3 = 1 \; . \qquad [53b]$$

The second term on the right hand side of [50] thus vanishes for $r_e >> 1$, but is non-zero for $r_e << 1$. The instantaneous changes in the intrinsic viscosity and normal stress differences for a collision-free suspension of spheroids of $r_e = 10$ are shown in Fig. 2(b) and (c) respectively. Inspection of [48] shows that the contribution to $[\eta]$ from a single particle is, if a particle is a prolate spheroid, maximum at the orientations $\theta_1 = \pi/2$ and $\phi_1 = \pi/4$ or $3\pi/4$ at which $[\eta] = C_1 + C_2$ and minimum at $\theta_1 = 0$ corresponding to $[\eta] = C_2$. On the other hand for an oblate spheroid the maximum occurs at $\theta_1 = 0$ corresponding to $[\eta] = C_2$ and the minimum at $\theta_1 = \pi/2$ and $\phi_1 = 0, \pi/2, \pi, 3\pi/2$, at which $[\eta]$ takes the value of C_3. It is also noted that the normal stress differences vanish at every quarter period when the orientation distribution $p_t(\theta_1,\phi_1)$ is symmetrical about the X_1X_3-plane.

It also should be noted that when $r_e = 1$ (i.e. a=b) the spheroidal integrals given by [40] reduce to $\alpha_o' = \beta_o' = 2/5\ a^5$ and $\alpha_o'' = \beta_o'' = 4/15\ a^3$ and the coefficients become $C_1 = 0$ and $C_2 = C_3 = 2.5$, and $[\eta] = 5/2$, the well-known Einstein result for rigid spheres with all the other stress components P_{ij} vanishing.

$$A'_{11} = \frac{1}{8\pi\eta_o}\int_{-a}^{+a} \mathcal{F}'_1 x'_1 dx'_1 = \frac{Ga^3}{12(\ell n 2r_p + K)} \sin^2\theta_1 \sin 2\phi_1 \qquad [55]$$

where

$$K = -\frac{3}{2} + \frac{3}{4}\int_{-1}^{+1} s^2 \ell n \left(\frac{1 - s^2}{\lambda^2}\right) ds \qquad [56]$$

all other components vanishing. The tensor A_{ij}, by the transformation [41], is obtained as

$$A_{11} = \frac{C_1 Ga^3}{3r_p^2} \sin^2\theta_1 \cos^2\theta_1 \sin 2\phi_1$$

$$A_{22} = \frac{C_1 Ga^3}{3r_p^2} \sin^4\theta_1 \sin 2\phi_1 \cos^2\phi_1$$

$$A_{33} = \frac{C_1 Ga^3}{3r_p^2} \sin^4\theta_1 \sin 2\phi_1 \sin^2\phi_1$$

[57]

$$A_{12} = A_{21} = \frac{2C_1 Ga^3}{3r_p^2} \sin^3\theta_1 \cos\theta_1 \sin\phi_1 \cos^2\phi_1$$

$$A_{13} = A_{31} = \frac{2C_1 Ga^3}{3r_p^2} \sin^3\theta_1 \cos\theta_1 \sin^2\phi_1 \cos\phi_1$$

$$A_{23} = A_{32} = \frac{C_1 Ga^3}{6r_p^2} \sin^4\theta_1 \sin^2 2\phi_1$$

where

$$C_1 = \frac{r_p^2}{4(\ell n 2 r_p + K)} \qquad [58]$$

For a spheroid ($\lambda^2 = 1 - s^2$), the constant $K = -1.5$, the present C_1 being identical to that given by [53a]. However for a cylindrical rod ($\lambda = 1$), the value of K is $(\ell n 2 - \frac{17}{6}) = -2.14$.

If the particle has an orientation with either $\theta_1 = 0$ or $\phi_1 = 0$ or $\pi/2$, the disturbance flow given by the above value of A_{ij} is identically zero. Thus, for these cases we must evaluate the disturbance flow to the next higher order. Firstly, when the particle has an orientation with either $\phi_1 = 0$ or $\pi/2$, by writing the undisturbed flow velocity and particle center-line velocity relative to the x_i'-axes and making use of the theory for long slender particles[11,16], it may be shown that for a particle with pointed ends (such as a spindle or double cone) the disturbance produced by the particle is that produced by a line of force per unit length ($-\mathcal{F}_i'$) and a line of force doublets of magnitude g_{ij}' acting at the particle center-line (g_{ij}' being the moment of a doublet of forces directed in the i-th direction with a relative separation in the j-th direction) where

$$\mathcal{F}_1' = \mathcal{F}_2' = 0$$

$$\mathcal{F}_3' = \frac{4\pi\eta_o Ga}{r_p^2} \sin\theta_1 \left[-\lambda \frac{d\lambda}{ds} + \frac{1}{\ell n r_p} \left\{ \lambda \frac{d\lambda}{ds} + \left(\frac{r_p}{r_e}\right)^2 s \right\} + O\left(\frac{1}{\ell n r_p}\right)^2 \right] \qquad [59]$$

and

$$g'_{13} = \frac{2\pi\eta_o Ga^2\lambda^2\sin\theta_1}{r_p^2} \qquad [60]$$

$$g'_{23} = g'_{32} = \frac{2\pi\eta_o Ga^2\lambda^2\cos\theta_1}{r_p^2}$$

all other components of g'_{ij} being zero. By making use of the relation[11)]

$$\left(\frac{r_p}{r_e}\right)^2 = \frac{3}{4}\Lambda + 0\left(\frac{1}{\ell n r_p}\right) \qquad [61a]$$

where

$$\Lambda = \int_{-1}^{+1} \lambda^2 ds \qquad [61b]$$

between r_e and r_p for slender bodies with pointed ends, the above value of $\mathcal{F}'_3$ may be written as

$$\mathcal{F}'_3 = \frac{4\pi\eta_o Ga}{r_p^2}\sin\theta_1\left[-\frac{d\lambda}{ds} + \frac{1}{\ell n r_p}\left\{\lambda\frac{d\lambda}{ds} + \frac{3}{4}s\Lambda\right\} + 0\left(\frac{1}{\ell n r_p}\right)^2\right] \qquad [62]$$

The tensor A'_{ij}, given by

$$A'_{ij} = \frac{1}{8\pi\eta_o}\int_{-a}^{+a}(g'_{ij} + \mathcal{F}'_i x'_j)dx'_1 \qquad [63]$$

may be evaluated as

$$A'_{23} = A'_{32} = \frac{1}{8\pi\eta_o}\int_{-a}^{+a} g'_{23}dx'_1 = \frac{Ga^3}{4r_p^2}\Lambda\sin\theta_1$$

$$A'_{13} = \frac{1}{8\pi\eta_o} \int_{-a}^{+a} g'_{13}dx'_1 = \frac{Ga^3}{4r_p^2} \Lambda \cos\theta_1$$

$$A'_{31} = \frac{1}{8\pi\eta_o} \int_{-a}^{+a} \mathcal{F}'_3 x'_1 dx'_1 = \frac{Ga^3}{4r_p^2} \Lambda \cos\theta_1 \qquad [64]$$

so that A_{ij}, by the transformation [41], is

$$A_{23} = A_{32} = \frac{Ga^3}{4r_p^2} \Lambda \qquad [65]$$

all other components being zero. While this analysis is valid only for bodies with pointed ends, the final result [65] nevertheless applies to particles with blunt ends (such as cylindrical rods) since, for such particles, the disturbance flow is still produced by a line of force doublets given by [60], together with a line of force $-\mathcal{F}'_{\not i} = (0,0,-\mathcal{F}'_3)$ of unknown strength. The values of A'_{23}, A'_{32} and A'_{13} are therefore as given by [64]. However since there is no external couple on the particle, the tensor A'_{ij} must be symmetric[13] and so

$$A'_{31} = A'_{13} = \frac{Ga^3}{4r_p^2} \Lambda \cos\theta_1 \qquad [66]$$

which is the same value as obtained for particles with pointed ends. Thus [65] is valid whether or not the particle has pointed ends.

For the other case which must be considered, namely $\theta_1 = 0$, the disturbance flow is entirely that which is produced by a line of force doublets[11] with magnitude

$$g'_{22} = - g'_{33} = \frac{2\pi\eta_o Ga^2\lambda^2}{r_p^2} \sin 2\phi_1$$
$$g'_{23} = + g'_{32} = \frac{2\pi\eta_o Ga^2\lambda^2}{r_p^2} \cos 2\phi_1 \qquad [67]$$

Substitution into [63] and transformation into the x_i-system of axes yields

$$A_{23} = A_{32} = \frac{Ga^3}{4r_p^2} \Lambda \qquad [68]$$

all other components of A_{ij} being zero. This result is valid whether or not the particle has pointed ends, since it may be shown that for a particle rotating in a shear flow in the orientation $\theta_1 = 0$, the effects of the particle ends are negligible[11]. Thus for a general axisymmetric slender particle one has

$$A_{23} = A_{32} = \frac{C_1 Ga^3}{6r_p^2} \sin^4\theta_1 \sin^2 2\phi_1 + \frac{Ga^3}{4r_p^2} \Lambda \qquad [69]$$

all other components of A_{ij} being given by [57].

The shear stress P_{23} within a suspension of such

particles is then given by [45] so that the intrinsic viscosity $[\eta]$ defined by [46] may be obtained as

$$[\eta] = \frac{8\bar{A}_{23}}{ab^2 G\ \Lambda} \qquad [70]$$

where the volume fraction of particles is given by $\pi ab^2 N\ \Lambda$. Substitution of the value of $\bar{A}_{23}$ from [69] yields

$$[\eta] = \frac{4}{3}\ \Lambda\ C_1\ \overline{\sin^4\theta_1 \sin^2 2\phi_1} + 2 \quad . \qquad [71]$$

While there are errors of order (Ga^3/r_p^2) in the values of A_{ij} given by equations [57] and [69] for $\theta_1 \neq 0$ and $\phi_1 \neq 0$, $\pi/2$, the inclusion of the term $(Ga^3/4r_p^2)\ \Lambda$ in the expression for $A_{23} = A_{32}$ ensures that the fractional error in A_{ij} is small even near $\theta_1 = 0$ or $\phi_1 = 0, \pi/2$. For a spheroid ($\lambda^2 = 1 - s^2$), the value of $[\eta]$ given by [71] reduces to the equation [48] with C_1, C_2 and C_3 given by [53a], while for a cylindrical rod ($\lambda = 1$), the value of $[\eta]$ is

$$[\eta] = \frac{2}{3}\ C_1\ \overline{\sin^4\theta_1 \sin^2 2\phi_1} + 2 \quad . \qquad [72]$$

with C_1 given by [58]. Thus we see that, for the same

orientation distribution, the viscosity of a suspension of rods is higher than that for a suspension of spheroids with the same axis-ratio and number density N. However the converse is true for a suspension of rods and spheroids with the same axis-ratio and concentration c.

The normal stress differences for a suspension of long slender particles of general shape may be obtained from [57] and [69] and are thus given by

$$[\xi_{12}] = \frac{4C_1}{3\Lambda}\left(2\,\overline{\sin^2\theta_1\sin 2\phi_1} - 3\,\overline{\sin^4\theta_1\sin 2\phi_1} - \tfrac{1}{2}\,\overline{\sin^4\theta_1\sin 4\phi_1}\right)$$

$$[\xi_{23}] = \frac{4C_1}{3\Lambda}\,\overline{\sin^4\theta_1\sin 4\phi_1} \qquad [73]$$

$$[\xi_{31}] = \frac{4C_1}{3\Lambda}\left(3\,\overline{\sin^4\theta_1\sin 2\phi_1} - 2\,\overline{\sin^2\theta_1\sin 2\phi_1} - \tfrac{1}{2}\,\overline{\sin^4\theta_1\sin 4\phi_1}\right)$$

where C_1 is given by [58]. For a spheroid ($\lambda^2 = 1 - s^2$), these equations reduce to the values given by [50] with C_1, C_2 and C_3 given by [53a].

The other stress components $P_{12} = P_{21}$ and $P_{13} = P_{31}$ obtained from [57] are similar to [51] except that the coefficient of the first term is given by 4 times that given by [73] and the second term vanishes.

Since the equations describing the non-Newtonian rheological properties of suspensions of spheroids ([48], [50] and [52]) and of long slender rods ([71] and [73]) are given in terms of particle orientation, then if the distribution of particle orientations is known $[\eta]$ and $[\xi_{ij}]$ can be evaluated from the appropriate mean orientation parameters. The examples shown in Fig. 2 are calculated for a collision-free suspension of spheroids of $r_e = 10$ are also representative of all prolate spheroids and long slender rods. It should be noted that $[\xi_{ij}]$ vanishes when the probability distribution $p_t(\phi_1) = p_t(\pi - \phi_1)$ (i.e., $p_t(\phi_1)$ is symmetrical about $\phi_1 = \pi/2$ and π, for example at t = 0, T/4, T/2, 3T/4 etc., as in Fig. 1).

Although a theory for the rheology of dilute suspensions of discs is not yet available, it is speculated that the equations for large discs ($r_p << 1$) are not very different from those of oblate spheroids at the limit of $r_e \to 0$ since the disturbances produced by the two particles are probably very similar, unlike the cases of prolate spheroids and of rods of $r_e >> 1$ considered above.

4. EFFECT OF VARIATION IN PARTICLE SHAPE

(a) General

As will be shown in the following Chapter[5], the measured orientation distributions in a flowing suspension of cylindrical particles show damped oscillations which die away after a few particle rotations in contrast to the undamped oscillations discussed previously. One of the possible sources of damping is the variation of r_e amongst the particles of the suspension to cause variations in the angular velocities corresponding to a given θ_1, ϕ_1, and variations in the period T. Thus while all contributions to $p_t(\theta_1,\phi_1)$ initially oscillate in phase with one another, they gradually get out of phase as time proceeds. As a result the oscillations of the probability orientation distribution $p_t(\theta_1,\phi_1)$ for such a suspension will be damped out; $p(C)$, however, remains unchanged since each particle maintains its original orbit; the variation of $p(\kappa)$ in this case will be discussed later[5].

Let the probability distribution $g(r_e)$ of equivalent axis ratios r_e of particles in the suspension be Gaussian with a mean $\bar{r}_e$ and a standard deviation σ, assumed to be very small compared with $\bar{r}_e$, so that

$$g(r_e) = \frac{1}{\sqrt{2\pi}\sigma} \exp\left[\frac{-(r_e - \bar{r}_e)^2}{2\sigma^2}\right] . \qquad [74]$$

The probability orientation distribution $p_{\sigma,t}(\theta_1,\phi_1)$ for the suspension is then given by the integral

$$p_{\sigma,t}(\theta_1,\phi_1) = \int_o^\infty p_t(\theta_1,\phi_1)g(r_e)dr_e \qquad [75]$$

and the mean particle projections $\bar{r}_i$ and $\bar{S}_{jk}$ become

$$\bar{r}_{i\sigma} = \bar{S}_{jk\sigma} = \int_o^{2\pi}\int_o^{\pi} r_i \int_o^\infty p_t(\theta_1,\phi_1)g(r_e)dr_e d\theta_1 d\phi_1 \quad . \qquad [76]$$

Integration of [76] with respect to θ_1 and ϕ_1 yields the mean projections $\bar{r}_i$, $\bar{S}_{jk}$ for a monodisperse suspension (i.e., $\sigma = 0$), so that

$$\bar{r}_{i\sigma} = \bar{S}_{jk\sigma} = \frac{1}{\sqrt{2\pi}\ \sigma}\int_o^\infty \bar{r}_i(r_e, \tfrac{4\pi t}{T}) \exp\left[\frac{-(r_e - \bar{r}_e)^2}{2\sigma^2}\right] dr_e \quad . \qquad [77]$$

Since $\bar{r}_i(r_e, 4\pi t/T)$ is a periodic function of time with an angular frequency $\nu = 4\pi/T = 2G/(r_e + r_e^{-1})$, it can be expanded as a Fourier series:

$$\bar{r}_i(r_e, \tfrac{4\pi t}{T}) = \tfrac{1}{2} B_o + \sum_{n=1}^{\infty} \{A_n \sin n\nu t + B_n \cos n\nu t\} \qquad [78]$$

where the Fourier coefficients A_n and B_n are functions of r_e. However, for $\sigma << \bar{r}_e$, A_n and B_n can be approximated by using the mean $\bar{r}_e$, the error involved being of order σ.

Substituting $r_e - \bar{r}_e = \sigma y$ and with the use of [78], [77] becomes

$$\bar{r}_{i\sigma} = \bar{S}_{jk\sigma} = \tfrac{1}{2}B_o + \frac{1}{\sqrt{2\pi}} \sum_{n=1}^{\infty} \int_{-\infty}^{\infty} \{A_n \sin \frac{2nGt}{\bar{r}_e + \sigma y + (\bar{r}_e + \sigma y)^{-1}}$$

$$+ B_n \cos \frac{2nGt}{\bar{r}_e + \sigma y + (\bar{r}_e + \sigma y)}\} \exp [-\tfrac{1}{2} y^2] \, dy \qquad [79]$$

where the lower limit of integration - $\bar{r}_e/\sigma$ is replaced by - ∞ since $\sigma << \bar{r}_e$. The argument of the sine and cosine in [79] may be expanded in terms of y:

$$\frac{2nGt}{\bar{r}_e + \sigma y + (\bar{r}_e + \sigma y)^{-1}} = n\bar{\nu}t - a_2 y - a_3 y^2 \qquad [80]$$

where

$$\bar{\nu} = \frac{2G}{\bar{r}_e + \bar{r}_e^{-1}} \quad ,$$

$$a_2 = \frac{2nGt(1 - \bar{r}_e^{-2})}{(\bar{r}_e + \bar{r}_e^{-1})^2} \sigma \quad , \qquad [81]$$

$$a_3 = \frac{2nGt(1 - 3\bar{r}_e^{-2})}{(\bar{r}_e + \bar{r}_e^{-1})^3} \sigma^2 \quad .$$

Then [79] can be written

$$\bar{r}_{i\sigma} = \bar{S}_{jk\sigma} = \tfrac{1}{2}B_o + \frac{1}{\sqrt{2\pi}} \sum_{n=1}^{\infty} \{A_n \sin n\bar{\nu}t + B_n \cos n\bar{\nu}t\}$$

$$x \{ \int_{-\infty}^{\infty} \cos(a_2 y + a_3 y^2) \exp[-\tfrac{1}{2}y^2] dy \qquad [82]$$

$$- \int_{-\infty}^{\infty} \sin(a_2 y + a_3 y^2) \exp[-\tfrac{1}{2}y^2] dy \}$$

To obtain the solution of [82] requires evaluation of the following types of integral

$$I = \int_{-\infty}^{\infty} \exp[-a_1 y^2] \begin{matrix}\cos \\ \sin\end{matrix} [a_2 y] \begin{matrix}\cos \\ \sin\end{matrix} [a_3 y^2] \, dy \qquad [83]$$

where $a_1 = \frac{1}{2}$ and either the sine or cosine is taken in each of the last two terms. However any integrations involving the sine function in the second term will vanish, so that the only non-zero integrals are[13)]

$$I_1 = \int_{-\infty}^{\infty} \exp[-a_1 y^2] \cos a_2 y \cos a_3 y^2 dy$$

$$= \sqrt{\frac{\pi}{2(a_1^2 + a_3^2)}} \exp\left[\frac{-a_1 a_2^2}{4(a_1^2 + a_3^2)}\right] \qquad [84a]$$

$$x \left[(\sqrt{a_1^2 + a_3^2} + a_1)^{\frac{1}{2}} \cos \frac{a_3 a_2^2}{4(a_1^2 + a_3^2)} + (\sqrt{a_1^2 + a_3^2} - a_1)^{\frac{1}{2}} \sin \frac{a_3 a_2^2}{4(a_1^2 + a_3^2)} \right]$$

$$I_2 = \int_{-\infty}^{\infty} \exp\,[-a_1 y^2]\cos a_2 y \sin a_3 y^2\, dy$$

$$= \sqrt{\frac{\pi}{2(a_1^2 + a_3^2)}}\ \exp\left[\frac{-a_1 a_2^2}{4(a_1^2 + a_3^2)}\right] \qquad [84b]$$

$$\times \left[(\sqrt{a_1^2 + a_3^2} - a_1)^{\frac{1}{2}}\cos\frac{a_3 a_2^2}{4(a_1^2 + a_3^2)} - (\sqrt{a_1^2 + a_3^2} + a_1)^{\frac{1}{2}}\sin\frac{a_1 a_2^2}{4(a_1^2 + a_3^2)}\right].$$

Three specific cases depending on the value of $\bar{r}_e$ are now considered and followed by several sample calculations of mean projections.

(b) $\underline{\bar{r}_e > 1 \quad \text{and} \quad \bar{r}_e < 1.}$

When $\bar{r}_e$ is not close to 1, in the expansion [80] a_3 is always small compared with a_2, and as a first order approximation may be neglected since A_n and B_n have already an error of order σ. The integrals of [82] are thus simplified, with the use of [84], to give

$$\bar{r}_{i\sigma} = \bar{S}_{jk\sigma} = \tfrac{1}{2}B_o + \sum_{n=1}^{\infty}\{A_n \sin n\bar{\nu}t + B_n \cos n\bar{\nu}t\}$$

$$\times \{\exp\left[\frac{-2n^2G^2\sigma^2(\bar{r}_e^2 - 1)^2}{(\bar{r}_e^2 + 1)^4}\ t^2\right]\} \qquad [85]$$

where the Fourier expansion represents an undamped oscillation for $r_e = \bar{r}_e$ and $\sigma = 0$, similar to that shown in Fig.2(a). However because of the last term in [85] the oscillation of

$\bar{r}_{i\sigma}$ will be damped exponentially with t^2. Defining the relaxation time τ_{ln} as that in which the amplitude of oscillation of the n th harmonic reduces to 1/e, then it follows from [85] that

$$\tau_{ln} = \frac{1}{G\sigma} f_n(\bar{r}_e) \qquad [86a]$$

where

$$f_n(\bar{r}_e) = \frac{(\bar{r}_e^{\,2} + 1)^2}{\sqrt{2}\, n\, |\bar{r}_e^{\,2} - 1|} \qquad [86b]$$

the absolute value of $(\bar{r}_e^{\,2} - 1)$ being used so that τ_{ln}, which varies inversely with G and σ, is positive.

For large t, the contribution from $n > 1$ to $\bar{r}_{i\sigma}$ or $\bar{S}_{jk\sigma}$ is very small and may be neglected, so that [85] becomes

$$\bar{r}_{i\sigma} = \bar{S}_{jk\sigma} = \tfrac{1}{2} B_o + D_1 \sin [n\bar{\nu}t + \delta(\bar{r}_e)] \exp \left[\frac{-2G^2\sigma^2(\bar{r}_e^{\,2} - 1)}{(\bar{r}_e^{\,2} + 1)^4} t^2 \right] \qquad [87]$$

where

$$D_1 = \sqrt{A_1^2 + B_1^2}$$

and

$$\delta(\bar{r}_e) = \sin^{-1}(B_1/D_1) = \cos^{-1}(A_1/D_1) \quad .$$

Eq. [87] shows that $\bar{r}_{i\sigma}$ (or $\bar{S}_{jk\sigma}$) becomes a sinusoidal

function which decays with a relaxation time

$$\tau_{11} = \frac{1}{G\sigma} f_1(\bar{r}_e) \qquad [88]$$

The analysis given here applies for all values of $\bar{r}_e$ except $\bar{r}_e = 1$ (for which we are concerned both with particles equivalent to oblate spheroids $r_e < 1$ and to prolate spheroids $r_e > 1$) and $\bar{r}_e$ very close to unity; these two cases are considered next.

(c) $\underline{\bar{r}_e = 1}$

When $\bar{r}_e = 1$, then $a_2 = 0$ and $a_3 = -nGt\sigma^2/2$, so that [82] becomes

$$\bar{r}_{i\sigma} = \bar{S}_{jk\sigma} = \tfrac{1}{2} B_o + \sum_{n=1}^{\infty} \{A_n \sin n\bar{\nu}t + B_n \cos n\bar{\nu}t\} \left[\frac{1 + \sqrt{1 + n^2G^2\sigma^4t^2}}{2 + 2n^2G^2\sigma^4t^2} \right]^{\frac{1}{2}} , \qquad [89]$$

corresponding to an oscillation which is damped with a relaxation time given by the solution of

$$\left[\frac{1 + \sqrt{1 + n^2G^2\sigma^4\tau_{1n}^2}}{2 + 2n^2G^2\sigma^4\tau_{1n}^2} \right]^{\frac{1}{2}} = \frac{1}{e} \qquad [90]$$

which is

$$\tau_{1n} = \frac{4.401}{nG\sigma^2} \quad ; \qquad [91]$$

τ_{1n} is thus proportional to σ^{-2} unlike the preceding case where it varies with σ^{-1}.

(d) $|\bar{r}_e - 1| = 0(\sigma)$

When $|\bar{r}_e - 1|$ is of order σ, both a_2 and a_3 must be included in the integrations of [83], since both are of order $nGt\sigma^2$. Therefore the characteristic relaxation time τ_{1n} is proportional to $(nG\sigma^2)^{-1}$, as is also true for $\bar{r}_e = 1$.

(e) Examples of mean projections $\bar{r}_{2\sigma}$ and $\bar{S}_{12\sigma}$

Eqs. [76] to [91] are general relationships applicable to all $\bar{r}_{i\sigma}$, $\bar{S}_{jk\sigma}$ and to all initial distributions of orientations, the only differences being in the Fourier coefficients A_n and B_n. To illustrate the use of the theory, numerical values of $\bar{r}_{2\sigma}$ and $\bar{S}_{12\sigma}$ for initially isotropic suspensions of $r_e = 10$ and $1/10$ respectively as functions of $t/\bar{T}$ are shown in Fig. 3. Fig. 3(a) shows the undamped oscillations for a monodisperse suspension ($\sigma = 0$) calculated from the equations in Table II, and Fig. 3(b) the damped oscillations for $\sigma/\bar{r}_e = 0.03$ obtained by numerical integration of [77]; it is readily seen from [85] and the argument given in Section 3(b) that $\bar{r}_{2\sigma}$ and $\bar{S}_{12\sigma}$ are identical for

FIGURE 3

The effect of a spread in r_e on $\bar{r}_2$ (or $\bar{s}_{12}$) for $\bar{r}_e = 10$ (or 0.1) for initially random orientations.

(a) $\sigma = 0$, calculated from the equation listed in Table II;

(b) $\sigma/\bar{r}_e = 0.03$, calculated through the numerical integration of [77];

(c) $\sigma/\bar{r}_e = 0.03$, calculated from [94].

The broken lines in (b) and (c) indicate the equilibrium value $\frac{1}{2}B_o = 0.155$. The arrow indicates $\tau_{11}/\bar{T} = 3.83$ given by [86].

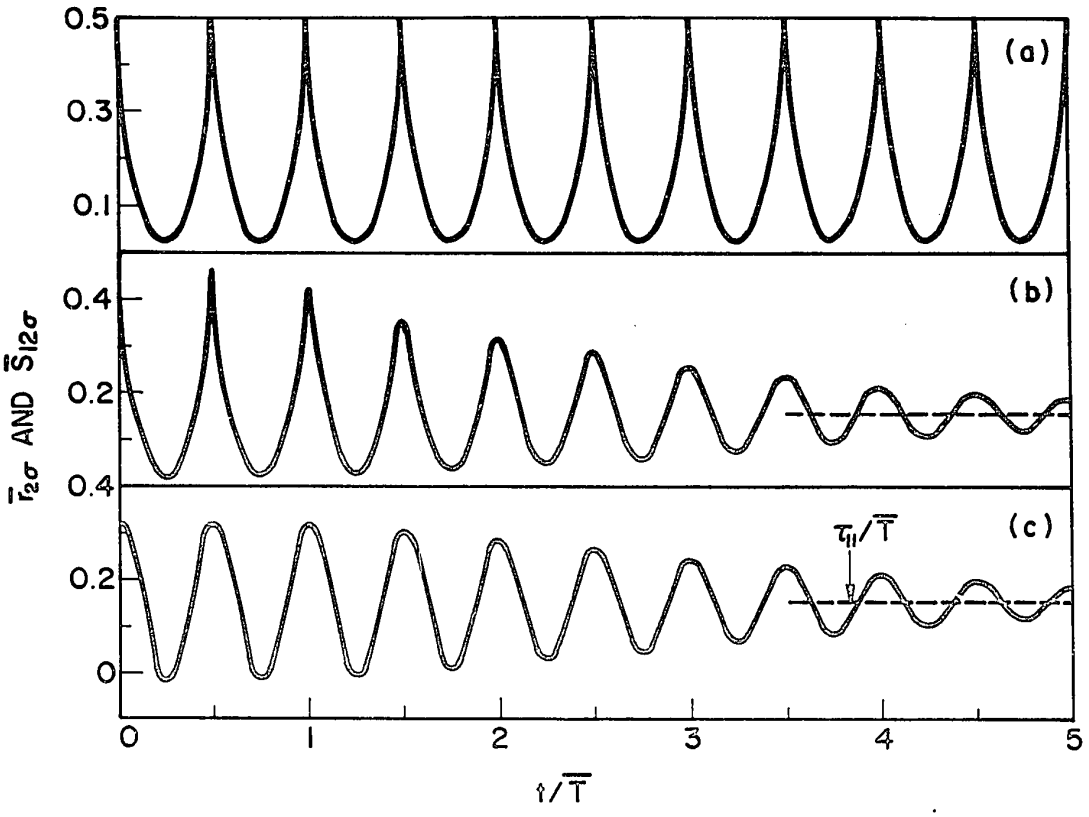
0.5
0.3
0.1
(a)
0.4
0.2
(b)
0.4
0.2
0
$\tau_{11}/\overline{T}$
(c)
0
1
2
3
4
5
$\bar{r}_{2\sigma}$ AND $\bar{S}_{12\sigma}$
$t/\overline{T}$

these two cases when $\bar{r}_e$ (for rods) = $\bar{r}_e^{-1}$ (for discs) and $\sigma/\bar{r}_e \ll 1$ ($|\bar{r}_e - 1| \gg \sigma$).

It is also of interest to calculate the same quantities from the appropriate equations involving the Fourier series. Since the oscillation of $\bar{r}_{2\sigma}$ (or $\bar{S}_{12\sigma}$ with $\bar{r}_e$ replaced by $\bar{r}_e^{-1}$ and $\sigma/\bar{r}_e$ fixed) starts with a finite positive value and decreases at the start, $A_n = 0$. Hence from [85]

$$\bar{r}_{2\sigma} = \bar{S}_{12\sigma} = \tfrac{1}{2} B_o + \sum_{n=1}^{\infty} B_n \cos n\bar{\nu}t \exp\left[\frac{-2n^2G^2\sigma^2(\bar{r}_e^2 - 1)^2}{(\bar{r}_e^2 + 1)^4} t^2\right] . \qquad [92]$$

Here the Fourier coefficient B_n by definition is given by

$$B_n = 4/\bar{T} \int_o^{\bar{T}/2} (\bar{r}_2)_{\sigma=0} \cos n\bar{\nu}t \, dt . \qquad [93]$$

where $\bar{T}$ is the period of rotation for $\bar{r}_e$, i.e., $\bar{T} = 2\pi(\bar{r}_e + \bar{r}_e^{-1})/G$. As a first order approximation, terms in [92] with $n \geq 2$ may be neglected, so that

$$\bar{r}_{2\sigma} = \bar{S}_{12\sigma} = \tfrac{1}{2}B_o + B_1 \cos n\bar{\nu}t \exp\left[\frac{-2G^2\sigma^2(\bar{r}_e^2 - 1)^2}{(\bar{r}_e^2 + 1)^4} t^2\right] \qquad [94a]$$

which can be written in terms of $t/\bar{T}$ as

$$\bar{r}_{2\sigma} = \bar{S}_{12\sigma} = \tfrac{1}{2}B_o + B_1 \cos \frac{4\pi t}{\bar{T}} \exp\left[\frac{-8\pi^2\sigma^2(\bar{r}_e^2 - 1)^2}{\bar{r}_e^2(\bar{r}_e^2 + 1)^2} \left(\frac{t}{\bar{T}}\right)^2\right] . \qquad [94b]$$

The mean projection $\bar{r}_{2\sigma}$ (or $\bar{S}_{12\sigma}$) for $\bar{r}_e = 10$ and $\sigma = 0.3$ (or $\bar{r}_e = 0.1$ and $\sigma = 0.003$) calculated by means of [94b] with $\frac{1}{2}B_o = 0.155$ and $B_1 = 0.171$ obtained by numerical integration of [93] is shown in Fig. 3(c). Since [94b] is only a first order approximation, the initial value of $\bar{r}_{2\sigma}$ obtained by [94b] is lower than 0.5 and becomes negative at $t = \bar{T}/4$. However the values of $\bar{r}_{2\sigma}$ in Fig. 3(b) and (c), are nearly the same and become identical after 3 particle rotations, as is readily shown by superposing the curves, which proves that $\bar{r}_{2\sigma}$ becomes a damped sinusoidal function at large t as predicted above (Eq. [88]). The equilibrium value $\frac{1}{2}B_o$ shown by the broken lines in Fig. 3(b) and (c) depends upon $\bar{r}_e$ (Table III). As $\bar{r}_e$ of rods (or $\bar{r}_e^{-1}$ of discs) increases, $\frac{1}{2}B_o$ decreases gradually, indicating increased alignment of the axes of rods and the faces of discs in the direction of flow (the X_3-axes).

The relative relaxation time $\tau_{1n}/\bar{T}$, calculated from [86] as

$$\frac{\tau_{1n}}{\bar{T}} = \frac{\bar{r}_e(\bar{r}_e^{\,2} + 1)}{2\sqrt{2}\ \pi n\sigma\ |\bar{r}_e^{\,2} - 1|} \quad , \qquad [95]$$

is indicated by the arrow in Fig. 3(c) using n = 1.

For this approximation, the appropriate function in [86] is $f_1(\bar{r}_e)$, numerical values of which are plotted

TABLE III

Numerical values of $\frac{1}{2} B_o$ calculated from [93] and Table I

$\bar{r}_e$ or $\bar{r}_e^{-1}$	$\frac{1}{2} B_o$	$\bar{r}_e$ or $\bar{r}_e^{-1}$	$\frac{1}{2} B_o$
1	0.500	10	0.155
2	0.374	20	0.097
3	0.308	30	0.073
4	0.265	40	0.059
5	0.234	50	0.050
6	0.211	60	0.044
7	0.192	70	0.039
8	0.177	80	0.035
9	0.165	90	0.032
10	0.155	100	0.029

FIGURE 4

The function $f_1(\bar{r}_e)/\bar{r}_e$ versus $\log_{10} \bar{r}_e$ calculated from Eq. [86b]. For reasons explained in the text, the calculated values shown by the dashed portion in the region $|\bar{r}_e - 1| = 0(\sigma)$ are not applicable. Because of the permutability of R and R^{-1} in [96], the curve is symmetrical about $\log_{10} r_e = 0$.

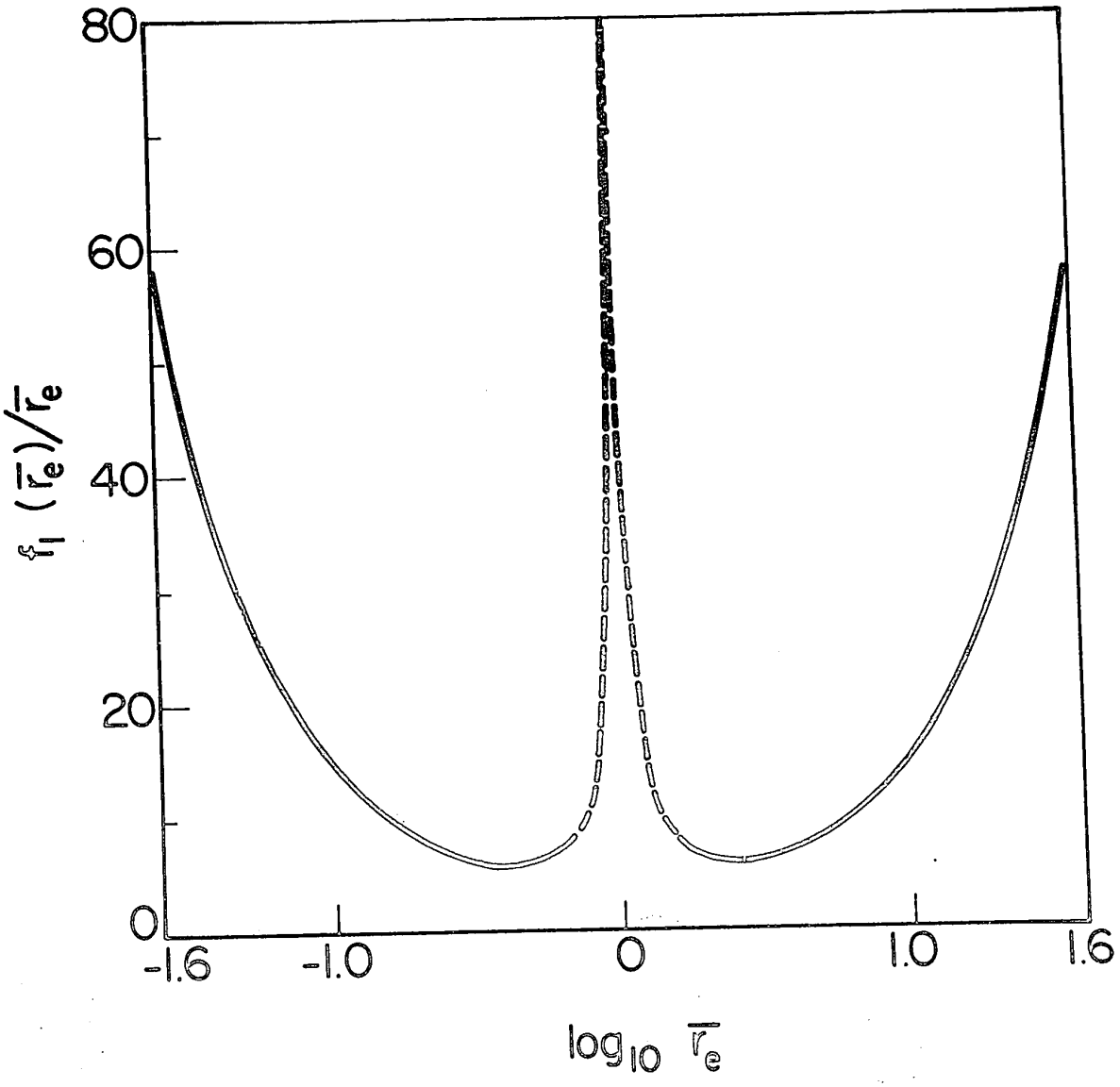
80
60
40
20
0
$\xi_1(\bar{r}_e)/\bar{r}_e$
-1.6
-1.0
0
1.0
1.6
$\log_{10} \bar{r}_e$

against $\log_{10}\bar{r}_e$ in Fig.4, and are valid in the region shown by the solid line, and for reasons already given, invalid in the region shown by the broken line near $\bar{r}_e = 1$. It is of interest to note that $f_n(\bar{r}_e)/\bar{r}_e$ has the property that

$$\frac{f_n(R)}{R} = \frac{f_n(R^{-1})}{R^{-1}} \qquad [96]$$

for any given values of $R = \bar{r}_e$; therefore τ_{1n} is identical for a prolate spheroid (or equivalent) of $\bar{r}_e = R$ and an oblate spheroid (or equivalent) of $\bar{r}_e = R^{-1}$, provided that $\sigma/\bar{r}_e$ are also the same.

5. EFFECT OF PARTICLE INTERACTIONS

(a) General

In the foregoing analysis the suspensions were assumed to be so dilute that interactions (also termed collisions) between particles could be neglected, with each particle undergoing a periodic rotation given by [4] and [5] with constant C and κ. It therefore follows that for such a collision-free suspension (with $\sigma = 0$) the distribution $p(C,\kappa)$ is constant for all time, being determined uniquely by the particle orientations at $t = 0$. However in any real

suspension of infinite volume undergoing shear flow, particles will always interact given sufficient time, no matter how dilute the suspension. Thus the motion of an individual particle no longer satisfies [4] and [5] exactly. However, at any given time t, the quantities C and κ for a particle may still be defined by these equations, their values now changing with time as a result of collisions. The distribution $p(C,\kappa)$ would then also be expected to vary with time.

A theory of the effect of interactions recently developed by Cox[17] is summarized for use in the following Chapter[5]; the theory is limited to suspensions of long slender axisymmetric particles of length ℓ ($r_e >> 1$) at concentrations of N particles per unit volume so low that interactions involving more than two particles may be neglected (i.e., $N\ell^3 << 1$ so that the average distance between the particles $r >> \ell$).

(b) Types of 2-Body Interaction

Due to the variation of the angular velocity $d\phi_1/dt$ with ϕ_1 for a collision-free suspension, it follows from [3] that particles with $r_e >> 1$ spend a time of order $r_e G^{-1}$ during one particle rotation in orientations which differ from $\phi_1 = \pi/2$ or $3\pi/2$ by an amount of order r_e^{-1} or

less , while spending only a time of order G^{-1} at orientations for which $\phi_1 - \pi/2 = 0(1)$ (i.e., they spend a time of order $r_e G^{-1}$ almost aligned with the flow and then flip over in a time of order G^{-1}). In addition to these two characteristic ϕ_1 orientations, the particles can also be classified according to their orbits: those with $C = 0$ (r_e^{-1}) and those with $C = 0(1)$.

Using these characteristic values of ϕ_1 and C, a particle orientation may be designated to be one of the following four types according to the scheme in Fig. 5: (i) $C = 0(1)$ with ϕ_1 not near $\pi/2$ or $3\pi/2$, (ii) $C = 0(1)$ with ϕ_1 near $\pi/2$ or $3\pi/2$, (iii) $C = 0(r_e^{-1})$ with ϕ_1 not near $\pi/2$ or $3\pi/2$, and (iv) $C = 0(r_e^{-1})$ with ϕ_1 near $\pi/2$ or $3\pi/2$.

The effect of each interaction may be measured by the changes $\Delta\kappa$ and ΔC which result from the angular displacement $\Delta\phi_1$ and $\Delta\theta_1$ of each of the two interacting particles, $\Delta\phi_1$ and $\Delta\theta_1$ being defined as the additional displacements that occur over those for an isolated particle in shear during the period of interaction Δt. From [4] and [5] the values of $\Delta\kappa$ and ΔC are therefore given by

$$\Delta\kappa = \frac{\partial\kappa}{\partial\phi_1}\Delta\phi_1 = \frac{r_e}{r_e^2\cos^2\phi_1 + \sin^2\phi_1}\Delta\phi_1 \qquad [98a]$$

FIGURE 5

Schematic diagrams of the four characteristic values of ϕ_1, C for a long slender rod whose rotational orbit is shown by a heavy curve.

Type (i): $C = 0(1)$ with ϕ_1 not near $\pi/2$ or $3\pi/2$.

Type (ii): $C = 0(1)$ with ϕ_1 near $\pi/2$ or $3\pi/2$.

Type (iii): $C = 0(r_e^{-1})$ with ϕ_1 not near $\pi/2$ or $3\pi/2$.

Type (iv): $C = 0(r_e^{-1})$ with ϕ_1 near $\pi/2$ or $3\pi/2$.

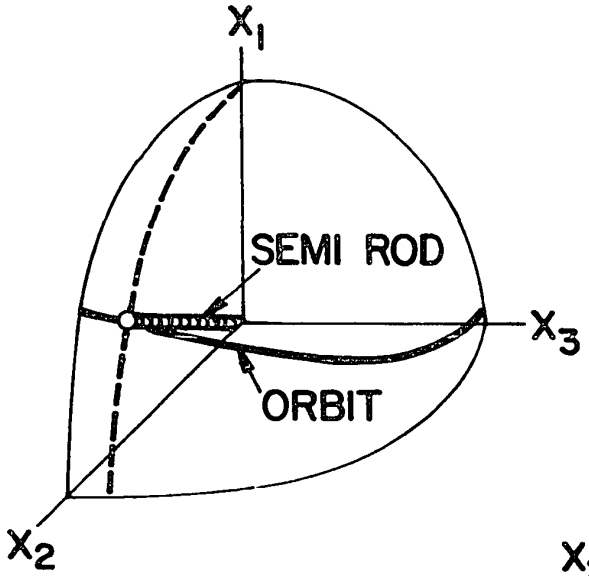

(i) $\begin{cases} C = O(1) \\ \phi_1 \neq \pi/2 \end{cases}$

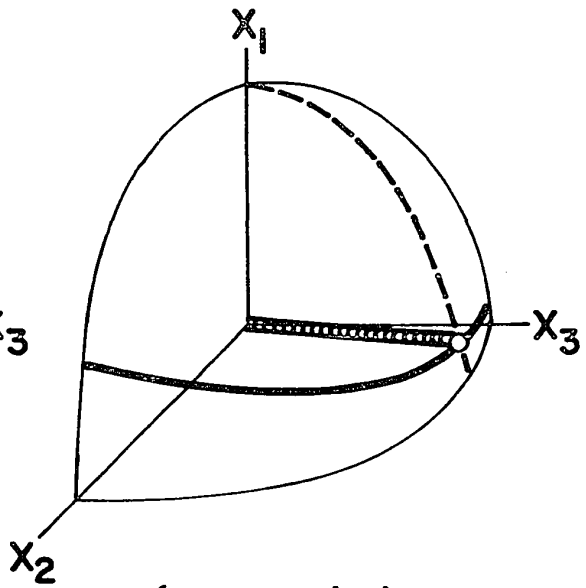

(ii) $\begin{cases} C = O(1) \\ \phi_1 \simeq \pi/2 \end{cases}$

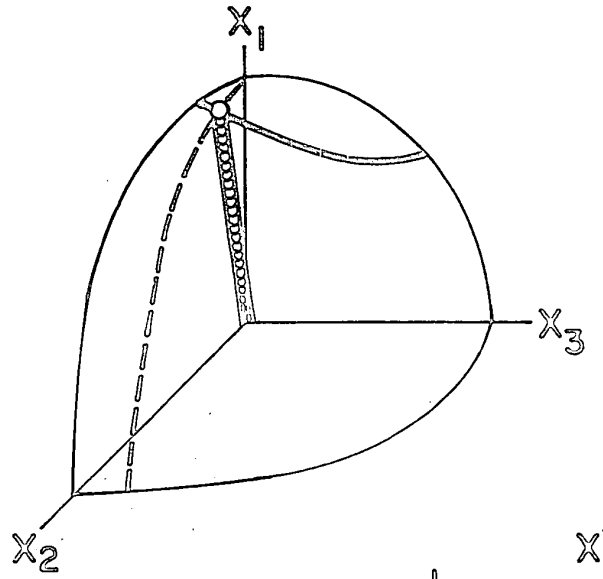

(iii) $\begin{cases} C = O(r_e^{-1}) \\ \phi_1 \neq \pi/2 \end{cases}$

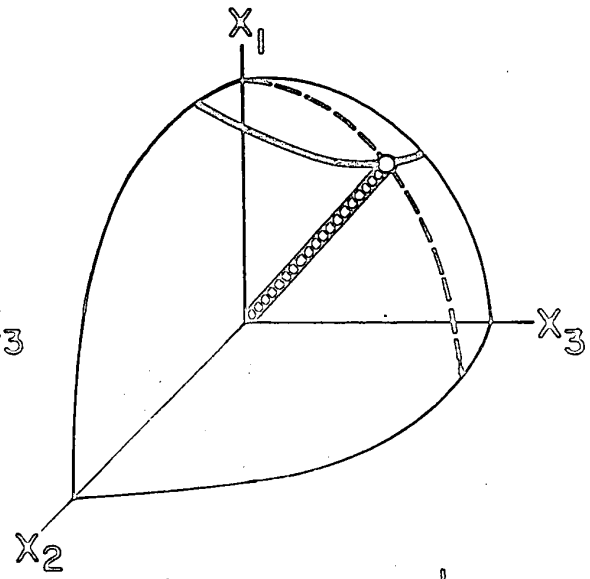

(iv) $\begin{cases} C = O(r_e^{-1}) \\ \phi_1 \simeq \pi/2 \end{cases}$

$$\Delta C = \frac{\partial C}{\partial \theta_1}\Delta\theta_1 + \frac{\partial C}{\partial \phi_1}\Delta\phi_1 \qquad [98b]$$

$$= \frac{(r_e^2\cos^2\phi_1 + \sin^2\phi_1)^{\frac{1}{2}}}{r_e\cos^2\theta_1}\Delta\theta_1 + \frac{(1 - r_e^2)\tan\theta_1\sin\phi_1\cos\phi_1}{r_e(r_e^2\cos^2\phi_1 + \sin^2\phi_1)^{\frac{1}{2}}}\Delta\phi_1 \quad ,$$

the value of $\Delta\theta_1$ and $\Delta\phi_1$ being assumed to be small. The effect of type (i) particle on one of type (ii) is not necessarily the same as that of (ii) on (i); thus for the four types of particle orientation listed above, the interactions should be examined separately for the effect of one particle upon the other, and vice versa; thus $4^2 = 16$ classes of interaction α-β, designating the effect of α upon β, are possible with each of α, β having all possible values between (i) and (iv); thus interactions α-β and β-α are not identical except when $\alpha=\beta$.

For a particle of type (i) the disturbance velocity produced at a large distance $r >> \ell$ is of order $G\ell(\ell/r)^2/\ell n\ r_e$ [16], corresponding to a disturbance in velocity gradient of $G(\ell/r)^3/\ell n\ r_e$*. Since the particle spends a time of order $\Delta t = G^{-1}$ interacting with a second particle (during which time ϕ_1 of type (i) particle is not close to $\pi/2$ or $3\pi/2$), the additional angular displacement of the second particle located at a distance r is therefore such that $\Delta\phi_1$ and $\Delta\theta_1$ are of order $\ell^3/r^3\ \ell n\ r_e$.

* The value r_e is used throughout this Section since the analysis is limited to a particle of $r_e >> 1$ for which $r_e = O(r_p)$ as mentioned in Section 2.

If this second particle is type (ii), then substitution into [98] shows that $\Delta\kappa = 0(1)$ and $\Delta C = 0(1)$ if the distance between particles is of order $\ell(r_e/\ell n\ r_e)^{1/3}$. On the other hand if the second particle is one of type (iv), then $\Delta\kappa = 0(1)$ with $\Delta C = 0(r_e^{-1})$ for such an interaction. An examination of all other types of interaction shows that $\Delta\kappa$ and ΔC are always smaller than the two mentioned above by amounts at least of order r_e^{-1} and thus may be neglected.

Therefore it appears (somewhat surprisingly) that the dominant interactions affecting the orientation probability distribution are the very distant interactions (i.e., with r of order $r_o = \ell(r_e/\ell n\ r_e)^{1/3}$), and not those previously defined as close and distant collisions[3].

The frequency $f_{\alpha-\beta}$ of the interaction α-β per particle per unit time is given, from the analogy to the equation for the two-body collision frequency of spheres[18], by

$$f_{\alpha-\beta} = NGr_o^3\ p(\alpha) \cdot p(\beta) \quad , \qquad [99]$$

where $p(\alpha)$ is the probability that a particle is of type α, so that $\sum_{\alpha=i}^{iv} p(\alpha) = 1$. For the two dominant classes of interaction described above, (i-ii) and (i-iv), only the fraction r_e^{-1} of particles have orientation such that ϕ_1 is not close to $\pi/2$ or $3\pi/2$. Thus

$$f_{i\text{-}ii} = NGr_o^3/r_e = NG\ell^3/\ell n\ r_e \qquad [100a]$$

$$f_{i\text{-}iv} = NGr_o^3/r_e^2 = NG\ell^3/r_e\ \ell n\ r_e \qquad [100b]$$

if we assume that there is not an excess of particles in orbits with $C = 0(r_e^{-1})$ and that at no stage particles are so aligned one with another that r_e^{-1} times the number of particles in orientations with $\phi_1 - \pi/2 = 0(r_e^{-1})$ are orders of magnitude larger or smaller than those in other orientations.

This last assumption, which is equivalent to stating that the probability distribution of orientations is not very different from the time-independent (i.e. equilibrium) distribution, is not strictly valid for an initially random distribution for which $p_t(\theta_1,\phi_1)$ is initially periodic, the frequency $f_{\alpha\text{-}\beta}$ therefore also being periodic. However it is observed experimentally[5] that as a result of particle interaction, $p_t(\theta_1,\phi_1)$ undergoes a damped oscillation tending to the time-independent value, so that [100] may be expected to apply to the later stages of the damping. On the other hand the frequency $f_{i\text{-}iv}$ is r_e^{-1} times smaller than $f_{i\text{-}ii}$; although $\Delta\kappa$ is of order unity for interaction (i-iv), it may therefore be neglected. Thus, after a sufficient period of time, the most dominant type of interaction is type (i-ii) for which a detailed calculation has been made[17].

(c) Relaxation Times

It has been shown[17] that the change in the probability $p_t(C,\kappa)$ in time Δt resulting from the interactions (i-ii) is of order $GN\ell^3\Delta t/\ell n\ r_e$. Since the period of rotation is approximately $T = 2\pi r_e/G$ for $r_e >> 1$, the change in $p_t(C,\kappa)$ during one particle rotation is of order $r_e N\ell^3/\ell n\ r_e$. Therefore the characteristic time period for the change in $p_t(C,\kappa)$ is of order $\ell n\ r_e/GN\ell^3$, corresponding to $\ell n\ r_e/N\ell^3 r_e$ particle rotations. This characteristic time may be considered as a measure of relaxation time required to reduce the amplitude of oscillation in $p_t(\phi_1)$ or the value of $|p_t(\kappa) - p_\infty(\kappa)|$ to 1/e of the initial value and be denoted by τ_2 (see Fig. 6), thus

$$\tau_2 = \ell n\ r_e/GN\ell^3 \quad . \qquad [101]$$

Alternatively one may obtain τ_2 by noting that it should be of the same order of magnitude as the mean time between interactions of type (i-ii), and thus equal to $\{f_{i-ii}\}^{-1}$. For the case in which $\tau_2 = 0(\ell n\ r_e/GN\ell^3) >> T$, the chance of an interaction for any given particle in one rotation is very small, so that $p_t(C,\kappa)$ does not change much in a time T.

Also if we consider the time-independent distribution which is obtained as the solution of steady state continuity equation (i.e., the rotational flux $p(\phi_1)\cdot(d\phi_1/dt)$ of particles is the same for all ϕ_1) and is given by[1,4]

$$p_\infty(\phi_1) = \frac{r_e}{2\pi(r_e^2\cos^2\phi_1 + \sin^2\phi_1)} \quad , \qquad [102]$$

then the frequency $f_{\alpha-\beta}$ of any type of particle interaction does not alter with time; therefore the probability distribution for changes in $\Delta\kappa$, denoted by $p(\Delta\kappa)$, at any given value of $\kappa(=\kappa_o)$ and $t(=t_o)$ would be equal to that for any later time $t = t_o + t'$ evaluated at a value of $\kappa = \kappa_o - 2\pi t'/T$. If, when the distribution $p_t(\phi_1)$ is given by [102], we take the average over T, $p(\Delta\kappa)$ becomes independent of κ. Thus we would expect $p(\kappa)$ to become random, i.e.,

$$p_\infty(\kappa) = 1/2\pi \qquad [103]$$

This is also the probability distribution corresponding to the time-independent distribution $p_\infty(\phi_1)$ given by [102] obtained from [5] and the identity

$$p_\infty(\phi_1)d\phi_1 \equiv p_\infty(\kappa)d\kappa \quad , \qquad [104]$$

so that we see that [102] and [103] are allowable distributions even when we take into account particle interactions (so long as $\tau_2 >> T$).

It is important to note that the probability distributions $p_\infty(\phi_1)$ and $p_\infty(\kappa)$ given by [102] and [103], which are shown in Fig. 1(a), (b) and (d), are independent of the mechanisms by which the equilibrium state is attained.

However, [102] applies strictly only when all the particles have the same r_e (i.e., $\sigma = 0$) and when $\tau_2 >> T$. For a distribution in r_e, it follows from [75] that

$$p_{\sigma,t}(\phi_1) = \int_0^\infty p_t(\phi_1) g(r_e) dr_e \quad . \qquad [105]$$

Employing the scheme of analysis given in Section 4, $p_t(\phi_1)$ may be expanded as a Fourier series, with the equilibrium distribution $p_{\sigma,\infty}(\phi_1)$ given approximately as the leading coefficient in the series (cf. [79] and [93]), from which it follows that

$$p_{\sigma,\infty}(\phi_1) = \frac{2}{\bar{T}} \int_0^{\bar{T}/2} p_t(\phi_1, \bar{r}_e)\, dt \quad . \qquad [106]$$

Substituting $p_t(\phi_1, \bar{r}_e)$ from [22] into [106] yields

$$p_{\sigma,\infty}(\phi_1) = \frac{1}{\pi \bar{T}} \int_0^{\bar{T}/2} \frac{dt}{\chi^2} \qquad [107]$$

which on integration yields

$$p_{\sigma,\infty}(\phi_1) = \frac{\bar{r}_e}{2\pi(\bar{r}_e^{\,2}\cos^2\phi_1 + \sin^2\phi_1)} \qquad [108]$$

which is identical to [102] for $r_e = \bar{r}_e$. Because of the Fourier expansion, however, this is an approximation. The

error in [108] can be estimated by calculating the axis ratio of the polar diagram $p_{\sigma,\infty}(\phi_1)$, which can be shown[13] from [74], [102] and [105] to be

$$\frac{p_{\sigma,\infty}(\pi/2)}{p_{\sigma,\infty}(0)} = \bar{r}_e^{\,2}\left(1 + \frac{\sigma^2}{\bar{r}_e^{\,2}}\right) \qquad [109]$$

which reduces to $\bar{r}_e^{\,2}$ when $\sigma = 0$, the value calculated from [102]. Thus using [108] introduces an error of order σ^2 in the ratio, which is negligible when $\sigma << \bar{r}_e$ as in the suspensions studied experimentally[5].

For $\tau_2 >> T$, $p_t(\kappa)$ for an initially random distribution would tend to $p_\infty(\kappa)$ in a steady manner since $p_t(\kappa)$ is not altered much during one particle rotation T. During this time, however, both $p_t(\phi_1)$ and $p_t(\theta_1)$ will show damped oscillations as illustrated in Fig. 6(a) and (b). If τ_2 is not very much longer than T, interactions during one period will have an appreciable effect and since $f_{\alpha-\beta}$ is cyclic with a period of T/2 (at least until some time-independent state is established), it follows that $p_t(\kappa)$ in tending to its final state will possess an oscillation of magnitude $r_e N\ell^3/\ell n\ r_e$ superimposed on its steady variation. As will be shown in the following Chapter[5] a small oscillation in addition to the steady change in $p_t(\kappa)$ was observed with cylindrical particles. Also when the effect of interactions during the time period T is appreciable, we would expect the final values of $p_\infty(\phi_1)$ to shift toward a random orientation

from that given by [102] by an amount of magnitude $r_e N\ell^3/\ell n\ r_e$. This change in $p_\infty(\phi_1)$ results in the value of $p_\infty(\kappa)$ given by [104] showing an undamped oscillation of amplitude of order $r_e N\ell^3/\ell n\ r_e$.

If the suspension is so concentrated that $\tau_2 << T$, then the damping of $p_t(\theta_1,\phi_1)$ is so fast that we would expect a monotonic change in $p_t(\theta_1,\phi_1)$.

When the time-independent $p_\infty(\phi_1)$ is established, there is then a slow change in $p_t(\theta_1)$ and $p_t(C)$ with a relaxation time $\tau_3 (>> \tau_2)$, these changes occurring also as a result of particle interactions (see Fig. 6). During the initial period (with time of order τ_2) the interactions of the types discussed above cause a change in $p_t(C)$ which, according to the experimental data of Anzurowski et al[3] for rods, results in an increase of a number of particles in lower orbits. But particles with $C = 0(r_e^{-1})$ [types (iii) and (iv) in Fig. 5] produce a much smaller disturbance flow than those which have been discussed [type (i)]. Thus it takes a much longer time τ_3 for $p_t(C)$ to attain equilibrium than for τ_2. To estimate this relaxation time τ_3, which may also be proportional to $(GN)^{-1}$, it would be necessary to re-examine all the possible types of interactions in detail. On the other hand experimentally it is found that τ_3 corresponds to a period of several hundred particle

FIGURE 6

Schematic plots of the variation of the probability distributions with time for a dilute suspension with 2-particle interactions:

(a) $p_t(\phi_1)$ for $\phi_1 = \phi_1^*$,

(b) $p_t(\theta_1)$ for $\theta_1 = \theta_1^*$,

(c) $p_t(\kappa)$ for $\kappa = \kappa^*$,

(c) $p_t(C)$ for $C = C^*$.

For higher concentrations $p_t(\kappa)$ is expected to show an oscillation superimposed on the steady change as shown by the broken line, all other probability functions exhibiting variations of those shown here. Note that the periods of oscillation are T/2 applying for the case where particle ends are not distinguishable; when they are distinguishable the periods are T.

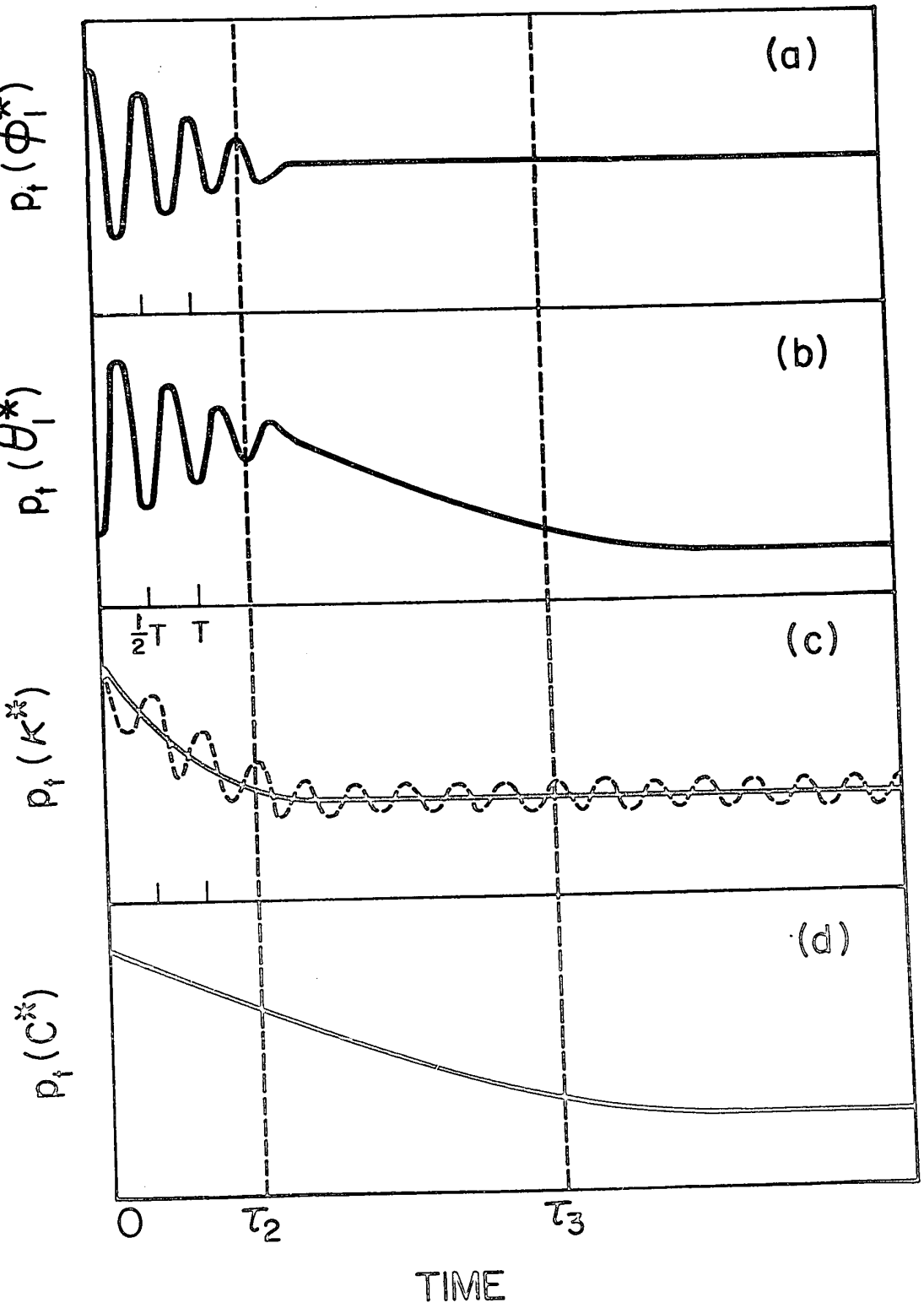
(a)
(b)
(c)
(d)
$p_t(\phi_1^*)$
$p_t(\theta_1^*)$
$p_t(K^{*})$
$p_t(C^{*})$
$\frac{1}{2}T$
T
0
τ_2
τ_3
TIME

rotations[3] for a very dilute suspension of rods ($c = 4.3 \times 10^{-5}$ ml/ml, $r_e = 20.8$).

These changes in orientation distribution would produce corresponding changes in the various rheological properties of the suspension. Thus if $\tau_2 = 0(\ell n\, r_e/N\ell^3 r_e)$ is much greater than T, the viscosity and normal stress differences would show a damped oscillation, followed by a slow monotonic change to equilibrium values (over a time τ_3).

A further mechanism for establishing equilibrium orientations is provided by rotary Brownian movement. This has been considered most recently by Leal and Hinch[19] and will be discussed briefly in the following Chapter[5].

We have thus presented an a priori theory of the rheological properties of dilute suspensions which in systems where $r_e \neq 1$ predicts general non-Newtonian behaviour, i.e. with time dependent viscosity changes and non-zero normal stress differences etc., until equilibrium is reached when Newtonian behaviour, i.e. with constant $[\eta]$ and vanishing $[\xi_{ij}]$ is exhibited.

REFERENCES

1. Anczurowski, E. and Mason, S.G., J. Colloid Interface Sci., 23, 522 (1967).

2. Anczurowski, E. and Mason, S.G., ibid, 23, 533 (1967).

3. Anczurowski, E., Cox, R.G. and Mason, S.G., ibid, 23, 547 (1967).

4. Manley, R.St.J. and Mason, S.G., Proc. Roy. Soc. (London), A238, 117 (1956).

5. This thesis, Chapter III.

6. Jeffery, G.B., Proc. Roy. Soc. (London), A102, 161 (1922).

7. Bretherton, F.P., J. Fluid Mech., 14, 284 (1962).

8. Trevelyan, B.J. and Mason, S.G., J. Colloid Sci., 6, 354 (1951).

9. Goldsmith, H.L. and Mason, S.G., J. Fluid Mech., 12, 88 (1962).

10. Anczurowski, E. and Mason, S.G., Trans. Soc. Rheology, 12, 209 (1968).

11. Cox, R.G., J. Fluid Mech., 45, 625 (1971).

12. Eisenschitz, R., Z. Phys. Chem., A158, 85 (1932).

13. This thesis, Appendix I.

14. Cox, R.G. and Brenner, H., Chem. Eng. Sci., 26, 65 (1971).

15. Guth, E., Kolloid-Zeit., 74, 147 (1936).

16. Cox, R.G., J. Fluid Mech., 44, 791 (1970).

17. Cox, R.G., To be published.

18. Manley, R.St.J. and Mason, S.G., J. Colloid Sci., 7, 354 (1952).

19. Leal, L.G. and Hinch, E.J., J. Fluid Mech., 46, 685 (1971).

CHAPTER III

OSCILLATORY BEHAVIOR OF RODS AND DISCS IN SHEAR FLOW

ABSTRACT

Damped oscillations of the orientation distributions of rods and discs were measured in the early stages of shearing. As a result of the spread in the particle axis ratio and of particle interactions, equilibrium orientation distributions were established in the plane normal to the vorticity axis after a few particle rotations. Oscillations of the distribution of phase angles superimposed on a monotonic change due to particle interactions were also observed. The reciprocal of the measured relaxation times of the decrement of oscillations of the mean projections of rods varied linearly with the particle concentration, in good agreement with theory. It was concluded that rotary Brownian motion of the particles played a negligible role in the experiments. The theory and supporting experimental data provide methods for *a priori* predictions of constitutive equations of the non-Newtonian rheological properties of dilute suspensions.

LIST OF SYMBOLS

For symbols other than those listed below, see Reference 1.

$A(n_1\bar{T}/4)$	=	amplitude of oscillation
b_1, b_2	=	constants defined in [31]
d	=	diameter of a cylinder
d_{23}	=	minor axis of the projected ellipse of the face of a disc on X_2X_3-plane.
D_r	=	rotary diffusion constant
k_o	=	constant of integration
$\bar{\ell}$	=	mean length of rods
ℓ_{23}	=	projected length of a rod on X_2X_3=plane
$p_E(\phi_{im})$, $p_t(\phi_{im})$	=	probability distribution of ϕ_{im} (i = 2,3)
$p_t(Pé,\phi_1)$, $p_t(Pé,\kappa)$	=	probability distribution of ϕ_1 and κ as function of Pé.
Pé	=	rotary Péclet number
$P_E(\phi_{im})$, $P_t(\phi_{im})$	=	cumulative distribution function of ϕ_{im} (i = 2,3)
$q_t(\theta_1)$	=	probability distribution defined in [21]
T_{κ_1}	=	period of oscillation for $p_{\sigma,t}(\kappa)$
κ_1	=	defined in [17]
σ_m, σ_e, σ_p	=	standard deviations for $P_t(\phi_{im})$, r_e and r_p respectively
τ, τ_σ, τ_4	=	relaxation times measured, due to the spread in r_e and due to Brownian motion

ϕ_{im} = orbit parameters defined in [1] (i = 2,3)

$\omega(\phi_1)$ = angular velocity ($d\phi_1/dt$) in shear field

1. INTRODUCTION

(a) General

The oscillatory behavior of particle orientations and of various rheological properties in dilute suspensions of spheroidal and cylindrical particles subjected to a simple shear (Couette) flow in the creeping flow regime was investigated theoretically in the preceding Chapter[1]. It was shown that for an initially isotropic suspension the probability orientation distribution $p_t(\theta_1,\phi_1)$ is generally anisotropic and oscillates with frequency $2/T$, with corresponding oscillations in rheological properties such as the intrinsic viscosity $[\eta]$ and normal stress differences $[\xi_{ij}]$. Two mechanisms (the spread in particle axis ratio r_e, and 2-body interactions) which cause damping of the oscillations and eventual establishment of an equilibrium state were examined in detail[1].

This Chapter describes an experimental study of particle orientations undertaken to test the theory, and to serve as a basis for discussion of several of its implications. The experiments extend earlier work by Anczurowski *et al*[2] on the slow changes in the distributions of the rotational orbits of rods and discs, and deal mainly with the oscillatory behavior of orientation distributions $p_t(\phi_1)$ and $p_t(\theta_1)$ in

the early stages of shearing when the distribution of orbits remained fixed. Distributions of orbits and various orientation parameters were measured in initially isotropic suspensions of rods ($r_e > 1$) and discs ($r_e < 1$), and in an initially parallel alignment of rods, for various intervals of time until the equilibrium probability distribution $p_\infty(\phi_1)$ was established. The measured particle orientations were then used to calculate the mean projection length $\bar{r}_2$ and area $\bar{S}_{12}$ from which relaxation times for damping of the oscillations were measured and compared with the theory, using a variety of methods of analysis and display of the statistical data.

The possible effects in the experiments of rotary Brownian motion, assumed in the theory to be negligible, and some interesting rheological consequences of the results are then considered. Before presenting the results, we consider several useful conventions and methods of analyzing the experimental data.

(b) Distributions of Orbit Constants

It is convenient to use in place of the spherical elliptical orbit constant C ($-\infty < C < \infty$) of the axis of revolution of a particle, the maximum values of the azimuthal angles $\pm \phi_{2m}$ for discs ($r_e < 1$) and $\pm \phi_{3m}$ for rods ($r_e > 1$). As illustrated in Fig. 1, these are the angles between the X_1-axis and the particle axis when it crosses the X_1X_3 and

FIGURE 1

Coordinate systems for rods and discs and the projections of orbits on the three coordinate planes. The orbit of a rod ($r_e > 1$, illustrated by heavy solid lines) is a spherical ellipse. The projection of one end of the axis of revolution on the X_2X_3-plane is a plane ellipse (i). The projection on the X_1X_3-plane (ii) rocks back and forth between $\pm \phi_{2m}$ and the projection on the X_1X_2-plane (iii) between $\pm \phi_{3m}$. The projection lengths r_1, r_2, r_3 of a rod are indicated in (i) and (ii).

The axis of revolution of a disc rotates similarly to a rod as shown by the heavy broken lines.

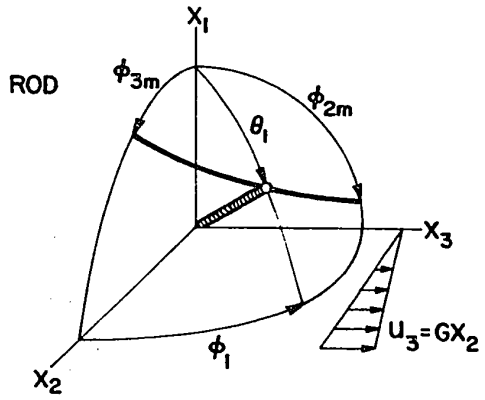
ROD
X_1
ϕ_{3m}
ϕ_{2m}
θ_1
X_3
$U_3 = GX_2$
ϕ_1
X_2

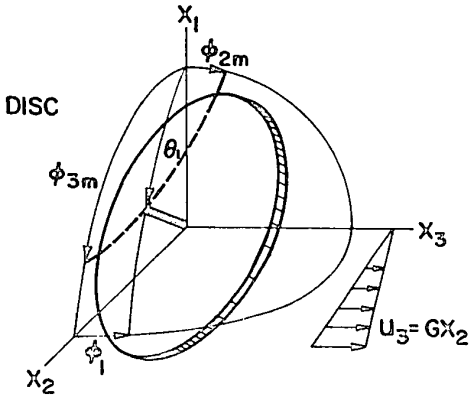
DISC
X_1
ϕ_{2m}
θ_1
ϕ_{3m}
X_3
$U_3 = GX_2$
ϕ_1
X_2

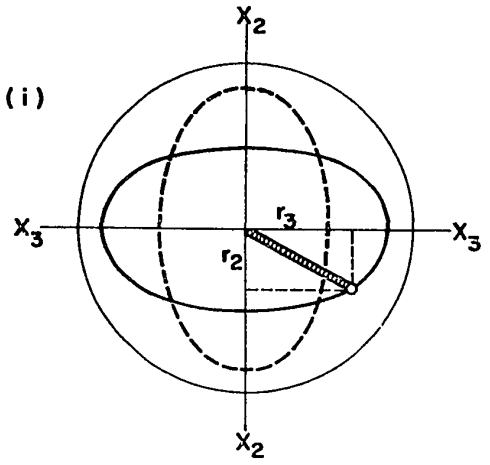
(i)
X_2
X_3
r_3
r_2
X_3
X_2

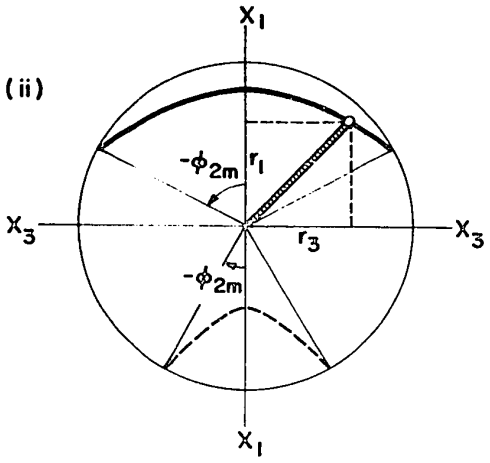
(ii)
X_1
$-\phi_{2m}$
r_1
X_3
r_3
X_3
$-\phi_{2m}$
X_1

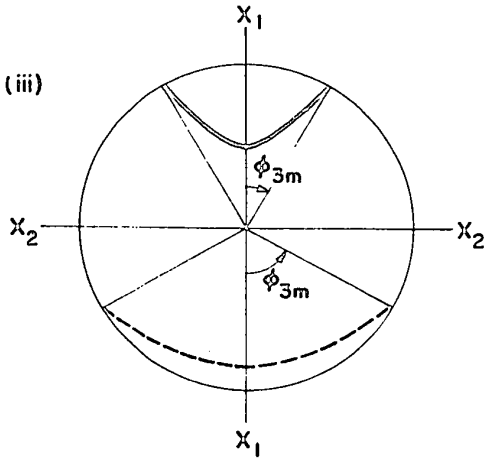
(iii)
X_1
ϕ_{3m}
X_2
X_2
ϕ_{3m}
X_1

and X_1X_2-planes respectively, from which it follows[3,4] that

$$\phi_{2m} = \tan^{-1} Cr_e, \quad (-\pi/2 \text{ to } \pi/2) \qquad [1a]$$

$$\phi_{3m} = \tan^{-1} C \quad . \quad (-\pi/2 \text{ to } \pi/2) \qquad [1b]$$

The probability distribution function $p_E(\phi_{im})$ $(i = 2,3)$ corresponding to an initially random orientation may be obtained from the relation:

$$p_E(\phi_{im})\, d\phi_{im} = p_E(C)\, dC \qquad [2]$$

where $p_E(C)$ is the Eisenschitz distribution of orbits given by [26]-1*. The calculations are straightforward and are summarized in Table I which also includes the cumulative distributions $P_E(\phi_{im})$. It should be noted that the following equalities in the distribution functions occur for rods and discs whose r_e's are reciprocals:

$$p_E(\phi_{2m})_{r_e = R} = p_E(\phi_{3m})_{r_e = 1/R} \quad , \qquad [3a]$$

$$P_E(\phi_{2m})_{r_e = R} = P_E(\phi_{3m})_{r_e = 1/R} \quad . \qquad [3b]$$

When $r_e >> 1$, $p_E(\phi_{3m})$ becomes nearly constant since $m_1 \simeq 2/\pi$ and $k_1^2 \simeq 1$ except near $\phi_{3m} = 0$; and when $r_e << 1$, $p_E(\phi_{3m})$

* Designating Eq. [26] of Reference 1 from which many other equations are cited.

TABLE I

DISTRIBUTION FUNCTIONS OF ORBIT CONSTANTS
INITIALLY RANDOM ORIENTATION

$P_E(\phi_{2m})$ or $P_E(\phi_{3m}) = m_1 E(k_1)$				$P_E(\phi_{2m})$ or $P_E(\phi_{3m}) = 1 - m_2 \Pi(\alpha_1^2, k_1)$	
		m_1	m_2	α_1^2	k_1^2
ϕ_{2m}	$r_e > 1$	$\dfrac{2r_e \sin\phi_{2m}}{\pi(\sin^2\phi_{2m} + r_e^2\cos^2\phi_{2m})}$	$\dfrac{2\sin\phi_{2m}}{\pi r_e}$	$1 - r_e^{-2}$	$(1 - r_e^{-2})\sin^2\phi_{2m}$
	$r_e < 1$	$\dfrac{2}{\pi(1 + r_e^2\cot^2\phi_{2m})}$	$\dfrac{2r_e}{\pi(1 + r_e^{-2}\tan^2\phi_{2m})^{\frac{1}{2}}}$	$1 - r_e^2$	$\dfrac{1 - r_e^2}{1 + r_e^2\cot^2\phi_{2m}}$
ϕ_{3m}	$r_e > 1$	$\dfrac{2}{\pi(1 + r_e^{-2}\cot^2\phi_{3m})}$	$\dfrac{2}{\pi r_e(1 + r_e^2\tan^2\phi_{3m})^{\frac{1}{2}}}$	$1 - r_e^{-2}$	$\dfrac{1 - r_e^{-2}}{1 + r_e^{-2}\cot^2\phi_{3m}}$
	$r_e < 1$	$\dfrac{2\sin\phi_{3m}}{\pi r_e(\sin^2\phi_{3m} + r_e^{-2}\cos^2\phi_{3m})}$	$\dfrac{2r_e \sin\ 3m}{\pi}$	$1 - r_e^2$	$(1 - r_e^2)\sin^2\phi_{3m}$

$E(k_1)$ and $\Pi(\alpha_1^2, k_1)$ are complete elliptic integrals of the second and third kinds respectively

is also nearly constant except near $\phi_{2m} = 0$, indicating that $P_E(\phi_{3m})$ for $r_e >> 1$ and $P_E(\phi_{2m})$ for $r_e << 1$ are almost linear with respect to ϕ_{3m} and ϕ_{2m} respectively.

Since one end (or face) of a cylindrical particle used in the experiments was indistinguishable from the other, ϕ_{im} and $-\phi_{im}$ are equivalent; as a matter of convenience the range of ϕ_{im} was taken from 0 to $\pi/2$. Similarly measurements of ϕ_1 could only be made in the range between 0° and 180° and of θ_1 between 0° and 90°; from symmetry considerations, however, the distributions were readily expressed for the ranges $\phi_1 = 0°$ to 360°, and $\theta_1 = 0°$ to 180°. The ranges of the phase angle κ, obtained only between 0° and 180°, can also be extended to $\kappa = 0°$ to 360°.

(c) Suspensions of Initially Parallel Alignment

Although the orientation theory given in the previous Chapter[1] is applicable to any initial orientation, most of the detailed calculations were made for an initially random orientation. We wish now to consider the case of initially parallel alignment of the particles. This is easily achieved with rods by applying an electric field parallel to the X_2-axis before the onset of shear motion, causing the rods to assume identical orientations[5] $\theta_1 = \pi/2$ and $\phi_1 = 0$ corresponding to $\kappa = 0$ and $C = \infty$. When shear is applied after removal of an electric field, each

particle rotates according to Jeffery's equations[6] at constant $\kappa(=0)$ and $C(=\infty)$, so that from [4]-1 and [5]-1,

$$\theta_1 = \pi/2 \qquad [4a]$$

$$\tan \phi_1 = r_e \tan \frac{2\pi t}{T} \qquad [4b]$$

where T is the period of rotation about the X_1-axis given by

$$T = \frac{2\pi}{G} (r_e + r_e^{-1}) \quad . \qquad [5]$$

In this case all the particles rotate synchronously with identical projections of unit length

$$\bar{r}_1 = 0 \quad ,$$

$$\bar{r}_2 = [1 + r_e^2 \tan^2 \frac{2\pi t}{T}]^{-\frac{1}{2}} \quad , \qquad [6]$$

$$\bar{r}_3 = [1 + r_e^{-2} \cot^2 \frac{2\pi t}{T}]^{-\frac{1}{2}} \quad ,$$

$\bar{r}_2$ and $\bar{r}_3$ oscillating with frequency 2/T and amplitude unity.

As discussed previously[1], the oscillations of $\bar{r}_i$ will decay from (i) spreads in r_e and (ii) particle interactions. We now consider the effect (i) to provide some theoretical basis for the experimental study, effect (ii) being discussed later. Assuming a Gaussian distribution

of r_e:

$$g(r_e) = \frac{1}{\sqrt{2\pi}\,\sigma_e} \exp\left[\frac{-(r_e - \bar{r}_e)^2}{2\sigma_e^2}\right] \quad , \qquad [7]$$

the fraction of particles oriented in the interval $d\phi_1$ at ϕ_1 corresponds to that of r_e in the interval dr_e at r_e at any given time (except at t = 0) so that

$$p_{\sigma,t}(\phi_1)d\phi_1 = g(r_e)dr_e \quad . \qquad [8]$$

Since the partial derivative $(\partial r_e/\partial \phi_1)_t$, which may be obtained from [4b], is not explicitly expressed in terms of ϕ_1, $p_{\sigma,t}(\phi_1)$ is most conveniently given in terms of r_e:

$$p_{\sigma,t}(\phi_1) = \frac{1}{\sqrt{2\pi}\,\sigma_e} \exp\left[\frac{-(r_e - \bar{r}_e)^2}{2\,\sigma_e^2}\right] \cdot \frac{\cos^2\frac{2\pi t}{T} + r_e^2 \sin^2\frac{2\pi t}{T}}{\sin\frac{2\pi t}{T}\cos\frac{2\pi t}{T} - \frac{2\pi t(r_e^2 - 1)}{T\,(r_e^2 + 1)}} \, . \qquad [9]$$

The evaluation of $p_{\sigma,t}(\phi_1)$ can be made in the following way: for each value of r_e the orientation ϕ_1 at a given time is obtained from [4b], then the corresponding $p_{\sigma,t}(\phi_1)$ is calculated from [9].

If one considers the rods of axis ratio $r_e^* = \bar{r}_e - \Delta r_e^*$ and $r_e^{**} = \bar{r}_e + \Delta r_e^{**}$ for the same $\bar{r}_e$, then the corresponding

orientations $\phi_1^* = \bar{\phi}_1 + \Delta\phi_1^*$ and $\phi_1^{**} = \bar{\phi}_1 - \Delta\phi_1^{**}$ are obtained from [4b] at any given time, $\bar{\phi}_1$ being the orientation for $\bar{r}_e$. Changes of sign for the differences ($-\Delta r_e^*$ to $+\Delta\phi_1^*$ and $+\Delta r_e^{**}$ to $-\Delta\phi_1^{**}$) are due to rods of smaller axis ratio always rotating ahead of that of higher axis ratio at constant G (see [4b]). However when $\Delta r_e^* = \Delta r_e^{**}$ so that $g(r_e^*) = g(r_e^{**})$, but in general $\Delta\phi_1^* \neq \Delta\phi_1^{**}$. It follows that, although the Gausian distribution $g(r_e)$ is symmetrical with respect to the mean $\bar{r}_e$, the probability $p_{\sigma,t}(\phi_1)$ is generally not symmetrical with respect to the mean $\bar{\phi}_1$.

Due to the differences in angular velocity amongst rods, the spread in ϕ_1 increases as shear proceeds until a time is reached at which the most rapidly rotating rod (of least r_e) catch up the slowest (of greatest r_e) so that the differences in orientation ϕ_1 between the two is 180°. In this case, the distribution $p_{\sigma,t}(\phi_1)$ is not given simply by [9]; instead the summation over the range overlapped by the two different axis ratios is required. This behaviour of $p_{\sigma,t}(\phi_1)$ for initially aligned rods eventually determines the equilibrium distribution $p_\infty(\phi_1)$ given by [102]-1. Since [9] is not given in terms of ϕ_1 and for the reason just mentioned is not valid after some finite time, the equilibrium distribution $p_{\sigma,\infty}(\phi_1)$ cannot be obtained analytically, but only by numerical evaluation of [9] at large t and summation at given ϕ_1 for different values of r_e.

The mean projection lengths $\bar{r}_i$ given by [6] resulting from the spread in r_e are then modified to

$$\bar{r}_{2\sigma} = \frac{1}{\sqrt{2\pi}\,\sigma_e} \int_0^\infty \frac{\exp\left[\dfrac{-(r_e - \bar{r}_e)^2}{2\sigma_e^2}\right]}{(1 + r_e^2 \tan^2 \frac{2\pi t}{T})^{\frac{1}{2}}}\, dr_e \qquad [10]$$

$$\bar{r}_{3\sigma} = \frac{1}{\sqrt{2\pi}\,\sigma_e} \int_0^\infty \frac{\exp\left[\dfrac{-(r_e - \bar{r}_e)^2}{2\sigma_e^2}\right]}{(1 + r_e^{-2} \cot^2 \frac{2\pi t}{T})^{\frac{1}{2}}}\, dr_e \quad , \qquad [11]$$

which show damped oscillations with time.

(d) Reversibility

When shear flow is reversed the motion of rigid particles is known to be also reversible[7,8], i.e. the translational and rotational paths of each particle will be retraced to the original position, provided that the same boundary conditions exist for the reversed flow. Various demonstrations of this phenomenon have been described by Heller[9], Goldsmith and Mason[10], and in a cine-film by Taylor[11]. For example, letters of dyed liquid written in the annulus of Couette apparatus which was filled with the same (but undyed) liquid can be made to disappear by rotating one of the cylinders and then to reappear slightly

blurred by diffusion of the dye, on rotating backwards[10]. Multi-particle interactions and orientation distributions of spheres[12], rods[2] and discs[2,13] have also been demonstrated to be reversible. Reversible oscillations of $\bar{r}_2$ are demonstrated for a suspension of initially aligned rods in Section 3(e).

2. EXPERIMENTAL PART

(a) Apparatus and Materials

Experiments were carried out in a Couette apparatus consisting of two counter-rotating concentric cylinders capable of producing a plane shear flow and permitting observations along the X_1-axis[14].

Rods of uniform length were prepared by sectioning, in a sliding microtome, Nylon monofilaments embedded in a block of Tissuemat wafers (Fisher, m.p. = 67°C). By using single filaments instead of the 20- to 40-filament yarns used in earlier work[4], it was possible to reduce the standard deviations σ_p from the mean axis ratio $\bar{r}_p$ from values of $\sigma_p/\bar{r}_p$ up to 10% to $\leq$ 3% (Table II).

The distribution of r_p of rods for $\bar{r}_p$ = 15.9 obtained from the measurement of 106 rods is shown by the histogram in Fig. 2, where r_p values spread over the range of 15 to 16.9, which conforms reasonable well with a Gaussian distribution, similar to [7] with r_p in place of r_e.

TABLE II

DESCRIPTION OF SUSPENSIONS

System	Material	d(μ)	ℓ(μ)	$\bar{r}_p$	$\bar{r}_e$	Medium	N($m\ell^{-1}$)	c x 10^3 ($m\ell/m\ell$)
I Rods	Nylon[a)]	45	720	15.9(2.4)[g)]	11.6(3.6)	Silicone Fluid 200[b)] + Freon BF[c)]	20.0 50.0 100.0	0.023 0.057 0.115
II Rods	Aluminium[f)] coated Nylon	175	870	4.96(3.0)	3.96(4.8)	Castor oil AA[d)] + $C_2H_2Br_4$	10.0 20.0 50.0 100.0 200.0	0.21 0.42 1.05 2.09 4.19
III Discs	Mylar[c)]	1170	130	0.11(1.6)	0.2(2.7)	Ucon Oil HB 1715[e)] + $C_2H_2Br_4$	10.0 25.0 50.0	1.37 3.42 6.85

a) Canadian Industries Limited, b) Dow Corning, c) Du Pont, d) Fisher Scientific Co.,
e) Union Carbide, f) Coating by National Research Co., Cambridge, Mass.,
g) Bracketed values are percent standard deviations 100 $\sigma_p/\bar{r}_p$ or 100 $\sigma_e/\bar{r}_e$ from the mean.

The standard deviation σ_p was obtained from the measured values of r_p using

$$\sigma_p^2 = \frac{1}{N_1} \sum_{i=1}^{N_1} (r_{pi} - \bar{r}_p)^2 \qquad [12]$$

N_1 being the total number of particles measured. However, since continuous monofilaments were only available in several diameters, and the microtomed sections had to be less than 1 mm, the number and size of axis ratios that could be obtained by this method were limited. Aluminium-coated Nylon monofilaments were also used to produce electrically conducting rods used in the experiments in which the rods were aligned electrically.

Discs of uniform diameter and thickness were made by passing a polyester computer tape 1 inch wide and 130μ thick through an IBM punching machine to produce two sizes of discs (1170 and 1820μ in diameter)[15]. The mixture was separated by sieving and the smaller discs were used. This method has the advantages of high productivity and uniformity over the technique used earlier[16] of pressing thermoplastic spheres in a heated hydraulic press.

Liquids of viscosity in the range 10 to 50 poise, to which tetrabromoethane was added to equalize the densities of the fluid and the particles, were used as suspending media. The viscosity of each liquid was measured in a rotational viscometer (Rheomat 15, A.G. Epprecht, Zurich), and found

FIGURE 2

Histogram of the measured particle axis ratios r_p and the Gausian probability function (broken line) calculated from [7] for rods of $\bar{r}_p = 15.9$ and $\sigma_p = 0.38$ ($100\ \sigma_p/\bar{r}_e = 2.4\%$).

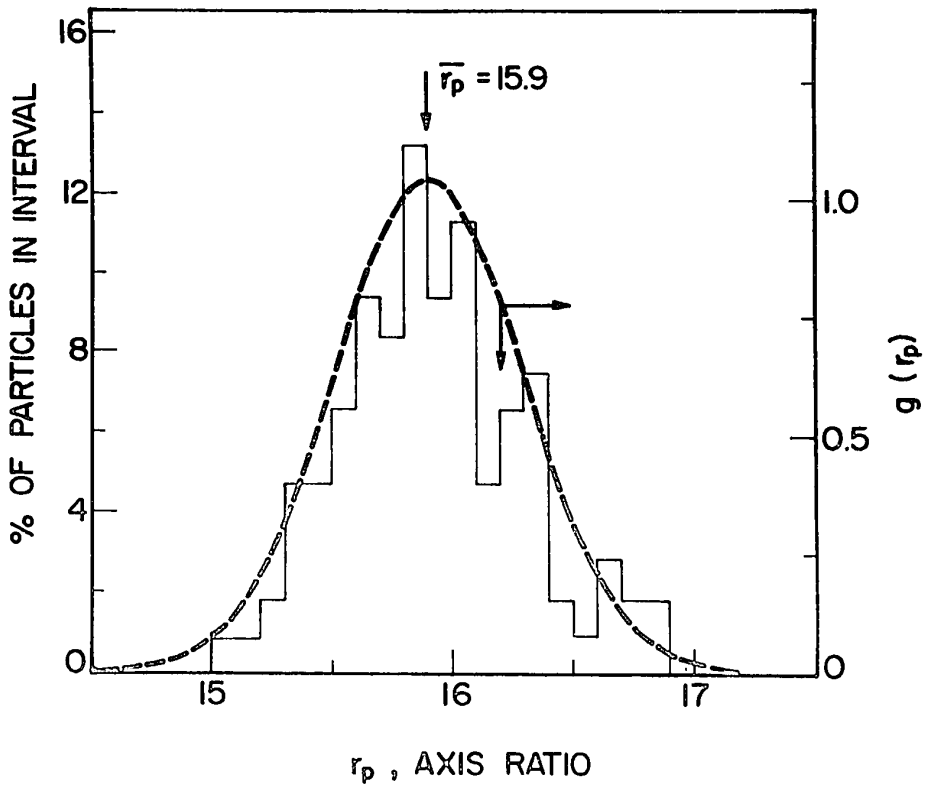
16
12
8
4
0
% OF PARTICLES IN INTERVAL
$\bar{r_p}$ = 15.9
1.0
0.5
0
g (r_p)
15
16
17
r_p , AXIS RATIO

to show Newtonian behavior up to velocity gradients of 100 sec^{-1}. No observable sedimentation occurred over a period of several days in any of the suspensions used; their properties are listed in Table II.

All experiments were conducted in a temperature-controlled room at 21 ± 0.5°C.

(b) Procedures

To avoid end effects in the Couette apparatus[14], the suspensions were floated on an insoluble layer of a much less viscous but denser liquid such as saturated aqueous cadmium nitrate or glycerine. Two types of initial orientation were sought; one random and the other, with rods only, with parallel alignment. To obtain random orientations, the suspensions were stirred with a needle probe after being introduced into the apparatus. As will be seen later, the randomness with respect to ϕ_1 was satisfactory, but only partially so with respect to θ_1. Shear at G = 0.5 to 1 sec^{-1} was then applied and photographs of particles were taken at regular time intervals in the vertical direction (along the X_1-axis) using an automatic camera (Robot Motor Recorder 36 ME 35mm camera with a 30 ft. film magazine) capable of taking up to 250 frames. The time of each frame was recorded from a stopwatch through a separate lens on the upper right corner of the frame.

To obtain initially parallel orientations, the coated rods were aligned by applying an electric field (60 Hz, 2 kv) across the annulus between the two cylinders (i.e. along the X_2-axis) using glycerine as the substrate. After several minutes the rods become aligned along the direction of the field[5], i.e. at $\phi_1 = 0°$ and $\theta_1 = 90°$. Following removal of the electric field, shear at $G = 0.5$ sec^{-1} was applied to the suspension, and photographs of the particles were taken as before.

With rods, the two quantities ℓ_{23}, the projected length on the X_2X_3-plane (the plane of the photographs), and ϕ_1 of each rod was measured from the photographs which were projected on an analysing table. With discs, d and d_{23}, the major and minor axes of the elliptical projection of the face on the X_2X_3-plane and ϕ_1 of each disc were measured. The angle θ_1 of each particle was calculated from the following geometrical relationships

$$\sin \theta_1 = \ell_{23}/\bar{\ell} \quad , \qquad \cos\theta_1 = d_{23}/d \quad . \qquad [13]$$

Since the length of a rod could not be determined directly from the photographs, $\bar{\ell}$, the mean length measured separately, was used in the calculation; this introduced errors which were minimized by using rods of small σ_p.

The orbit constant C and the phase angle κ of a given particle in a suspension at time t are defined by[1]

$$C = \frac{1}{r_e} \tan\theta_1 (r_e^2 \cos^2\phi_1 + \sin^2\phi_1)^{\frac{1}{2}} \qquad [14a]$$

$$\kappa = \tan^{-1} \left(\frac{\tan\phi_1}{r_e} \right) - \frac{2\pi t}{T} \qquad [14b]$$

and are constant in a collision-free suspension; thus under collisionless conditions $p_t(C)$ and $p_t(\kappa)$ should remain constant. However, the calculations of C and κ from [14] require θ_1, ϕ_1, r_e and T to be known for each individual particle. In practice, it was not feasible to determine r_e for each particle whose ϕ_1 was measured. Instead C and κ of each particle were calculated by inserting the means $\bar{r}_e$ and $\bar{T}$ ($= 2\pi(\bar{r}_e + 1/\bar{r}_e)/G$) in [14]; these were obtained by measuring T for 30 particles of each stock at a known G and calculating r_e by means of [5] and then taking the mean value $\bar{r}_e$ and the standard deviation σ_e using [12] with r_e in place of r_p (Table II). Although the number of measurements of r_e was not always sufficient to determine the distribution function reliably, it was assumed to be Gaussian (as for r_p) in order to calculate the effect of spread in values of r_e on the orientation distributions[1)]. The two measured axis ratios r_p and r_e are in good agreement with the empirical relationship[17,18)]

$$\log_{10} r_e = 0.78 \log_{10} r_p + 0.051 \qquad [15]$$

which gives better agreement with the experimental data for the entire range of r_e including discs ($r_e < 1$) than the relation obtained by Cox[1,19] which is applicable only for $r_e >> 1$. If the variance in r_e is determined solely by that in r_p, it follows from differentiation of [15] that

$$\frac{\sigma_e}{\bar{r}_e} = 0.78 \frac{\sigma_p}{\bar{r}_p} \quad . \qquad [16]$$

For the particles employed (Table II), the proportionality constant was found to be 1.6 instead of 0.78, from which we conclude additional factors such as curvature and irregularities in the shapes of the edges caused by the cutting contributed to σ_e.

Using the mean values $\bar{r}_e$ and $\bar{T}$ introduces errors into C and κ, but the error in C becomes only significant when θ_1 is very small (see [14a]), so that the effects of the spread in r_e on $p_t(C)$ and $p_t(\phi_{im})$ are small and may be neglected. On the other hand the error in κ does not depend on the orientation ϕ_1 since the first and the second terms in [14b] are nearly the same order of magnitude. It is convenient to introduce a new quantity κ_1 defined by

$$\kappa_1 = \tan^{-1} \left(\frac{\tan\phi_1}{\bar{r}_e} \right) - \frac{2\pi t}{\bar{T}} \qquad [17]$$

which is different from κ defined by [14b]. The effects of

FIGURE 3

(a) Tracings of photographs showing the orientation distributions of rods ($\bar{r}_e$ = 11.6) at N = 100 particles/ml, for initially random orientations at t = 0 (frames A1 to A4) and for t = $\bar{T}/4$ (frames B1 to B4). The X_1-axis is normal to the plane of page.

(b) Projections of discs ($\bar{r}_e$ = 0.2, N = 50 particles/ml), the long bars corresponding to the diameter d and the short bars (having orientations ϕ_1) corresponding to the projection d_{23}. A complete disc face is shown in each frame. Frame A1 to A4 correspond to initially random orientation, and B1 to B4 to t = $\bar{T}/4$.

Analysis of orientations ϕ_1 and projection lengths ℓ_{23} and d_{23} were made for each particle from which all of the orientation parameters and orbit constants were calculated using [13] and [14].

(a)

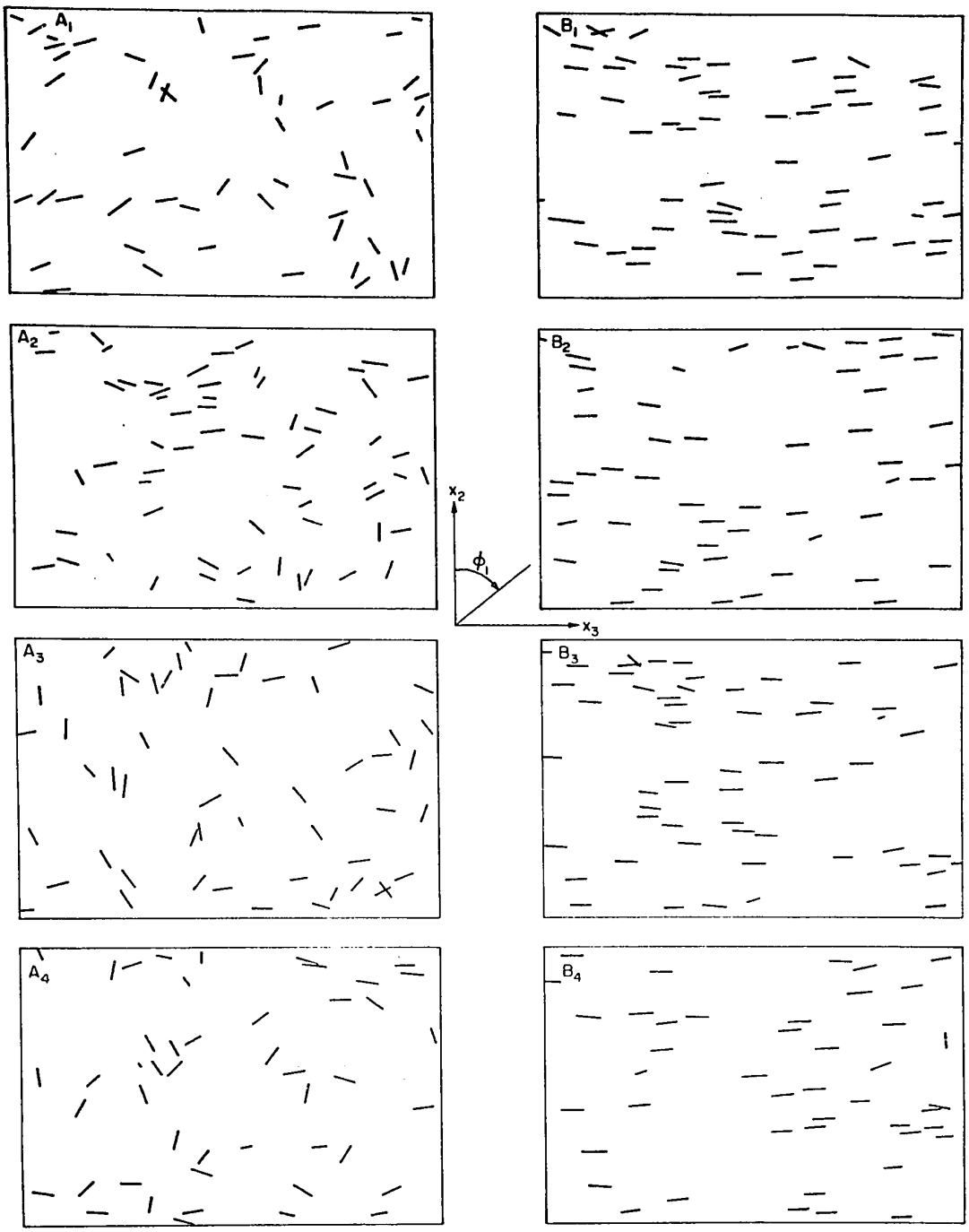

(b)

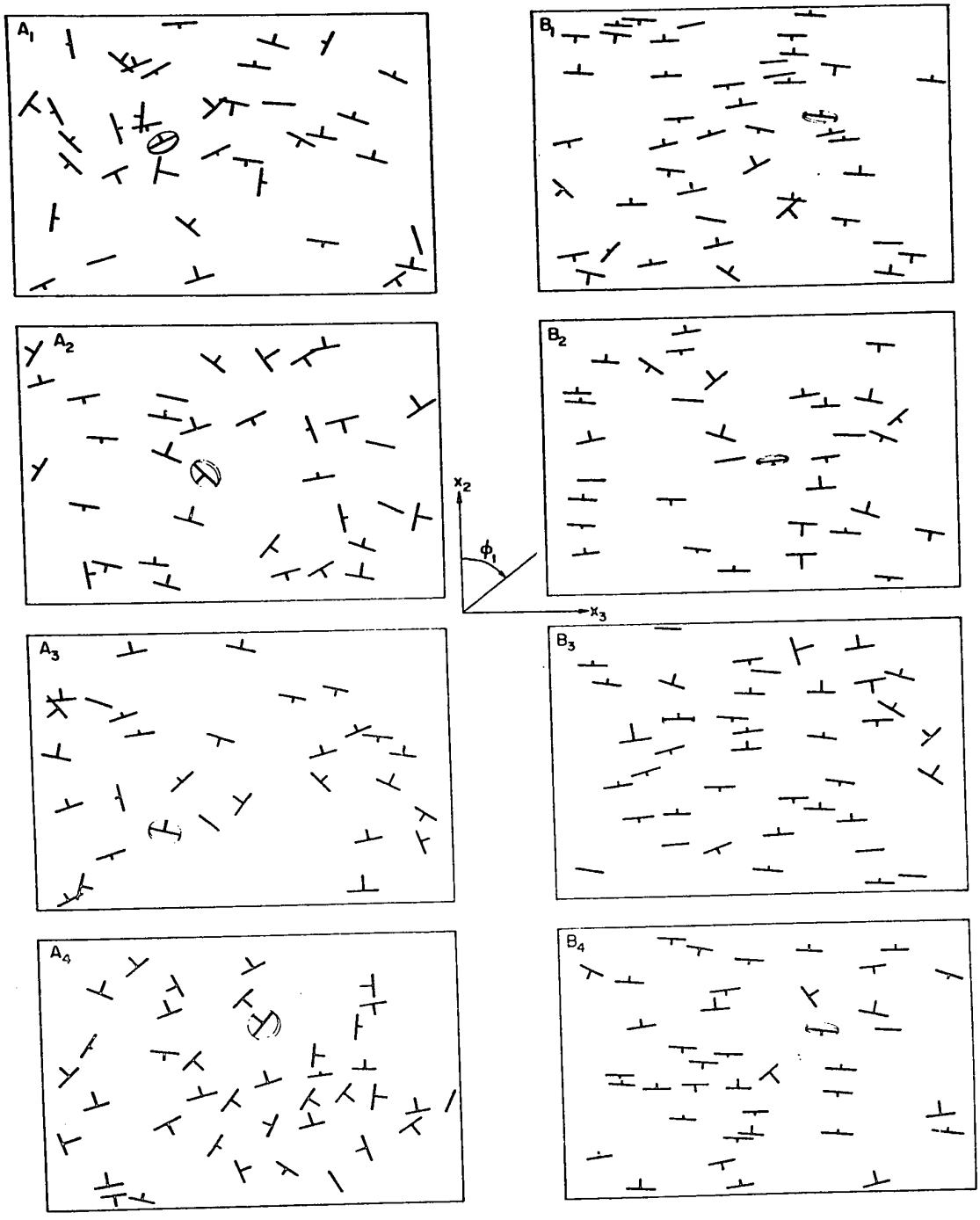

the spread in r_e on $p_t(\kappa_1)$ will be discussed in Section 3(c).

Examples of particle projections traced from photographs are shown in Fig. 3. To obtain the distributions of particle orientations over 100 to 200 particles, it was necessary to photograph several different fields since each contained less than 50 particles. The mean orientation parameters $\bar{r}_i$, $\bar{S}_{ij}$ (i,j = 1,2,3) and the rheological properties of the suspension were calculated using [31]-1, [48]-1 and [50]-1.

3. RESULTS AND DISCUSSION

(a) Distribution of Orbits

The orbit distributions $P_t(\phi_{im})$ for rods ($\bar{r}_e = 11.6$, $N = 50\ ml^{-1}$) and discs ($\bar{r}_e = 0.2$, $N = 25\ ml^{-1}$) which were initially randomly oriented were determined by calculating ϕ_{im} from the measured orientations θ_1, ϕ_1 of each particle and $\bar{r}_e$. The results, summarized in Table III, show that $P_t(\phi_{im})$ remained effectively constant in the time interval up to 4 particle rotations. The mean values of $P_t(\phi_{im})$ (denoted by a bar over the symbol) over the time $t/\bar{T} = 4$ given in the last column (Table III) are plotted in Fig. 4, where the standard deviation from the mean is indicated by the vertical bar about each point. As expected from the

TABLE III

MEASURED ORBIT DISTRIBUTIONS

Rods ($\bar{r}_e$ = 11.6, N = 50 $m\ell^{-1}$); Discs ($\bar{r}_e$ = 0.2, N = 25 $m\ell^{-1}$)

$\bar{r}_e$	ϕ_{im} (deg.)	C	$P_E(\phi_{im})$ [a]	$P_t(\phi_{im})$					$\overline{P_t(\phi_{im})}$ [b]
				$t/\bar{T} = 0$	$t/\bar{T} = 1$	$t/\bar{T} = 2$	$t/\bar{T} = 3$	$t/\bar{T} = 4$	
11.6 (i = 3)	10	0.176	0.091	0.079	0.052	0.014	0.022	0.020	0.037
	20	0.364	0.208	0.208	0.187	0.190	0.292	0.218	0.219
	30	0.577	0.323	0.348	0.302	0.296	0.416	0.306	0.334
	40	0.839	0.436	0.470	0.417	0.415	0.532	0.428	0.452
	50	1.192	0.549	0.585	0.573	0.528	0.635	0.545	0.573
	60	1.732	0.662	0.704	0.687	0.668	0.723	0.660	0.688
	70	2.747	0.775	0.773	0.802	0.768	0.810	0.776	0.786
	80	5.671	0.888	0.857	0.927	0.874	0.920	0.885	0.893
	90	∞	1.000	1.000	1.000	1.000	1.000	1.000	1.000
0.2 (i = 2)	10	0.882	0.061	0.096	0.025	0.047	0.057	0.041	0.053
	20	1.820	0.175	0.212	0.124	0.119	0.204	0.105	0.158
	30	2.887	0.294	0.288	0.240	0.238	0.329	0.306	0.280
	40	4.196	0.414	0.399	0.397	0.398	0.489	0.487	0.433
	50	5.959	0.532	0.490	0.488	0.500	0.546	0.595	0.524
	60	8.660	0.649	0.615	0.636	0.619	0.647	0.727	0.649
	70	13.737	0.766	0.707	0.760	0.726	0.705	0.776	0.735
	80	28.356	0.883	0.822	0.843	0.822	0.784	0.844	0.823
	90	∞	1.000	1.000	1.000	1.000	1.000	1.000	1.000

a) Calculated from the equations listed in Table I

b) Mean value over the five values of $t/\bar{T}$

theoretical calculations of $P_E(\phi_{im})$ in the third column of Table III or by the solid lines in Fig. 4, $\overline{P_t(\phi_{3m})}$ for rods and $\overline{P_t(\phi_{2m})}$ for discs were linear with respect to ϕ_{im} except near 0° (i.e., near C = 0), indicating a nearly constant $p_t(\phi_{im})$. Similar constancy in orbit distributions was observed at all other concentrations listed in Table II.

For suspensions of rods of initially parallel alignment achieved by applying an electric field across the annulus between the Couette cylinders, 88.5% of rods were initially in the X_2X_3-plane (i.e., C = ∞ and $\phi_{3m} = 90°$), and 87% of rods remained in the same orbit after shearing for 5 particle rotations.

Thus in all of the experiments, the distribution of orbits, and by inference (but not proven) the orbit constant of each particle in an assembly, remained constant over the first 4 to 5 rotations; this is the region in which the detailed analysis of orientation distributions discussed below have been made.

On the other hand it was expected from the observations of Anczurowski *et al*[2,4] over several hundred particle rotations at comparable concentrations, that $P_t(\phi_{3m})$ for rods would drift slowly toward lower orbit constants and $P_t(\phi_{2m})$ for discs toward slightly higher orbits; the latter case was confirmed in the present experiments over 112 rotations as shown in Fig. 4 (b).

FIGURE 4

The mean values of $P_t(\phi_{3m})$ for rods of $\bar{r}_e = 11.6$ at $N = 50\ ml^{-1}$ (part a) and of $P_t(\phi_{2m})$ for discs of $\bar{r}_e = 0.2$ at $N = 25\ ml^{-1}$ (part b) over 4 particle rotations. The vertical spread at each point indicates twice the standard deviation from the mean. The theoretical distributions corresponding to random orientation calculated from the equations given in Table I are given by the solid lines. The equilibrium distributions of orbits after 112 rotations of the discs are given by the open triangles and the broken line drawn through the points.

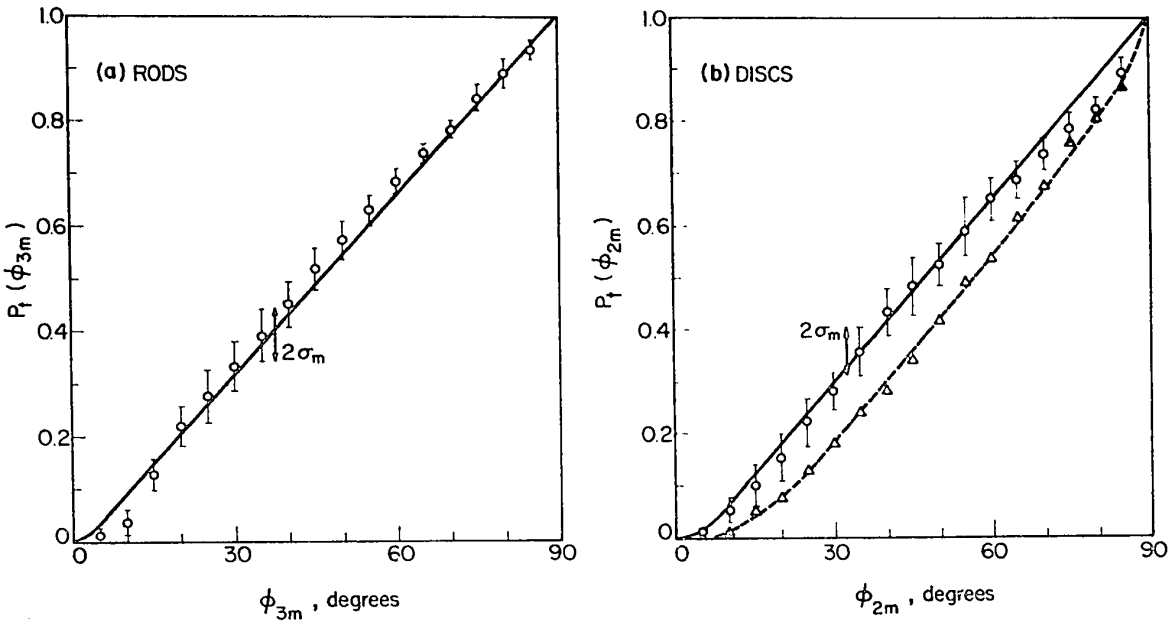
(a) RODS
(b) DISCS
$P_t(\phi_{3m})$
$P_t(\phi_{2m})$
$2\sigma_m$
ϕ_{3m}, degrees
ϕ_{2m}, degrees
0
0.2
0.4
0.6
0.8
1.0
30
60
90

(b) Oscillations in Orientation Distributions

(i) Initially Random Orientation

Oscillatory distributions of particle orientations ϕ_1 and θ_1 were observed during the early stages when the orbit distributions remained constant for initially random orientations, described in this section, and for initially parallel alignment, described in the following section.

The probability distributions $p_t(\phi_1) = dP_t(\phi_1)/d\phi_1$, obtained from the slope of the smoothed curves drawn through the experimental integral distribution $P_t(\phi_1)$, are shown in the polar diagrams in Fig. 5 for both rods and discs, using $[p_t(\phi_1)]^{\frac{1}{4}}$ as the radial coordinate in order to decrease the axis ratio of the resulting envelopes. The initial distributions were close to the circle of radius $[1/2\pi]^{\frac{1}{4}}$ corresponding to random orientation (Fig. 5(i)). When shear was applied a periodic change of frequency $2/\overline{T}$ in $p_t(\phi_1)$ was observed as predicted from the theory[1].

For rods, the maximum in $p_t(\phi_1)$ first appeared in the range of ϕ_1 between 45° and 90°, and occurred at $\phi_1 = 90°$ after one quarter of a particle rotation ($t = \overline{T}/4$, Fig. 5(iii)); the maximum then rotated into the region of ϕ_1 between 90° and 135°, and the initial distribution was nearly, but not completely, restored at $t = \overline{T}/2$ (Fig. 5(v)). Similar changes in $p_t(\phi_1)$ occurred with the discs except

FIGURE 5

Polar plots of the measured values of $[p_t(\phi_1)]^{\frac{1}{4}}$ versus ϕ_1 for rods of $\bar{r}_e = 11.6$, $N = 100\ ml^{-1}$ (open circles) and for discs of $\bar{r}_e = 0.2$, $N = 25\ ml^{-1}$ (closed circles) at various times indicated in each plot. The circle of radius $[1/2\pi]^{\frac{1}{4}}$ in (i) corresponds to a random orientation. The solid lines in (ii) to (v) are calculated from [18] for $\bar{r}_e$ and standard deviations listed in Table II. In (v) the maximum occurred at $\phi_1 = 70°$, 110°, 250° and 290° for rods, and at $\phi_1 = 33°$, 147°, 213° and 227° for discs. The equilibrium distributions $p_\infty(\phi_1)$ (given by the curve in (vi) and calculated from [102]-1) were reached after only 4 particle rotations.

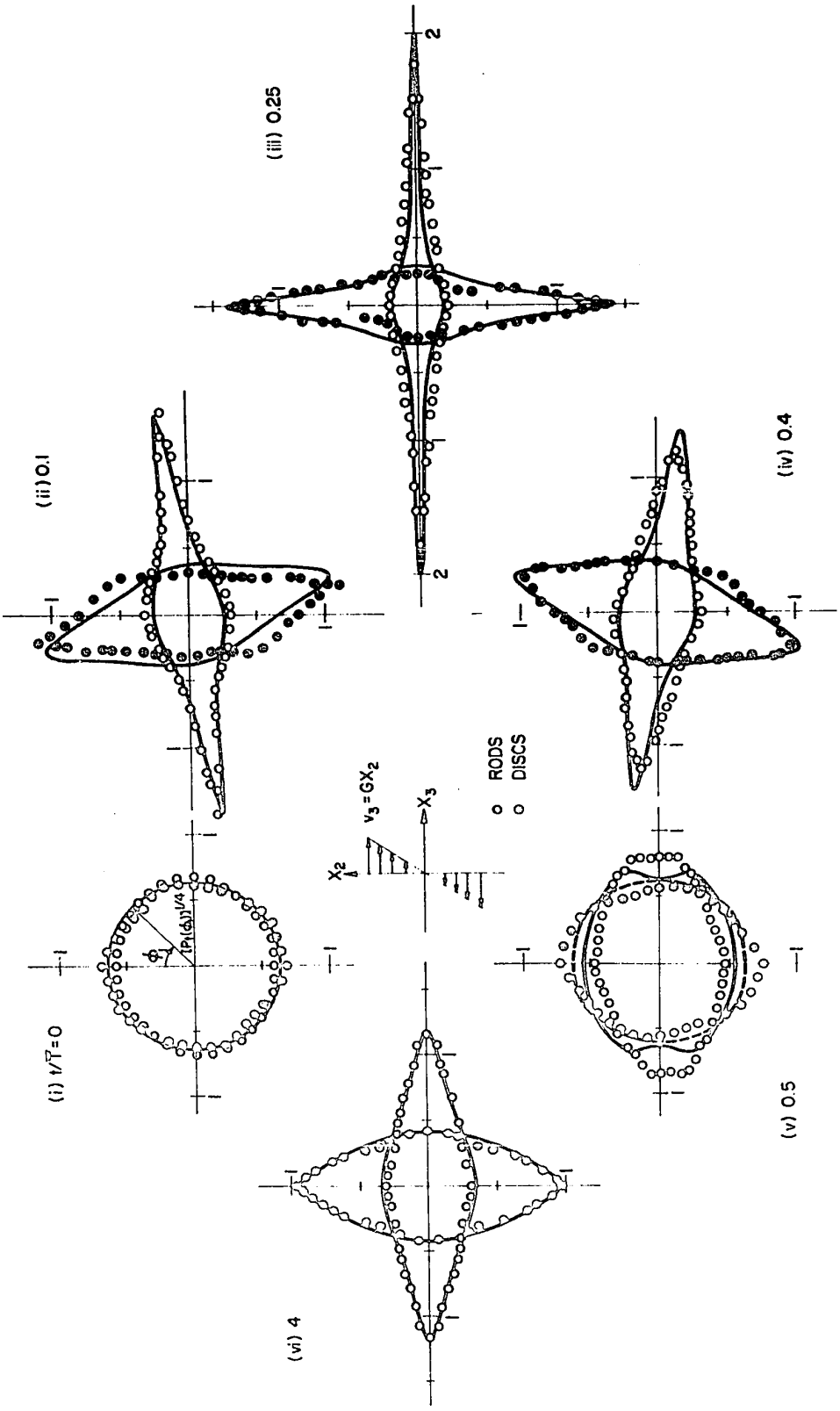
(i) t/T=0
(ii) 0.1
(iii) 0.25
(iv) 0.4
(v) 0.5
(vi) 4
RODS
DISCS
$v_3 = GX_2$
X_2
X_3
$(P_1(\phi_1))^{1/4}$
ϕ_1
2
2

that the maxima were shifted by 90°. Since the particle angular velocity $d\phi_1/dt$ is at a minimum at $\phi_1 = 90°$ for rods and $\phi_1 = 0°$ for discs, rods spend most of their time close to the direction of flow (in the X_1X_3-plane), and discs with their axes normal to it (in the X_1X_2-plane). As seen in Fig. 5 (ii), the maxima of $p_t(\phi_1)$ for rods thus moved quickly (i.e., within $t/\bar{T} < 0.1$) toward the direction of flow and for discs toward $\phi_1 = 0°$. At $t = \bar{T}/4$, more than 85% of rods had orientations with $\phi_1 = 90 \pm 5°$, whereas about 90% of discs were within $\phi_1 = \pm 5°$ (Fig. 5(iii)), corresponding to a calculated major semi-axis $[p_{T/4}(90°)]^{\frac{1}{4}} = [r_e^2/2\pi]^{\frac{1}{4}}$ and a minor semi-axis $[p_{T/4}(0°)]^{\frac{1}{4}} = [1/2\pi r_e^2]^{\frac{1}{4}}$ for rods and the converse for discs ([25]-1). The measured probability distributions $p_{T/2}(\phi_1)$ were not the same as $p_o(\phi_1)$ [Fig. 4(i) and (v)]; this could have been due to the small spread in r_e of the particles in a given suspension[1] and, as will be seen later, to interactions between particles.

The effect of the spread in r_e can be estimated from the known distribution in r_e by writing the probability function

$$p_{\sigma,t}(\phi_1) = \int_0^\infty p_t(\phi_1, r_e) g(r_e) dr_e \qquad [18]$$

where $p_t(\phi_1, r_e)$ is the probability function of ϕ_1 for a truly monodisperse (i.e., $\sigma = 0$) and collision-free suspension obtained previously[1] and $g(r_e)$ is taken to be Gaussian

and given by [7]. The solid lines in Fig. 5(ii) to (v) were calculated by numerical integration of [18] with $\sigma = 0.418$ (3.6%) for rods of $\bar{r}_e = 11.6$ and $\sigma = 0.0054$ (2.7%) for discs of $\bar{r}_e = 0.2$.

The dimples in the calculated curve at $t = \bar{T}/2$ [Fig. 5(v)] can be explained in the following way. Consider a rotation of rods of r_e^* differing slightly from $\bar{r}_e$. The orientation ϕ_1^* at $t/\bar{T}$ is given by

$$\tan \phi_1^* = r_e^* \tan \left[\frac{2\pi t}{\bar{T}} \frac{(\bar{r}_e + \bar{r}_e^{-1})}{(r_e^* + r_e^{*-1})} + \kappa \right] . \qquad [19]$$

At $t = \bar{T}/2$, rods of r_e^* assume the orientation given by

$$\tan \phi_1^* = r_e^* \tan \left[\frac{\pi(\bar{r}_e + \bar{r}_e^{-1})}{r_e^* + r_e^{*-1}} + \kappa \right] \qquad [20a]$$

whereas rods of $\bar{r}_e$ assume the original orientation

$$\tan \phi_1 = \bar{r}_e \tan \kappa . \qquad [20b]$$

If both rods start off with the same orientation, for example, $\phi_1 = 0°$ (corresponding to $\kappa = 0°$), the orientation ϕ_1^* at $t = \bar{T}/2$, as seen from [20a], differs appreciably from $\phi_1 = 0°$. If, on the other hand, the initial orientation is $\phi_1 = 90°$ (corresponding to $\kappa = 90°$) then the deviation of ϕ_1^* from $\phi_1 = 90°$ at $t = \bar{T}/2$ is very small. Therefore

$p_{\sigma,t}(\phi_1)$ at $t = \bar{T}/2$ decreases around $\phi_1 = 0°$ but remains nearly equal to $p_o(\phi_1)$ at $\phi_1 = 90°$; thus it possesses a maximum somewhere between $\phi_1 = 0°$ and 90° depending upon σ_e. Similarly $p_{\sigma,t}(\phi_1)$ for discs at $t = \bar{T}/2$ has minima and maxima but shifted by 90°. In Fig. 5(v) this is evident for rods, but not so for discs because of the very small spread in r_e for the discs ($\sigma_e/\bar{r}_e < 0.03$). The experimental points are not in perfect agreement with the theoretical values, suggesting that, even though the orbit distributions did not change appreciably, there were particle interactions in the suspensions which caused the deviations.

Although not shown in Fig. 5, the oscillations of $p_t(\phi_1)$ continued with decreasing amplitude until equilibrium was established after only 4 particle rotations as illustrated in Fig. 5(vi). The experimental points for the equilibrium distribution $p_\infty(\phi_1)$ were in good agreement with the theoretical values based on the time-independent solution of the continuity equation, namely $p_\infty(\phi_1)(d\phi_1/dt) = \text{const.}$, the solution of which is given by [102]-1, from which it also follows that the equilibrium orientation distribution $p_{\sigma,\infty}(\phi_1)$ obtained as a limit of [18] has an error of order σ_e^2 in comparison with $p_\infty(\phi_1)$. Thus the curves in Fig. 5(vi) for $p_\infty(\phi_1)$ are indistinguishable from $p_{\sigma,\infty}(\phi_1)$.

For the distribution of orientations θ_1 a new quantity $q_t(\theta_1)$ is introduced here defined by

$$q_t(\theta_1) = \frac{d\, p_t(\theta_1)}{d(1 - \cos\theta_1)} = p_t(\theta_1)\ \text{cosec}\ \theta_1 \qquad [21]$$

and chosen as a matter of convenience since the integral distribution $P_t(\theta_1)$ for a random orientation is given by

$$P_o(\theta_1) = \tfrac{1}{2} (1 - \cos \theta_1) \qquad [22a]$$

so that

$$q_o(\theta_1) = \tfrac{1}{2} \qquad [22b]$$

In Fig. 6, the experimental points are plotted in a polar diagram with $[q_t(\theta_1)]^{\frac{1}{2}}$ as the radial coordinate, obtained from the slope of smoothed experimental curves of $P_t(\theta_1)$ versus $(1 - \cos \theta_1)$, in the range of θ_1 between 0° and 90°. To avoid excessive superposition of experimental points only one half of each curve is shown, either in the upper or the lower quadrant of Fig. 6. As already mentioned, the initial distribution $q_o(\theta_1)$ for rods was not perfectly random [Fig. 6a(i)], probably because of insufficient stirring before starting the experiment. On the other hand, $q_o(\theta_1)$ for discs showed satisfactory randomness [Fig. 6b(i)]. At $t = \overline{T}/4$ more than 60% of rods had $\theta_1 > 80°$, whereas 75% of discs had $\theta_1 > 70°$. The calculated distribution $q_{T/4}(\theta_1)$ was obtained by means of [21] using $p_t(\theta_1)$ given by [21]-1. Good agreement with the experimental points except near $\theta_1 = 0°$ is seen from Fig. 6-a(ii) and -b(ii). It is also noted from Fig. 6, that the experimental values at $t = 0$ and $\overline{T}/2$ were nearly identical, and similarly for $t = \overline{T}/4$ and $3\overline{T}/4$, showing that $q_t(\theta_1)$ oscillated synchronously with

FIGURE 6

Polar plot of $[q_t(\theta_1)]^{\frac{1}{2}}$ versus θ_1 for the same suspension as in Fig. 5 [(a) for rods and (b) for discs] after each quarter rotation. The heavy solid semi-circle of radius $1/\sqrt{2}$ corresponds to a random orientation given by [22b]. The theoretical distributions $q_{T/4}(\theta_1)$ calculated from [21] are also shown by the solid lines in both (a) and (b).

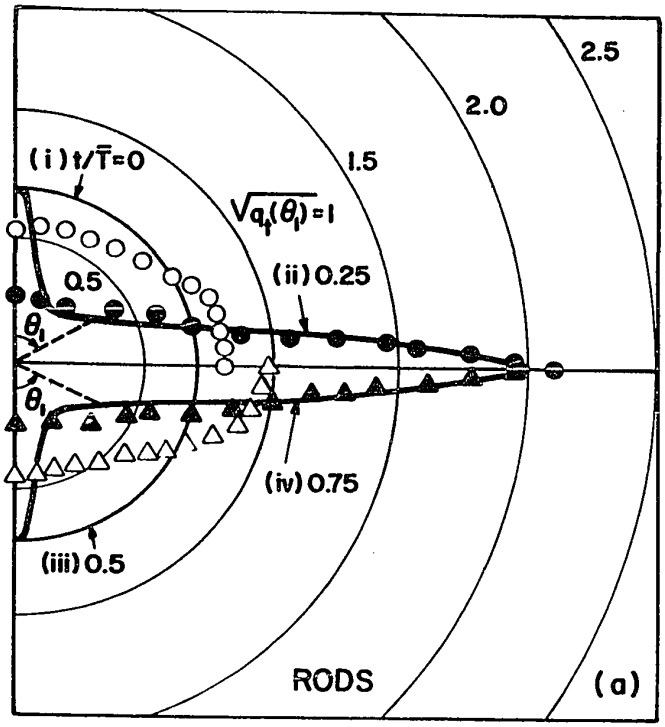
2.5
2.0
1.5
(i) t/T̄=0
√q_t(θ_t)=1
(ii) 0.25
0.5
θ_t
θ_t
(iv) 0.75
(iii) 0.5
RODS
(a)

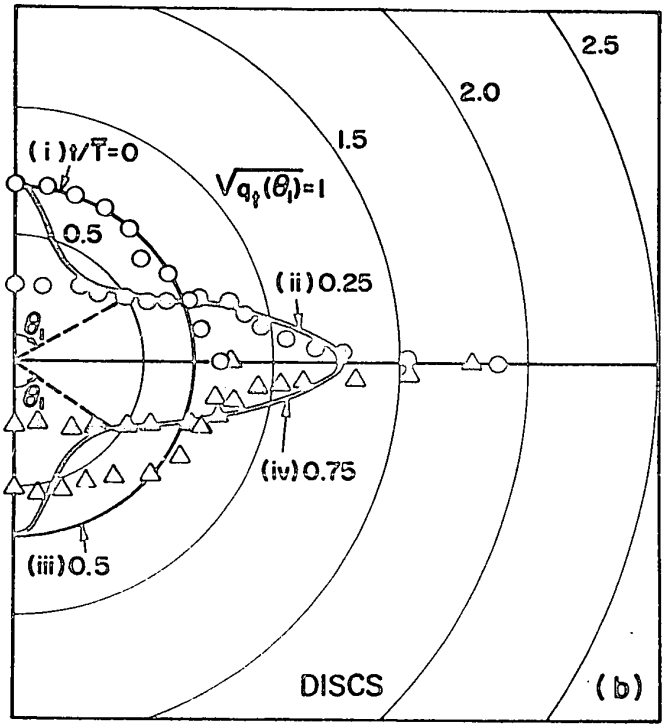
2.5
2.0
1.5
(i) t/T̄=0
√q_t(θ_t)=1
0.5
(ii) 0.25
θ_t
θ_t
(iv) 0.75
(iii) 0.5
DISCS
(b)

the oscillation of $p_t(\phi_1)$.

As observed before for $p_t(\phi_1)$, the spread in r_e also influences the distribution function $q_t(\theta_1)$, which may be evaluated by means of a relation analogous to [18]. However the calculation of $q_{\sigma,t}(\theta_1)$, similar to that for $p_{\sigma,t}(\phi_1)$, showed only a small difference from $q_t(\theta_1)$ at $t = \bar{T}/4$ and $3\bar{T}/4$; therefore the curves in Fig. 6 are given for the monodisperse suspension (i.e., for $\sigma_e = 0$).

The experiments described here thus confirm the theory based on the hypothetical collision-free suspension developed previously[1] that the distributions of particle orientations oscillated with a frequency 2/T. The oscillation, moreover, was damped and died away after about 4 particle rotations. The relaxation time τ_{11} resulting from the spread in r_e calculated from the theory ([88]-1) for the rods of $\bar{r}_e = 11.6$ is, expressed as a number of particle rotations,

$$\frac{\tau_{11}}{\bar{T}} = \frac{\bar{r}_e(\bar{r}_e^2 + 1)}{2\sqrt{2}\,\pi\sigma_e\,|\bar{r}_e^2 - 1|} = 3.2 \qquad [23]$$

The relaxation time τ_2 due to the particle interactions is ([101]-1)

$$\frac{\tau_2}{\bar{T}} = \frac{\ell n\, r_e}{N\ell^3 r_e} = 6.9 \qquad [24]$$

for $\bar{r}_e = 11.6$ at $N = 100\ ml^{-1}$. Thus each of τ_{11} and τ_2 is

too large to account for the experimentally observed rate of damping; it is therefore reasonable to conclude that the damping resulted from the combination of the two effects.

(ii) Initially Parallel Alignment

Oscillations in the distributions of ϕ_1 were also found for rods ($\bar{r}_e = 3.96$) initially aligned along the X_2-axis by means of the electric field, so that all the rods were near $\phi_1 = 0°$ and $\theta_1 = 90°$, corresponding to $\kappa = 0°$ and $C = \infty$. When shear was applied after removing the electric field, each rod rotated about the X_1-axis at constant $\theta_1 (= 90°)$ and $C (= \infty)$. Because of the singularity in $p_o(\phi_1)$ the method of display used in Fig. 5 was not feasible; instead changes in the spread of ϕ_1 with time were employed. These are illustrated in Fig. 7 where the spread of ϕ_1 for the middle 90% of rods measured at each $t/\bar{T}$ is shown as a sector; actually the spread is given by two diametrically opposed sectors, but for simplicity only one is shown. Included in Fig. 7 are the distributions of ϕ_1 (shown as hatched sectors) obtained when the flow was reversed at $t/\bar{T} = 0.95$, discussed later.

Initially ($t = 0$) the 90% spread about $\phi_1 = 0$ was $\pm 4°$, increasing to $\pm 5°$ as shear was applied ($t/\bar{T} = 0.06$) and then decreasing to $\pm 3°$ at $t = \bar{T}/4$ with the rods oriented near the direction of flow ($\phi_1 = 90°$). After a

FIGURE 7

Changes in the measured 90% of spread of orientations ϕ_1 (unhatched sectors) for initially aligned rods of $\bar{r}_e = 3.96$ at $N = 10\ ml^{-1}$ for forward rotations at various times until $t/\bar{T} = 0.95$ when the flow reversed; the corresponding spreads for reversed flow are given by the hatched sectors. To avoid confusion only one of the two sectors (separated by 180°) is shown for each value of $t/\bar{T}$. The inward radial arrows indicate the corresponding spreads calculated for collision-free suspensions resulting from the spread in r_e of the particles. The outward radial arrows show the calculated orientations for rods of $r_e = 3.96$.

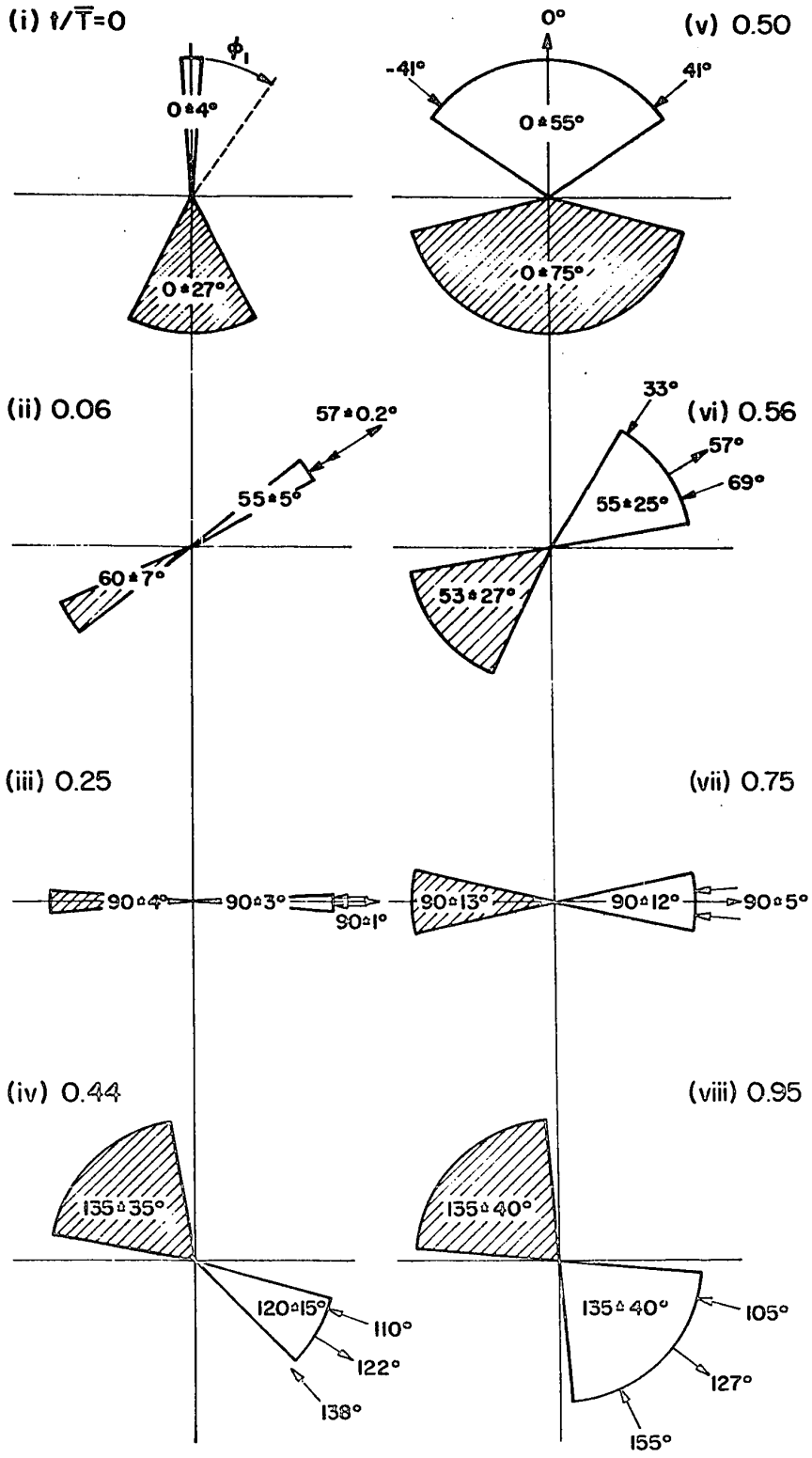
(i) f/T̄=0
φ1
0±4°
0±27°
(ii) 0.06
57±0.2°
55±5°
60±7°
(iii) 0.25
90±4°
90±3°
90±1°
(iv) 0.44
135±35°
120±15°
110°
122°
138°
(v) 0.50
0°
-41°
41°
0±55°
0±75°
(vi) 0.56
33°
57°
69°
55±25°
53±27°
(vii) 0.75
90±13°
90±12°
90±5°
(viii) 0.95
135±40°
135±40°
105°
127°
155°

half particle rotation ($t = \bar{T}/2$) the spread increased to ± 55° with less than 15% lying within initial range $\phi_1 = 0 \pm 4°$. At $t = 3\bar{T}/4$ the rods again oriented near $\phi_1 = 90°$ with the spread increasing from ± 3° (at $t = \bar{T}/4$) to ± 5°.

The effect of the distribution in r_e in a collision-free suspension on the calculated spread in ϕ_1 for 90% of rods is also shown in Fig. 7. The limits correspond to rods of r_e between 3.65 and 4.27 for $\bar{r}_e = 3.96$ and $\sigma_e = 0.19$ (4.8%), these lower and upper values of r_e being obtained from the numerical evaluations:

$$\int_0^{r_e} g(r_e)\, dr_e = 0.05 \text{ and } 0.95 \quad . \qquad [25]$$

The orientations ϕ_1 for rods of these extreme axis ratios at various values of $t/\bar{T}$ were calculated by means of [4b] and are shown by the inward radial arrows in Fig. 7. The orientations ϕ_1 corresponding to the rods of $r_e = 3.96$ are also shown by the outward radial arrows which, because of lack of symmetry mentioned earlier, do not necessarily coincide with the center of the range between two inward arrows. The additional spreads in ϕ_1 observed experimentally over those calculated in this way can be attributed to the imperfect initial orientation which yielded the initial spread in ϕ_1 [Fig. 7(i)], to the particle interactions or

to both; these effects are not easily separated by this method of analysis of the data.

Although not shown in Fig. 7, when shear was applied beyond $t/\overline{T} = 0.95$, oscillations in the distribution of ϕ_1 persisted, accompanied by an increasing spread of ϕ_1. It was also observed that the spread in ϕ_1 increased as the concentration increased; for example the spread in ϕ_1 for 90% of rods at $t = \overline{T}/2$ were $\pm 65°$, $\pm 73°$ and $\pm 85°$ for N = 50, 100 and 200 ml^{-1} respectively, clear indications of the effect of particle interactions. The steady state orientation $p_\infty(\phi_1)$ at N = 10 ml^{-1} was not attained within the duration of the experiments (up to $t/\overline{T} = 5$); however, for N = 100 ml^{-1} it was found after about 3 particle rotations. As will be seen later the effect of concentration is better analyzed by the use of $\overline{r}_i$.

(c) Distribution of Phase Angles

The polar plots of the probability distribution $p_t(\kappa_1)$ obtained from the slope of the smoothed curves of the measured integral distribution $P_t(\kappa_1)$ vs. κ_1 are shown in Fig. 8 for rods and discs of initially random orientations, using $\sqrt{p_t(\kappa_1)}$ as the radial coordinate, the results at various times being shown only in the region of κ_1 between - 90° and 90°, the other half being the mirror image. The initial distribution $p_o(\kappa_1)$ was in good agreement with the theoretical distribution corresponding

to the random orientation of ϕ_1 [Fig. 8(i)]. Thus initially 80% of the rods fell within $\kappa_1 = 0 \pm 15°$, whereas nearly 60% of discs were within $\kappa_1 = 90 \pm 15°$.

The sequential plots in the upper half of each diagram in Fig. 8(i) to (vi) showed oscillation in $p_t(\kappa_1)$ when shear was applied, the amplitude of oscillation of $p_t(\kappa_1)$ decreasing until it reached the equilibrium distribution $p_\infty(\kappa_1) = 1/2\,\pi$, corresponding to $p_\infty(\phi_1)$, after 3 to 4 particle rotations (Fig. 8(vii) and (viii)). Similar behavior was observed for a suspension of discs as shown in the lower half of each plot in Fig. 8.

Since, as already mentioned, each individual particle could not be identified, κ_1 was calculated from [17] from the measured orientation ϕ_1. Accordingly the probability $p_{\sigma,t}(\phi_1)$ given by [18] using the relation:

$$p_{\sigma,t}(\kappa_1) = p_{\sigma,t}(\phi_1)\left(\frac{\partial\phi_1}{\partial\kappa_1}\right)_t \quad , \qquad [26]$$

the partial derivative $(\partial\phi_1/\partial\kappa_1)_t$ being obtained from [17]. The calculated $p_{\sigma,t}(\kappa_1)$ obtained by the numerical integration of [18] and with the use of [26] for rods ($\bar{r}_e = 11.6$ and $\sigma = 0.418$) and for discs ($\bar{r}_e = 0.2$ and $\sigma = 0.0054$) are shown by the broken lines in Fig. 8(ii) to (vi), indicating that it changes monotonically with time. However it may be shown analytically[20] that $p_{\sigma,t}(\kappa_1)$ undergoes a damped oscillation with a period T_{κ_1} relative

FIGURE 8

Polar plates of $\sqrt{p_t(\kappa_1)}$ versus κ_1 for rods (open circles, $\bar{r}_e = 11.6$, $N = 50\ m\ell^{-1}$) and discs (solid circles, $\bar{r}_e = 0.2$, $N = 25\ m\ell^{-1}$) at various times. The solid lines in (i) are calculated from Eq. [27], corresponding to random orientations. The circles of radius $1/\sqrt{2\pi}$ in (vii) and (viii) correspond to the equilibrium distribution $p_\infty(\kappa_1)$ given by [29]. The other solid lines in (ii) to (vi) are drawn through the experimental points. The broken lines are $p_{\sigma,t}(\kappa_1)$ resulting from the spread in r_e and calculated from [26]. Note that the calculated $p_{\sigma,t}(\kappa_1)$, for example at $\kappa_1 = 0$, decreases without oscillating. The times in (ii) and (iv) are chosen to correspond to the maximum values in the oscillation of $\overline{|\sin\kappa_1|}$ for rods and of $\overline{|\cos\kappa_1|}$ for discs (see Fig.9(a) and (b)).

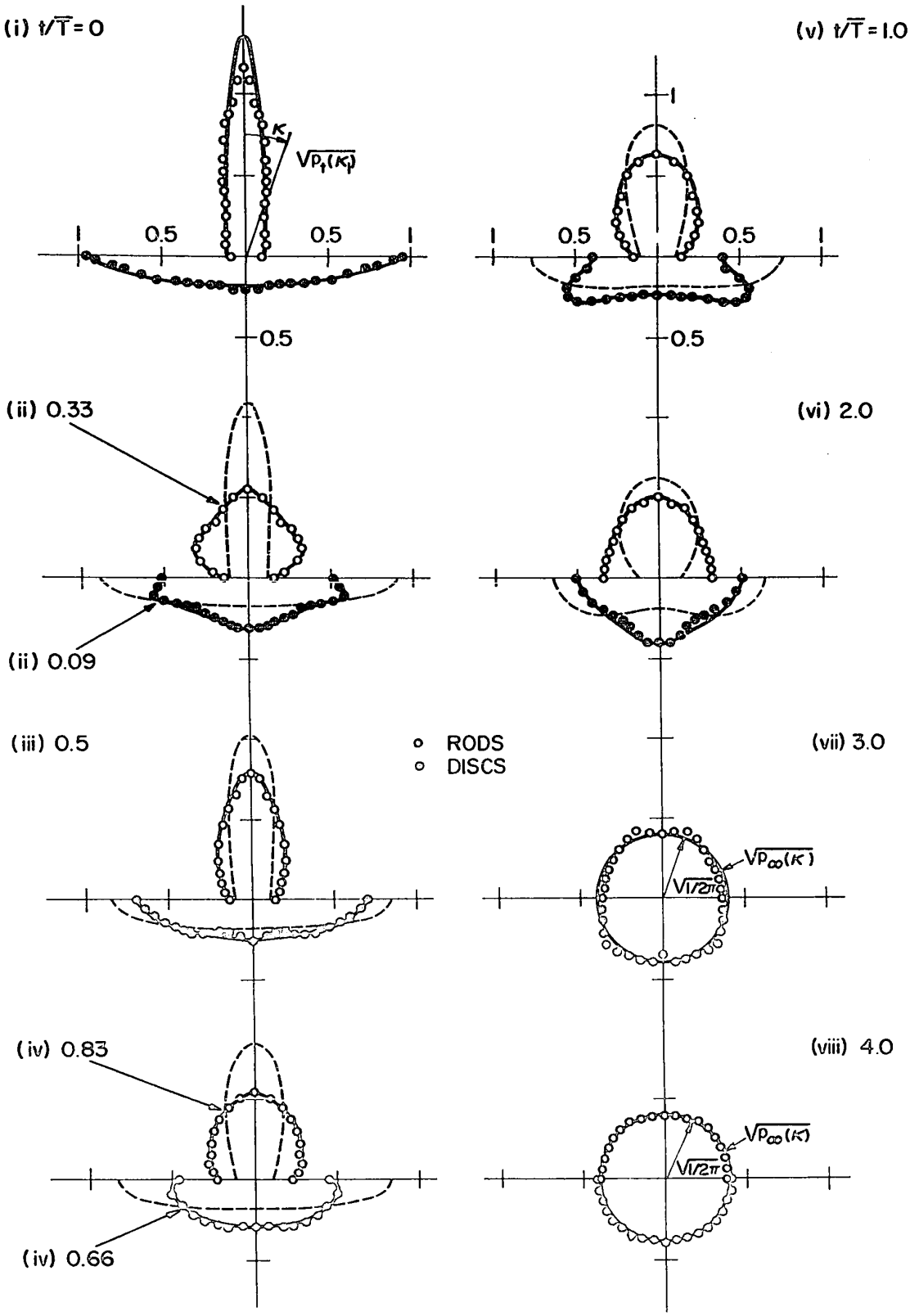
(i) t/T = 0
(v) t/T = 1.0
κ
√p_t(κ)
0.5
1
(ii) 0.33
(ii) 0.09
(vi) 2.0
(iii) 0.5
RODS
DISCS
(vii) 3.0
√p_∞(κ)
√1/2π
(iv) 0.83
(iv) 0.66
(viii) 4.0

to $\bar{T}$ given by

$$\frac{T_{\kappa_1}}{\bar{T}} \simeq \frac{\bar{r}_e}{\sigma_e} \quad , \qquad [27]$$

which for the system used (Table II) corresponds to a period of 20 to 30 particle rotations. Therefore $p_{\sigma,t}(\kappa_1)$ appears as a monotonic change during the time of experiments covering about 5 particle rotations.

The large discrepancies in $p_{\sigma,t}(\kappa)$ found between those obtained experimentally and those calculated from [26] are more clearly illustrated by calculating the mean phase angle functions $\overline{|\sin \kappa_1|}$ and $\overline{|\cos \kappa_1|}$, chosen as a matter of convenience, which are shown in Fig. 9. The mean $\overline{|\sin \kappa_1|}$ and $\overline{|\cos \kappa_1|}$ obtained from the measured orientations of rods and discs showed oscillations superimposed on a slow monotonic change and eventually oscillated about $2/\pi$. The corresponding values for collision-free suspensions resulting from the spread in r_e were calculated by the numerical integrations;

$$\overline{|\sin \kappa_1|} = \int_0^{2\pi} p_{\sigma,t}(\kappa_1) \; |\sin\kappa_1| \; d\kappa_1 \qquad [28a]$$

$$\overline{|\cos \kappa_1|} = \int_0^{2\pi} p_{\sigma,t}(\kappa_1) \; |\cos\kappa_1| \; d\kappa_1 \qquad [28b]$$

which are shown by the broken lines in Fig. 9. As seen from $p_{\sigma,t}(\kappa_1)$, the calculated $\overline{|\sin\kappa_1|}$ and $\overline{|\cos\kappa_1|}$ increase or decrease monotonically and asymptotically reach the equilibrium

value $2/\pi$, corresponding to $p_\infty(\kappa_1) = 1/2\pi$ ([103]-1).

It was shown previously[1] that, when there is a spread in r_e, $p_{\sigma,\infty}(\phi_1)$ has a deviation from $p_\infty(\phi_1)$ by the amount of order σ_e^2, but that the equilibrium distribution $p_{\sigma,\infty}(\kappa_1)$ is given exactly by

$$p_{\sigma,\infty}(\kappa_1) = 1/2\pi \qquad [29]$$

since $p_\infty(\kappa_1)$ for $\sigma = 0$ is a constant ($= 1/2\pi$) and independent of κ_1 and r_e. On the other hand, when taking account of interactions between particles, $p_t(\kappa_1)$ for a dilute suspension is expected to change steadily, whereas as the concentration increases it should show an oscillatory change of frequency $2/\overline{T}$ superposed on the steady change[1]. The latter behavior in $p_t(\kappa_1)$, clearly shown by $\overline{|\sin \kappa_1|}$ and $\overline{|\cos \kappa_1|}$ in Fig. 9, was observed at all concentrations studied. It is concluded therefore that the additional damping in the oscillations of $p_t(\phi_1)$ observed experimentally from $p_{\sigma,t}(\phi_1)$ is caused by particle interactions (Fig. 5 and 7).

In Fig. 9(c) and (d) the comparisons are made for two suspensions of rods of the same axis ratio ($r_e = 3.96$) at the same concentration ($N = 50\ m\ell^{-1}$) but with different initial orientations; one with parallel alignment (part c) and the other random (part d). For the initially parallel alignment all rods were initially near $\kappa_1 = 0°$, so that $\overline{|\sin\kappa_1|} = 0$ and $\overline{|\cos\kappa_1|} = 1$. The oscillations of $\overline{|\sin \kappa_1|}$ and $\overline{|\cos \kappa_1|}$ were also observed as in the

FIGURE 9

Oscillation of $\overline{|\sin\kappa_1|}$ and $\overline{|\cos\kappa_1|}$ for

(a) initially random rods of $\bar{r}_e = 11.6$, $N = 50\ m\ell^{-1}$,

(b) initially random discs of $\bar{r}_e = 0.2$, $N = 25\ m\ell^{-1}$,

(c) initially aligned rods of $\bar{r}_e = 3.96$, $N - 50\ m\ell^{-1}$,

(d) initially random rods of $\bar{r}_e = 3.96$, $N = 50\ m\ell^{-1}$.

The solid lines are drawn through the experimental points, and the broken lines are the values calculated from [28] resulting from the spread in r_e in collision-free suspensions. All of the curves asymptotically approach the value $2/\pi$.

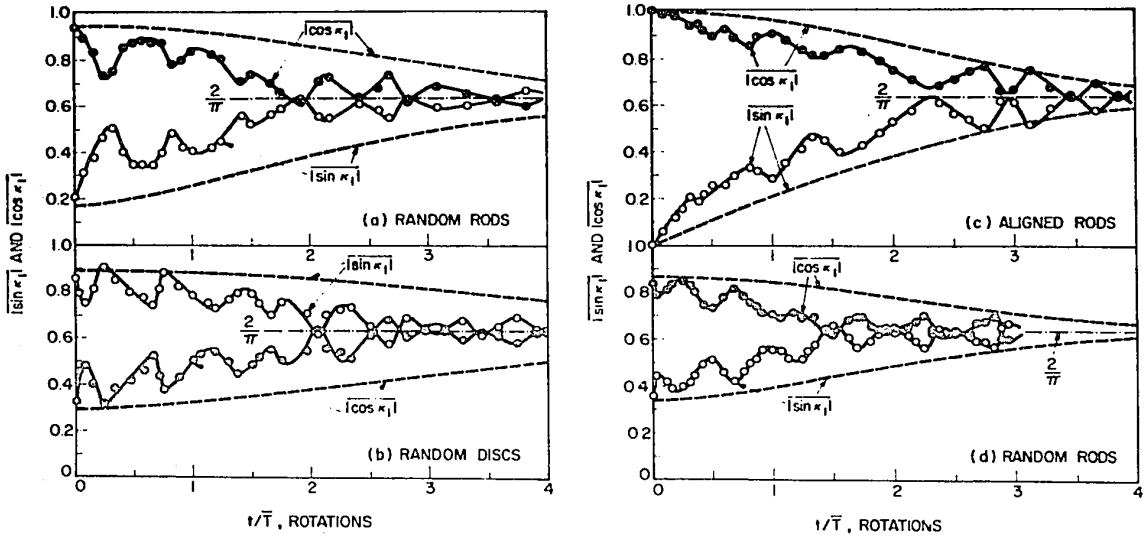
(a) RANDOM RODS
(b) RANDOM DISCS
(c) ALIGNED RODS
(d) RANDOM RODS
t/T̄ , ROTATIONS
t/T̄ , ROTATIONS

case of initially random orientations; however, their amplitudes were initially small and then increased with elapsed time. On the other hand, for initially random rods (Fig. 9(d)), large oscillations were observed from the start. This may be explained as follows. In the initially parallel case, since the rods were oriented in a small range of ϕ_1 (Fig. 7) and were always at $C = \infty$, the only types of interaction occurring in the early stages are (i)-(i) and (ii)-(ii) which produce very small changes in $\Delta\kappa$ and ΔC (only of order r_e^{-2}) [1]. As the spread in ϕ_1 increased, other types of interaction, for example type (i)-(ii) which produces large changes in $\Delta\kappa$ and ΔC (of order unity)[1], became possible. On the other hand, with initially random rods all types of interactions were possible from the beginning, so that here the amplitude was large. This clearly indicates that the effects of particle interactions depend upon the initial orientation distribution.

The amplitude of oscillation in $p_t(\kappa_1)$ due to particle interactions was predicted[1] to be of order $r_e N\ell^3/\ell n\, r_e$, so that the amplitudes of $\overline{|\sin\kappa_1|}$ and $\overline{|\cos\kappa_1|}$ are expected to be the same order of magnitude. The experimental amplitudes of $\overline{|\sin\kappa_1|}$ for the first 2 to 3 oscillations were found to be approximately 0.22 for $\bar{r}_e = 11.6$ and $N = 50\ m\ell^{-1}$ [Fig. 9(a)], and 0.11 for $\bar{r}_e = 3.96$ and $N = 50\ m\ell^{-1}$ [Fig. 9(d)], which agreed well

with the predicted values of $r_e N\ell^3/\ell n\ r_e = 0.189$ and 0.095 respectively.

Similar oscillatory changes in $\overline{|\sin\kappa_1|}$ and $\overline{|\cos\kappa_1|}$ were also found at all concentrations in the range studied, among which, however, only slight differences in changes of amplitude could be detected. The effect of concentration on the damped oscillations of orientation distribution is much more clearly revealed by $\bar{r}_i$ and $\bar{S}_{ij}$ as discussed in the next section.

(d) Effect of Concentration

The distributions of particle orientations, orbits and phase angle were obtained for each suspension, examples of which have been shown in the preceding sections. However for analysis of the effects of particle concentration, the mean projections $\bar{r}_i$ and $\bar{S}_{ij}$ defined previously[1] were used, among which $\bar{r}_2$ for rods and $\bar{S}_{12}$ for discs were chosen since these two quantities showed the largest amplitudes of oscillation. The means $\bar{r}_2$ and $\bar{S}_{12}$ obtained from the measured orientations for the initially isotropic suspensions are shown in Fig. 10 and 11 respectively, each experimental point representing measurements on about 100 particles.

Initially $\bar{r}_2$ and $\bar{S}_{12}$ were close to 0.5, corresponding to random orientations, after which, because of the changes in $p_t(\phi_1)$ and $p_t(\theta_1)$ (Fig. 5 and 6), they underwent damped oscillations of period $\bar{T}/2$. The minima observed at

$t = \bar{T}/4$, $3\bar{T}/4$ etc. reflect alignment of the rods near $\phi_1 = 90°$ and of the discs near $\phi_1 = 0°$. The amplitudes of oscillation $A(n_1\bar{T}/4)$ calculated at each quarter period of rotation using the relation

$$A(n_1\bar{T}/4) = \left|\tfrac{1}{2}\{\bar{r}_2[(n_1 + 1)\bar{T}/4] + \bar{r}_2[(n_1 - 1)\bar{T}/4]\} - \bar{r}_2(n_1\bar{T}/4)\right| , \qquad [30]$$

and similarly for $\bar{S}_{12}$, are shown by the closed circles in Fig. 10 and 11. Taking the amplitudes calculated this way to be continuous functions of time as indicated by the broken lines, the relaxation times τ for the damped oscillations of $\bar{r}_2$ and $\bar{S}_{12}$ corresponding to a decay in amplitude to 1/e of the initial value obtained from $\bar{r}_2$ and $\bar{S}_{12}$ for a monodisperse ($\sigma_e = 0$) and collision-free suspension (Tables I and II of Reference 7) were estimated graphically and are indicated by the arrows in Fig. 10 and 11 and listed in Table IV. It is clear that $\tau/\bar{T}$ decreased as N increased.

The calculated $\bar{r}_{2\sigma}$ and $\bar{S}_{12\sigma}$ resulting from the spread in r_e obtained by numerical integration of [77]-1 for collision-free suspensions are also shown in Fig. 10(i) and 11 (i) respectively, including the amplitude calculated from [30]. The corresponding relaxation times τ_σ for $\bar{r}_{2\sigma}$ and $\bar{S}_{12\sigma}$ obtained graphically from the plots like Fig. 10(i) are listed in the third row in Table IV, which are in good agreement with the approximate theoretical values $\tau_{11}/\bar{T}$ obtained from [95]-1 with the exception ($\bar{r}_e = 11.6$); this discrepancy is reasonable since at large r_e

FIGURE 10

Damped oscillations of $\bar{r}_2$ (open circles) for initially random rods ($\bar{r}_e$ = 11.6) calculated from the measured orientations at various particle concentrations N $m\ell^{-1}$ [(ii) to (iv)]. The calculated $\bar{r}_{2\sigma}$ by numerical integration of [30] for a collision-free suspension is shown in (i). The amplitudes of the oscillations shown by the closed circles are calculated by means of [30] at each quarter of rotation, the broken lines being drawn through these points. The relaxation times τ corresponding to the point at which the amplitude decayed by 1/e are indicated by the arrows.

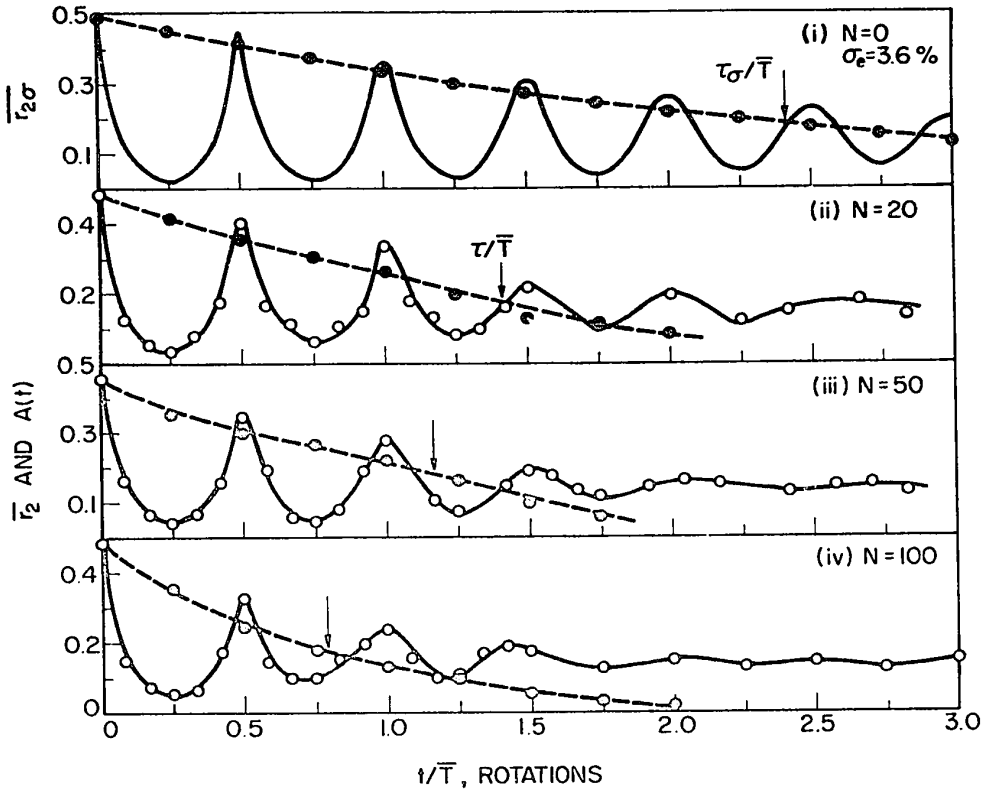
(i) N=0
σ_e=3.6 %
$\tau_\sigma/\overline{T}$
(ii) N=20
$\tau/\overline{T}$
(iii) N=50
(iv) N=100
$\overline{r_{2\sigma}}$
$\overline{r_2}$ AND A(t)
0.5
0.3
0.1
0.4
0.2
0
0.5
1.0
1.5
2.0
2.5
3.0
$t/\overline{T}$, ROTATIONS

FIGURE 11

Damped oscillations of $\overline{S}_{12}$ (open circles) and the amplitude (closed circles) for initially random discs ($\overline{r}_e = 0.2$) at various particle concentrations N $m\ell^{-1}$ [(ii) to (iv)]. The calculated $\overline{S}_{12\sigma}$ shown in (i) was obtained by numerical integration of [77]-1, for which the relaxation time $\tau_\sigma/\overline{T}$ was found to be 4.25 which is beyond the scale of abscissa. $\tau/\overline{T}$ for (ii) to (iv) are indicated by the arrows.

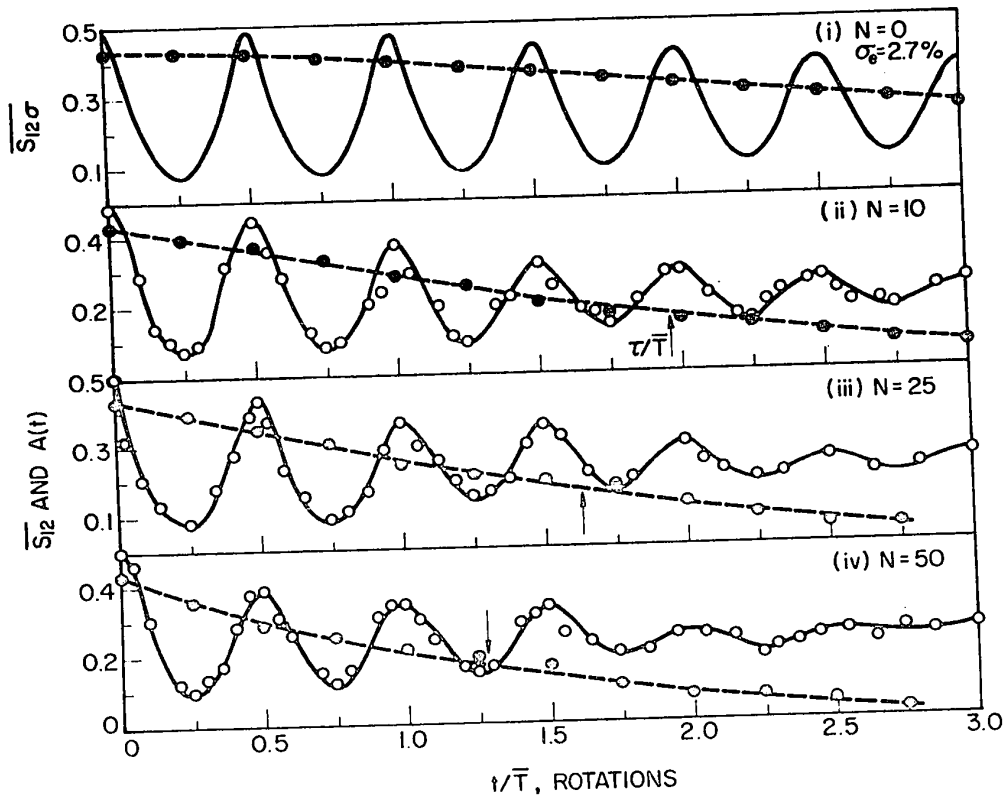
(i) N=0
σ_θ=2.7%
(ii) N=10
τ/T̄
(iii) N=25
(iv) N=50
$\overline{S_{12}\sigma}$
$\overline{S_{12}}$ AND A(t)
0.5
0.3
0.1
0.4
0.2
0
0.5
1.0
1.5
2.0
2.5
3.0
t/T̄, ROTATIONS

FIGURE 12

Damped oscillations of $\bar{r}_2$ for rods ($\bar{r}_e = 3.96$) at various particle concentrations N $m\ell^{-1}$, initially aligned along the X_2-axis are shown by the open circles and the solid lines drawn through these points. The solid line in (i) gives $\bar{r}_{2\sigma}$ obtained by numerical integration of [9]. The closed circles are the amplitudes calculated from [30] at each quarter rotation. The relaxation times τ indicated by the arrows are obtained from the broken lines drawn to fit the closed circles.

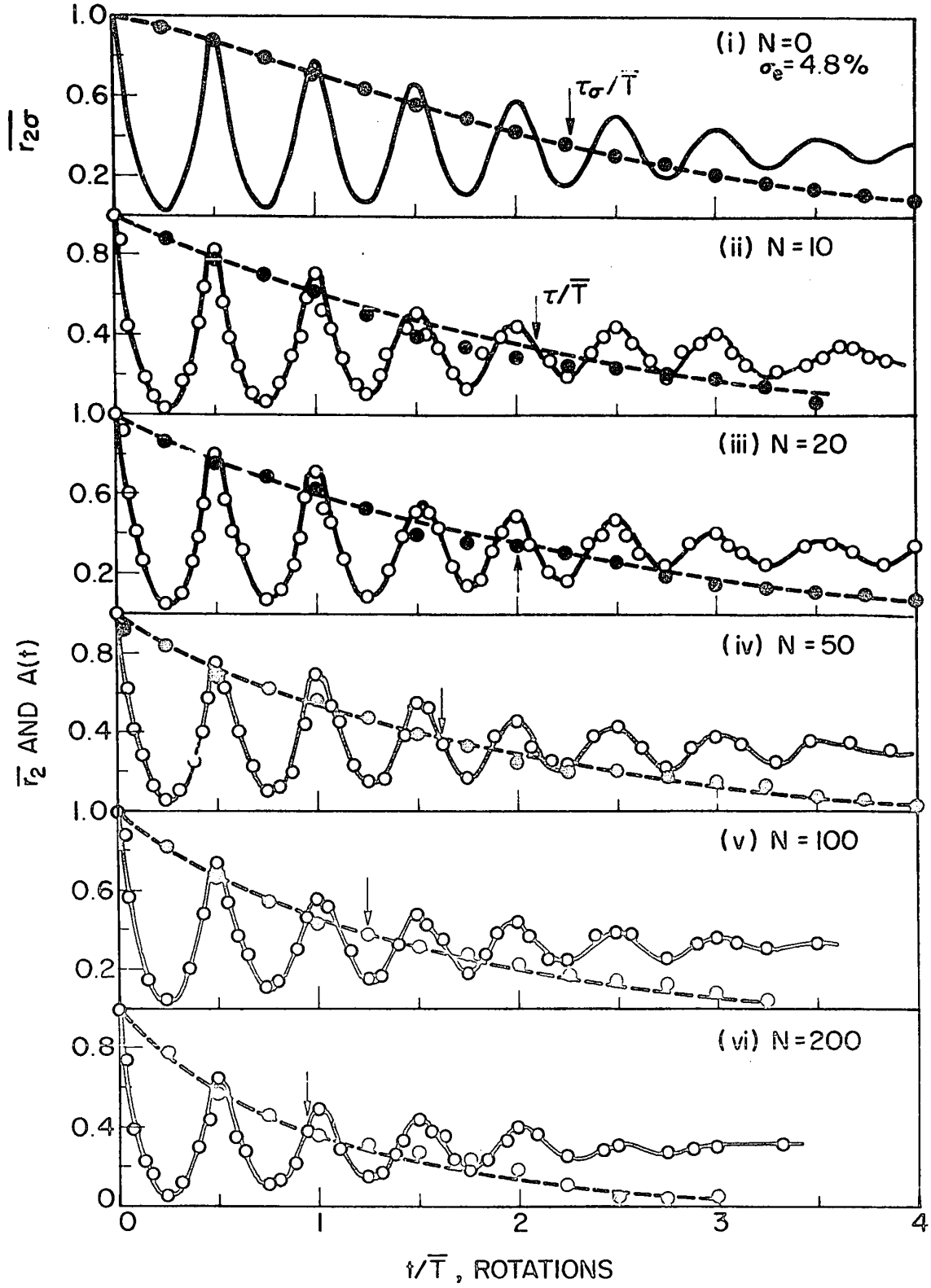
(i) N=0
σ_e=4.8%
$\tau_\sigma/\bar{T}$
(ii) N=10
$\tau/\bar{T}$
(iii) N=20
(iv) N=50
(v) N=100
(vi) N=200
$\bar{r}_{2\sigma}$
$\bar{r}_2$ AND A(t)
t/$\bar{T}$, ROTATIONS

the contribution of τ_{1n} with $n \geq 2$ becomes important.

The same method of analysis was applied to $\bar{r}_2$ for initially aligned rods ($\bar{r}_e = 3.96$) with the results shown in Fig. 12 and summarized in Table IV. Initially all rods had ϕ_1 near 0° and θ_1 near 90° so that $\bar{r}_2$ was effectively unity, yet, at $t = \bar{T}/4$, $\bar{r}_2$ was not zero since the rods were not initially perfectly aligned in the direction of field [Fig. 7(i)]. Thus damped oscillations of $\bar{r}_2$ were observed as the result of the initial spread in ϕ_1 and of the spread in r_e. The calculated $\bar{r}_{2\sigma}$ from [9] is also shown in Fig. 12(i). The amplitude of each oscillation was calculated using [30] and $\tau/\bar{T}$ obtained graphically.

According to the theory, relaxation at $N > 0$ is due to superposition of the effects of the spread in r_e and 2-body collisions (which disappear at $N = 0$); it follows from [88]-1 and [101]-1 that the net relaxation time τ is given by

$$\frac{\bar{T}}{\tau} = \frac{\bar{T}}{\tau_{11}} + \frac{\bar{T}}{\tau_2} \qquad [31a]$$

which may be written by substitution from [95]-1 and [101]-1

$$\frac{T}{\tau} = b_1 + b_2 N \qquad [31b]$$

where

$$b_1 = \frac{\sqrt{8}\ \pi\sigma_e(\bar{r}_e^{\,2} - 1)}{\bar{r}_e(\bar{r}_e^{\,2} + 1)}\ , \qquad b_2 = \frac{2\pi(\bar{r}_e^{\,2} + 1)\ell^3}{\bar{r}_e\ \ell n\ \bar{r}_e}\ . \qquad [31c]$$

It should be noted that the relationship for b_2 applies only when $r_e > 1$, since no detailed interaction theory for oblate spheroids and discs is available. The damping expressed by the last term in [31b], due to 2-body interactions, follows 2nd order kinetics as predicted some years ago[21].

As expected from [31], linear variation of $\bar{T}/\tau$ with N is shown for the rod suspensions in Fig. 13 where T/τ_σ is taken to be the value at N = 0. Applying the least squares method, values of b_1 and b_2 were obtained from the plots and are listed in Table IV. The agreement with theoretical values, especially for b_2, is excellent except for the initially aligned rods ($r_e = 3.96$). Here a discrepancy is not surprising since b_2 given by [31c] is valid[1] only when the distribution $p_t(\phi_1)$ does not differ greatly from $p_\infty(\phi_1)$, which was certainly not the case.

With the discs, shown in the inset of Fig. 13, the variation of $\bar{T}/\tau$ with concentration was not linear over the range of the experiments. It follows from [31] that a more realistic measure of concentration than N is the volume fraction c which has been used in the inset of Fig. 13, and which with discs was 10^2 greater than rods at the same N. We have no doubt that, at values of c

TABLE IV

MEASURED AND CALCULATED RELAXATION TIMES
AND EQUILIBRIUM PROJECTIONS

Quantity		$r_e = 11.6$	$r_e = 3.96$	$r_e = 3.96$ [a]	$r_e = 0.2$
$\tau_{11}/\overline{T}$ [b]		3.2	2.7	2.7	4.5
$\tau_\sigma/\overline{T}$ [c]		2.4	2.6	2.3	4.3
$\tau/\overline{T}$	N $m\ell^{-1}$				
	10	-	-	2.1	1.95
	20	1.5	-	2.0	-
	25	-	-	-	1.6
	50	1.2	1.1	1.6	1.3
	100	0.8	-	1.2_5	-
	200	-	-	0.9	-
τ_4 [d] (sec)		5.9×10^9	1.8×10^{10}	1.8×10^{10}	2.7×10^{11}
b_2 (mℓ)	calc. [e]	11.2×10^{-3}	12.7×10^{-3}	12.7×10^{-3}	-
	meas. [f]	7.9×10^{-3}	10.7×10^{-3}	3.4×10^{-3}	-
b_1	calc. [e]	0.32	0.38	0.38	-
	meas. [f]	0.46	0.39	0.45	-
$\overline{r}_{2\sigma}$ or $\overline{S}_{12\sigma}$	calc. [g]	0.140	0.266	0.266	0.234
	meas. [h]	0.130	0.265	0.260	0.230

a. Initially parallel alignment; all other cases were initially random.
b. Calculated from [88]-1.
c. Obtained graphically from $\overline{r}_{2\sigma}$ and $\overline{S}_{12\sigma}$ for a collision-free suspension.
d. Calculated from [39] with D_r given by [34].
e. Calculated from [31c].
f. Obtained least squares.
g. Calculated from [93]-1 for $\frac{1}{3}B_o$.
h. The error involved is $\pm$ 0.005 for the various values of N.

FIGURE 13

Linear plots of $\overline{T}/\tau$ versus N for initially random rods ($\overline{r}_e$ = 11.6, open circles) and for initially aligned rods ($\overline{r}_e$ = 3.96, closed circles). The points given at N = 0 are $\overline{T}/\tau_\sigma$ obtained graphically from $\overline{r}_{2\sigma}$ resulting from the spread in r_e for a collision-free suspension listed in Table IV.

Inset: $\overline{T}/\tau$ versus c for initially random discs ($\overline{r}_e$ = 0.2); the broken line for initially random rods ($\overline{r}_e$ = 11.6) indicates the different magnitudes of concentration used in the experiments.

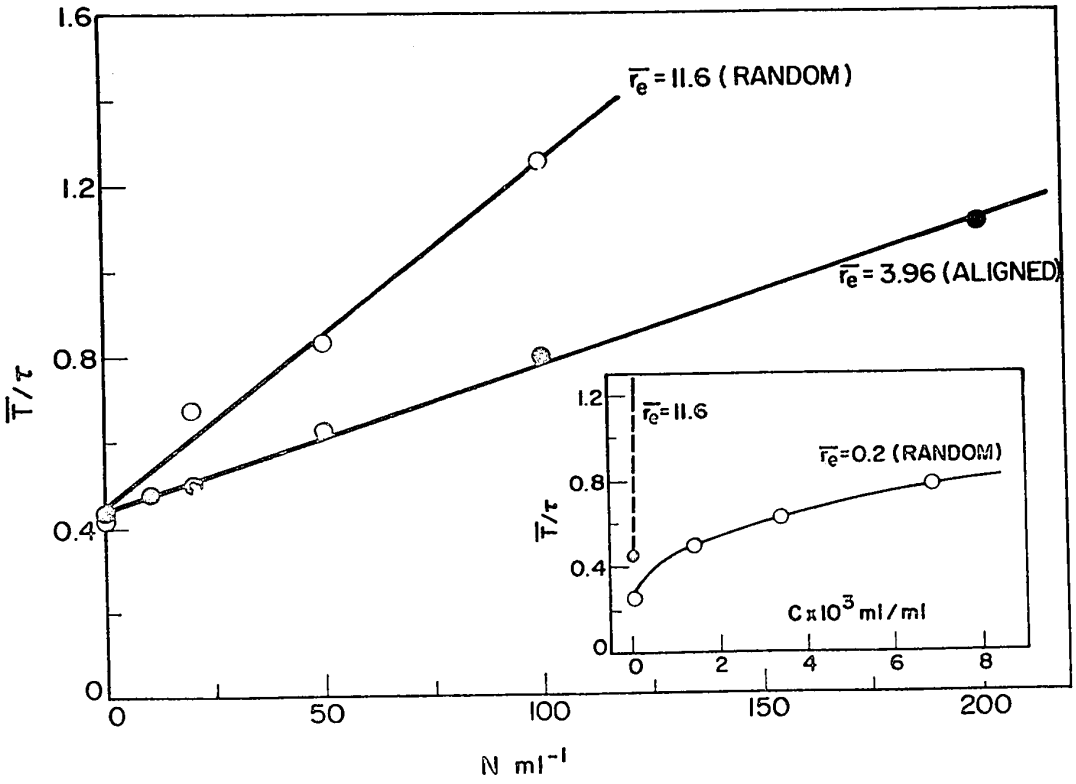
1.6
1.2
0.8
0.4
0
$\overline{T}/\tau$
$\overline{r_e}$ = 11.6 (RANDOM)
$\overline{r_e}$ = 3.96 (ALIGNED)
0
50
100
150
200
N ml^{-1}
1.2
0.8
0.4
0
$\overline{T}/\tau$
$\overline{r_e}$= 11.6
$\overline{r_e}$=0.2 (RANDOM)
C x10^3 ml / ml
0
2
4
6
8

comparable to those of the rods, the plots would be linear. The deviation from linearity at high concentrations suggests that n-body (n > 2) interactions contribute to the damping; at first sight these interactions would enhance the damping (i.e. increase $\bar{T}/\tau$) and cause the curve to bend upwards from the c axis and not to level off as observed. The resolution of this point, however, requires more experimental data and an extension of the theory of interactions.

The measured equilibrium values $\bar{r}_{2,\infty}$ and $\bar{S}_{12,\infty}$ were found to be independent of concentration (as expected) and are seen (Table IV) to be in good agreement with $\frac{1}{2}B_o$ corresponding to $\bar{r}_{2\sigma}$ and $\bar{S}_{12\sigma}$ at $t = \infty$ ([98]-1 and Table III of Reference 1). This indicates that the equilibrium obtained here corresponds to $p_\infty(\phi_1)$ with no change in distribution of orbits. However a slow change in orbit distribution over several hundred particle rotations was observed by Anczurowski et al[2], which would result in slow monotonic changes in $\bar{r}_2$ and $\bar{S}_{12}$.

(e) Flow Reversal

The effects of flow reversal on the orientation distributions of particles were observed in the suspension of initially aligned rods ($\bar{r}_e = 3.96$, $N = 10\ m\ell^{-1}$) and are illustrated in Figs. 7 and 14. As seen from Fig. 7, when the flow was reversed at $t/\bar{T} = 0.95$, the particle orienta-

tions were approximately reproduced and restored to the initial values at $t/T = 0$. The recovery was not perfect, however, presumably because of irreversible effects due to possible (but not detectable) sedimentation and Brownian rotation of the particles and interparticle attraction or repulsion, to imperfections in the flow caused by convection currents and to other disturbances. For example the 90% spread in ϕ_1 at $t/\overline{T} = 0.5$ increased from ± 55° for forward flow to ± 75° for the reversal flow, and at $t/\overline{T} = 0$ from ± 4° to ± 27°.

The reversibility in the same system is more strikingly shown by $\overline{r}_2$ (Fig. 14) where the damped oscillation regrows on reversal and the initial conditions are restored at $t/\overline{T} = 0$; in negative time damping occurs as a mirror image of the forward direction as predicted by Anczurowski *et al*[2]. In a perfect experiment it should be possible to move back and forth indefinitely with reproducible decay and growth of the oscillations.. However, because of the irreversible effects mentioned above, this is difficult, if not impossible to achieve. We therefore expect the system to drift to an eventual equilibrium, $\overline{r}_{2\infty}$ for example, after which no change occurs on reversing flow. Expressed another way, the system exhibits a fading memory. This has a number of interesting and important implications which are discussed elsewhere[22].

FIGURE 14

The change of $\bar{r}_2$ calculated from the measured orientations of rods ($\bar{r}_e$ = 3.96, N = 10 $m\ell^{-1}$) showing the reversibility of the orientation distribution in the sheared suspension. Upon reversing flow (solid circles) the path was retraced until $t/\bar{T} = 0$ was reached. In negative time the damped oscillations are nearly mirror images of the oscillations in positive time.

Note that $\bar{r}_e$ is continuous at all points including $t/\bar{T} = 0$. [1)]

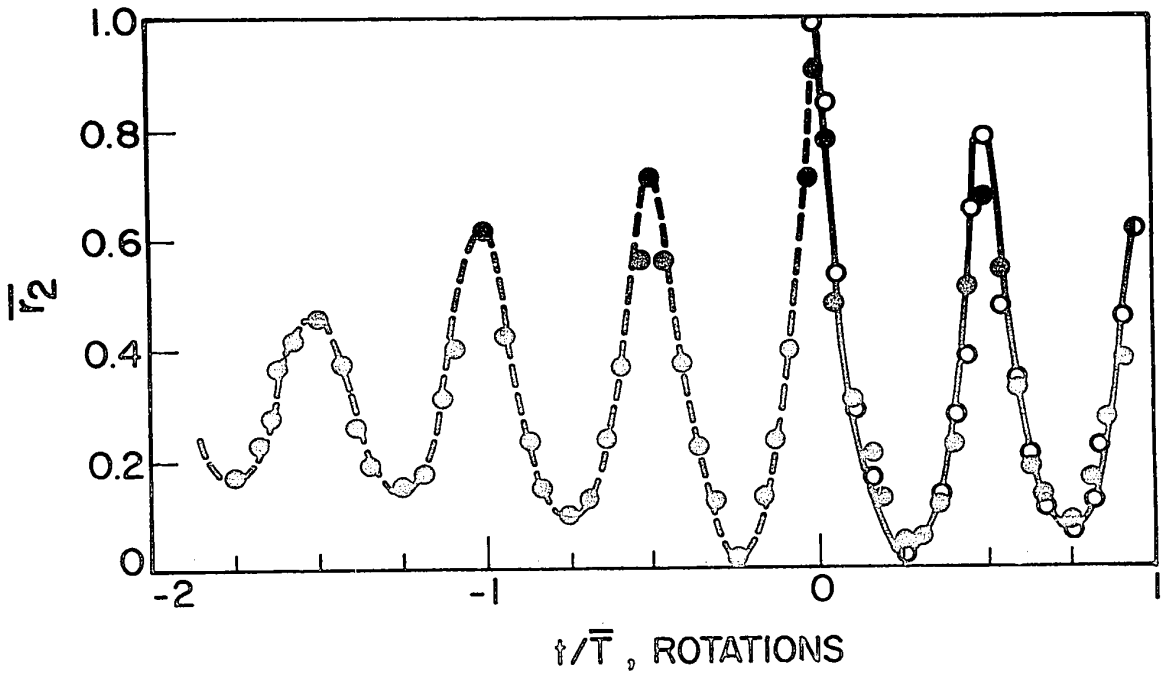
1.0
0.8
0.6
0.4
0.2
0
$\overline{r}_2$
-2
-1
0
1
$t/\overline{T}$, ROTATIONS

4. CONCLUDING REMARKS

(a) General

Most of the details of the theory[1] of damped oscillations of the various particle orientation distribution functions have been confirmed experimentally, with the measured relaxation times in generally good accord with values predicted from the two damping mechanisms proposed, the first (with a concentration-independent rate) due to the spread in r_e and the second (with a concentration-dependent rate) due to particle-particle interactions.

We conclude by considering the possible influence (excluded from the theory[1]) of rotary Brownian motion in our experiments, and some consequences of the measured orientation effects on the rheological properties.

(b) Effect of Rotary Brownian Motion

Rotary Brownian motion of the particles can of course cause a redistribution of particle orientations in shear flow, and is of paramount importance in determining streaming birefringence, shear thinning and other consequences of preferred orientation of anisometric particles of colloidal dimensions where the rotary Brownian diffusion coefficient D_r is very much greater than in our experimental systems. However, even when D_r is very small it can be

important because of its cumulative effect with passing time as has been pointed out by Brenner[23] and Leal and Hinch[24]. We wish to demonstrate, however, that it played a negligible role in our experiments.

Following Boeder's theoretical analysis of streaming birefringence of spheroidal particles[25], based on one-dimensional rotary diffusion (with respect to ϕ_1), the probability distribution of orientations ϕ_1 at time t is given by

$$\frac{\partial p_t(Pé,\phi_1)}{\partial t} = D_r \frac{\partial^2 p_t(Pé,\phi_1)}{\partial \phi_1^2} + \frac{\partial}{\partial \phi_1}\left[p_t(Pé,\phi_1)\cdot \omega(\phi_1)\right] \qquad [32]$$

where $\omega(\phi_1)$ is the angular velocity of the particle in the shear field alone given by [3]-1; $p_t(Pé,\phi_1)$ is distinguished from $p_t(\phi_1)$ used previously and reflects the effect of rotary Brownian motion superimposed on the shear; Pé is the rotary Péclet number defined by Brenner[23] by analogy with its conventional use in convective heat transfer as

$$Pé = G/2\ D_r \quad ; \qquad [33]$$

D_r is the rotary diffusion coefficient of the major axis of the particle given by [26]

for $r_e > 1$:

$$D_r = \frac{3kT_1}{16\pi\eta_o a^3}\ (2\ \ell n\ 2r_e - 1) \quad , \qquad [34a]$$

and for $r_e \ll 1$:

$$D_r = \frac{3kT_1}{32\pi\eta_o b^3} \qquad [34b]$$

k being the Boltzman constant and T_1 the absolute temperature. In the steady state at $t = \infty$, [32] is identically zero, from which it follows on reduction and integration that

$$\frac{\partial p_\infty(Pé,\phi_1)}{\partial \phi_1} + 2Pé\ p_\infty(Pé,\phi_1)\left[\frac{r_e^2\cos^2\phi_1 + \sin^2\phi_1}{r_e^2 + 1}\right] = k_o \qquad [35a]$$

where the constant of integration k_o is chosen so as to normalize $p_\infty(Pé,\phi_1)$. Using the approximation $\omega = G\cos^2\phi_1$, valid only when $r_e \gg 1$([3]-1), [35a] simplifies to

$$\frac{\partial p_\infty(Pé,\phi_1)}{\partial \phi_1} + 2Pé\ p_\infty(Pé,\phi_1)\cos^2\phi_1 = k_o \quad . \qquad [35b]$$

Numerical solutions of [35b], similar to those obtained by Boeder[25], are plotted in Fig. 15(a). In the limit Pé = 0, [35] yields the isotropic distribution (identical to [22]-1 for $p_o(\phi_1)$)

$$p_\infty(Pé,= 0,\phi_1) = \frac{1}{2\pi} \quad . \qquad [36]$$

When Pé $\to \infty$ (i.e. $D_r \to 0$), [35] reduced to

$$p_\infty(Pé = \infty,\phi_1) = \frac{r_e}{2\pi(r_e^2\cos^2\phi_1 + \sin^2\phi_1)} \qquad [37]$$

FIGURE 15

(a) Polar plots of $\sqrt{p_\infty(Pé,\phi_1)}$ at various Pé calculated from [35b] (ii to iv) and [36] and [37] (i and v respectively). Note that the angle of maximum orientation goes from 45° at Pé = 0 to 90° at Pé = ∞.

(b) Corresponding polar plots of $\sqrt{p_\infty(Pé,\kappa)}$ for $r_e = 5$ calculated from [38].

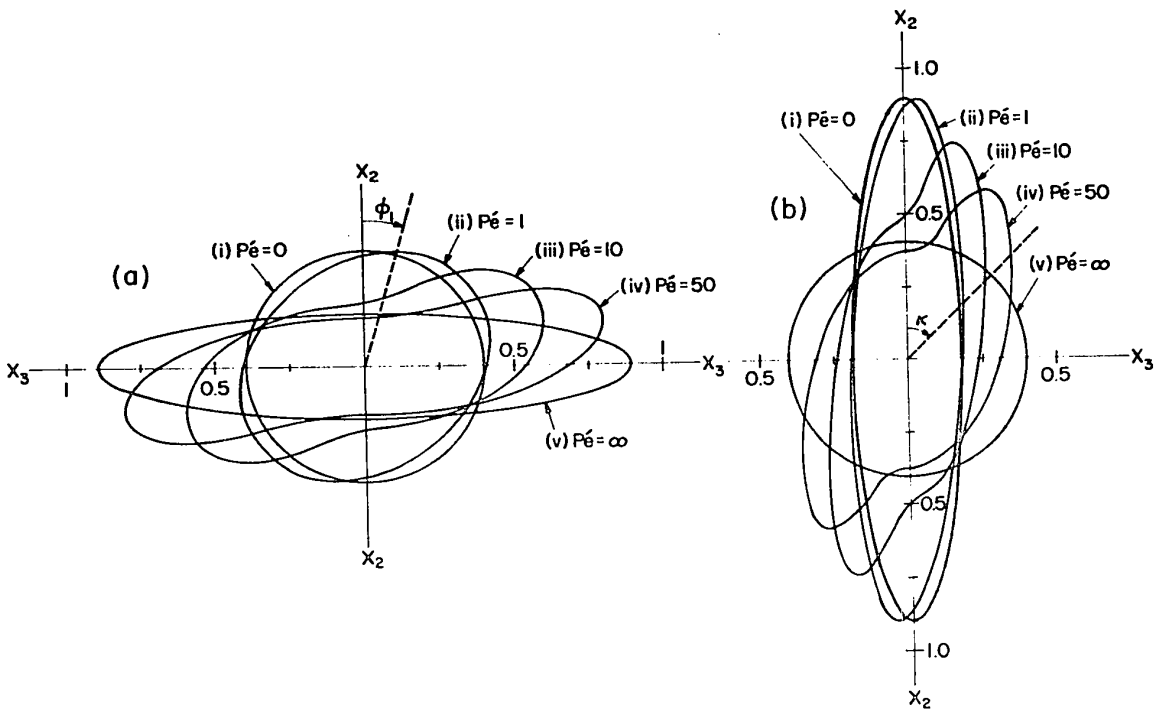
(a)
X_2
ϕ
(i) Pé=0
(ii) Pé = 1
(iii) Pé=10
(iv) Pé=50
(v) Pé=∞
X_3
0.5
1
X_2
(b)
X_2
1.0
(i) Pé=0
(ii) Pé=1
(iii) Pé=10
(iv) Pé=50
(v) Pé=∞
0.5
κ
X_3
0.5
0.5
1.0
X_2

which is identical to [102]-1 for $p_\infty(\phi_1)$.

It is interesting to note that the optical angle of isocline measured in streaming birefringence[27] is the angle ϕ_1 of preferred orientation which changes from 45° at the limit of Pé = 0 to 90° at Pé = ∞. Similar behaviour is predicted for the initial transients in a randomly oriented system with Pé = ∞ ($D_r = 0$), since the angle of maximum $p_t(\phi_1)$ changes from $\phi_1 = 45°$ at the limit $t \to 0$, as can readily be shown from the relation for maximum $p_t(\phi_1)$ $dp_t(\phi_1)/d\phi_1 = 0$ (see [22]-1), to $\phi_1 = 90°$ at $t/\overline{T} = \frac{1}{4}$ (Fig.5) with corresponding changes in the angle of isocline.

Although the equations of particle rotation ([4]-1 and [5]-1) are no longer valid when $D_r > 0$, the phase angle κ and orbit constant C may still be defined as before, but now they change with time for an isolated particle. The equilibrium distributions $p_\infty(Pé,\kappa)$ can be calculated from [35], [36] and [37] using the relation:

$$p_\infty(Pé,\kappa)d\kappa \equiv p_\infty(Pé,\phi_1)d\phi_1 \qquad [38]$$

and [14b]. Numerical values for $r_e = 5$ are shown in Fig. 15(b). It is clear from [36] and [37] that the distribution $p_\infty(Pé,\kappa)$ for Pé = 0 is equivalent to initially random orientation ([27]-1), and $p_\infty(Pé,\kappa)$ for Pé → ∞ to the equilibrium distribution $p_\infty(\kappa)$ ([103]-1). There are marked similarities in the changes with time of the phase angle distribution resulting from the spread in r_e in a collision-free suspension

where $p_t(\kappa)$ changes monotonically from $p_o(\kappa)$ to $p_\infty(\kappa) = 1/2\pi$ (Fig. 8), and the changes with Pé (at equilibrium) as it increases from 0 to ∞.

Leal and Hinch[24] have treated the problem at Pé >> 1 (i.e. weak Brownian rotation) using a two-dimensional diffusion equation, analogous to [32], involving both θ_1 and ϕ_1, which was then transformed to a coordinate system involving the orbit constant C and time, and in this way obtained the steady state orbit distribution $p_\infty(C)$. Fig. 16 shows the values of $P_\infty(C)$ calculated from their equations and compared with the experimental results obtained by Anczurowski and Mason[4] (for $r_e = 12.8$) at Pé = 10^{10} (approx.), similar to our experiments. Theoretical curves were obtained from the exact solution for $p_\infty(C)$ given by [17]-24 for $r_e = 12.8$ (curve ii), the approximate solution for $r_e >> 1$ of [19b]-24 (curve iii) and the Eisenschitz distribution for $r_e = 12.8$ ([28]-1, curve iv). It is seen that the calculated values of $P_\infty(C)$ due to weak Brownian rotation (curve ii) lie between those obtained experimentally (curve i) and the Eisenschitz distribution (curve iv). However the approximate solution (curve iii) is very close to the Eisenschitz distribution (curve iv). It is concluded that Brownian rotation cannot account for the equilibrium distribution $P_\infty(C)$ observed by Anczurowski *et al*[4]. Since a spread in r_e cannot by itself cause changes in orbit constants, it is evident that in the experiments the $P_\infty(C)$ was established by particle interactions

FIGURE 16

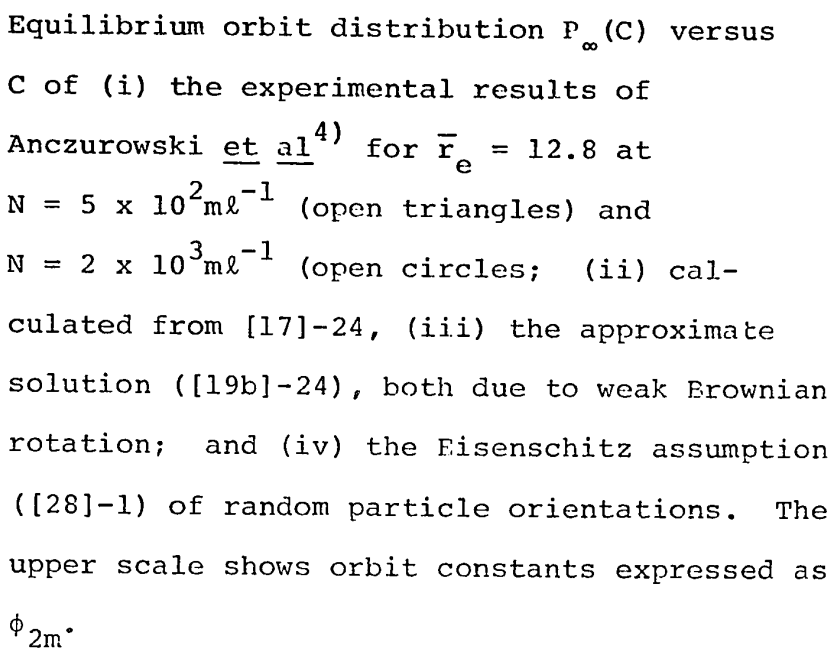

Equilibrium orbit distribution $P_\infty(C)$ versus C of (i) the experimental results of Anczurowski *et al*[4] for $\bar{r}_e = 12.8$ at $N = 5 \times 10^2 m\ell^{-1}$ (open triangles) and $N = 2 \times 10^3 m\ell^{-1}$ (open circles; (ii) calculated from [17]-24, (iii) the approximate solution ([19b]-24), both due to weak Brownian rotation; and (iv) the Eisenschitz assumption ([28]-1) of random particle orientations. The upper scale shows orbit constants expressed as ϕ_{2m}.

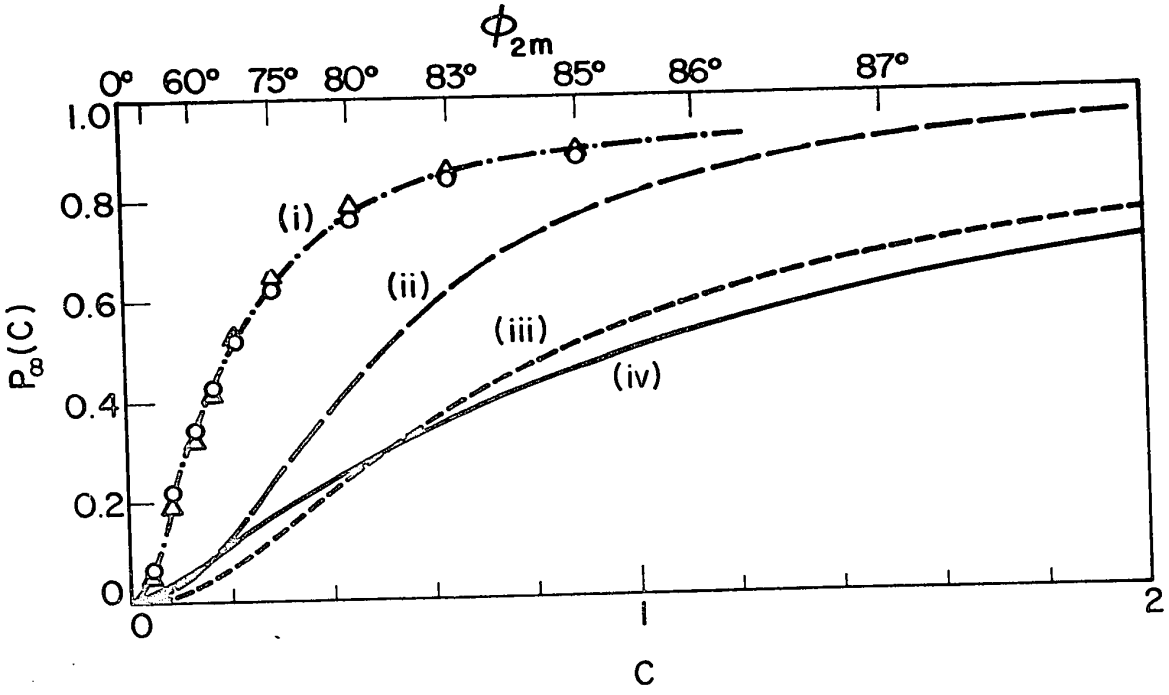
ϕ_{2m}
0° 60° 75° 80° 83° 85° 86° 87°
1.0
0.8
0.6
0.4
0.2
0
$P_8(C)$
(i)
(ii)
(iii)
(iv)
0
1
2
C

as already suggested[4]. Since there is not yet a theory for the changes in orbit constants caused by interactions, there is no a priori method of calculating $P_\infty(C)$. Since shear motion of the fluid produces only an undamped oscillation in orientation distribution in a collisionless suspension, the relaxation time τ_4 for the establishment of $p_\infty(P\acute{e},\phi_1)$ is independent of G and is therefore of the same order of magnitude as for the pure rotational diffusion (i.e., at G = 0), so that[28]

$$\tau_4 = \frac{1}{6D_r} \quad . \qquad [39]$$

For the particles used in the present experiments τ_4 calculated from [34] and [39] are many orders of magnitude greater than those found experimentally, e.g. for $r_p = 15.9$ (Table II) $\tau_4 = 5.9 \times 10^9$ sec, whereas the observed τ was about 200 sec and in agreement with [31].

Recently Leal and Hinch[29] investigated the time-dependent viscosity of a suspension with weak Brownian rotations and showed two relaxation processes, the first associated with the diffusion of κ with $\tau_4' \simeq (D_r \cdot r_2^4)^{-1}$ and the second with C with $\tau_4'' \simeq (D_r \cdot r_e^2)^{-1}$. Both τ_4' and τ_4'' are still very much greater than we observed experimentally and thus cannot account for our results. The evidence of the role of interactions in our experiments seems to be indisputable.

(c) Rheological Properties

Numerical values of the rheological properties of the suspensions can be calculated from the measured orientation distributions, using the equations given in the preceding Chapter[1]. Examples of oscillatory changes in the intrinsic viscosity $[\eta]$ and the intrinsic normal stress difference $[\xi_{23}] = (P_{22} - P_{33})/\eta_o Gc$ using [48]-1, [50]-1, [72]-1 and [73]-1 are illustrated in Fig. 17. Like $\bar{r}_2$ and other measures of orientation the rheological properties are predicted to undergo damped oscillations of frequency $2/\bar{T}$ until $[\xi_{23}] = 0$ and $[\eta]$ assumes a constant value independent of G, i.e. the systems pass through transient non-Newtonian regimes until they become truly Newtonian, with all of the rheological parameters calculable from first principles.

The effects of a spread in r_e were calculated by the numerical integration of the mean orientation parameters using the probability distribution $p_{\sigma,t}(\theta_1,\phi_1)$ given by [75]-1; these are shown by the solid lines in Fig. 17. The points calculated from the measured orientations were in good agreement with the calculated $[\eta]$ and $[\xi_{23}]$ in the early stages of shearing, but began to deviate around $t/\bar{T} = 1$, because of particle interactions as demonstrated earlier by the various orientation parameters.

Anisotropy of particle orientations induced by flow, or any other mechanism, will cause anisotropy in the

FIGURE 17

Changes in intrinsic viscosity [η] for rods ($\bar{r}_e$ = 11.6, N = 50 $m\ell^{-1}$, part a) and for discs ($\bar{r}_e$ = 0.2, N = 25 $m\ell^{-1}$, part b) estimated from the measured orientations by means of [72]-1 and [48]-1 respectively. Intrinsic normal stress differences [ξ_{23}] for the same suspensions are given in (c) for rods and (d) for discs estimated using [73]-1 and [50]-1 respectively. The broken lines are drawn through the points. The calculated values using $p_{\sigma,t}(\theta_1,\phi_1)$ given by [75]-1 and the measured σ_e (Table II) are shown by the solid lines.

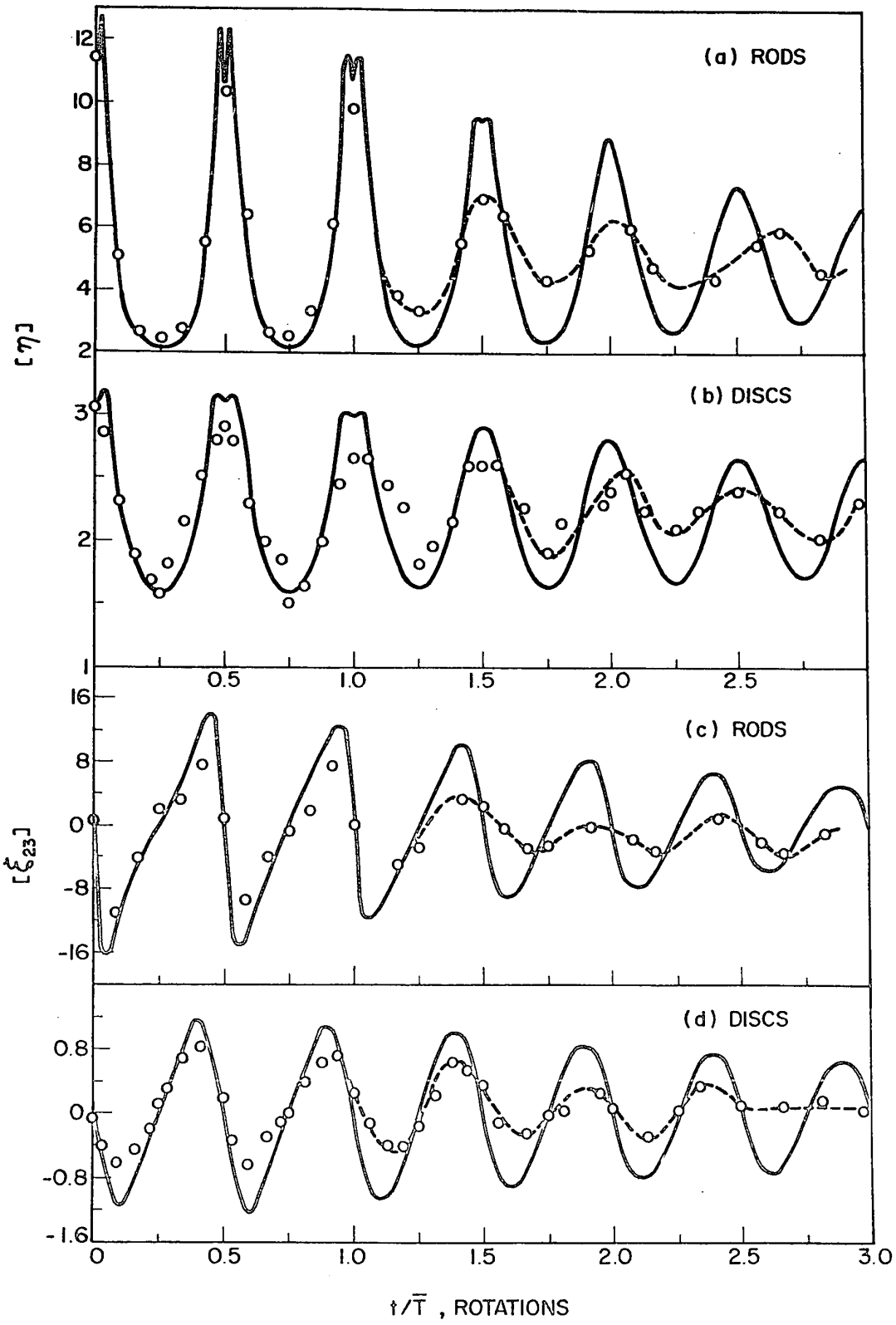
(a) RODS
(b) DISCS
(c) RODS
(d) DISCS
[η]
[ξ23]
t/T̄ , ROTATIONS

viscosity which can be revealed by changing the orientation of the field of shear flow. As two simple examples, we consider the effect of rotating the field of shear flow about the vorticity axis (X_1) through 45° and 90° as illustrated in Fig. 18, in a monodisperse collisionless suspension of r_e = 10.0. Assuming that in the original flow equilibrium distribution of orientations $p_\infty(\phi_1)$ and the Eisenschitz distribution of orbits $p_E(C)$ were established, $[\eta]$ is calculated[20] for the original flow in which it remains constant at 3.3 (line i). Stopping the flow, and rotating the flow field but not the particles about the vorticity axis and then resuming flow, $[\eta]$ will be changed and undergo an oscillation of frequency 2/T. For the flow along the X_2-axis, $[\eta]$ (line ii) is initially almost the same (curve iii) as the equilibrium value for the original flow, and then increases to $[\eta]$ = 10.2. On the other hand, for the flow with 45° rotation, $[\eta]$ is initially very high (8.6), since the maximum probability is directed 45° to the flow direction the orientation at which rods make their maximum contribution to the viscosity. In a real system, however, with particle interactions and/or rotary Brownian movement these differences in $[\eta]$ would disappear in time and assume equilibrium values independent of the orientation of the shear flow. Such anisotropy of viscosity in solutions of extended macromolecules may be one cause of drag reduction and turbulence suppression observed in many dilute polymer solutions[30].

FIGURE 18

Effect of rotation of shear flow about vorticity axis on calculated intrinsic viscosity for an initially random collisionless monodisperse suspension of spheroids (r_e = 10) which has been allowed to assume the equilibrium $p_\infty(\phi_1)$ in the initial flow (i). Details of calculation are given in reference (21).

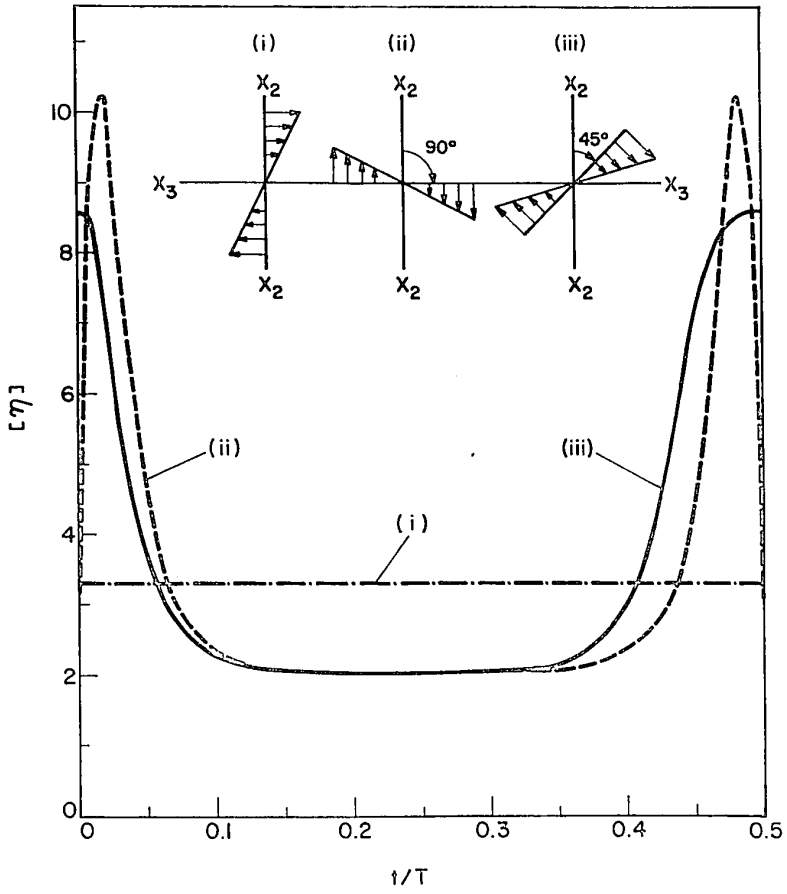
(i)
(ii)
(iii)
X2
X3
90°
45°
[η]
(ii)
(iii)
(i)
10
8
6
4
2
0
0
0.1
0.2
0.3
0.4
0.5
t/T

REFERENCES

1. This thesis, Chapter II.

2. Anczurowski, E., Cox, R.G. and Mason, S.G., J. Colloid and Interface Sci., 23, 547 (1967).

3. Anczurowski, E. and Mason, S.G., ibid, 23, 522 (1967).

4. Anczurowski, E. and Mason, S.G., ibid, 23, 533 (1967).

5. Allan, R.S. and Mason, S.G., Proc. Roy. Soc., (London) A267, 62 (1962).

6. Jeffery, G.B., ibid, A102, 161 (1922).

7. Bretherton, F.P., J. Fluid Mech., 14, 284 (1962).

8. Slattery, J.C., ibid, 19, 625 (1964).

9. Heller, J.P., Am. J. Phys., 28, 348 (1960).

10. Goldsmith, H.L. and Mason, S.G., "Rheology, Theory and Application", Vol. IV, Chapter 2, Academic Press, N.Y. (1967).

11. Taylor, G.I., "Low Reynolds Number Flow" (16mm cine film), Distr. by Educational Services Inc., Newton, Mass. (1966).

12. Darabaner, C.L. and Mason, S.G., Rheol. Acta, 6, 273 (1967).

13. Karnis, A., Goldsmith, H.L. and Mason, S.G., J. Colloid Sci., 22, 531 (1966).

14. This thesis, Appendix IV.

15. Lingard, P.S. and Whitmore, R.L., J. Sci. Instrum., 44 656 (1967).

16. Goldsmith, H.L. and Mason, S.G., J. Fluid Mech., 12, 88 (1962).

17. Anczurowski, E. and Mason, S.G., Trans. Soc. Rheol., 12, 209 (1968).

18. Gauthier, F., Goldsmith, H.L. and Mason, S.G., Rheol. Acta, 10, 344 (1972).

19. Cox, R.G., J. Fluid Mech., 45, 625 (1971).

20. This thesis, Appendix I.

21. Mason, S.G., and Manley, R.St.J., Proc. Roy. Soc. (London) A238, 117 (1956).

22. This thesis, Appendix II.

23. Brenner, H., J. Colloid and Interface Sci., 34, 103 (1970).

24. Leal, L.G. and Hinch, E.J., J. Fluid Mech., 46, 685 (1971).

25. Boeder, P., Z. Phys., 75, 258 (1932).

26. Alexander, A.E. and Johnson, P., "Colloid Science", Clarendon Press, Oxford (1949).

27. Edsall, J.T., "Advances in Colloid Science", vol. I, Interscience, New York (1942).

28. Peterlin, A., Z. Physik., 111, 232 (1938).

29. Leal, L.G. and Hinch, E.J., J. Fluid Mech. (1972) to appear.

30. Patterson, G.K., Zakin, J.L. and Rodriguez, J.M., Ind. Eng. Chem., 61, 22 (1969).

CHAPTER IV

THE MICRORHEOLOGY OF RIGID SPHEROIDS IN SHEAR AND ELECTRIC FIELDS

ABSTRACT

A general theory for the rotation of a single ellipsoidal particle without Brownian motion in a flowing dielectric Newtonian fluid subjected to an electric field is developed. The particle experiences hydrodynamic and electric torques, the latter resulting from permanent and induced polarization of the particle, which cause the particle to rotate in a manner which depends upon the relative magnitudes of the two torques. Demetriades' analysis of the motion of a dielectric spheroid in a simple shear (Couette) flow and an electric field normal to velocity and vorticity vectors is a special case of the theory.

The distribution functions of particle orientations in a dilute monodisperse and collision-free suspension of dielectric spheroids subjected to shear and electric fields are calculated for transient and steady states. When the electric field is below the critical value (so that particles execute complete rotations about the vorticity axis), the orientation distribution function for an initially randomly oriented spheroid is an oscillating function of time. Above the critical field, when the particles no longer execute complete rotations, the orientation distribution changes monotonically with time. The significance of particle orientations to suspension rheology is discussed with particular reference to viscosity enhancement due to the electric field, and to the development of transient and permanent

normal stress differences and other manifestations of non-Newtonian behavior. The extension of the theory to the case in which an electric field is replaced by a magnetic field is briefly considered in the appendix.

LIST OF SYMBOLS

a_1, a_2, a_3	= semi-axes of an ellipsoid
a, b	= major and minor semi-axes of a spheroid
A	= function of r_e defined in [17]
$\underset{\sim}{B}$	= magnetic induction of the applied field
A_{ij}	= tensor representing the point force doublet
c	= volume fraction of particles in suspension
C	= spherical elliptic orbit constant
C_E, C_o	= integration constants
C_1, C_2, C_3, C_4	= coefficients in stress equations
$\underset{\sim}{E}_o$; $\underset{\sim}{E}_+$	= external electric field; electric field inside a particle
E_{crit}	= critical electric field defined in [37]
f	= dimensionless parameter defined in [30]
$F(\theta_1, \phi_1)$	= arbitrary function of θ_1, ϕ_1
G	= velocity gradient
$\underset{\sim}{H}_o$; $\underset{\sim}{H}_+$	= external magnetic field; magnetic field inside a particle
$J(C_o, \kappa_1/\theta_1, \phi_1)$	= Jacobian
k_1, k_2	= modulus of elliptic integrals
K_1, K_{ij}; K_2	= dielectric constants of isotropic and anisotropic particle; that of fluid
$K(k_1)$, $E(k_1)$	= complete elliptic integrals of the first and second kinds
m	= permanent dipole moment per unit volume

m_i $(i = 1,2,3,4,5,6)$ = functions defined in [55], [68] and [71]

$\underset{\sim}{M}$ = magnetic moment of a particle

N = number of particles per unit volume of suspension

p = fluid pressure

$\underset{\sim}{p}_1$, $\underset{\sim}{p}_2$ = permanent and induced polarization per unit volume

$\underset{\sim}{p}$, $\underset{\sim}{p}_1$, $\underset{\sim}{p}_2$ = total, permanent and induced dipole moments of a particle

p_{ij}, P_{ij} = stress tensor for medium and suspension

$[^{H}P_{ij}]$, $[^{E}P_{ij}]$ = intrinsic viscous and electric stresses

$p_t(n)$ = probability function of $n = \theta_1,\phi_1,\theta_2,\phi_2$

$p_t(\ell,n)$ = two-dimensional probability function of $\ell,n = \theta_1,\phi_1;\ \theta_2,\phi_2;\ C_o,\kappa_1;\ C_o,\kappa_c;\ C,\kappa$.

$p_\infty(\phi_1)$, $P_\infty(\phi_1)$ = steady state probability and distribution of ϕ_1

$P_t(n)$ = cumulative distribution function of $n = \theta_1,\phi_1,\theta_2,\phi_2$

$P(q,r_e)$ = function of q and r_e defined in [19b]

q, q_{ij} = dielectric or permeability ratio

$Q(r_e)$ = function of r_e defined in [19a]

r = distance from the center of a particle

$\bar{r}_i$ $(i = 1,2,3)$ = mean projection length of unit axis length of prolate spheroids and rods

r_e = axis ratio of a spheroid (= a/b)

s_{ij} = component of the rate of strain

$\bar{s}_{ij}$ $(i \neq j = 1,2,3)$ = mean projection area of unit equatorial area of oblate spheroids and discs

T, T_1, T_2; T_3 = period of rotation at $f = 0$, $f^2 < 1$, $\infty > f^2 > 1$; characteristic time when $G = 0$

$\underset{\sim}{u}$; $\underset{\sim}{v}$ = total fluid velocity; disturbance velocity

x_i, x_i' $(i = 1,2,3)$ = Cartesian coordinate axes relative to shear and electric fields, and relative to the particle axes.

Y_1, Y_2, Y_3 = functions defined in [85c], [85d] and [85e]

$\alpha_i, \beta_i, \gamma_i$ $(i = 1,2,3)$ = elliptic integrals given by [6], [73c] and [73d]

δ_{ij} = Kronicker delta

$\delta(\theta_1)$ = Dirac delta function

ε_{ijk} = permutation symbol

$\underset{\sim}{\Gamma}, \underset{\sim}{\Gamma}_H, \underset{\sim}{\Gamma}_E, \underset{\sim}{\Gamma}_M$ = total, hydrodynamic, electrostatic and magnetic torques

ζ_i = components of fluid vorticity

η_o, η = viscosity of fluid and suspension

$[\eta]$ = intrinsic viscosity of suspension

θ_1, ϕ_1, ψ_1 = Eulerian angles of particle axis (polar axis x_1)

κ = phase angle of ϕ_1 of a rotating particle

$\kappa_c, \kappa_E, \kappa_1, \kappa_2$ = integration constants

μ_2, μ_{ij} = magnetic permeability of fluid and particle

ν = function defined in [49]

$[\xi_{ij}]$ = intrinsic normal stress difference of suspension

ξ_i = induced magnetic dipole moment per unit volume

$\phi_{crit.}$ = critical orientation angle

$\phi_{1\infty}$; $\phi'_{1\infty}$, $\phi''_{1\infty}$ = steady orientation at $E_o > E_{crit}$; stable and unstable values

χ; χ_1, χ_2, χ_3 = functions defined in [50] and Table II

Ψ_1, Ψ_2 = functions defined in [47] and [58c]

ω_i $(i = 1,2,3)$ = spins of particle about x_i

NOTE:

Symbols with prime superscripts indicate values relative to x'_i, excepting $\phi'_{1\infty}$ and $\phi''_{1\infty}$.

1. INTRODUCTION

The macroscopic rheological properties of suspensions are determined by the microrheological behavior of the individual particle under given conditions of flow. In this Chapter we consider suspensions of spheroids in which external electric fields are superimposed on shear fields thus generating electric torques on each of the particles and affecting their individual rotations and, in turn, the orientation distributions and rheological properties of particle assemblies. The theory serves as a framework for the experimental studies of orientation distributions in suspensions of rods and discs described in the following Chapter[1] and is an extension of earlier theories of particle rotation by Demetriades[2], Allan and Mason[3], Chaffey and Mason[4] and of viscosity by Chaffey and Mason[5,6], under similar conditions.

We present a generalized theoretical analysis of the rotational motion of neutrally buoyant rigid ellipsoids in a general viscous Newtonian flow and a uniform and parallel electric field. The particles may be anisotropic in their electrical properties and may have permanent dipoles directed arbitrarily with respect to the particle axis, but are assumed to have no Brownian motion. Exact equations are derived for the specific case of rotation of a single spheroid with no permanent dipole in a simple shear (Couette) flow with an electric field perpendicular to the velocity and vorticity vectors of the macroscopic fields, which are then

used to obtain the orientation distribution functions in dilute suspensions. Probability distribution functions of particle orientations in transient and steady states are calculated using our earlier scheme of analysis for shear alone[7]. Rheological properties of dilute suspensions such as the intrinsic viscosity and normal stress differences are then calculated from the orientation distribution functions.

2. SINGLE PARTICLES

In this section, we discuss the rotational motion of a single rigid ellipsoidal particle suspended in a dielectric (i.e., non-conducting) viscous incompressible fluid undergoing creeping flow in an externally applied electric field. First we consider the hydrodynamic torque on the particle in a general viscous flow, and then the electrostatic torque in a uniform electric field. Setting the sum of the two equal to zero as the condition for mechanical equilibrium of the particle, we calculate its angular velocity in the combined hydrodynamic and electric fields. Whenever convenient the equations in the following two sections are expressed in either vector or vector component form in which summation over a repeated subscript index is understood and each component is obtained by cyclic permutation of indices.

(a) Hydrodynamic Torque on an Ellipsoid

We assume that the ellipsoid (with semi-axes a_1, a_2, a_3) is rigid and suspended in a neutrally buoyant condition in a viscous Newtonian fluid undergoing creeping flow, and employ moving Cartesian coordinates x_i' (i = 1,2,3) with axes coinciding with the principal axes of the ellipsoid. The undisturbed fluid motion may thus be expanded as a Taylor series in x_i', there being no constant terms independent of x_i' if it is assumed there is no external force on the particle; even if there is an external force on the particle, the only effect that this would have would be to translate the particle, there being no effect on its rotation. Assuming that the particle is so small that quadratic term in x_i' may be neglected, the undisturbed flow may be written in the form

$$u_i' = s_{ij}'x_j' + \varepsilon_{ijk}\zeta_j'x_k' \qquad [1]$$

where u_i', s_{ij}' and $2\zeta_{ij}'$ are the components of the velocity, rate of strain and vorticity of the fluid at a position $r' = (x_1', x_2', x_3')$, and ε_{ijk} is the permutation symbol. Throughout this Chapter a prime superscript indicates that the quantity is given relative to the x_i'-axis, unless otherwise stated. If we consider that the fluid undergoes creeping flow, the equation of motion is the linearized form of Navier-Stokes equation:

$$\eta_o \nabla^2 \underset{\sim}{u}' - \nabla p = 0 \qquad [2]$$

FIGURE 1

(a) Generalized coordinate systems x_1, x_2, x_3 and x_1', x_2', x_3', and Eulerian angles θ_1, ϕ_1, ψ_1 of an axis of an ellipsoid.

(b) Coordinate systems for the axis of revolution (heavy line) of a spheroid for the specific combination of shear and electric fields considered in the detailed calculation.

(a)

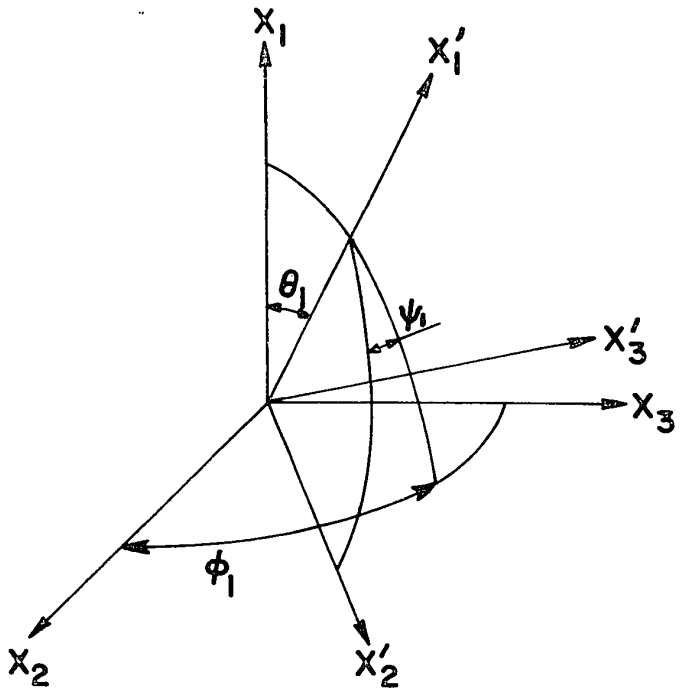
X_1
X_1'
θ_1
ψ_1
X_3'
X_3
ϕ_1
X_2
X_2'

(b)

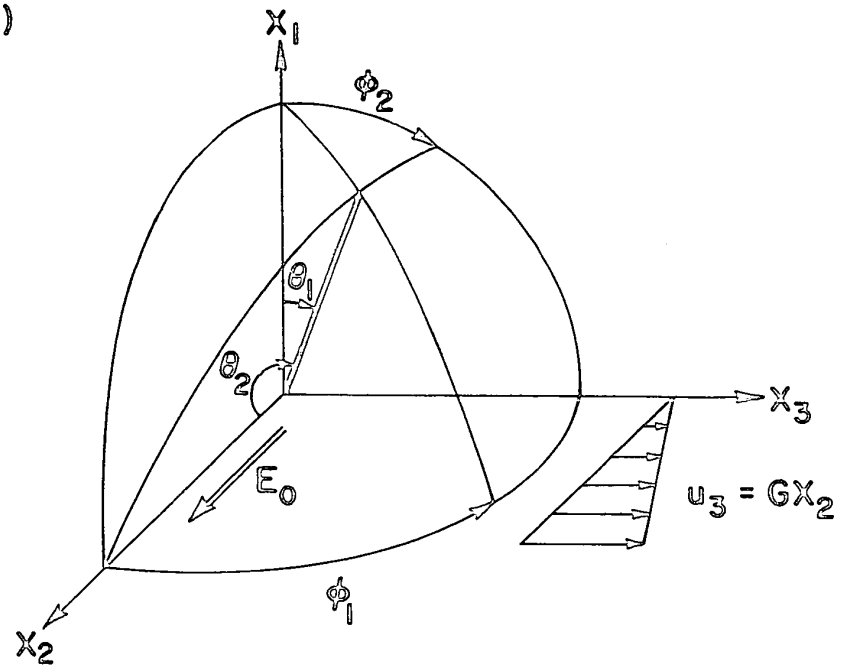
X_1
ϕ_2
θ_1
θ_2
X_3
E_0
$u_3 = GX_2$
ϕ_1
X_2

with the equation of continuity:

$$\nabla \cdot \underset{\sim}{u}' = 0 \qquad [3]$$

where η_o and p are the viscosity and pressure of the suspending fluid respectively. When the ellipsoid is placed in the fluid flow, it rotates with the angular velocity $\underset{\sim}{\omega}'$ (to be determined) and produces a disturbance flow in the neighbourhood of the particle which may be obtained as the solution of [2] and [3] with the boundary conditions that the fluid velocity reduces to [1] at large distances from the origin, while satisfying the no-slip condition

$$\underset{\sim}{u}' = \underset{\sim}{\omega}' \times \underset{\sim}{r}' \qquad [4]$$

on the particle surface $x_1'^2/a_1^2 + x_2'^2/a_2^2 + x_3'^2/a_3^2 = 1$. The disturbance flow so obtained may then be used to calculate the force per unit area acting on the surface of the ellipsoid and hence the hydrodynamic torque $\underset{\sim}{\Gamma}_H'$:

$$\Gamma_{Hi}' = \frac{16\pi\eta_o(a_j^2 + a_k^2)}{3(a_j^2\alpha_j + a_k^2\alpha_k)} \left\{ \frac{a_j^2 - a_k^2}{a_j^2 + a_k^2} \, s_{jk}' + \zeta_i' - \omega_i' \right\} \qquad [5]$$

which is equivalent to [36]-8* and where α_i is the elliptic integral defined by

$$\alpha_i = \int_o^\infty \frac{d\lambda}{(a_i^2 + \lambda)\sqrt{(a_1^2 + \lambda)(a_2^2 + \lambda)(a_3^2 + \lambda)}} \, . \qquad [6]$$

* Designating Equation [36] of Reference (8).

If there is no external torque to balance the hydrodynamic torque, then the resultant couple on the particle must vanish at every instant. Thus the angular velocity $\underset{\sim}{\omega}'$ of the particle is obtained by writing $\underset{\sim}{\Gamma}'_H = 0$. If however the particle is subjected to an external force field, the hydrodynamic torque must be balanced by the external torque for steady motion of the particle. This is treated in the next section.

(b) Electrostatic Torque on an Ellipsoid

We now consider an ellipsoidal particle suspended in a homogeneous isotropic fluid of dielectric constant K_2 under the influence of a uniform and parallel external electric field of strength $\underset{\sim}{E}'_o$. Since the absolute electrostatic system of units (e.s.u.) has been employed in previous publications[3,4] from this laboratory, we continue to use the same system instead of the rationalized MKS units used by others cited later.

If the dipole moment of the ellipsoid above that which would exist if the ellipsoid were replaced by the suspending medium is $\underset{\sim}{P}'$, then the electrostatic torque $\underset{\sim}{\Gamma}'_E$ acting on the particle is given by

$$\underset{\sim}{\Gamma}'_E = \underset{\sim}{P}' \times \underset{\sim}{E}'_o \qquad [7]$$

$\underset{\sim}{\Gamma}'_E$, $\underset{\sim}{P}'$ and $\underset{\sim}{E}'_o$ being relative to the x'_i-axis defined in the previous section. The dipole moment $\underset{\sim}{P}'$ consists of two parts: (i) that due to the permanent polarization of the

particle (denoted by $\underset{\sim}{P}_1'$) and (ii) that due to induced polarization (denoted by $\underset{\sim}{P}_2'$), so that

$$\underset{\sim}{\Gamma}_E' = \underset{\sim}{P}_1' \times \underset{\sim}{E}_o' + \underset{\sim}{P}_2' \times \underset{\sim}{E}_o' \qquad [8]$$

By definition the permanent dipole exists in the absence of the external electric field, and is a consequence of the structure and orientation of molecules which constitute the material of the particle. Also included in $\underset{\sim}{P}_1'$ is the polarization induced by the internal field produced by the permanent dipoles. If $\underset{\sim}{p}_1'$ is the permanent dipole moment per unit volume of a particle and these dipoles are assumed to be uniformly distributed inside the particle and are all aligned parallel to one another in a given direction (not necessarily in the direction of particle axis), the total moment is given by multiplying by the volume of the particle, i.e.

$$\underset{\sim}{P}_1' = \frac{4\pi}{3} \; a_1 a_2 a_3 \; \underset{\sim}{p}_1' \qquad . \qquad [9]$$

In the theory of electrical birefringence (the Kerr effect)[9,10] and of electrical streaming birefringence[11] of macromolecular solutions, the permanent dipole is assumed to be a point dipole situated at the center of each molecule. Therefore the electric torque on this dipole is given by the cross product of the dipole moment and the electric field <u>inside</u> molecules. However under the present more realistic assumption of uniform permanent polarization, the electric torque on the permanent dipole is given by the cross product

of the dipole moment $\underset{\sim}{P}'_1$ and the electric field $\underset{\sim}{E}'_o$ outside the particle as given by [8].

The induced dipole moment of a homogeneous dielectric ellipsoid in a dielectric medium can be evaluated using the analysis given by Stratton[12] and Jones[13]. In general a particle which is electrically anisotropic has six independent components K'_{ij} $(= K'_{ji})$ of dielectric constant relative to the x'_i-axis. However for simplicity we assume in the present theory that the dielectric constant has only diagonal components, so that $K'_{ij} = \delta_{ij}K'_{ij}$, δ_{ij} being the Kronecker delta. The earlier theoretical analyses by Demetriades[2] and Chaffey and Mason[4] assumed that particles were isotropic (i.e., $K'_{11} = K'_{22} = K'_{33}$).

Jones[13] has shown that the electric field inside an anisotropic ellipsoid $\underset{\sim}{E}'_+$ is, in component form,

$$E'_{+i} = E'_{oi}\,[1 + \tfrac{1}{2}a_1a_2a_3(q'_{ii} - 1)\alpha_i]^{-1} \qquad [10]$$

where $q'_{ii} = K'_{ii}/K_2$, the dielectric ratio of the particle to that of medium, and α_i is defined in [6]. The effective induced dipole which must be used to calculate the torque on the particle is equal to the polarization of the particle itself minus that of the suspending medium which would occupy the same volume as the ellipsoid if it were absent. Hence, from the definition of polarization, the effective induced polarization per unit volume $\underset{\sim}{p}'_2$ of the ellipsoid relative to the x'_i-axis is

$$p'_{2i} = \frac{K_2}{4\pi} (q'_{ii} - 1) E'_{+i} \quad . \qquad [11]$$

Therefore the induced dipole moment of the ellipsoid $\underset{\sim}{P}'_2$ above that which would exist if the particle were replaced by the suspending medium is obtained from [10] and [11] as

$$P'_{2i} = \frac{1}{3} a_1 a_2 a_3 K_2 (q'_{ii} - 1) E'_{oi} [1 + \tfrac{1}{2} a_1 a_2 a_3 (q'_{ii} - 1)\alpha_i]^{-1} \quad . \qquad [12]$$

Substituting [9] and [12] into [8] yields the total electric torque acting on the dipolar ellipsoid:

$$\Gamma'_{Ei} = \frac{1}{3} a_1 a_2 a_3 \varepsilon_{ijk} [4\pi p'_{ij} E'_{ok} + \frac{K_2 (q'_{jj} - 1)}{1 + \tfrac{1}{2} a_1 a_2 a_3 (q'_{jj} - 1)\alpha_j} E'_{oj} E'_{ok}] \quad . \qquad [13a]$$

It is readily shown that if the particle has no permanent dipole ($\underset{\sim}{P}'_1 = 0$) and is isotropic ($K'_{11} = K'_{22} = K'_{33} = qK_2$, q being the dielectric ratio), then [13a] reduces to the result given by Chaffey and Mason[4]:

$$\Gamma'_{Ei} = \frac{1}{3} a_1 a_2 a_3 K_2 (q - 1) \varepsilon_{ijk} \frac{E'_{oj} E'_{ok}}{1 + \tfrac{1}{2} a_1 a_2 a_3 (q - 1)\alpha_j} \quad . \qquad [13b]$$

(c) Angular Velocity of an Ellipsoid in Shear and Electric Fields

When the ellipsoid is subjected to viscous flow and an electric field simultaneously, the total torque acting on it is given by the sum of the hydrodynamic and electrostatic torques: $\underset{\sim}{\Gamma}' = \underset{\sim}{\Gamma}'_H + \underset{\sim}{\Gamma}'_E$. If the particle is free to rotate,

$\underset{\sim}{\Gamma}'$ must vanish. Equating the sum of [5] and [13a] to zero yields the angular velocity ω_i' of the ellipsoid relative to the x_i'-axis:

$$\omega_1' = \frac{a_2^2 - a_3^2}{a_2^2 + a_3^2} s_{23}' + \zeta_1' + \frac{a_1 a_2 a_3 (a_2^2\alpha_2 + a_3^2\alpha_3)}{16\pi\eta_o(a_2^2 + a_3^2)} \left[4\pi(p_{12}'E_{o3}' - p_{13}'E_{o2}') \right. \tag{14a}$$

$$\left. + \left\{ \frac{K_2(q_{22}' - 1)}{1 + \frac{1}{2}a_1a_2a_3(q_{22}' - 1)\alpha_2} - \frac{K_2(q_{33}' - 1)}{1 + \frac{1}{2}a_1a_2a_3(q_{33}' - 1)\alpha_3} \right\} E_{o2}'E_{o3}' \right],$$

$$\omega_2' = \frac{a_3^2 - a_1^2}{a_3^2 + a_1^2} s_{31}' + \zeta_2' + \frac{a_1 a_2 a_3 (a_3^2\alpha_3 + a_1^2\alpha_1)}{16\ \pi\eta_o(a_3^2 + a_1^2)} \left[4\pi(p_{13}'E_{o1}' - p_{11}'E_{o3}') \right. \tag{14b}$$

$$\left. + \left\{ \frac{K_2(q_{33}' - 1)}{1 + \frac{1}{2}a_1a_2a_3(q_{33}' - 1)\alpha_3} - \frac{K_2(q_{11}' - 1)}{1 + \frac{1}{2}a_1a_2a_3(q_{11}' - 1)\alpha_1} \right\} E_{o3}'E_{o1}' \right],$$

$$\omega_3' = \frac{a_1^2 - a_2^2}{a_1^2 + a_2^2} s_{12}' + \zeta_3' + \frac{a_1 a_2 a_3 (a_1^2\alpha_1 + a_2^2\alpha_2)}{16\ \pi\eta_o(a_1^2 + a_2^2)} \left[4\pi(p_{11}'E_{o2}' - p_{12}'E_{o1}') \right. \tag{14c}$$

$$\left. + \left\{ \frac{K_2(q_{11}' - 1)}{1 + \frac{1}{2}a_1a_2a_3(q_{11}' - 1)\alpha_1} - \frac{K_2(q_{22}' - 1)}{1 + \frac{1}{2}a_1a_2a_3(q_{22}' - 1)\alpha_2} \right\} E_{o1}'E_{o2}' \right].$$

Taking the axes x_1, x_2, x_3 as fixed in space with the origin coinciding with the center of the ellipsoid, the orientation of the particle may be defined in terms of the Eulerian angles θ_1, ϕ_1, ψ_1 giving the orientation of the x_1', x_2', x_3' axes in the conventional way (Fig. 1a). The time rates of change of these angles are then related to the

components of angular velocity of the particle by

$$\frac{d\theta_1}{dt} = \omega_2' \sin\psi_1 + \omega_3' \cos\psi_1 \quad , \qquad [15a]$$

$$\frac{d\phi_1}{dt} = (\omega_3' \sin\psi_1 - \omega_2' \cos\psi_1) \operatorname{cosec}\theta_1 \quad , \qquad [15b]$$

$$\frac{d\psi_1}{dt} = \omega_1' - (\omega_3' \sin\psi_1 - \omega_2' \cos\psi_1) \cot\theta_1 \quad . \qquad [15c]$$

Substitution of [14] into [15] and integrating [15] gives the variation of particle orientations θ_1, ϕ_1, ψ_1 with time. In general these integrations cannot be performed analytically; in view of this several examples of limiting cases are now considered.

(i) Isotropic spheroid with permanent dipole

If the particle is a spheroid ($a_1 = a$, $a_2 = a_3 = b$) of axis ratio r_e (= a/b), then the elliptic integral α_1 may be evaluated as[5)]

$$\alpha_1 = \frac{2}{b^3 r_e}(1 - A), \qquad \alpha_2 = \alpha_3 = \frac{A}{b^3 r_e} \qquad [16]$$

where

$$A = \frac{r_e^2}{r_e^2 - 1} - \frac{r_e \cosh^{-1} r_e}{(r_e^2 - 1)^{3/2}} \quad , \quad \text{for } r_e > 1 \qquad [17a]$$

$$A = \frac{r_e \cos^{-1} r_e}{(1 - r_e^2)^{3/2}} - \frac{r_e^2}{1 - r_e^2} \quad , \quad \text{for } r_e < 1 \qquad [17b]$$

$$A = 2/3 \quad , \quad \text{for } r_e = 1 \quad . \qquad [17c]$$

If, in addition, we consider an isotropic spheroid of dielectric constant qK_2 and with permanent dipole parallel to the axis of revolution ($p'_{11} = m$, $p'_{12} = p'_{13} = 0$), then the angular velocity ω'_i given by [14] becomes

$$\omega'_1 = \zeta'_1 \quad , \qquad [18a]$$

$$\omega'_2 = \frac{1 - r_e^2}{r_e^2 + 1} s'_{31} + \zeta'_2 - \frac{mQ(r_e)}{\eta_o} E'_{o3} + \frac{2K_2 P(q,r_e)}{\eta_o} E'_{o3}E'_{o1} \quad , \qquad [18b]$$

$$\omega'_3 = \frac{r_e^2 - 1}{r_e^2 + 1} s'_{12} + \zeta'_3 + \frac{mQ(r_e)}{\eta_o} E'_{o2} - \frac{2K_2 P(q,r_e)}{\eta_o} E'_{o1}E'_{o2} \quad , \qquad [18c]$$

where the parameters $mQ(r_e)$ and $P(q,r_e)$, which reflect the effect of the permanent and induced polarization respectively, are defined by

$$Q(r_e) = \frac{2r_e^2 + (1 - 2r_e^2)A}{4(r_e^2 + 1)} \quad , \qquad [19a]$$

$$P(q,r_e) = \frac{(3A - 2)(q - 1)^2 Q(r_e)}{8\pi\{2 + (q-1)A\}\{(q-1)A - q\}} \quad . \qquad [19b]$$

(ii) Couette flow and electric field parallel to the x_2-axis

We now consider the fluid flow to be Couette flow defined, relative to the x_i-axis (Fig. 1b), by

$$u_1 = u_2 = 0, \qquad u_3 = Gx_2 \quad . \tag{20}$$

Since $a_2 = a_3$ we can choose $\psi_1 \equiv 0$ without loss of generality and thus simplify the calculation of the rate of strain s'_{ij} and vorticity $2\zeta'_i$ which become

$$\begin{aligned}
&2s'_{11} = G\sin^2\theta_1 \sin 2\phi_1 \quad , \quad 2s'_{22} = G\cos^2\theta_1 \sin 2\phi_1 \quad , \\
&2s'_{33} = -G\sin 2\phi_1 \quad , \quad 4s'_{12} = 4s'_{21} = G\sin 2\theta_1 \sin 2\phi_1 \quad , \\
&2s'_{23} = 2s'_{32} = G\cos\theta_1 \cos 2\phi_1 \quad , \quad 2s'_{13} = 2s'_{31} = G\sin\theta_1 \cos 2\phi_1 \quad , \\
&2\zeta'_1 = G\cos\theta_1 \quad , \quad 2\zeta'_2 = -G\sin\theta_1 \quad , \quad 2\zeta'_3 = 0 \quad .
\end{aligned} \tag{21}$$

Of special interest is the case, corresponding to the usual experimental arrangement[1,3,5], in which the electric field is parallel to the x_2-axis (Fig. 1b), so that

$$E_{o1} = E_{o3} = 0 \quad , \quad E_{o2} = E_o \quad , \tag{22}$$

and relative to the x'_i-axes,

$$\begin{aligned}
&E'_{o1} = E_o \cos\phi_1 \sin\theta_1 \quad , \\
&E'_{o2} = E_o \cos\phi_1 \cos\theta_1 \quad , \\
&E'_{o3} = -E_o \sin\phi_1 \quad .
\end{aligned} \tag{23}$$

Substitutions of [21] and [23] into [18] and then into [15] yield the rotation of the spheroid:

$$\frac{d\theta_1}{dt} = \frac{G(r_e^2 - 1)}{4(r_e^2 + 1)} \sin 2\phi_1 \sin 2\theta_1 + \frac{mQ(r_e)}{\eta_o} E_o \cos\phi_1 \cos\theta_1$$

$$- \frac{K_2 P(q, r_e)}{\eta_o} E_o^2 \cos^2\phi_1 \sin 2\theta_1 \quad , \qquad [24a]$$

$$\frac{d\phi_1}{dt} = \frac{G}{r_e^2 + 1} (r_e^2 \cos^2\phi_1 + \sin^2\phi_1) - \frac{mQ(r_e)}{\eta_o} E_o \sin\phi \operatorname{cosec}\theta_1$$

$$+ \frac{K_2 P(q, r_e)}{\eta_o} E_o^2 \sin 2\phi_1 \quad . \qquad [24b]$$

It should be noted that the angular velocities $d\theta_1/dt$ and $d\phi_1/dt$ due to shear (the first term on r.h.s. of [24]) depend linearly upon G, while those due to the permanent and induced dipoles vary linearly with E_o (thus depending upon the polarity of the field) and E_o^2 (independent of polarity) respectively. The effect of the induced polarization in an alternating field of frequency much greater than G is the same as that in a steady field except that E_o is replaced by the root mean square value of the electric field. On the other hand in an alternating field of frequency much greater than G permanent polarization has no effect since the mean field $\overline{E}_o = 0$.

It is also interesting to note that, from [18a], the axial spin ω_1' of the particle:

$$\omega_1' = \frac{G}{2} \cos\theta_1 \qquad [25]$$

is independent of E_o, except insofar as it affects θ_1. This is the result derived by Jeffery[8] for the motion of spheroids in Couette flow alone, and confirmed experimentally with rods by Forgacs and Mason[14].

(iii) Properties of A, $Q(r_e)$ and $P(q,r_e)$

Since $A > 0$ over the range $0 < r_e < \infty$ as is evident from [17], it follows from [19a] that $Q(r_e)$ is zero at the extremes of r_e and otherwise positive as shown in Fig. 2, passing through a maximum (= 0.169) at $r_e = 0.842$. Near the extremes of r_e, A and $Q(r_e)$ can be approximated as follows:

$$\text{for } r_e << 1 \qquad A = \pi r_e/2 \ , \quad Q(r_e) = \pi r_e/8 \ , \qquad [26a]$$

$$\text{for } r_e >> 1 \qquad A = 1 \ , \quad Q(r_e) = 1/4\ r_e^2 \ , \qquad [26b]$$

$$\text{when } r_e = 1 \qquad A = 2/3 \ , \quad Q(r_e) = 1/6 \ . \qquad [26c]$$

Three-dimensional plots of numerical values of $P(q,r_e)$ versus q and r_e are shown in Fig. 3 where it is seen that $P(q,r_e)$ is positive for $r_e < 1$ (part a), negative for $r_e > 1$ (part b), and identically zero at $r_e = 1$ and/or $q = 1$. It is evident that when $q = 1$ there is no net induced polarization so that the external electric field does not affect the rotation of the particle if it has no permanent dipole. When the particle is spherical ($r_e = 1$), the induced polarization is always parallel to the electric field, so that there is no electric torque. Since $Q(r_e) = 0$ at $r_e \to 0$ and ∞, $P(q,r_e)$, in general, also vanishes when $r_e \to 0$ and ∞,

FIGURE 2

Log-log plots of A and $Q(r_e) \times 10^2$ <u>versus</u> r_e. When $r_e = 1$, A = 2/3 and when $r_e \to \infty$, A asymptotically approaches unity. $Q(r_e)$, which is unsymmetrical with respect to $\log_{10} r_e = 0$, exhibits a maximum (= 0.169) at $r_e = 0.842$; at the extremes of $r_e = 0$ and ∞, $Q(r_e) = 0$.

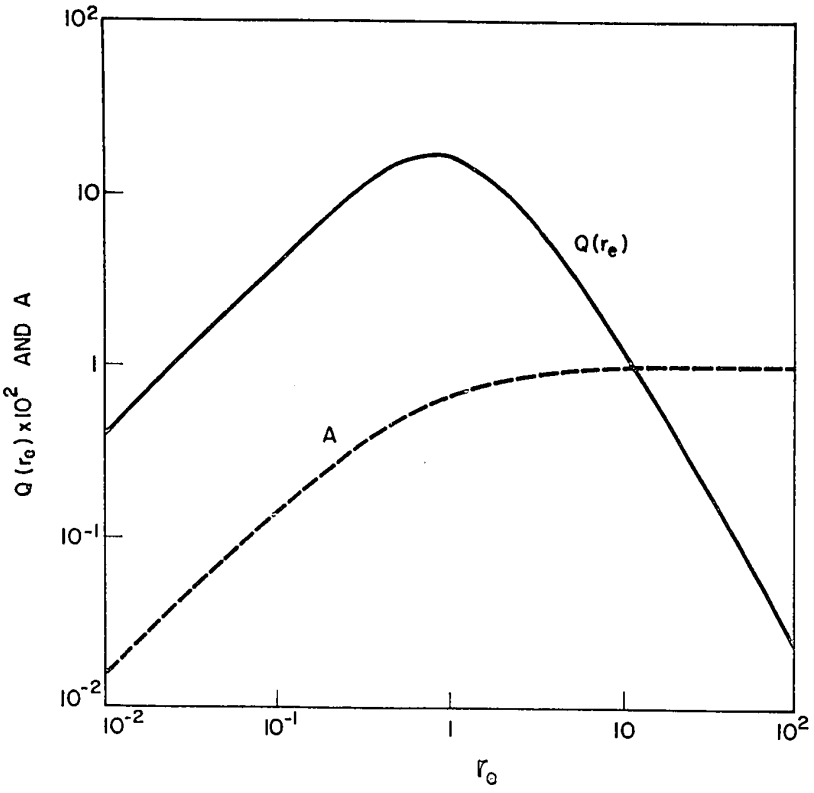
10^2
10
1
10^{-1}
10^{-2}
$Q(r_e)$
A
$Q(r_e) \times 10^2$ AND A
10^{-2}
10^{-1}
1
10
10^2
r_e

except at the limits $q \to 0, \infty$. In the former case, [19b] yields

$$\lim_{q \to 0} P(q,r_e) = \frac{(3A - 2)\, Q(r_e)}{8\pi\, A(A - 2)} \qquad [27a]$$

from which $P(0,r_e) = 1/32\pi$ at $r_e = 0$ and $P(0,r_e) = 0$ at $r_e = \infty$. On the other hand if $q \to \infty$, which is equivalent to suspending an electrically conductive particle in a dielectric medium (and corresponding to the experiments described in the following Chapter[1]), [19b] becomes

$$\lim_{q \to \infty} P(q,r_e) = \frac{(3A - 2)\, Q(r_e)}{8\pi\, A(A - 1)} \qquad [27b]$$

from which $P(\infty,r_e) = 1/16\pi$ at $r_e = 0$ and $P(\infty,r_e) = -1/16\pi$ at $r_e = \infty$. $P(q,r_e)$ for $q = \infty$ has a maximum ($= 2.04 \times 10^{-2}$) at $r_e = 0.093$, and a minimum ($= -2.34 \times 10^{-2}$) at $r_e = 10.4$, as noted previously[4].

The parameter $P(q,r_e)$ is equivalent to $B\mu/\{A_y(a^2 + b^2)\varepsilon_w\}$ in Demetriades' notation[2] but differs by the factor 4π since we have used e.s.u.; thus [24] for the case $m = 0$ is equivalent to his result.

However for particles with permanent dipoles all terms in [24] must be used. We cite, as an example, the evidence of permanent dipoles in platelets of guanine recently observed ~~obtained~~ in this laboratory[15]. It is also interesting to consider electrets[16] (the electrical equivalent of permanent

FIGURE 3

Three-dimensional plots of $P(q,r_e)$ versus q and r_e for $r_e \leq 1$ (part a) and for $r_e \geq 1$ (part b for which the axis of $P(q,r_e)$ has been reversed because of negative values). Since $P(q,r_e) \equiv 0$ for $q = 1$ and/or $r_e = 1$, the lines at constant r_e pass through zero minima ($r_e < 1$) and maxima ($r_e > 1$) at $q = 1$.

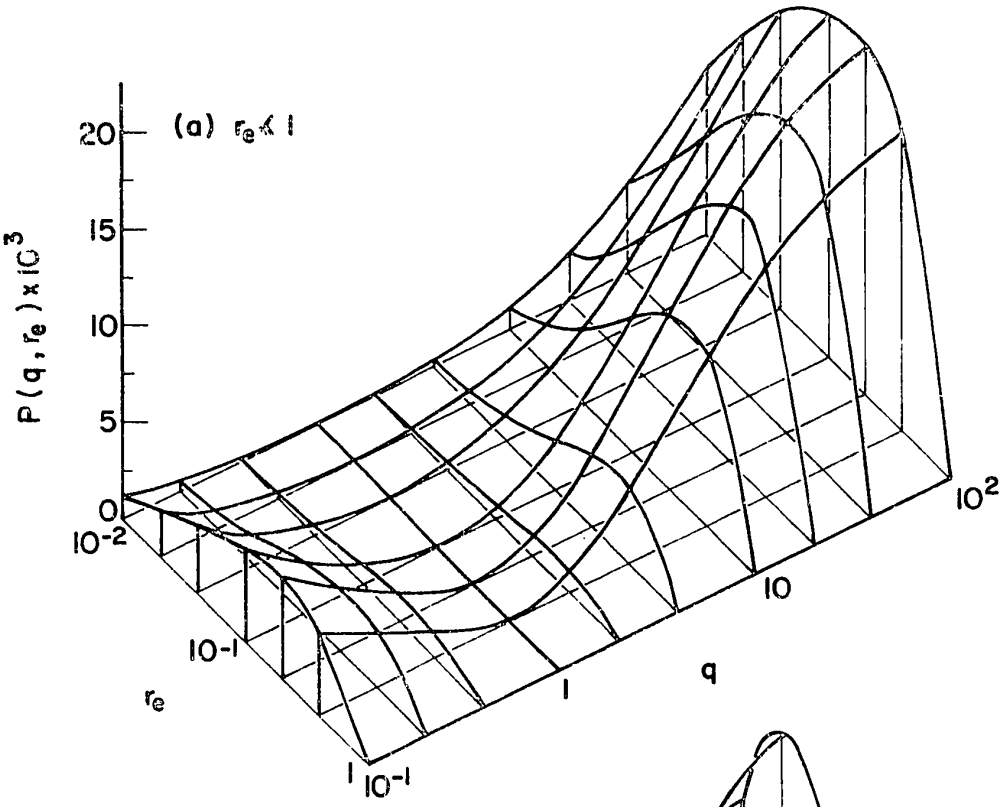
(a) $r_e \ll 1$
$P(q, r_e) \times 10^3$
20
15
10
5
0
10^{-2}
10^{-1}
1
r_e
1
10
10^2
q

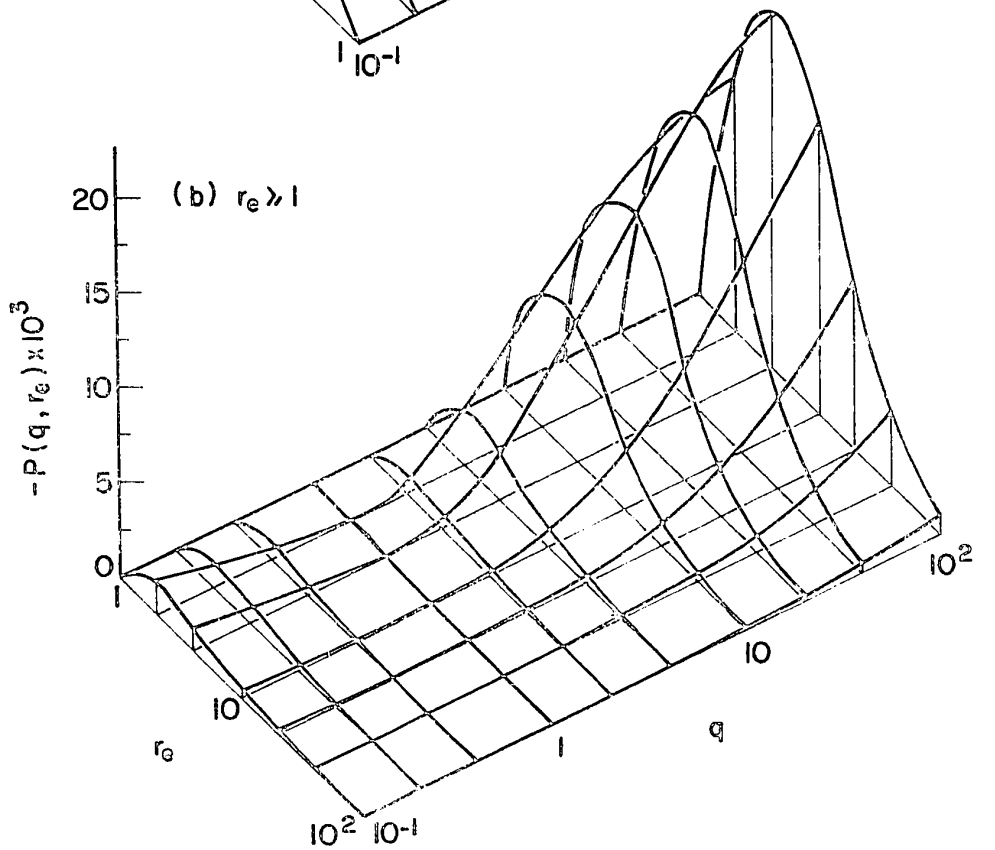
(b) $r_e \gg 1$
$-P(q, r_e) \times 10^3$
20
15
10
5
0
1
10
10^2
r_e
1
10
10^2
q

magnets) and ferroelectric particles[17,18] with electrical properties analogous to ferromagnetism, such as Rochelle salt, for which the permanent dipoles may be so large that the induced dipole in the particles may be neglected; in this event the angular velocity will be given only by the first two terms on r.h.s. of [24].

(d) Motion of Spheroids

In this section we describe the rotation of a spheroid with no permanent dipole in shear and electric fields in order to derive relations for the orientation probability distributions and rheological properties in suspensions in the following section. Writing m = 0 in [24] gives the two basic equations from which the variations of θ_1 and ϕ_1 are obtained for various combinations of E_o and G.

(i) General

Integration of [24] for m = 0 yields[4]

$$\tan\theta_1 = \frac{C_o r_e}{(r_e^2\cos^2\phi_1 + \sin^2\phi_1 - f r_e \sin 2\phi_1)^{\frac{1}{2}}} \exp\left[\frac{-K_2 P(q,r_e)}{\eta_o} E_o^2 t\right], \quad [28a]$$

$$\tan\phi_1 = r_e \sqrt{1 - f^2}\ \tan\left(\frac{2\pi t}{T_1} + \kappa_1\right) + f r_e \quad , \quad [28b]$$

C_o and κ_1 being integration constants, T_1 the period of one rotation about the x_1-axis given by

$$T_1 = \frac{2\pi}{G\sqrt{1-f^2}}\,(r_e + r_e^{-1}) \quad , \qquad [29]$$

and f, a dimensionless quantity which appears frequently in the subsequent equations being defined by

$$f = \frac{-K_2 P(q,r_e) E_o^2 (r_e^2 + 1)}{G\eta_o r_e} \quad , \qquad [30]$$

so that $f \geq 0$ for $r_e \geq 1$ and $f \leq 0$ for $r_e \leq 1$.

The solutions of [28b] and [29] are real only for $f^2 < 1$, in which case it follows that the spheroid rotates periodically so that the projection of one end of the particle axis on the x_2x_3-plane describes an elliptical spiral. This is shown schematically in the middle of Fig. 4 where the particles are represented by rods for $r_e > 1$ and by discs for $r_e < 1$; the similarities between the rotations of spheroids and cylinders will be discussed later[1]. It is seen from [28a] that the particle drifts toward $\theta_1 = \pi/2$ for $r_e > 1$ and $\theta_1 = 0$ for $r_e < 1$ when $t \to \infty$. In other words, the axis of a prolate spheroid ($r_e > 1$) and the equator of an oblate spheroid ($r_e < 1$) will lie on the x_2x_3-plane at equilibrium.

(ii) Impeded rotation at and above the critical field ($f^2 \geq 1$).

It can be seen from [28] that as f^2 increases the effect of the electric field on the rotation increases until $f^2 = 1$, corresponding to the critical electric field $E_{crit.}$,

FIGURE 4

Schematic diagrams of the orbit of one end of a rod (representing[1]) a prolate spheroid, $r_e > 1$) and a disc (oblate spheroid, $r_e < 1$) projected on the x_2x_3-plane.

TOP: Curve 1 - rotation in an electric field ($G = 0$). When $r_e > 1$ the axis becomes fully aligned in the direction of E_o; when $r_e < 1$ the equatorial plane becomes aligned in the field direction; cf. Table I.

Curve 2 - spherical elliptical orbit in a shear field alone ($E_o = 0$, $f = 0$).

MIDDLE: Spiral paths at $E_o < E_{crit.}$ ($0 < f^2 < 1$).

BOTTOM: Rotation toward the steady orientation $\phi'_{1\infty}$ at $E_o > E_{crit.}$ ($f^2 > 1$), and the counter rotation in the region $\phi'_{1\infty} < \phi_{1\infty} < \phi''_{1\infty} = \phi''_{1\infty}$ when $E_o = E_{crit.}$ ($f^2 = 1$).

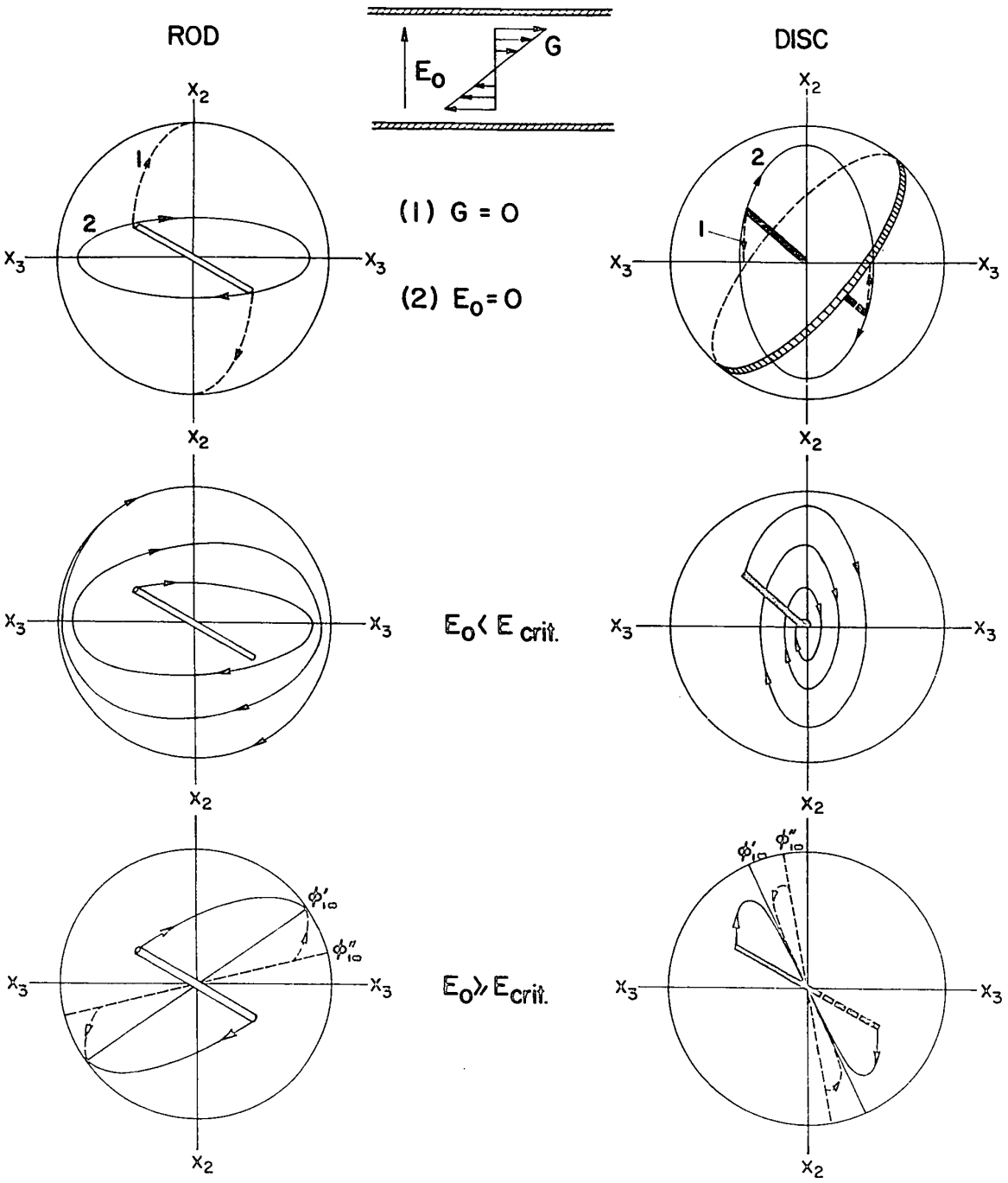
ROD
DISC
E_0
G
X_2
X_3
1
2
(1) G = 0
(2) E_0 = 0
$E_0 < E_{crit.}$
$E_0 > E_{crit.}$
ϕ'_{10}
ϕ''_{10}

at and above which the particle can no longer execute a complete rotation about the vorticity axis; the period of rotation T_1 then becomes infinite or imaginary. Instead, the particle will eventually assume steady orientations $\theta_1 = \theta_{1\infty}$, $\phi_1 = \phi_{1\infty}$ at which $d\theta_1/dt = 0$ and $d\phi_1/dt = 0$ and [24] reduces to

$$\sin 2\theta_{1\infty} = 0 \quad , \tag{31a}$$

$$\tan^2\phi_{1\infty} - 2fr_e\tan\phi_{1\infty} + r_e^2 = 0 \quad . \tag{31b}$$

From [31a]

$$\theta_{1\infty} = 0 \quad \text{or} \quad \pi/2 \quad . \tag{32}$$

It is evident from [28a] that $\theta_{1\infty} = 0$ for $r_e < 1$ (except for particles with $\theta_1 = \pi/2$ initially which rotate with $\theta_1 = \pi/2$ at all times), and $\theta_{1\infty} = \pi/2$ for $r_e > 1$ (except for particles with $\theta_1 = 0$ initially which spin with $\theta_1 = 0$ at all times). The solution of [31b] yields two values of $\phi_{1\infty}$ for $f^2 > 1$, one stable and the other unstable[3], designated respectively $\phi'_{1\infty}$ and $\phi''_{1\infty}$ (note that these are not relative to the x'_i-axis) given by

$$\phi'_{1\infty} = \tan^{-1}\left[r_e(f - \sqrt{f^2 - 1})\right] \quad , \tag{33a}$$

$$\phi''_{1\infty} = \tan^{-1}\left[r_e(f + \sqrt{f^2 - 1})\right] \quad . \tag{33b}$$

If the spheroid has an initial orientation $\phi''_{1\infty} - \pi < \phi_1 < \phi'_{1\infty}$, integration of [24b] for $m = 0$ yields

$$\tan\phi_1 = - r_e \sqrt{f^2 - 1} \coth\left(\frac{2\pi t}{T_2} + \kappa_2\right) + f r_e \qquad [34]$$

where κ_2 is an integration constant and $T_2 (= \sqrt{- T_1^2})$ is the absolute value of the imaginary period of rotation T_1 given by [29]:

$$T_2 = \frac{2\pi}{G\sqrt{f^2 - 1}} (r_e + r_e^{-1}) \quad . \qquad [35]$$

The particle thus rotates toward increasing ϕ_1 (i.e., in the direction of flow) until it reaches $\phi_{1\infty}'$ as shown at the bottom of Fig. 4.

If, on the other hand, the initial orientation is between $\phi_{1\infty}'$ and $\phi_{1\infty}''$ it rotates counter to the flow (Fig. 4 bottom), the motion then being given by

$$\tan\phi_1 = - r_e \sqrt{f^2 - 1} \tanh\left(\frac{2\pi t}{T_2} + \kappa_2\right) + f r_e \quad . \qquad [36]$$

The condition $f^2 = 1$ corresponds to the critical field which from [30] becomes

$$E_{crit.}^2 = \left| \frac{-r_e \eta_o G}{K_2 P(q, r_e)(r_e^2 + 1)} \right| \quad . \qquad [37]$$

Integration of [24b] for $f^2 = 1$ yields

$$\tan \phi_1 = \frac{-(r_e^2 + 1)}{Gt + \kappa_c} \mp r_e \qquad [38]$$

the minus sign being for $r_e < 1$ and the plus for $r_e > 1$.

The notation that the upper and lower signs refer respectively to $r_e < 1$ and $r_e > 1$ will be used throughout. When $f^2 = 1$, $\phi'_{1\infty}$ and $\phi''_{1\infty}$ coincide at $\phi_{crit.}$ found by setting $t \to \infty$ in [38]:

$$\phi_{crit.} = \mp \tan^{-1} r_e \quad . \qquad [39]$$

For all values $1 \leq f^2 < \infty$ the variation of θ_1 is given by [28a], thus showing that when $t \to \infty$, $\theta_1 \to \pi/2$ for prolate spheroids ($r_e > 1$) and $\theta_1 \to 0$ for oblate spheroids ($r_e < 1$) as mentioned before. It should be noted from [25] that when $r_e > 1$ all rotation ceases ($\omega'_1 = \omega'_2 = \omega'_3 = 0$) at equilibrium ($t = \infty$), whereas when $r_e < 1$ the particle has an axial spin $\omega'_1 = G/2$ with $\omega'_2 = \omega'_3 = 0$. At equilibrium ϕ_1 for $r_e < 1$ becomes indeterminate, however $\phi'_{1\infty}$ and $\phi_{crit.}$ given by [33a] and [39] for $r_e < 1$ give the direction of the asymptote along which the particles approach $\theta_1 = 0$ as shown at the bottom of Fig. 4.

Equations [28] to [39] are equivalent to the equations derived by Allan and Mason[3] and Chaffey and Mason[4]. Good agreement with most of these equations was observed experimentally with single discs[1,4] and rods[1,3].

It is interesting to consider two extreme cases: $f = 0$ corresponding to either $E_o = 0$ (shear alone) or $r_e = 1$ and $E_o \neq 0$ (spherical particles in shear and electric fields) and $G = 0$ (electric field alone); we do this below.

(iii) Rotation in shear flow (f = 0)

Here the rotation is periodic as shown by integrating [24] for $E_o = 0$ to give Jeffery's solution[8] as listed in Table I, where the integration constants C and κ are the orbit constant and phase angle respectively. It should be noted that these equations can be also obtained from the general solution [28] by setting f = 0. In Couette flow the axis of a single spheroid rotates in a periodic manner in a fixed spherical elliptic orbit (Fig. 4 top) whose ellipticity is determined by C[7,8]. The limiting orbits $C = \pm \infty$ and 0 respectively correspond to (i) rotation of the particle axis in the x_2x_3-plane ($\theta_1 = \pi/2$) and (ii) aligned parallel to the x_1-axis ($\theta_1 = 0$) so that the particle spins with angular velocity $\omega_1' = G/2$ (cf. [25]). Experiments with single rods[14,19] and discs[20] have shown excellent agreement with Jeffery's equations[8].

(iv) Rotation in an electric field (G = 0)

The rotational motions obtained by integrating [24] for m = 0 and G = 0 are listed in Table I, where C_E and κ_E are constants of integration which vary from $-\infty$ to $+\infty$, and are determined by the initial orientation. The equilibrium orientations, found by setting $t \to \infty$, are

$$\underline{\text{for } r_e < 1} \qquad \theta_{1\infty} = \frac{C_E}{\sqrt{2}} \exp \kappa_E, \qquad \phi_{1\infty} = \pi/2 \quad , \qquad [40a]$$

$$\underline{\text{for } r_e > 1} \qquad \theta_{1\infty} = \pi/2 \quad , \qquad \phi_{1\infty} = 0 \quad . \qquad [40b]$$

TABLE I

Equations for Rotation of Single Spheroids at Various Values of f

CONDITION	$\tan\phi_1$	$\tan\theta_1$
$f = 0$ [a] ($E_o = 0$)	$r_e \tan(\frac{2\pi t}{T} + \kappa)$	$\frac{C\, r_e}{(r_e^2 \cos\phi_1 + \sin\phi_1)^{\frac{1}{2}}}$
$0 < f^2 < 1$ [b] ($E_o < E_{crit.}$)	Eq. [28b]	Eq. [28a]
$f^2 = 1$ [b] ($E_o = E_{crit.}$)	Eq. [37]	Eq. [28a]
$f^2 > 1$ [b] ($E_o > E_{crit.}$)	$\phi''_{1\infty} - \pi < \phi_1 < \phi'_{1\infty}$: Eq. [33] $\phi'_{1\infty} << \phi_1 < \phi''_{1\infty}$: Eq. [35]	Eq. [28a]
$G = 0$ [b,c]	$\exp[\pm \frac{2\pi t}{T_3} + \kappa_E]$	$\frac{C_E}{\sqrt{\sin 2\phi_1}} \exp[\pm \frac{\pi t}{T_3}]$

$T = 2\pi\,(r_e + r_e^{-1})/G$; $T_3 = |\pi\eta_o/\{K_2 P(q, r_e) E_o^2\}|$; T_1 and T_2 are given by [29] and [35] respectively and are related to T by $T/T_1 = \sqrt{1 - f^2}$ and $T/T_2 = \sqrt{f^2 - 1}$.

a) Solutions for ϕ_1 and θ_1 correspond to [48]-8 and [49]-8.

b) Solutions correspond to [28]-4, [34]-4, [35]-4, [36]-4, [39]-4 and [40]-4.

c) Solutions correspond to [18]-3; upper sign for $r_e < 1$ and lower for $r_e > 1$.

These motions are schematically shown at the top of Fig. 4.

Since the electric field is applied along the x_2-axis, it is more convenient to use the angles θ_2, ϕ_2 (i.e. the x_2-axis as a polar axis as shown in Fig. 1b). Using the transformations:

$$\cos\theta_2 = \sin\theta_1\cos\phi_1 \quad , \qquad \tan\phi_2 = \tan\theta_1\sin\phi_1 \quad , \qquad [41]$$

The equations of particle motion listed in Table I become

$$\tan\theta_2 = \left(\frac{2}{C_E^2} + \exp \kappa_E\right)^{\frac{1}{2}} \cdot \exp\left[\pm \frac{2\pi t}{T_3} + \frac{\kappa_E}{2}\right] \quad , \qquad [42a]$$

$$\tan\phi_2 = \frac{C_E}{2} \exp\left(\frac{\kappa_E}{2}\right) \quad , \qquad [42b]$$

where the sign in [42a] is plus for $r_e < 1$ and minus for $r_e > 1$. It is seen from [42] that ϕ_2 is constant so that the particle axis moves along a line of constant ϕ_2 with θ_2 changing exponentially with time at the rate $2\pi/T_3$. Because of the sign in [42a] oblate spheroids ($r_e < 1$) move toward $\theta_2 = \pi/2$ and prolate spheroids ($r_e > 1$) move toward $\theta_2 = 0$. Experiments with single rods[1,3] and single discs[1,4], have shown fair agreement with the theory.

It should be mentioned that when $G \to 0$, corresponding to $f^2 \to \infty$ (but $G \neq 0$), the rotational motions of the particle given by [28a], [34] and [36] are nearly the same, but not identical to those for $G = 0$ given in Table I. However we note that, for $r_e > 1$, the equilibrium orientations $\theta_{1\infty}$ and $\phi_{1\infty}$ given by [32] and [33a] when $f^2 \to \infty$ (i.e. $\theta_{1\infty} = \pi/2$,

$\phi_{1\infty} = 0$) are identical with [40b] for G = 0. On the other hand, for $r_e < 1$, although $\phi_{1\infty}$ for two cases is the same (i.e. $\phi_{1\infty} = \pi/2$ from [33a] and [40a]) $\theta_{1\infty} = 0$ when $f^2 \to \infty$ (c.f. [32]) but $\theta_{1\infty} = C_E \exp \kappa_E/\sqrt{2}$ for G = 0 (c.f. [40a]).

3. DILUTE SUSPENSIONS

In a suspension so dilute that interactions between particles can be neglected, each particle rotates in accordance with the equations discussed in the preceding section. We now employ these relationships to calculate instantaneous distribution of particle orientations and various rheological properties by methods analogous to those used for shear fields alone[2]. We will consider a suspension of isotropic dielectric spheroids with no permanent dipoles which is subjected to Couette flow and an electric field across the shear so that the results of section 2-(d) apply. The particles in a given suspension are assumed to be of identical size; the effect of a spread in r_e is considered later[1].

(a) Transient Orientations θ_1 and ϕ_1.

(i) General

The following analysis is for $0 < f^2 < 1$; that for $f^2 \geq 1$ is similar, so for brevity only the results are given. The results for f = 0, corresponding to $E_o = 0$, have previously been presented in detail[7] and showed good agreement with the experimental results for rods and discs[21].

At any instant the fraction of particles having orientations in the interval $d\theta_1 d\phi_1$ at θ_1, ϕ_1 is identical to the fraction of particles having C_o, κ_1 in the corresponding interval $dC_o d\kappa_1$ at C_o, κ_1, i.e.

$$p_t(\theta_1,\phi_1)d\theta_1 d\phi_1 \equiv p_t(C_o,\kappa_1)dC_1 d\kappa_1 \qquad [43]$$

where $p_t(\theta_1,\phi_1)$ with $0 \leq \theta_1 \leq \pi$ and $0 \leq \phi_1 \leq 2\pi$ and $p_t(C_o,\kappa_1)$ with $-\infty < C_o < +\infty$, and $0 \leq \kappa_1 \leq 2\pi$ are the probability functions of θ_1,ϕ_1 and C_o, κ_1 respectively, which are therefore related by

$$p_t(\theta_1,\phi_1) = p(C_o,\kappa_1)\ J\left(\frac{C_o,\kappa_1}{\theta_1,\phi_1}\right) \quad . \qquad [44]$$

The Jacobian, obtained from [28] is

$$J\left(\frac{C_o,\kappa_1}{\theta_1,\phi_1}\right) = \frac{\sqrt{1-f^2}}{\cos^2\theta_1 (r_e^2\cos^2\phi_1 + \sin^2\phi_1 - fr_e\sin 2\phi_1)^{\frac{1}{2}}} \exp\left[\frac{K_2 P(q,r_e)}{\eta_o} E_o^2 t\right] .$$

[45]

Since C_o and κ_1 are constant for each particle in the assembly, the probability $p(C_o,\kappa_1)$ is constant and equals its value at $t = 0$, which, from [28], [44] and [45], is seen to be

$$p(C_o,\kappa_1) = \frac{r_e(1-f^2)}{\Psi_1^{\frac{1}{2}}\ (1 - f^2 + C_o^2\Psi_1)}\ p_o(\theta_{10},\phi_{10}) \qquad [46]$$

where

$$\Psi_1 = r_e^2(1-f^2)\sin^2\kappa_1 + fr_e\sqrt{1-f^2}\,\sin 2\kappa_1 + (1+f^2r_e^2)\cos^2\kappa_1 \qquad [47]$$

and $p_o(\theta_{10},\phi_{10})$ is the probability distribution at $t = 0$, ϕ_{10} and θ_{10} being given in terms of C_o and κ_1 by the relation [28] with $t = 0$. Substitution of [46] into [44] yields the probability function $p_t(\theta_1,\phi_1)$ at a general time t as

$$p_t(\theta_1,\phi_1) = \frac{p_o[\tan^{-1}(\chi\tan\theta_1),\ \tan^{-1}\nu]}{\chi(\cos^2\theta_1 + \chi^2\sin^2\theta_1)} \exp\left[\frac{2K_2P(q,r_e)}{\eta_o}\,E_o^2t\right] , \qquad [48]$$

where

$$\nu = \frac{r_e\sqrt{1-f^2}\,\tan\phi_1 - (r_e^2 - fr_e\tan\phi_1)\tan\frac{2\pi t}{T_1}}{r_e\sqrt{1-f^2} + (\tan\phi_1 - fr_e)\tan\frac{2\pi t}{T_1}} , \qquad [49]$$

$$\chi^2 = (\chi_1\sin^2\phi_1 + \chi_2\sin\phi_1\cos\phi_1 + \chi_3\cos^2\phi_1)\exp\left[\frac{2K_2P(q,r_e)}{\eta_o}\,E_o^2t\right] , \qquad [50]$$

the quantities χ_1, χ_2 and χ_3 being functions of time, formulas for which are listed in Table II for the present case ($E_o < E_{crit.}$) as well as those for $E_o \geq E_{crit.}$ and for $G = 0$; values for $E_o = 0$ have already been given (cf. [16]-7) and are also obtained by setting $f = 0$ in the equations for

TABLE II

Equations for χ_1, χ_2, χ_3 in [50]

CONDITION	EQUATIONS
$0 \leq f^2 < 1$ $0 \leq E_o < E_{crit.}$	$\chi_1 = \frac{1}{2(1-f^2)} \left[1 + r_e^{-2} + (1 - r_e^{-2}) \cos \frac{4\pi t}{T_1} - 2f^2 \cos \frac{4\pi t}{T_1} + 2f\sqrt{1-f^2} \sin \frac{4\pi t}{T_1}\right]$
	$\chi_2 = \frac{1}{1-f^2} \left[\sqrt{1-f^2}\,(r_e^{-1} - r_e) \sin \frac{4\pi t}{T_1} - f(r_e + r_e^{-1})\left(1 - \cos \frac{4\pi t}{T_1}\right)\right]$
	$\chi_3 = \frac{1}{2(1-f^2)} \left[1 + r_e^2 + (1 - r_e^2) \cos \frac{4\pi t}{T_1} - 2f^2 \cos \frac{4\pi t}{T} - 2f\sqrt{1-f^2} \sin \frac{4\pi t}{T_1}\right]$
$f^2 = 1$ $E_o = E_{crit.}$	$\chi_1 = 1 + \frac{G^2}{r_e^2 + 1} t^2 - \frac{K_2 P(q, r_e) E_o^2}{\eta_o} t$
	$\chi_2 = \frac{2(r_e^2 - 1)G}{r_e^2 + 1} t + \frac{2K_2 P(q, r_e) G\, E_o^2}{\eta_o (r_e^2 + 1)} t$
	$\chi_3 = 1 + \frac{G^2 r_e^2}{r_e^2 + 1} t^2 + \frac{K_2 P(q, r_e) E_o^2}{\eta_o} t$
$f^2 > 1$ $E_o > E_{crit.}$	$\chi_1 = \frac{1}{2(1-f^2)} \left[1 + r_e^{-2} + (1 - r_e^{-2}) \cosh \frac{4\pi t}{T_2} - 2f^2 \cosh \frac{4\pi t}{T_2} - 2f\sqrt{f^2-1} \sinh \frac{4\pi t}{T_2}\right]$
	$\chi_2 = \frac{1}{f^2 - 1} \left[\sqrt{f^2-1}\,(r_e^{-1} - r_e) \sinh \frac{4\pi t}{T_2} + f(r_e + r_e^{-1})\left(1 - \cosh \frac{4\pi t}{T_2}\right)\right]$
	$\chi_3 = \frac{1}{2(1-f^2)} \left[1 + r_e^2 + (1 - r_e^2) \cosh \frac{4\pi t}{T_2} - 2f^2 \cosh \frac{4\pi t}{T_2} + 2f\sqrt{f^2-1} \sinh \frac{4\pi t}{T_2}\right]$
$G = 0$	$\chi_1 = \exp\left[\mp \frac{2\pi t}{T_3}\right]$, $\chi_2 = 0$, $\chi_3 = \exp\left[\pm \frac{2\pi t}{T_3}\right]$

Note: The corresponding equations for $f = 0$ ($E_o = 0$) are given by [17]-7 and may be obtained from the equations for $0 \leq f^2 < 1$ by setting $f = 0$

$f^2 < 1$ in Table II. Thus if the initial orientation distribution $p_o(\theta_{10},\phi_{10})$ for a suspension is known, the instantaneous probability function $p_t(\theta_1,\phi_1)$ at all future time may be calculated by means of [48].

(ii) Random initial orientation

We now consider an initially isotropic suspension, for which

$$p_o(\theta_{10},\phi_{10}) = \frac{\sin\theta_{10}}{4\pi} = \frac{\chi \sin\theta_1}{4\pi(\cos^2\theta_1 + \chi^2\sin^2\theta_1)^{\frac{1}{2}}} \quad . \qquad [51]$$

It follows from [48] and [51] that at time t

$$p_t(\theta_1,\phi_1) = \frac{\sin\theta_1}{4\pi(\cos^2\theta_1 + \chi^2\sin^2\theta_1)^{3/2}} \exp\left[\frac{2K_2P(q,r_e)}{\eta_o} E_o^2 t\right] . \qquad [52]$$

The separate probability distributions of θ_1 (0 to π) and ϕ_1 (0 to 2π) are obtained by the integration of [52] as

$$p_t(\theta_1) = \int_o^{2\pi} p_t(\theta_1,\phi_1)d\phi_1 = \frac{\sin\theta_1}{\pi m_1^{\frac{1}{2}} m_2} E(k_1) \exp\left[\frac{2K_2P(q,r_e)}{\eta_o} E_o^2 t\right] \qquad [53]$$

and

$$p_t(\phi_1) = \int_o^{\pi} p_t(\theta_1,\phi_1)d\theta_1 = \frac{1}{2\pi(\chi_1\sin^2\phi_1 + \chi_2\sin\phi_1\cos\phi_1 + \chi_3\cos^2\phi_1)}$$

[54]

where $E(k_1)$ is the complete elliptic integral of the second kind with modulus $k_1 = 1 - m_2/m_1$ and

$$m_1 = \cos^2\theta_1 + \tfrac{1}{2}(\chi_1 + \chi_3 + \sqrt{(\chi_3 - \chi_1)^2 + \chi_2^2})\sin^2\theta_1 \exp\left[\frac{2K_2P(q,r_e)}{\eta_o} E_o^2 t\right] , \qquad [55a]$$

$$m_2 = \cos^2\theta_1 + \tfrac{1}{2}(\chi_1 + \chi_3 - \sqrt{(\chi_3 - \chi_1)^2 + \chi_2^2})\sin^2\theta_1 \exp\left[\frac{2K_2P(q,r_e)}{\eta_o} E_o^2 t\right] . \qquad [55b]$$

The corresponding cumulative distributions are then

$$P_t(\theta_1) = \int_o^{\theta_1} p_t(\theta_1)d\theta_1 = \frac{1}{\pi} \exp\left[\frac{2K_2P(q,r_e)}{\eta_o} E_o^2 t\right] \int_o^{\theta_1} \frac{\sin\theta_1}{m_1^{\frac{1}{2}} m_2} E(k_1)d\theta_1 . \qquad [56a]$$

and

$$P_t(\phi_1) = \int_o^{\phi_1} p_t(\phi_1)d\phi_1 = \frac{1}{2\pi} \tan^{-1}\left(\frac{4\chi_1\tan\phi_1}{2\chi_1\chi_2\tan\phi_1 + \chi_2^2 + 4}\right) . \qquad [56b]$$

The probability distribution $p(C_o,\kappa_1)$ is obtained from [46] for the initially isotropic suspension (i.e., $p_o(\theta_{10},\phi_{10})$ is given by [51]) as

$$p(C_o,\kappa_1) = \frac{C_o r_e(1 - f^2)}{4\pi(1 - f^2 + C_o^2\Psi_1)^{3/2}} . \qquad [57]$$

It should be noted that the limits of C_o and κ_1 are taken to be $(-\infty$ to $+\infty)$ and $(0$ to $2\pi)$ respectively, corresponding to

those
~~that~~ of θ_1 (0 to π) and ϕ_1 (0 to 2π).

The probability distributions $p(C_o,\kappa_c)$ for $f^2 = 1$ and $p(C_o,\kappa_2)$ for $f^2 > 1$ can be obtained using the same analysis given above for the initially isotropic suspensions; the results are

$$p(C_o,\kappa_c) = \frac{C_o r_e^2 \sqrt{r_e^2 + 1}}{4\pi[1 + r_e^2(1+C_o^2) + C_o^2 r_e^2 (r_e \pm \kappa_c)^2]^{3/2}} \quad , \quad [58a]$$

$$p(C_o,\kappa_2) = \frac{C_o r_e (f^2 - 1)}{4\pi(f^2 - 1 + C_o^2 \Psi_2)^{3/2}} \quad [58b]$$

where

$$\Psi_2 = r_e^2(f^2 - 1)\cosh^2\kappa_2 - f r_e\sqrt{f^2 - 1}\sinh 2\kappa_2 + (1 + f^2 r_e^2)\sinh^2\kappa_2. \quad [58c]$$

When f = 0 (shear flow alone) [57] reduces to $p(C,\kappa)$ given by [20]-7 which is

$$p(C,\kappa) = \frac{C r_e}{4\pi[1 + C^2(\cos^2\kappa + r_e^2\sin^2\kappa)]^{3/2}} \quad . \quad [59]$$

Values for $p(C_o)$, $p(\kappa_1)$, $p(\kappa_2)$ and $p(\kappa_c)$ can be obtained by the integration of [57] and [58]; the analytical solutions are not feasible for all of these probability functions.

As a set of examples, Fig. 5 shows polar diagrams of $\sqrt{p_t(\phi_1)}$ calculated from [52] for various values of f and t for a suspension of prolate spheroids of $r_e = 5$. When f = 0, $p_t(\phi_1)$ shows undamped oscillations with a period T/2 as noted

FIGURE 5

The probability distribution $\sqrt{p_t(\phi_1)}$ versus ϕ_1 for initially randomly oriented prolate spheroids ($r_e = 5$) at various f and t.

(a) in shear flow alone ($f = 0$, $E_o = 0$) at (i) $t/T = 0$, (ii) 0.03, (iii) 0.25, (iv) 0.47 calculated from [22]-7 and (v) $\sqrt{p_\infty(\phi_1)}$ from [102]-7. This case has already been discussed in detail[7].

(b) at $E_o < E_{crit.}$ ($f = 0.3$) at (i) $t/T_1 = 0$, (ii) 0.05, (iii) 0.3, (iv) 0.45 calculated from [54] and (v) $\sqrt{p_\infty(\phi_1)}$ from [65].

(c) at $E_o > E_{crit.}$ ($f = 1.1$) at (i) $t/T_2 = 0$, (ii) 0.023, (iii) 0.046, (iv) 0.069 calculated from [54]; the steady orientation $\phi'_{1\infty} = 72.7°$ is indicated by the broken line.

(d) in an electric field alone ($G = 0$) at (i) $t/T_3 = 0$, (ii) 0.105, (iii) 0.21 and (iv) 0.315 calculated from [54].

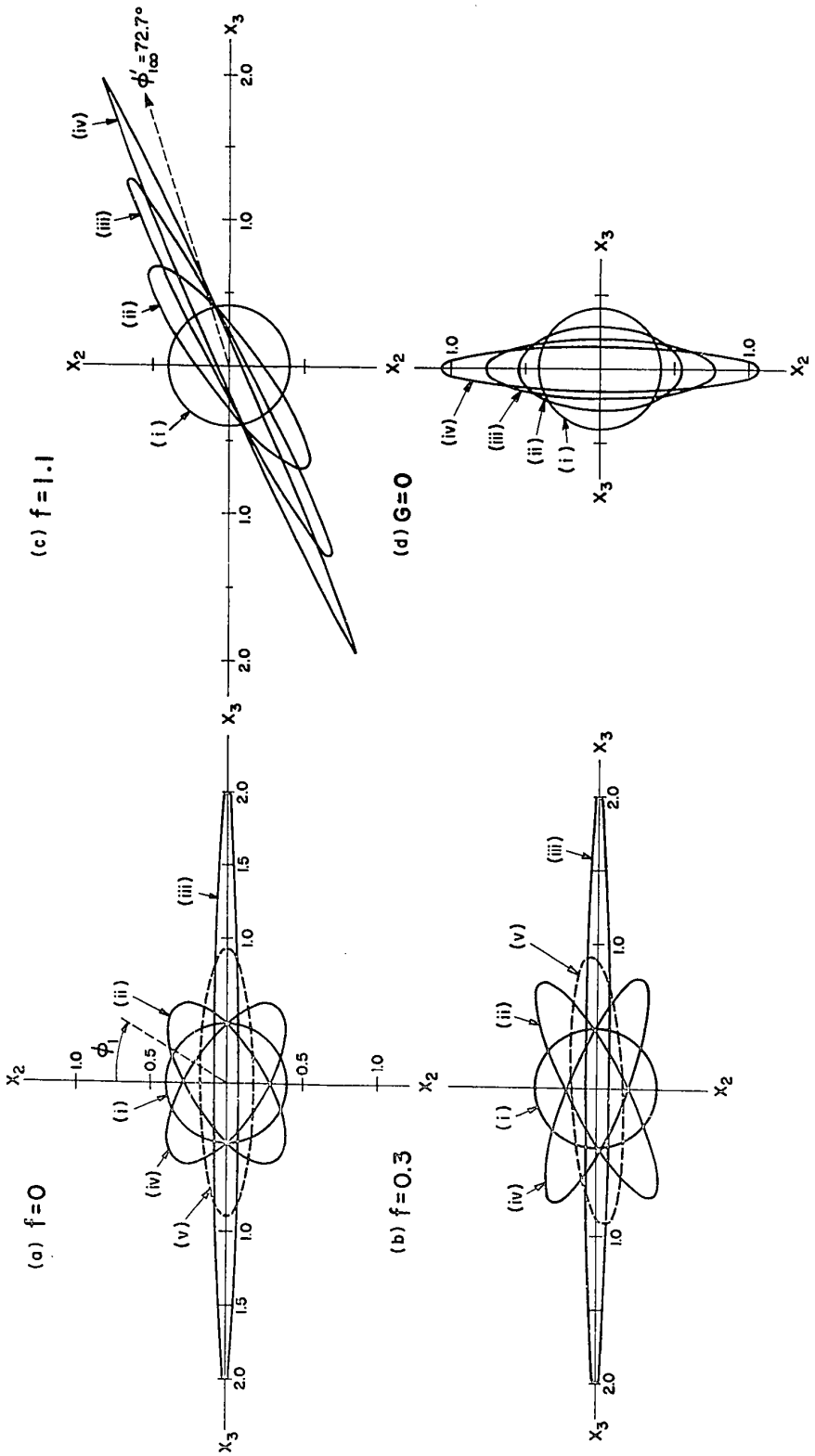
(a) f=0
(b) f=0.3
(c) f=1.1
(d) G=0
ϕ_1
$\phi'_{1\infty}$=72.7°
(i)
(ii)
(iii)
(iv)
(v)
X_2
X_3
0.5
1.0
1.5
2.0

previously[7]. At t = T/4 nearly all the particles become oriented in the direction of flow (x_3-axis), and then at t = T/2 resume their initial orientations. Similarly when $0 < f^2 < 1$, $p_t(\phi_1)$ oscillates with a period $T_1/2$. However because of the electrical torque acting on each particle, the rotational motion of a given particle is not symmetrical in the first and second quadrant, it takes a longer time ($t = 0.3\ T_1$) to reach a similar (but not identical) orientation distribution to that for f = 0 and t = T/4 [Fig. 5a-(iii) and b-(iii)]. When $f^2 > 1$, $p_t(\phi_1)$ changes monotonically to the steady orientation $\phi'_{1\infty}$(= 72.7° for f = 1.1) where the distribution may be described by the Dirac delta function $p_\infty(\phi_1) = \delta(\phi_1 - \phi'_{1\infty})$. At G = 0 the orientation distribution shows a monotonic increase in the direction of the electric field (Fig. 5d) until $p_\infty(\phi_1) = \delta(\phi_1)$.

The behavior of $p_t(\phi_1)$ for the reciprocal case $r_e = 1/5$ is similar to that shown by Fig. 5 when ϕ_1 is rotated through 90°. However the numerical values of $p_t(\phi_1)$ are not identical since $P(q,r_e)$, and hence f, does not possess the property of permutability of r_e and r_e^{-1} except when f = 0[7].

(b) Orientations θ_2 and ϕ_2 for G = 0

We consider here the orientation distribution $p_t(\theta_2,\phi_2)$ for the special case G = 0, which may be obtained from the identity:

$$p_t(\theta_2,\phi_2)d\theta_2 d\phi_2 \equiv p_t(\theta_1,\phi_1)d\theta_1 d\phi_1 \quad . \qquad [60]$$

where $p_t(\theta_1,\phi_1)$ is given by [52] for an initially isotropic suspension. From the transformation [41], [60] can be written by

$$p_t(\theta_2,\phi_2) = p_t(\theta_1,\phi_1) \cdot \frac{\sin\theta_2}{\sqrt{1 - \sin^2\theta_2\cos^2\phi_2}} \quad . \qquad [61]$$

Substitution of [52] into [61] for the present case G = 0 yields

$$p_t(\theta_2,\phi_2) = \frac{\sin\theta_2 \exp\left[\pm \frac{2\pi t}{T_3}\right]}{4\pi\{\sin^2\theta_2 + \cos^2\theta_2 \exp\left[\pm \frac{4\pi t}{T_3}\right]\}^{3/2}} \quad . \qquad [62]$$

It is evident from [42] and [62] that $p_t(\theta_2,\phi_2)$ is independent of ϕ_2. Thus $p_t(\phi_2) = p_o(\phi_2)$ remains constant and is given by

$$p_t(\phi_2) = \int_o^{\pi} p_t(\theta_2,\phi_2)d\theta_2 = 1/2\pi \quad , \qquad [63a]$$

the corresponding cumulative distribution being

$$p_t(\phi_2) = \int_o^{\phi_2} p_t(\phi_2)d\phi_2 = \phi_2/2\pi \quad . \qquad [63b]$$

The probability distribution $p_t(\theta_2)$ may be obtained from [62]:

$$p_t(\theta_2) = \int_o^{2\pi} p_t(\theta_2,\phi_2)d\phi_2 = \frac{\sin\theta_2 \exp\left[\pm \frac{2\pi t}{T_3}\right]}{2\{\sin^2\theta_2 + \cos^2\theta_2 \exp[\pm \frac{4\pi t}{T_3}]\}^{3/2}} \quad , \qquad [63c]$$

the corresponding cumulative distribution being

$$P_t(\theta_2) = \int_0^{\theta_2} p_t(\theta_2)d\theta_2 = \tfrac{1}{2} - \tfrac{1}{2}\{1+\tan^2\theta_2 \exp[\pm \tfrac{4\pi t}{T_3}]\}^{-\frac{1}{2}} \quad . \qquad [63d]$$

When $t \to \infty$, $p_t(\theta_2)$ shows a steady increase at $\theta_2 = \pi/2$ when $r_e < 1$ until $p_\infty(\theta_2) = \delta(\theta_2 - \pi/2)$, and at $\theta_2 = 0$ when $r_e > 1$ until $p_\infty(\theta_2) = \delta(\theta_2)$.

(c) Steady Orientations θ_1 and ϕ_1.

It has been shown in Section 2 that, when $0 < f^2 < \infty$, as $t \to \infty$ each particle approaches $\theta_1 = 0, \pi/2$ when $r_e < 1$ and $r_e > 1$ respectively; when $r_e > 1$, ϕ_1 depends upon f, whereas when $r_e < 1$ it is indeterminate (and trivial). In the former case ($r_e > 1$), if $0 < f^2 < 1$, $p_\infty(\phi_1)$ oscillates in accordance with [54] and $p_\infty(\theta_1)$ is given by the Dirac delta function as expressed in Table III. When $f^2 \geq 1$, $p_\infty(\phi_1)$ also becomes a delta function since all particles assume $\phi_1 = \phi'_{1\infty}$ where $\phi'_{1\infty}$ is given by [33a] (or by [39] for the case $f^2 = 1$).

If we consider the case for which the equilibrium distribution $p_\infty(\phi_1)$ is steady, then from the equation of continuity ([10a]-22):

$$\frac{\partial}{\partial \phi_1}\left[p_\infty(\phi_1)\left(\frac{d\phi_1}{dt}\right)\right] = 0 \qquad [64]$$

where the angular velocity $(d\phi_1/dt)$ of each particle is given

by [24b] with m = 0. Integration of [64] yields

$$p_\infty(\phi_1) = \frac{r_e\sqrt{1-f^2}}{2\pi(r_e^2\cos^2\phi_1 + \sin^2\phi_1 - fr_e\sin 2\phi_1)} \qquad [65]$$

which is normalized for the limits of $\phi_1 = 0$ to 2π. The corresponding cumulative distribution is

$$P_\infty(\phi_1) = \int_0^{\phi_1} p_\infty(\phi_1)d\phi_1 = \frac{1}{2\pi}\tan^{-1}\left(\frac{\sqrt{1-f^2}\tan\phi_1}{r_e - f\tan\phi_1}\right). \qquad [66]$$

The steady state distributions given by [65] and [66] depend upon r_e and f but are independent of the initial orientation of the particles and of the mechanism (provided one exists) by which the steady state is attained. When f = 0, [65] and [66] reduce to the results obtained previously for shear alone[22]. The polar plots of $\sqrt{p_\infty(\phi_1)}$ for $r_e = 5$ at f = 0 and 0.3 are shown by the broken lines in Fig. 5(a) and (b). The maximum probability occurs at $\phi_1 = 90°$ for f = 0 and at $\phi_1 = 86.5°$ for f = 0.3. We note that as $f \to 1$, $p_\infty(\phi_1)$ given by [65] tends to the value $\delta(\phi_1 - \tan^{-1}r_e)$ calculated for the case f = 1 in which monotonic changes in $p_t(\phi_1)$ occur. Experiments[7,23] with rods and discs at f = 0 have shown good agreement with the theory.

The formulas for steady orientation distributions at various values of f are summarized in Table III. Two possible mechanisms which enable a steady state to be estab-

TABLE III

Equations for Equilibrium Orientation Distributions
and Mean Projections

CONDITION	$p_\infty(\phi_1)$ a)	$p_\infty(\theta_1)$		$r_e > 1$			$r_e < 1$		
		$r_e > 1$	$r_e < 1$	$\bar{r}_{1\infty}$	$\bar{r}_{2\infty}$	$\bar{r}_{3\infty}$	$\bar{s}_{12\infty}$	$\bar{s}_{23\infty}$	$\bar{s}_{13\infty}$
$0 < f^2 < 1$	Eq. [65]	$\delta(\theta_1 - \pi/2)$	$\delta(\theta_1)$ b)	0	Eq. [71a]	Eq. [71b]	0	1	0
$f^2 = 1$	$\delta(\phi_1 - \tan^{-1} r_e)$	"	"	"	$1/\sqrt{1 + r_e^2}$	$r_e/\sqrt{1 + r_e^2}$	"	"	"
$f^2 > 1$	$\delta[\phi_1 - \tan^{-1}\{r_e(f - \sqrt{f^2 - 1})\}]$	"	"	"	$\dfrac{1}{\sqrt{1 + r_e^2(f - \sqrt{f^2 - 1})^2}}$	$\dfrac{r_e(f - \sqrt{f^2 - 1})}{\sqrt{1 + r_e^2(f - \sqrt{f^2 - 1})^2}}$	"	"	"
$G = 0$	$\delta(\phi_1)$	"	$1/\pi$	"	1	0	$2/\pi$	$2/\pi$	"

a) $p_\infty(\phi_1)$ for $r_e < 1$ is undefinable (and trivial) since $p_\infty(\theta_1) = \delta(\theta_1)$ except when $f^2 = \infty$ for which $p_\infty(\phi_1) = \delta(\phi_1 - \pi/2)$.

b) $\delta(\theta_1)$ etc. designate Dirac delta function.

lished when $f^2 < 1$ and ϕ_1 of individual particles is periodic, namely (1) the spread in particle shape and (2) particle interactions, will be discussed in the following Chapter[1]. When $f^2 \geq 1$ the steady state is attained directly as a result of monotonic changes in ϕ_1 and θ_1 of the individual particles (cf. [33]).

(d) Mean Projections

(i) Transient state

Following earlier practice[2,5] it is convenient to use mean orientation parameters such as the mean projections along the fixed coordinate axes of unit length of the particle axes for prolate spheroids and rods ($r_e > 1$) and the mean projections on the coordinate planes of unit area of the equatorial plane of the particles for oblate spheroids and discs ($r_e < 1$). These quantities are used in analyzing the experimental data given in the following Chapter[1] and are defined as

$$\bar{r}_1 = \bar{S}_{23} = \int_0^{2\pi}\int_0^{\pi} |\cos\theta_1|\, p_t(\theta_1,\phi_1)\, d\theta_1 d\phi_1 \quad , \qquad [67a]$$

$$\bar{r}_2 = \bar{S}_{13} = \int_0^{2\pi}\int_0^{\pi} |\sin\theta_1\cos\phi_1|\, p_t(\theta_1,\phi_1)\, d\theta_1 d\phi_1 \quad , \qquad [67b]$$

$$\bar{r}_3 = \bar{S}_{12} = \int_0^{2\pi}\int_0^{\pi} |\sin\theta_1\sin\phi_1|\, p_t(\theta_1,\phi_1)\, d\theta_1 d\phi_1 \qquad [67c]$$

where $\bar{r}_i$ is the mean projection length on each of the coordinate axis x_i and $\bar{S}_{ij}$ is the mean projection area on each of the coordinate plane $x_i x_j$ ($i \neq j$). If we consider an initially isotropic and collision-free suspension, $p_t(\theta_1,\phi_1)$ is given by [52], from which we obtain

$$\bar{r}_1 = \bar{S}_{23} = \frac{1}{2\pi} \exp\left[\frac{2K_2P(q,r_e)}{\eta_o} E_o^2 t\right] \int_o^{2\pi} \frac{d\phi_1}{\chi(\chi+1)} \quad , \qquad [68a]$$

$$\bar{r}_2 = \bar{S}_{13} = \frac{1}{\pi} \exp\left[\frac{2K_2P(q,r_e)}{\eta_o} E_o^2 t\right] \times \int_o^{\pi} \frac{\{\cos^2\theta_1 + \chi_1 \exp[\frac{2K_2P(q,r_e)}{\eta_o} E_o^2 t] \sin^2\theta_1\}^{\frac{1}{2}} \sin^2\theta_1}{m_3\sin^4\theta_1 + m_4\sin^2\theta_1 + 1} d\theta_1 , \qquad [68b]$$

$$\bar{r}_3 = \bar{S}_{12} = \frac{1}{\pi} \exp\left[\frac{2K_2P(q,r_e)}{\eta_o} E_o^2 t\right] \times \int_o^{\pi} \frac{\{\cos^2\theta_1 + \chi_3 \exp[\frac{2K_2P(q,r_e)}{\eta_o} E_o^2 t] \sin^2\theta_1\}^{\frac{1}{2}} \sin^2\theta_1}{m_3\sin^4\theta_1 + m_2\sin^2\theta_1 + 1} d\theta_1 \qquad [68c]$$

where

$$m_3 = 1 - (\chi_1 + \chi_3)\exp\left[\frac{2K_2P(q,r_e)}{\eta_o} E_o^2 t\right] + (\chi_1\chi_3 - \frac{\chi_2^2}{4}) \exp\left[\frac{4K_2P(q,r_e)}{\eta_o} E_o^2 t\right] , \qquad [68d]$$

$$m_4 = -2 + (\chi_1 + \chi_3) \exp\left[\frac{2K_2P(q,r_e)}{\eta_o} E_o^2 t\right] . \qquad [68e]$$

When f = 0 these equations reduce to the solutions given previously[7]; when $0 < f^2 < \infty$, [68] must be integrated numerically.

When G = 0, the solutions are

$$\bar{r}_1 = \bar{r}_3 = \bar{S}_{12} = \bar{S}_{23} = \frac{1}{\pi} \operatorname{csch} \left(\pm \frac{2\pi t}{T_3}\right) \left[E(k_2) - K(k_2)\right] \qquad [69a]$$

$$\bar{r}_2 = \bar{S}_{13} = \tfrac{1}{2} \operatorname{sech} \left(\pm \frac{2\pi t}{T_3}\right) \left\{\exp\left[\mp \frac{2\pi t}{T_3}\right] - 1\right\} \qquad [69b]$$

where $K(k_2)$ and $E(k_2)$ are the complete elliptic integrals of the first and the second kind respectively with modulus $k_2^2 = 1 - \exp[\pm 4\pi t/T_3]$, and as before the upper sign is for $r_e < 1$ and the lower for $r_e > 1$.

Examples for $r_e = 10$ are shown in Fig. 6. In a shear flow (f = 0, Fig. 6 a) $\bar{r}_i$ oscillates with constant amplitude and frequency 2/T. When $0 < f^2 < 1$, $\bar{r}_1$ oscillates with frequency $2/T_1$ with rapidly decreasing amplitude and approaches $\bar{r}_1 = 0$ when all the particles rotate with $\theta_1 = \pi/2$; $\bar{r}_2$ and $\bar{r}_3$ oscillate with varying amplitudes which approach asymptotic values. When $f^2 \geq 1$, $\bar{r}_2$ shows a small initial increase and levels off to the steady value $\bar{r}_2 = \cos\phi'_{1\infty}$ (= 0.159); $\bar{r}_3$ increases toward its steady value $\bar{r}_3 = \sin\phi'_{1\infty}$ (= 0.987), and $\bar{r}_1$ decreases to $\bar{r}_1 = 0$. Finally for G = 0 and $f^2 = \infty$, $\bar{r}_1 = \bar{r}_3$ decreases to zero, and $\bar{r}_2$ increases to unity.

When $r_e < 1$ (oblate spheroids, discs) the mean projections $\bar{S}_{23}$, $\bar{S}_{12}$ and $\bar{S}_{13}$ are similar to those of $\bar{r}_1$, $\bar{r}_2$

FIGURE 6

Mean projection lengths $\bar{r}_1$ (curve 1), $\bar{r}_2$ (curve 2) and $\bar{r}_3$ (curve 3) for initially randomly oriented prolate spheroids of $r_e = 10$ at various values of f.

(a) in shear flow ($E_o = 0$, $f = 0$) calculated from the equations given in Table II of reference 7.

(b) when $E_o < E_{crit.}$, obtained by numerical integration of [68] for $f = 0.275$.

(c) when $E_o > E_{crit.}$, from [68] for $f = 2.0$.

(d) in an electric field ($G = 0$) calculated from [69].

All abscissa are plotted using the dimensionless time scales t/T, t/T_1, t/T_2 and t/T_3 for (a), (b), (c) and (d) respectively.

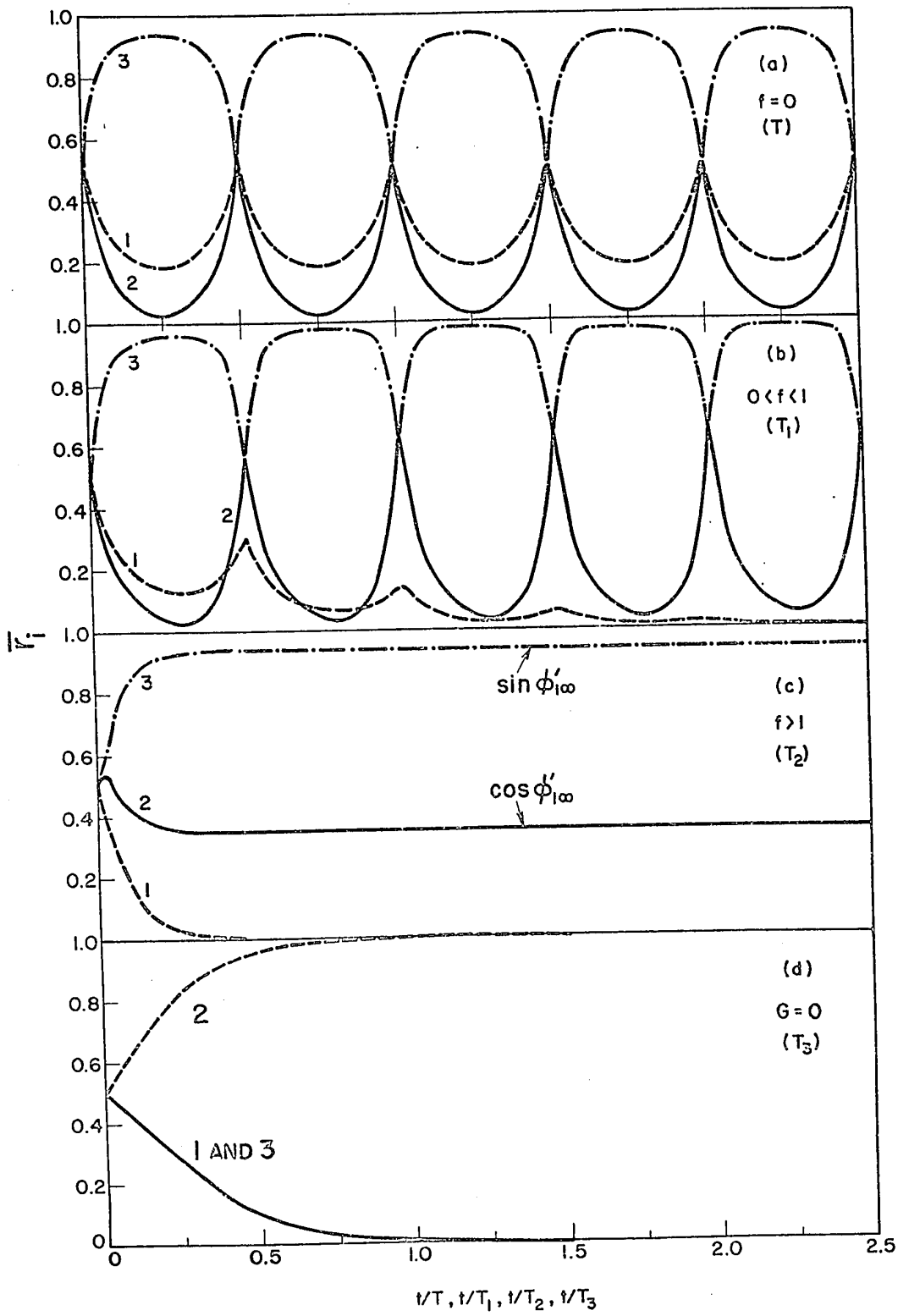
(a)
f = 0
(T)
(b)
0 < f < 1
(T1)
(c)
f > 1
(T2)
sin φ'1∞
cos φ'1∞
(d)
G = 0
(T3)
1 AND 3
1.0
0.8
0.6
0.4
0.2
0
0.5
1.5
2.0
2.5
t/T , t/T1 , t/T2 , t/T3

and $\bar{r}_3$ respectively (note the change in order from the equalities $\bar{r}_i$ and $\bar{S}_{jk}$ in [67]) shown in Fig. 6. For the special case f = 0 the curves are numerically identical when $r_e = 1/10$ because of the interchangibility of r_e and r_e^{-1} discussed previously[7].

(ii) Steady state

As mentioned earlier when $t \to \infty$ for $f^2 > 0$ each particle approaches $\theta_1 = 0, \pi/2$ when $r_e < 1$ and $r_e > 1$ respectively, from which it follows that the steady mean projections become $\bar{r}_{1\infty} = 0$ (for $r_e > 1$), and $\bar{S}_{12\infty} = \bar{S}_{13\infty} = 0$ and $\bar{S}_{23\infty} = 1$ (for $r_e < 1$). However when $0 < f^2 < 1$ and $r_e > 1$, the probability distribution $p_\infty(\phi_1)$ is given by [65] and the mean orientations $\bar{r}_2$ and $\bar{r}_3$ are thus

$$\bar{r}_{2\infty} = \int_0^{2\pi} |\cos\phi_1|\ p_\infty(\phi_1)\,d\phi_1 \quad , \qquad [70a]$$

$$\bar{r}_{3\infty} = \int_0^{2\pi} |\sin\phi_1|\ p_\infty(\phi_1)\,d\phi_1 \quad . \qquad [70b]$$

The solutions of these integrals are

$$\bar{r}_{2\infty} = \frac{1}{2\pi i}\left[\frac{1}{\sqrt{1+m_6^2}}\,\ell n\left(\frac{m_6 - \sqrt{1+m_6^2}}{m_6 + \sqrt{1+m_6^2}}\right) - \frac{1}{\sqrt{1+m_5^2}}\,\ell n\left(\frac{m_5 - \sqrt{1+m_5^2}}{m_5 + \sqrt{1+m_5^2}}\right)\right], \qquad [71a]$$

$$\bar{r}_{3\infty} = \frac{1}{2\pi i}\left[\frac{m_5}{\sqrt{1+m_5^2}}\,\ell n\left(\frac{m_5 - \sqrt{1+m_5^2}}{m_5 + \sqrt{1+m_5^2}}\right) - \frac{m_6}{\sqrt{1+m_6^2}}\,\ell n\left(\frac{m_6 - \sqrt{1+m_6^2}}{m_6 + \sqrt{1+m_6^2}}\right)\right], \qquad [71b]$$

where

$$m_5 = fr_e - ir_e\sqrt{1 - f^2} \qquad [71c]$$

$$m_6 = fr_e + ir_e\sqrt{1 - f^2} \qquad [71d]$$

and $i = \sqrt{-1}$. Since m_5 and m_6 are complex conjugates, the first and second terms in [71a] and [71b] are also complex conjugates. Therefore the difference is a pure imaginary quantity, and hence $\bar{r}_2$ and $\bar{r}_3$ are real.

When $f^2 \geq 1$ and $r_e > 1$, it is immediately seen from the steady orientations listed in Table III that $\bar{r}_{2\infty}$ and $\bar{r}_{3\infty}$ are given by the single values in the table including the case G = 0. It should be noted that since oblate spheroids and discs ($r_e < 1$) at G = 0 have a steady orientation distribution $p_\infty(\theta_1) = 1/\pi$, $\bar{S}_{23\infty} = 2/\pi$ and $\bar{S}_{13\infty} = 0$. On the other hand for $r_e > 1$ at G = 0, $\bar{r}_{2\infty} = 1$ and $\bar{r}_{1\infty} = \bar{r}_{3\infty} = 0$.

Although the steady distribution $p_\infty(\phi_1)$ is known when f = 0 (i.e. $E_o = 0$) $p_\infty(\theta_1,\phi_1)$ is not yet known since $p_\infty(\theta_1,\phi_1)$ depends on the mechanism by which the equilibrium is attained; hence $\bar{r}_{i\infty}$ and $\bar{S}_{jk\infty}$ for f = 0 can not be evaluated. The solution of [71] at f = 0 corresponds to the situation in which all the particles ($r_e > 1$) lie in the x_2x_3-plane ($\theta_1 = \pi/2$, $C = \infty$) with the orientation distribution given by [65] with f = 0. Variations of $\bar{r}_{i\infty}$ with f are discussed later.

(e) Rheological Properties

The macroscopic rheological properties of a dilute suspension of spheroids is determined by the distribution of particle orientations in a given field of flow. In the Sections 3(a) to (c) we have derived the orientation probability distributions in the transient and steady states at various values of f. We now consider the rheological properties of a suspension using the analytical method of Cox and Brenner[24], which permits the evaluation of a tensor describing the macroscopic stresses, the components of which yield the tangential and normal stresses. This yields more information than the energy dissipation method employed by Chaffey and Mason[5,6] to calculate the viscosity.

The general form of the disturbance flow v_i' (relative to the x_i'-axis) produced by a particle is given by

$$v_j' = A_{ik}' \left[\frac{1}{r^3}\left(x_i'\delta_{jk} + x_j'\delta_{ik} - x_k'\delta_{ij}\right) - \frac{3}{r^5} x_i'x_j'x_k'\right] \qquad [72]$$

where r is the distance from the center of a particle and A_{ik}' is a tensor component determined by the particle shape. The flow field given by [72] represents that produced by a point force doublet. Comparison with Jeffery's[8] calculation ([54]-8) shows A_{ij}' to be

$$A_{ij}' = \frac{2[\alpha_i S_{ij}' - a_j\beta_k(\zeta_k' - \omega_k')]}{3\beta_k(a_i^2\alpha_i + a_j\alpha_j)}, \qquad (i \neq j \neq k) \qquad [73a]$$

$$A_{ii}' = \frac{2[2\gamma_i S_{ii}' - \gamma_j S_{jj}' - \gamma_k S_{kk}']}{9(\gamma_i\gamma_j + \gamma_j\gamma_k + \gamma_k\gamma_i)} \qquad (i \neq j \neq k) \qquad [73b]$$

where α_i is defined in [6] and other elliptic integrals β_i and γ_i are

$$\beta_i = \int_o^\infty \frac{d\lambda}{(a_j^2+\lambda)(a_k^2+\lambda)\sqrt{(a_1^2+\lambda)(a_2^2+\lambda)(a_3^2+\lambda)}} \quad , \quad (i\neq j\neq k) \qquad [73c]$$

$$\gamma_i = \int_o^\infty \frac{\lambda d\lambda}{(a_j^2+\lambda)(a_k^2+\lambda)\sqrt{(a_1^2+\lambda)(a_2^2+\lambda)(a_3^2+\lambda)}} \quad . \quad (i\neq j\neq k) \qquad [73d]$$

In the present investigation of spheroids, by substituting ω_i', s_{ij}' and ζ_j' from [18] and [21] into [73] and using [22], we obtain

$$A_{11}' = \frac{G\, b^3 r_e (r_e^2 - 1)}{9\{2r_e^2 - (1 + 2r_e^2)A\}} \quad , \qquad [74a]$$

$$A_{22}' = \frac{G\, b^3 r_e (r_e^2 - 1)}{27(2r_e^2 - A)} \qquad [74b]$$

$$\times \left[\sin 2\phi_1 + 2\cos^2\theta_1 \sin 2\phi_1 - \frac{(4r_e^2 - 1)A - 2r_e^2}{4\{2r_e^2 - (1+2r_e^2)A\}} \sin^2\theta_1 \sin 2\phi_1\right] \quad ,$$

$$A_{33}' = \frac{-G\, b^3 r_e (r_e^2 - 1)}{27(2r_e^2 - A)} \qquad [74c]$$

$$\times \left[2\sin 2\phi_1 + \cos^2\theta_1 \sin 2\phi_1 - \frac{(4r_e^2 - 1)A - 2r_e^2}{4\{2r_e^2 - (1+2r_e^2)A\}} \sin^2\theta_1 \sin 2\phi_1\right] \quad ,$$

$$A_{12}' = \frac{G\, b^3 r_e (r_e^2 - 1)}{6(r_e^2 + 1)(3A - 2)} \sin 2\theta_1 \sin 2\phi_1 \qquad [74d]$$

$$- \frac{2K_2 b^3 r_e P(q, r_e)}{3\eta_o\{2r_e^2 - (2r_e^2 - 1)A\}} E_o^2 \cos^2\phi_1 \cos 2\theta_1 \quad ,$$

$$A'_{21} = \frac{G\, b^3 r_e (r_e^2 - 1)}{6(r_e^2 + 1)(3A - 2)} \sin 2\theta_1 \sin 2\phi_1$$

$$+ \frac{2K_2 b^3 r_e^3 P(q, r_e)}{3\eta_o \{2r_e^2 - (2r_e^2 - 1)A\}} E_o^2 \cos^2\phi_1 \cos 2\theta_1 \quad , \qquad [74e]$$

$$A'_{23} = A'_{32} = \frac{2Gb^3 r_e (r_e^2 - 1)}{3(2r_e^2 - 3A)} \cos\theta_1 \cos 2\phi_1 \quad , \qquad [74f]$$

$$A'_{13} = \frac{G\, b^3 r_e (r_e^2 - 1)}{3(r_e^2 + 1)(3A - 2)} \sin\theta \cos 2\phi_1$$

$$+ \frac{2K_2 b^3 r_e P(q, r_e)}{3\eta_o \{2r_e^2 - (2r_e^2 - 1)A\}} E_o^2 \sin\theta_1 \sin 2\phi_1 \quad , \qquad [74g]$$

$$A'_{31} = \frac{G\, b^3 r_e (r_e^2 - 1)}{3(r_e^2 + 1)(3A - 2)} \sin\theta \cos 2\phi_1$$

$$- \frac{2K_2 b^3 r_e^3 P(q, r_e)}{3\eta_o \{2r_e^2 - (2r_e^2 - 1)A\}} E_o^2 \sin\theta_1 \sin 2\phi_1 \quad . \qquad [74h]$$

The macroscopic stress tensor P_{ij} of a suspension is given by[24]

$$P_{ij} = p_{ij} + 8\pi\eta_o N \bar{A}_{ij} \qquad [75a]$$

where

$$p_{ij} = -p\delta_{ij} + \eta_o \left(\frac{\partial u_i}{\partial x_j} + \frac{\partial u_j}{\partial x_i} \right) \qquad [75b]$$

is the stress tensor of the suspending medium and N is the

number of particles per unit volume. The quantity $\bar{A}_{ij}$ (relative to the x_i-axis) is the mean value of A_{ij} over the assembly of particles at a given instant. Transforming A'_{ij} given by [74] to A_{ij} through the Eulerian angles θ_1 and ϕ_1, and substituting into [75a] we obtain the stress P_{ij} of the suspension. The shear stresses P_{23} and P_{32} are given by

$$P_{23} = \eta_o G + \eta_o Gc \left[C_1 \overline{\sin^4\theta_1 \sin^2 2\phi_1} + C_2 \overline{\cos^2\theta_1} + C_3 \overline{\sin^2\theta_1}\right] - \frac{8K_2 P(q,r_e) E_o^2 c}{2r_e^2 + (1-2r_e^2)A} \left[(r_e^2 - 1) \overline{\sin^4\theta_1 \sin\phi_1 \cos^3\phi_1} - r_e^2 \overline{\sin^2\theta_1 \sin\phi_1 \cos\phi_1}\right], \quad [76a]$$

$$P_{32} = \eta_o G + \eta_o Gc \left[C_1 \overline{\sin^4\theta_1 \sin^2 2\phi_1} + C_2 \overline{\cos^2\theta_1} + C_3 \overline{\sin^2\theta_1}\right] - \frac{8K_2 P(q,r_e) E_o^2 c}{2r_e^2 + (1-2r_e^2)A} \left[(r_e^2 - 1) \overline{\sin^4\theta_1 \sin\phi_1 \cos^3\phi_1} + \overline{\sin^2\theta_1 \sin\phi_1 \cos\phi_1}\right] \quad [76b]$$

where $c = 4\pi ab^2 N/3$ is the volume fraction of spheroids and

$$C_1 = (r_e^2 - 1)\left[\frac{6r_e^2 - 4r_e^2 A - 5A}{2(2r_e^2 - 3A)\{2r_e^2 - (2r_e^2 + 1)A\}} - \frac{2}{(r_e^2 + 1)(3A - 2)}\right], \quad [76c]$$

$$C_2 = \frac{4(r_e^2 - 1)}{2r_e^2 - 3A}, \quad [76d]$$

$$C_3 = \frac{2(r_e^2 - 1)}{(r_e^2 + 1)(3A - 2)}. \quad [76e]$$

It should be noted that C_1, C_2 and C_3 given above are equivalent

to those given by [48]-7 but expressed in a different form. The shear stress P_{32} is the quantity normally obtained experimentally when measuring the viscosity and is given in [76b] by the sum of (i) the stress due to the suspending medium alone (first term), (ii) that due to the shear flow on the particles (second term) and (iii) that due to the electric field on the particles (last term). In general, therefore, P_{ij} may be written

$$P_{ij} = p_{ij} + \eta_o G c \, [^H P_{ij}] + K_2 E_o^2 c \, [^E P_{ij}] \qquad [77]$$

where the dimensionless quantities $[^H P_{ij}]$ and $[^E P_{ij}]$ are the intrinsic viscous and intrinsic electric stresses, given for P_{32} by [76]:

$$[^H P_{32}] = C_1 \overline{\sin^4\theta_1 \sin^2 2\phi_1} + C_2 \overline{\cos^2\theta_1} + C_3 \overline{\sin^2\theta_1} \quad , \qquad [78a]$$

$$[^E P_{32}] = \frac{-8P(q,r_e)}{2r_e^2 + (1 - 2r_e^2)A} \left[(r_e^2 - 1) \overline{\sin^4\theta_1 \sin\phi_1 \cos^3\phi_1} + \overline{\sin^2\theta_1 \sin\phi_1 \cos\phi_1} \right] \quad . \qquad [78b]$$

If we define the viscosity of the suspension as the ratio $\eta = P_{32}/G$, and the intrinsic viscosity $[\eta] = (\eta - \eta_o)/\eta_o c$, then

$$\eta = \eta_o + \eta_o c \, [^H P_{32}] + \frac{K_2 E_o^2 c}{G} \, [^E P_{32}] \qquad [79a]$$

and

$$[\eta] = [^H P_{32}] + \frac{K_2 E_o^2}{\eta_o G} \, [^E P_{32}] \quad . \qquad [79b]$$

Thus $[\eta]$ is the sum of two terms, the first being the intrinsic viscosity for the same distribution of orientations but with no electric field ($f = 0$), and the second the effect of the electric field. Substituting [78] into [79b] yields

$$[\eta] = C_1 \overline{\sin^4\theta_1 \sin^2 2\phi_1} + C_2 \overline{\cos^2\theta_1} + C_3 \overline{\sin^2\theta_1} + fC_4 \left[(r_e^2 - 1) \overline{\sin^4\theta_1 \sin\phi_1 \cos^3\phi_1} + \overline{\sin^2\theta_1 \sin\phi_1 \cos\phi_1}\right] \qquad [80a]$$

where

$$C_4 = \frac{8r_e}{(r_e^2 + 1)\{2r_e^2 + (1 - 2r_e^2)A\}} \quad . \qquad [80b]$$

The intrinsic normal stress differences[7] defined by $[\xi_{ij}] = (P_{ii} - P_{jj})/\eta_o Gc$ are also given by two components, corresponding to the hydrodynamic and electric stresses, which generally cannot be separated experimentally when $f^2 > 0$. It follows, therefore, from [74] and [75] that

$$[\xi_{12}] = C_1\left(-\tfrac{1}{2} \overline{\sin^4\theta_1 \sin 4\phi_1} - 3 \overline{\sin^4\theta_1 \sin 2\phi_1} + 2 \overline{\sin^2\theta_1 \sin 2\phi_1}\right) + (C_2 - C_3) \overline{\sin^2\theta_1 \sin 2\phi_1} - f(r_e^2 - 1)C_4\left(\tfrac{1}{2} \overline{\sin^2 2\theta_1 \cos^2\phi_1} + \tfrac{1}{4} \overline{\sin^4\theta_1 \sin^2 2\phi_1}\right) \quad , \qquad [81a]$$

$$[\xi_{23}] = C_1 \overline{\sin^4\theta_1 \sin 4\phi_1} + f(r_e^2 - 1)C_4\left(\tfrac{1}{4} \overline{\sin^2 2\theta_1 \cos^2\phi_1} + \tfrac{1}{2} \overline{\sin^4\theta_1 \sin^2 2\phi_1}\right) \qquad [81b]$$

$$[\xi_{31}] = C_1 \left(-\tfrac{1}{2}\overline{\sin^4\theta_1 \sin 4\phi_1} + 3\,\overline{\sin^4\theta_1 \sin 2\phi_1} - 2\,\overline{\sin^2\theta_1 \sin 2\phi_1}\right)$$
$$- (C_2 - C_3)\,\overline{\sin^2\theta_1 \sin 2\phi_1} \qquad [81c]$$
$$+ f(r_e^2 - 1)\, C_4 \left(\tfrac{1}{4}\overline{\sin^2 2\theta_1 \cos^2\phi_1} - \tfrac{1}{4}\overline{\sin^4\theta_1 \sin^2 2\phi_1}\right)$$

where C_1, C_2, C_3 and C_4 are given by [76c-$\overset{e}{\phi}$], and [80b]. The remaining stress components are

$$\frac{P_{12}}{\eta_o G c} = 4C_1\,\overline{\sin^3\theta_1 \cos\theta_1 \sin\phi_1 \cos^2\phi_1} + (C_3 - C_2)\,\overline{\sin\theta_1 \cos\theta_1 \sin\phi_1}$$
$$+ fC_4 \left[(r_e^2 - 1)\,\overline{\sin^3\theta_1 \cos\theta_1 \cos^3\phi_1} + \overline{\sin\theta_1 \cos\theta_1 \cos\phi_1}\right] , \qquad [82a]$$

$$\frac{P_{21}}{\eta_o G c} = 4C_1\,\overline{\sin^3\theta_1 \cos\theta_1 \sin\phi_1 \cos^2\phi_1} + (C_3 - C_2)\,\overline{\sin\theta_1 \cos\theta_1 \sin\phi_1}$$
$$+ fC_4 \left[(r_e^2 - 1)\,\overline{\sin^3\theta_1 \cos\theta_1 \cos^3\phi_1} - r_e^2\,\overline{\sin\theta_1 \cos\theta_1 \cos\phi_1}\right] , \qquad [82b]$$

$$\frac{P_{13}}{\eta_o G c} = \frac{P_{31}}{\eta_o G c} = 4C_1\,\overline{\sin^3\theta_1 \cos\theta_1 \sin^2\phi_1 \cos\phi_1} + (C_3 - C_2)\,\overline{\sin\theta_1 \cos\theta_1 \cos\phi_1}$$
$$+ f(r_e^2 - 1)\, C_4\,\overline{\sin^3\theta_1 \cos\theta_1 \sin\phi_1 \cos^2\phi_1} \qquad [82c]$$

We note that, with the exception $P_{13} = P_{31}$, the macroscopic stress tensor P_{ij} for the suspension is no longer symmetrical because external couples act on the particles. All stresses P_{ij} given by [76], [81] and [82] at f = 0 reduce to the equations derived previously[7].

(i) Transient states

The mean values of the goniometric factors in [76] to [82] can then be evaluated by the integral

FIGURE 7

Transients of $[\eta]$ for initially randomly oriented prolate spheroids ($r_e = 10$) calculated from [80a] with the use of [83] and [52]. The conditions of (a), (b), (c) are the same as those in Fig. 6(a),(b),(c) respectively. The equilibrium value $[\eta]_\infty = 4.4$ for $f = 0.275$ and $[\eta]_\infty = 9.6$ for $f = 2$ (calculated from [87a]) are indicated by the broken lines in (b) and (c).

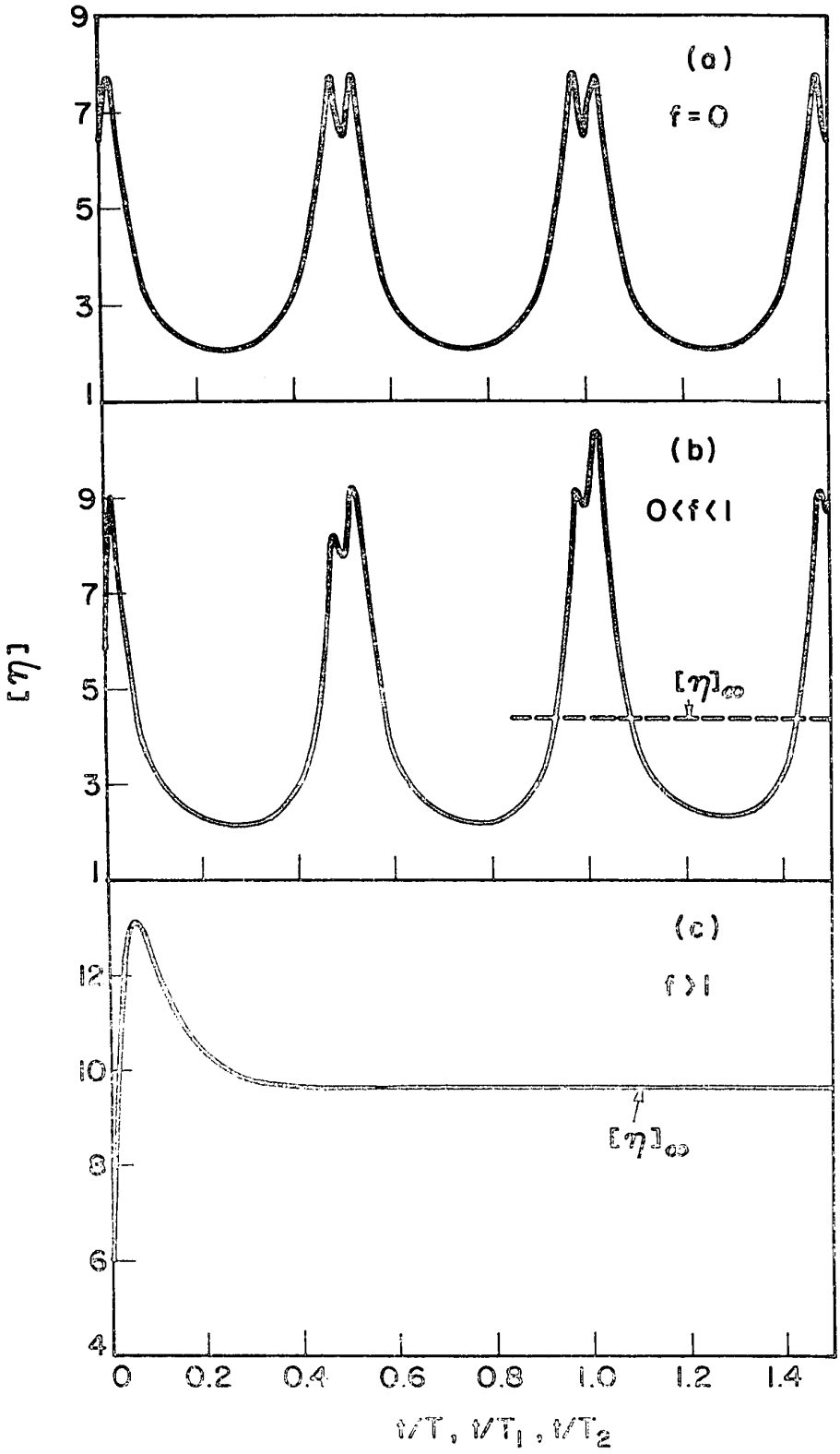
(a)
f = 0
(b)
0<f<1
$[\eta]_\infty$
(c)
f > 1
$[\eta]_\infty$
$[\eta]$
9
7
5
3
1
12
10
8
6
4
0
0.2
0.4
0.6
0.8
1.0
1.2
1.4
t/T , t/T1 , t/T2

$$\overline{F(\theta_1,\phi_1)} = \int_0^{2\pi}\int_0^{\pi} F(\theta_1,\phi_1)p_t(\theta_1,\phi_1)d\theta_1 d\phi_1 \qquad [83]$$

where $F(\theta_1,\phi_1)$ is any function whose mean value is required. As an example, we show in Fig. 7 the transient variation with time of $[\eta]$ obtained from [80a] and numerical integration of [83] at various values of f for an initially isotropic and collision-free suspensions (with $p_t(\theta_1,\phi_1)$ given by [52]) with $r_e = 10$. It is seen that $[\eta]$ undergoes oscillations (whose amplitude approaches asymptotically to the value corresponding to $\theta_{1\infty} = \pi/2$ for all particles) with a period $T_1/2$ when $f^2 < 1$, and changes monotonically to an equilibrium value when $f^2 \geq 1$, in each case reflecting similar changes in $p_t(\theta_1,\phi_1)$.

(ii) Steady state

Since, as shown earlier, prolate spheroids ($r_e > 1$) drift to $\theta_1 = \pi/2$ and oblate spheroids ($r_e < 1$) to $\theta_1 = 0$ at equilibrium ($t \to \infty$), [80] and [81] reduce to:

for $r_e > 1$

$$[\eta]_\infty = C_1\overline{\sin^2 2\phi_1} + C_3 + fC_4[(r_e^2-1)\overline{\sin\phi_1\cos^3\phi_1} + \overline{\sin\phi_1\cos\phi_1}] \quad , \qquad [84a]$$

$$[\xi_{12}]_\infty = -\tfrac{1}{2}C_1\overline{\sin 4\phi_1} - (C_1 - C_2 + C_3)\overline{\sin 2\phi_1} - \tfrac{1}{4}f(r_e^2-1)C_4\overline{\sin^2 2\phi_1}, \qquad [84b]$$

$$[\xi_{23}]_\infty = C_1\overline{\sin 4\phi_1} + \tfrac{1}{2}f(r_e^2-1)C_4\overline{\sin^2 2\phi_1} \quad , \qquad [84c]$$

$$[\xi_{31}]_\infty = -\tfrac{1}{2}C_1\overline{\sin 4\phi_1} + (C_1 - C_2 + C_3)\overline{\sin 2\phi_1} + \tfrac{1}{4}f(r_e^2-1)C_4\overline{\sin^2 2\phi_1}, \qquad [84d]$$

and for $r_e < 1$

$$[\eta]_\infty = C_2 \quad , \qquad [\xi_{ij}]_\infty = 0 \quad . \tag{84e}$$

Thus at equilibrium a suspension of oblate spheroids ($r_e < 1$) becomes Newtonian, i.e. the viscosity is independent of G and normal stress differences vanish, with $[\eta]_\infty$ depending only on r_e and not influenced by the electric field.

On the other hand, with prolate spheroids ($r_e > 1$) the orientation distribution $p_t(\phi_1)$ at $0 < f^2 < 1$ and $t \to \infty$ for a collision-free suspension, given by [54], is an oscillating function, so that $[\eta]_\infty$ and $[\xi_{ij}]_\infty$ will continue to oscillate indefinitely with frequency $2/T_1$ and known amplitude. When particle interactions are allowed so that the time-independent orientation distribution $p_\infty(\phi_1)$ given by [65] is established, the steady values $[\eta]_\infty$ and $[\xi_{ij}]_\infty$ can be evaluated by taking the average orientation factors obtained by substituting $p_\infty(\phi_1)$ in integrals of the type [83]. The results are

$$\overline{\sin^2 2\phi_1} = \int_0^{2\pi} \sin^2 2\phi_1 p_\infty(\phi_1) d\phi_1 = 2 r_e Y_1 Y_2^{-2} \tag{85a}$$

$$\overline{\sin\phi_1 \cos^3\phi_1} = \int_0^{2\pi} \sin\phi_1 \cos^3\phi_1 p_\infty(\phi_1) d\phi_1 = f r_e (1 + r_e\sqrt{1 - f^2}) Y_2^{-2} \tag{85b}$$

$$\overline{\sin 2\phi_1} = \int_0^{2\pi} \sin 2\phi_1 p_\infty(\phi_1) d\phi_1 = 2 f r_e Y_2^{-1} \tag{85c}$$

$$\overline{\sin 4\phi_1} = \int_0^{2\pi} \sin 4\phi_1 p_\infty(\phi_1) d\phi_1 = -4 f r_e (r_e^2 - 1) Y_2^{-2} \tag{85d}$$

where

$$Y_1 = 2r_e + (r_e^2 + 1)\sqrt{1 - f^2} \quad , \qquad [85e]$$

$$Y_2 = r_e^2 + 1 + 2r_e\sqrt{1 - f^2} \quad . \qquad [85f]$$

Substituting [85] into [84] we obtain, for $r_e > 1$ at $0 < f^2 < 1$:

$$[\eta]_\infty = (2r_eC_1 + f^2r_e^2C_4)\ Y_1Y_2^{-2} + C_3 \quad , \qquad [86a]$$

$$[\xi_{12}]_\infty = 2fr_e[-2(1 - r_e\sqrt{1 - f^2})C_1 + (C_2 - C_3)Y_2 + \tfrac{1}{4}\ C_4(r_e^2 - 1)Y_1]Y_2^{-2} \quad , \qquad [86b]$$

$$[\xi_{23}]_\infty = 4fr_e(r_e^2 - 1)[-C_1 - \tfrac{1}{4}\ C_4Y_1]\ Y_2^{-2} \quad , \qquad [86c]$$

$$[\xi_{31}]_\infty = 2fr_e[r_e(r_e + 2\sqrt{1 - f^2})C_1 - (C_2 - C_3)Y_2 + \tfrac{1}{4}\ C_4(r_e^2 - 1)Y_1]Y_2^{-2} \quad . \qquad [86d]$$

Next we consider the case $f^2 \geq 1$ for which the particle orientation ϕ_1 is uniquely determined by [33a]. Substituting [33a] into [84] yields

$$[\eta]_\infty = 4Y_3^2(C_1 + \tfrac{1}{2}\ f^2r_eC_4)(1 + Y_3^2)^{-2} + C_3 \quad , \qquad [87a]$$

$$[\xi_{12}]_\infty = 2Y_3[-2C_1 + (C_2 - C_3)(1 + Y_3^2) + \tfrac{1}{2}\ C_4f(r_e^2 - 1)Y_3](1 + Y_3^2)^{-2} \quad , \qquad [87b]$$

$$[\xi_{23}]_\infty = 4Y_3[C_1(1 - Y_3^2) - \tfrac{1}{2}\ C_4f(r_e^2 - 1)Y_3](1 + Y_3^2)^{-2} \quad , \qquad [87c]$$

$$[\xi_{31}]_\infty = 2Y_3[2C_1Y_3^2 + (C_2 - C_3)(1 + Y_3^2) + \tfrac{1}{2}\ C_4f(r_e^2 - 1)Y_3](1 + Y_3^2)^{-2} \qquad [87d]$$

where

$$Y_3 = r_e(f - \sqrt{f^2 - 1}) \quad . \qquad [87e]$$

It is easily shown that when f = 0, [86] reduces to Jeffery's result[8] for $[\eta]_\infty$ corresponding to maximum energy dissipation (i.e. for $\theta_1 = \pi/2$, $C = \infty$), and to $[\xi_{ij}]_\infty = 0$ signifying Newtonian behavior. When $f^2 > 0$ it is noted from [86] and [87] that $[\eta]_\infty$ varies with G (at constant E_o) and $[\xi_{ij}]_\infty \neq 0$, indicating permanent non-Newtonian behavior. The formulas for the steady state intrinsic viscosity $[\eta]_\infty$ given by [86a] and [87a] are equivalent to [32]-6 and [20]-5 of Chaffey and Mason[5,6] but are expressed in a different form.

Numerical values of $[\eta]_\infty$ for prolate spheroids calculated from [86a] and [87a], and $[\xi_{23}]_\infty$ from [86c] and [87c] are shown in three-dimensional plots in Fig. 8. It is seen that for a fixed r_e, e.g. $r_e = 20$, $[\eta]_\infty$ decreases slightly as f increases from zero, reaching a minimum (a cusp) at f = 1 and then increases very rapidly beyond f > 1; similarly $-[\xi_{23}]_\infty$ increases steadily from zero at f = 0 to f = 1 where it exhibits a discontinuous change in slope and then increases rapidly.

When $r_e = 1$, f = 0 and $[\eta]_\infty = 5/2$, the classical Einstein value for freely rotating spheres, independent of E_o. However if we let $r_e \to 1^+$ and adjust the ratio E_o^2/G so that f can vary upward continuously from zero, it follows from [86a] and [87a] that $[\eta]_\infty$ increases from 5/2 at f = 0 to 4 (corresponding to non-rotating spheres[25]) at f = 1, and then remains constant; this is the curve shown at $r_e = 1$ in Fig. 8a.

FIGURE 8

Three-dimensional plots of the equilibrium intrinsic viscosity $[\eta]_\infty$ (part a) and the conventional equilibrium intrinsic normal stress difference $[\xi_{23}]_\infty$ (part b) for prolate spheroids as functions of $r_e \geq 1$ and f calculated from [86] for $f \leq 1$ and [87] for $f \geq 1$. The minimum $[\eta]_\infty$ occurs at f = 1 except at $r_e = 1$ corresponding to spheres, for which $[\eta]_\infty$ increases from 5/2 to 4 at f = 1, above which it is constant. At f = 0 and/or $r_e = 1$, $[\xi_{23}]_\infty \equiv 0$ indicating Newtonian behavior. With oblate spheroids $[\xi_{23}]_\infty = 0$, and $[\eta]_\infty$ is independent of f (see text).

(a)

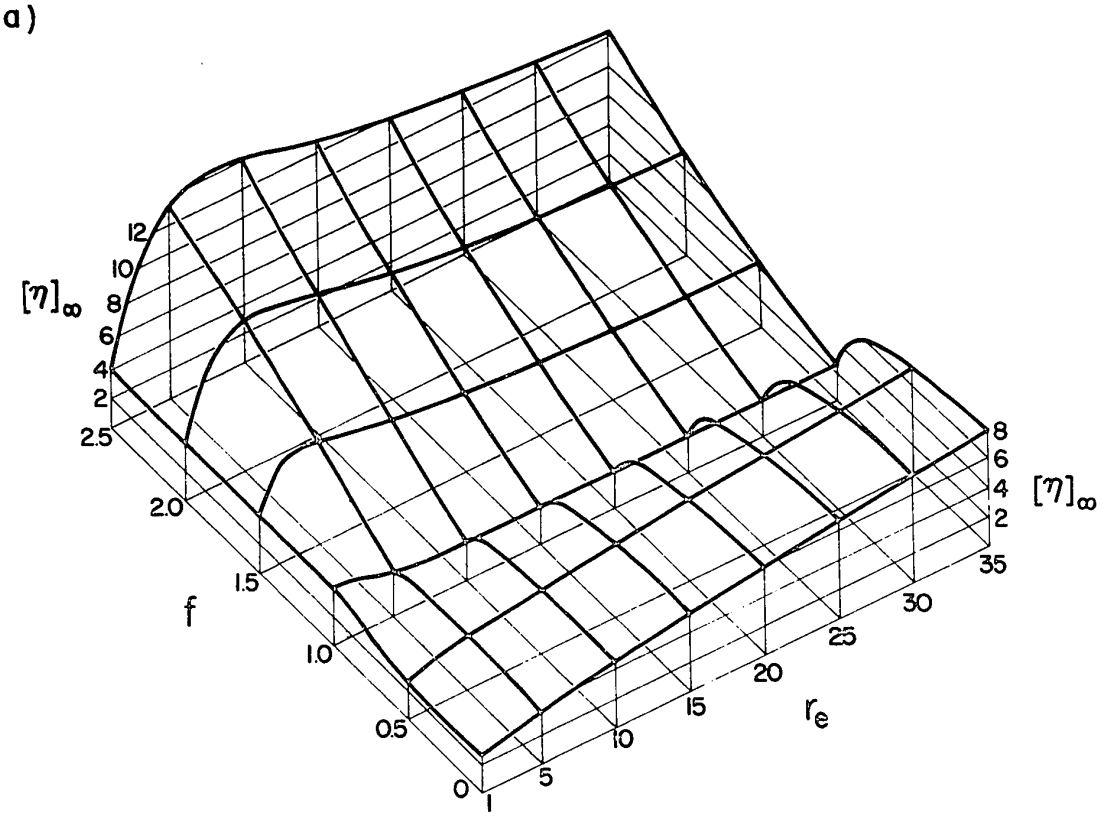
$[\eta]_\infty$
12
10
8
6
4
2
2.5
2.0
1.5
1.0
0.5
0
f
1
5
10
15
20
25
30
35
r_e
8
6
4
2
$[\eta]_\infty$

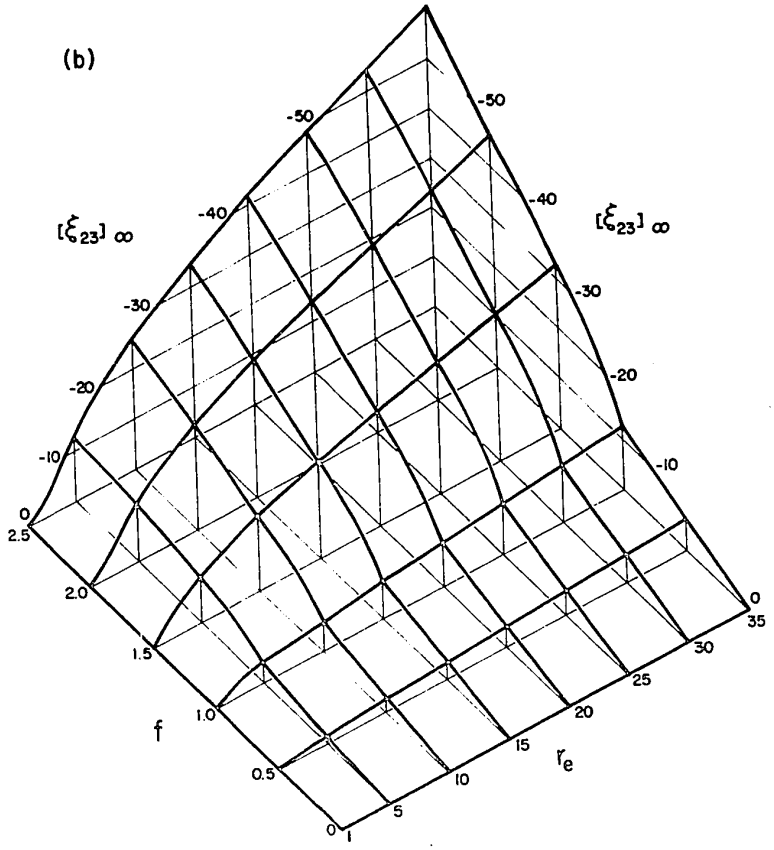
(b)
$[\xi_{23}]_\infty$
-50
-40
-30
-20
-10
0
2.5
2.0
1.5
1.0
0.5
0
f
1
5
10
15
20
25
30
35
r_e
$[\xi_{23}]_\infty$

For $f >> 1$, it is easily seen by making an expansion of $\sqrt{f^2 - 1}$ in [87e] that Y_3 is approximated by $Y_3 = r_e/2f$. Substituting this into [87a] to [87d] and taking a limit of $f \to \infty$ yields

$$\lim_{f \to \infty} [\eta]_\infty = \frac{2(2r_e^2 - 4r_e^2A + A)}{(2 - 3A)(2r_e^2 - 2r_e^2A + A)} , \qquad [88a]$$

$$\lim_{f \to \infty} [\xi_{ij}]_\infty = 0 , \qquad [88b]$$

indicating that $[\eta]_\infty$ approaches a finite asymptotic value, and that $-[\xi_{23}]_\infty$ exhibits a maximum between $1 < f < \infty$. Equation [88a] can also be obtained from [20]-5 by setting $\phi'_{1\infty} = 0$.

It should be noted that [84e] is valid all ranges of f. However, for the special case $G = 0$ (and thus f is undefined) and $t \to \infty$, oblate spheroids ($r_e < 1$) assume final orientations $\phi_{1\infty} = \pi/2$ with $p_\infty(\theta_1) = 1/\pi$ (Table III) and the intrinsic electric stress $[^E P_{32}]$ given by [78b] vanishes. If a small gradient is now applied, so that f is large and $[\eta]$ is definable, [84e] must now be replaced by $[\eta]_\infty = \frac{1}{2}(C_2 + C_3)$ and $[\xi_{ij}]_\infty = 0$ corresponding to Newtonian behavior.

To demonstrate the effect of an electric field on the microrheological and macroscopic rheological properties, Fig. 9 shows the calculated equilibrium mean projections $\bar{r}_{i\infty}$ (from [71] and Table III), the orientation $\phi'_{1\infty}$ (from [33a]),

FIGURE 9

Variations of equilibrium mean projections $\bar{r}_i$ (part a), orientation $\phi'_{1\infty}$ (part b), and intrinsic viscosity $[\eta]_\infty$ and intrinsic normal stress difference $[\xi_{23}]_\infty$ (part c) for $r_e = 100$ with f calculated from [71] and Table III, from [32a] and from [86] and [87] respectively. All quantities exhibit a discontinuous change in behavior at f = 1. At f = ∞, $[\eta]_\infty$ = 4169.0 (obtained from [88a]), the value corresponding to $\phi'_{1\infty}$ = 0, is indicated by the horizontal broken line in (c); $-[\xi_{23}]_\infty$ passes through a maximum around f = 70, corresponding to $\phi'_{1\infty}$ = 35.5°, and then decreases to $[\xi_{23}]_\infty$ = 0 at f = ∞.

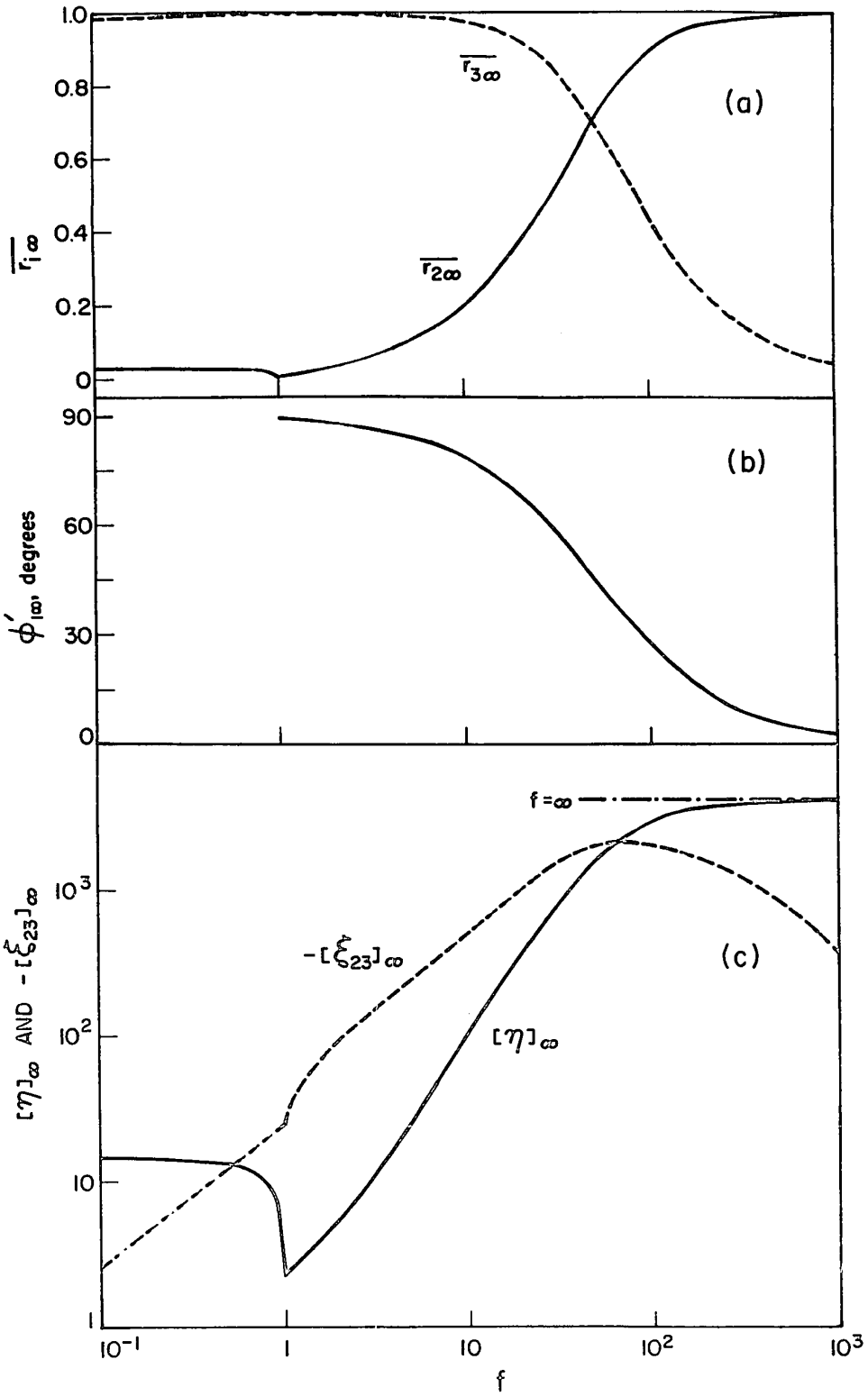
1.0
0.8
0.6
0.4
0.2
0
$\overline{r_{i\infty}}$
$\overline{r_{3\infty}}$
$\overline{r_{2\infty}}$
(a)
90
60
30
0
$\phi'_{1\infty}$, degrees
(b)
10^3
10^2
10
1
$[\eta]_\infty$ AND $-[\xi_{23}]_\infty$
f=∞
$-[\xi_{23}]_\infty$
$[\eta]_\infty$
(c)
10^{-1}
1
10
10^2
10^3
f

the intrinsic viscosity $[\eta]_\infty$ (from [86a] and [87a]) and the intrinsic normal stress difference $[\xi_{23}]_\infty$ (from [86c] and [87c]) as function of f when $r_e = 100$. As f increases from 0.1 to 1, there is little change in $\bar{r}_{i\infty}$, a small decrease in $[\eta]_\infty$ and a steady increase in $-[\xi_{23}]_\infty$. At $f = 1$, each quantity shows a sudden change of behavior. At higher f, $\bar{r}_{2\infty}$ increases and $\bar{r}_{3\infty}$ decreases, having equal values ($\bar{r}_{2\infty} = \bar{r}_{3\infty} = 0.707$) at $f = 50$ (corresponding to $\phi'_{1\infty} = 45°$), with $\bar{r}_{2\infty} \to 1$ and $\bar{r}_{3\infty} \to 0$ as $f \to \infty$; $\phi'_{1\infty}$ decreases to zero and $[\eta]_\infty$ increases to an asymptotic value (given by [88a]) about 10^2 times that for $f = 0$; $[\xi_{23}]_\infty$ exhibits its maximum around $f = 70$, then decreases to zero as $f \to \infty$. This behavior is representative of $r_e > 1$ and indicates the considerable effect of an electric field on the rheological properties of a suspension.

A general macrorheological description for all possible distributions of spheroid orientations is provided by [77] to [82]. These equations predict, in addition to effects already discussed, a number of interesting and perhaps surprising phenomena, but it is beyond the scope of this discussion to examine them in detail. Instead we draw attention briefly to the following possibilities:

(1) When $f^2 \to \infty$ and $p_t(\phi_1)$ is not symmetrical about $\phi_1 = 0$, [80a] indicates that $[\eta]$ can fall in the interval $\pm \infty$. This means that in transient states and at finite concentrations the suspensions may have any viscosity, positive, negative or zero.

(2) When $G = 0$ (and f and η are undefined), [77] indicates that the macroscopic stresses due to the electric field do not vanish when the orientations are not isotropic. Thus there are electrically generated shear stresses which can induce electrohydrodynamic flows. These flows can also exist when $f^2 \to \infty$ and are responsible for the negative viscosities mentioned above.

Finally, from the similarity between electric and magnetic field theory, we show in the Appendix how the present theory can be extended to a magnetic field.

REFERENCES

1. This thesis, Chapter V.
2. Demetriades, S.T., J. Chem. Phys., 29, 1054 (1958).
3. Allan, R.S. and Mason, S.G., Proc. Roy. Soc., (London) A267, 62 (1962).
4. Chaffey, C.E. and Mason, S.G., J. Colloid Sci., 19, 525 (1964).
5. Chaffey, C.E. and Mason, ibid, 20, 330 (1965).
6. Chaffey, C.E. and Mason, S.G., J. Colloid Interface Sci., 27, 115 (1968).
7. This thesis, Chapter II.
8. Jeffery, G.B., Proc. Roy. Soc. (London), A102, 161 (1922).
9. Peterlin, A. and Stuart, H.A., Z. Phys., 112, 129 (1939).
10. Benoit, H., Ann. Phys., 6, 561 (1951).
11. Ikeda, S., J. Chem. Phys., 38, 2839 (1963).
12. Stratton, J.A., Electromagnetic Theory, McGraw-Hill, New York (1941).
13. Jones, R.C., Phys. Rev., 68, 93 (1945).
14. Forgacs, O.L. and Mason, S.G., J. Colloid Sci., 14, 457 (1959).
15. Sorrentino, M. and Mason, S.G., unpublished results.
16. Gutmann, F., Rev. Modn. Phys., 20, 457 (1948).
17. Mathias, B.T., Science, 113, 591 (1951).
18. Zwikker, C., Physical Properties of Solid Materials, Pargamon Press, New York (1954).
19. Trevelyan, B.J. and Mason, S.G., J. Colloid Sci., 6, 354 (1951).

20. Goldsmith, H.L. and Mason, S.G., J. Fluid Mech., 12, 88 (1962).

21. This thesis, Chapter III.

22. Anczurowski, E. and Mason, S.G., J. Colloid Interface Sci., 23, 522 (1967).

23. Anczurowski, E. and Mason, S.G., ibid, 23, 533 (1967).

24. Cox, R.G. and Brenner, H., Chem. Eng. Sci., 26, 65 (1971).

25. Brenner, H., Phys. Fluid, 1, 338 (1958).

CHAPTER V

ORIENTATION DISTRIBUTION OF CYLINDERS IN SHEAR AND ELECTRIC FIELDS

ABSTRACT

Transient orientation distributions of electrically conductive rods and discs in suspensions subjected to combined shear and electric fields were determined experimentally. In sub-critical electric fields the orientation distribution oscillated at a frequency twice that of the individual particles rotation; the orbit distribution drifted towards higher orbits with rods and lower orbits with discs, so that eventually the axes of rods and the faces of discs lay in planes normal to the vorticity axis. In super-critical fields the orientation distributions no longer oscillated but changed gradually as each particle moved to a steady orientation. Monotonic changes in orientation distributions occurred in suspensions subjected to an electric field alone. All of these observations were as predicted from theory. The influence of electric fields on such rheological properties as the intrinsic viscosity and normal stress differences of the suspensions are discussed.

LIST OF SYMBOLS

Symbols are listed in Reference 1. The following additional symbols are used in this Chapter.

$A(t)$	=	amplitude of oscillation of $\bar{r}_2$
C_5	=	constant given by [22d]
D	=	relative amplitude given by [8]
D_r	=	rotary diffusion constant
$p_t(\phi_{im}, \kappa_1)$	=	two-dimensional probability distribution of ϕ_{im} and κ_1
$p_t(\phi_{im})$, $P(\phi_{im})$	=	probability and cumulative distribution of ϕ_{im}
r_{eH}, r_{eE}	=	hydrodynamically and electrically equivalent axis ratio
r_p	=	particle axis ratio for cylindrical particles
V	=	volume of a particle
$\Lambda(r_{eE})$	=	function defined by [17] and [19]
ν'_{ij}	=	electro-polarizability tensor
$[^E\xi_{ij}]$	=	intrinsic electric normal stress differences
τ, τ_{11}, τ_2, τ_4, τ_5	=	relaxation times for damping of oscillations of $\bar{r}_2$
ϕ_{im} $(i = 2,3)$	=	orbit parameters defined in [1]
Φ	=	function given by [2b]

1. INTRODUCTION

(a) General

In the preceding Chapter[1] we developed an *a priori* theory of the micro- and macro-rheological properties of dilute suspensions of rigid spheroids subjected to shear and electric fields, special emphasis being given to the case of electrically conductive particles with no permanent dipoles in an electric field directed normally to the velocity and vorticity of the shear flow. It was shown that the rotation of each particle depends upon the dimensionless factor

$$f = - \frac{K_2 P(q,r_e) E_o^2 (r_e^2 + 1)}{G\eta_o r_e} \qquad [1]$$

which is a measure of the relative effects of the electric field (of strength E_o in e.s.u.) and the shear field (of gradient G). When $f^2 < 1$ (designating a sub-critical electric field) the particles rotate about the vorticity axis, (the x_1-axis in Fig. 1); as a result the orientation distribution $p_t(\phi_1)$ oscillates with a frequency $2/T_1$. When $f^2 > 1$ (a super-critical field) the particle no longer executes complete rotations; instead of oscillating, $p_t(\phi_1)$ gradually approaches the delta function $\delta(\phi_1 - \phi'_{1\infty})$, the equilibrium orientation $\phi'_{1\infty}$ of all particles which is uniquely determined by r_e and f.

In this Chapter we present experimental confirmation of the equations for the rotations of single particles, for the distributions of orientations and orbits, and for the mean projections using dilute suspensions of rods ($r_e > 1$) and discs ($r_e < 1$) with initially random orientations in both sub- and super-critical fields and in an electric field alone ($G = 0$). The case when $f = 0$, corresponding to a shear flow alone, has been previously[2] described in detail.

The probability orientation distributions $p_t(\phi_1)$ at $f^2 < 1$ showed oscillations which were eventually completely damped out, in contrast to the undamped oscillations predicted from the theory for monodisperse and collision-free suspensions, so that equilibrium distributions $p_\infty(\phi_1)$ were established after a few particle rotations. The relaxation times for the damping of oscillations were measured from $\bar{r}_2$ for rods using an analytical method similar to that used at $f = 0$ [2]. The measured orientations were then used to calculate rheological properties of the suspensions from the theory using [77]-1* and [78]-1. Mechanisms of damping similar to those considered at $f = 0$ [2], and those due to the electric field are examined in Section 4.

Before presenting the experimental data and the calculations, we present some useful new relationships describing the rotational orbits.

* Equations, tables and figures from earlier papers are identified by appending the reference number; thus [77]-1 designates Equation [77] of Reference (1).

(b) Distributions of Particle Orbits

Although the constant C_o (defined in [28a]-1) determines the characteristic elliptical spiral orbit for the particle axis when $f^2 < 1$, it is convenient to use the orbit constant C (constant for an isolated particle when f = 0 and defined by [28a]-1) which now changes continuously with time. Rods move toward C = ∞ (i.e. $\theta_1 = \pi/2$) and discs toward C = 0 (i.e. $\theta_1 = 0$). The experimental results, however, are more conveniently expressed by the orbit parameters ϕ_{2m} for discs and ϕ_{3m} for rods, used previously for f = 0[2)], and defined as

$$\phi_{2m} = \tan^{-1} C\, r_e \quad , \qquad \phi_{3m} = \tan^{-1} C \quad , \qquad [2]$$

ϕ_{2m}, ϕ_{3m} being equivalent to θ_1 at $\phi_1 = \pi/2$ and 0 respectively (see Fig. 1). From the equations in Table I-1, C and C_o are related by

$$C = \frac{C_o}{\sqrt{1 - f^2}}\, \Phi^{\frac{1}{2}} \exp\left[\frac{-K_2 P(q, r_e) E_o^2}{\eta_o}\, t\right] \qquad [3a]$$

where

$$\Phi = 1 + f^2 \cos\left(\frac{4\pi t}{T_1} + 2\kappa_1\right) + f\sqrt{1 - f^2}\, \sin\left(\frac{4\pi t}{T_1} + 2\kappa_1\right) \quad . \qquad [3b]$$

The probability distribution of orbit constants at f = 0 corresponding to a random orientation of particles,

FIGURE 1

Coordinate systems: x_1, x_2, x_3 axes; Eulerian angles θ_1, ϕ_1 and θ_2, ϕ_2 with x_1- and x_2-axis as the respective polar axes. The orbit parameters ϕ_{2m} and ϕ_{3m} are identical for the orbit described by the end of the axis of revolution of a spheroid in a shear flow alone (shown by heavy solid line for $r_e > 1$ and heavy broken line for $r_e < 1$). The electric field (of strength E_o) is applied along the x_2-axis.

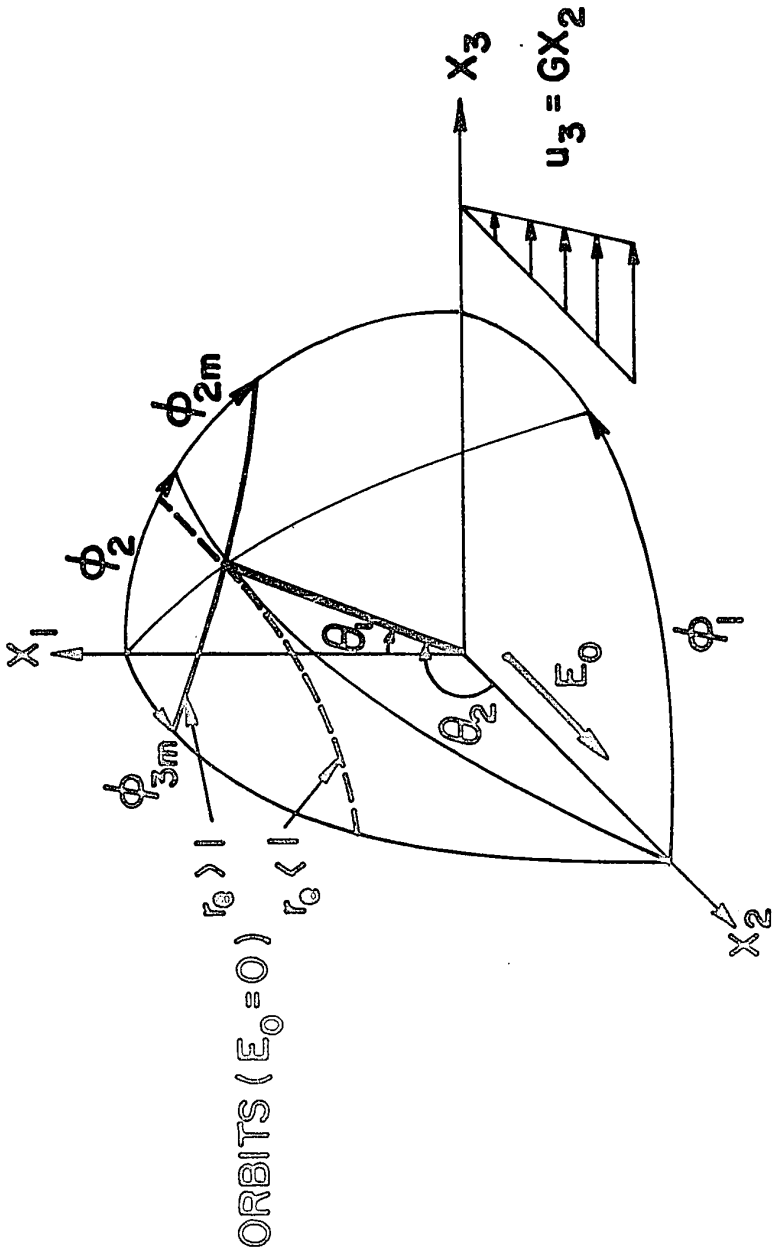
X_3
$u_3 = GX_2$
ϕ_{2m}
ϕ_2
X_1
θ_1
θ_2
E_0
ϕ_1
ϕ_{3m}
$r_0 > 1$
$r_0 < 1$
X_2
ORBITS ($E_0 = 0$)

denoted by $p_E(\xi)$ ($\xi = C, \phi_{2m}, \phi_{3m}$), has been given previously[2], and is nearly constant when $p_E(\phi_{3m})$ is used for rods and $p_E(\phi_{2m})$ for discs except near $\phi_{2m}, \phi_{3m} = 0°$ (see Table I-2).

We now consider the transient distribution $p_t(\phi_{im})$ when shear and electric fields are applied to a suspension of initially randomly oriented particles. The probability distribution $p(C_o,\kappa_1)$ given by [57]-1 may be converted to the probability $p_t(\phi_{im},\kappa_1)$ with $-\pi/2 \leq \phi_{im} \leq \pi/2$ using the identity:

$$p_t(\phi_{im},\kappa_1)d\phi_{im} \equiv p(C_o,\kappa_1)dC_o \quad . \qquad (i = 2,3) \qquad [4]$$

Substitution of the partial derivative $(\partial C_o/\partial \phi_{im})$ obtained from [2] and [3a] into [4] yields

$$p_t(\phi_{2m},\kappa_1) = \frac{r_e\sqrt{1-f^2}\,\Phi^{\frac{1}{2}}\sin\phi_{2m}\exp\left[\frac{-2K_2P(q,r_e)}{\eta_o}E_o^2t\right]}{4\pi\left\{r_e^2\Phi\cos^2\phi_{2m}+\Psi_1\sin^2\phi_{2m}\exp\left[\frac{-2K_2P(q,r_e)}{\eta_o}E_o^2t\right]\right\}^{3/2}} \quad , \qquad [5a]$$

$$p_t(\phi_{3m},\kappa_1) = \frac{r_e\sqrt{1-f^2}\,\Phi^{\frac{1}{2}}\sin\phi_{3m}\exp\left[\frac{-2K_2P(q,r_e)}{\eta_o}E_o^2t\right]}{4\pi\left\{\Phi\cos^2\phi_{3m}+\Psi_1\sin^2\phi_{3m}\exp\left[\frac{-2K_2P(q,r_e)}{\eta_o}E_o^2t\right]\right\}^{3/2}} \qquad [5b]$$

where Ψ_1 and Φ is given by [47]-1 and [3b] respectively. The probability distribution $p_t(\phi_{im})$ may be obtained from

the integral:

$$p_t(\phi_{im}) = \int_0^{2\pi} p_t(\phi_{im},\kappa_1)d\kappa_1 \quad . \qquad (i = 2,3) \qquad [6]$$

When $f = 0$, as noted previously[1], $C = C_o$ and $\kappa = \kappa_1$, so that the probability $p_t(\phi_{im})$ given by [6] reduces to $p_E(\phi_{im})$ which is constant at all times in a collision-free suspension[2]. In other words, $p_E(\phi_{im})$ corresponds to initially randomly oriented particles which rotate in a constant orbit in a shear flow ($f = 0$). The cumulative distribution $P_t(\phi_{im})$, by definition, is obtained by the integration:

$$P_t(\phi_{im}) = \int_0^{\phi_{im}} p_t(\phi_{im})d\phi_{im} = \int_0^{\phi_{im}}\int_0^{2\pi} p_t(\phi_{im},\kappa_1)d\kappa_1 d\phi_{im} \; . \qquad [7]$$

In general, analytical solutions of [6] and [7] are not available for $f^2 > 0$; $P_t(\phi_{im})$ is evaluated by numerical integration with the results given later.

2. EXPERIMENTAL

Experiments were made in a Couette apparatus[3] consisting of two stainless steel counter-rotating concentric cylinders, electrically insulated from one another to allow the application of an electric field across the annular gap (gap width

1.88 cm) in which shear flow occurred. An electric field was applied to the outer cylinder using a 60Hz a.c. power supply (0 to 25 KV) with the inner cylinder grounded. The electric field strength E_o (in e.s.u.) was calculated, taking wall curvature into account, from the peak-to-peak potential differences between two cylinders.

Electrically conductive rods of nearly uniform length were made by microtoming[2] Aℓ-coated Nylon monofilament of diameter 175μ. Discs were obtained by passing a polyester laminated Aluminium tape (with the metal film sandwiched between two layers of polyester) through an IBM punching machine[2]. The complications arising from the structure of the discs are discussed later. Two Newtonian suspending media were used: Castor oil AA and Pale-4-oil, the density of which was matched to that of particles by adding tetrabromoethane; no appreciable sedimentation was observed over a 24 hr. period. Properties of the suspensions used are listed in Table I, including values of standard deviation in r_e from the mean of the particles resulting from an unavoidable spread in particle dimensions caused by the methods of preparing the particles[2].

The viscosities η_o of the suspending media were measured in a bob and cup viscometer (Rheomat 15, A.G. Epprecht, Zurich). The dielectric constants K_2 of the media were measured by the substitution method using a Balsbough dielectric cell 2TN 50 and a General Radio capacitance bridge 716-C at 10 k Hz. All experiments were conducted in

TABLE I

Properties of Suspensions

	RODS		DISCS
Material	Aℓ-coated Nylon [a]		Polyester laminated Aℓ [b]
Diameter (μ)	175		1172
Length (μ)	900	870 [c]	95
r_p	5.14	4.96	0.081
$\bar{r}_e$ [d]	4.43 (4.2)	3.96 (4.8)	0.155 (2.6)
Medium	Castor oil AA [e] + $C_2H_2Br_4$		Pale-4-oil [f] + $C_2H_2Br_4$
η_o (poise)	9.9		15.5
K_2	4.5		6.9

a) Coating by National Research Co., Cambridge, Mass.

b) Chase-Foster, East Providence, R.I.

c) Rods used in Experiment III (Table II)

d) Mean equivalent axis ratio obtained from the measured period of rotation in shear flow by means of the relation $T = 2\pi(r_e + r_e^{-1})/G$ (Table I-1) and the bracketed values are percent standard deviations $\sigma/\bar{r}_e$ x 100 from the mean $\bar{r}_e$.

e) Fisher Scientific Co.

f) Baker Castor Oil Co., Bayonne, N.J.

TABLE II

Experimental Conditions

	RODS			DISCS		
Experiment Number	I $f^2 < 1$	II $f^2 > 1$	III $G = 0$	IV $f^2 < 1$	V $f^2 > 1$	VI $G = 0$
N ($m\ell^{-1}$)	30.0		50.0	20.0		
c($m\ell/m\ell$) x 10^2	0.065		0.105	1.75		
G (sec^{-1})	0.43	0.44	0	0.74	1.37	0
E_o (statvolts/cm)	1.63	3.26	2.14	1.75	4.62	1.11
T_i (sec) a)	72.7 (i = 1)	95.6 (i = 2)	95.2 (i = 3)	58.0 (i = 1)	45.0 (i = 2)	208.1 (i = 3)
f b)	0.32	1.22	-	-0.25	-1.21	-
$P(q,r_e)_{meas.}$ c)	-0.0242	-0.0238	-0.0160	0.0212	0.0263	0.0303
$P(q,r_e)_{calc.}$ d)	-0.0221	-0.0221	-0.0216	0.0201	0.0201	0.0201
$E_{crit.}$ e) (statvolts/cm)	2.90	2.97	-	3.43	4.20	-

a) Measured period of rotation for T_1; calculated from f for T_2; and calculated from the experimental conditions and measured $P(q,r_e)$ for T_3.

b) Calculated from measured T_1 ($f^2 < 1$) and from measured $\phi'_{1\infty}$ ($f^2 > 1$).

c) Calculated from f using [30]-1; for G = 0 from the slope of line $\log_{10}\tan\phi_1$ vs t using equation in Table I-1.

d) Calculated from [27b]-1 using r_e.

e) Calculated from [37]-1 using r_e, G, and measured $P(q,r_e)$

FIGURE 2

Tracings of photographs showing the orientation distribution of rods for initially random orientation at t = 0 (I-1 to III-1) and near equilibrium (I-2 to III-2). The Roman numerals correspond to the experimental conditions listed in Table II. The x_1-axis along which the photographs were made, is normal to the plane of the page. The orientation ϕ_1 and projected length of each particle was measured from which all of the orientation parameters were calculated[2].

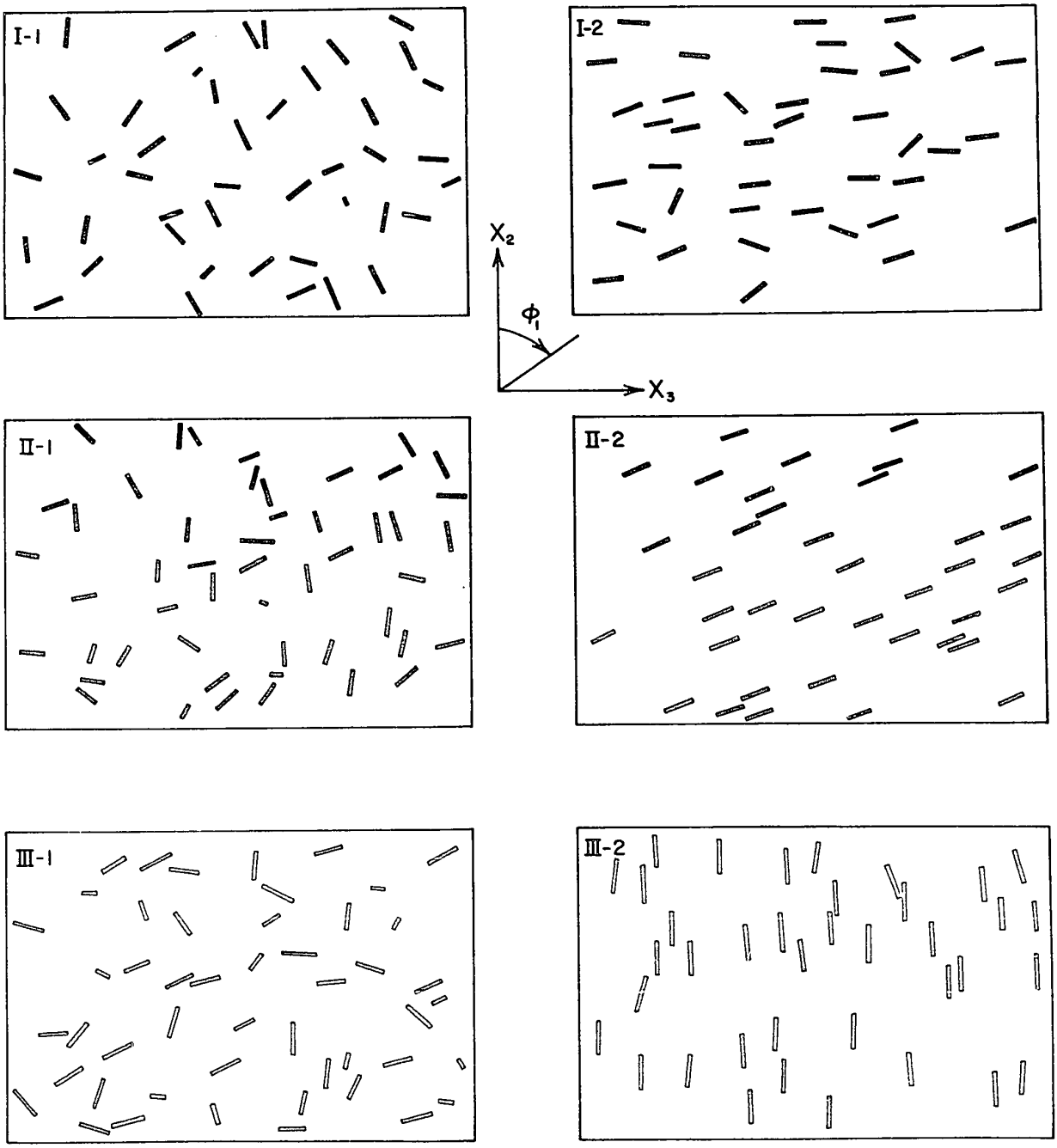
I-1
I-2
X2
Φ1
X3
II-1
II-2
III-1
III-2

a thermostatically controlled room at 21 ± 1°C.

The procedures and subsequent frame-by-frame analysis of photographs of the particles were the same as with shear fields alone[2], but now using the combinations of shear rate G and electric field strength E_o listed in Table II. Typical examples of projections of rods traced from series of photographs at each time are shown in Fig. 2. To obtain the distributions of particle orientations over 100 to 200 particles, it was necessary to photograph several different fields since each contained less than 40 particles. Photographic analysis yielded the orientations θ_1 and ϕ_1 from which r_i, S_{ij}, ϕ_2 were calculated directly using the definition equations[1]. The orbit constant C and ϕ_{im} were then calculated from the measured θ_1 and ϕ_1 using $\bar{r}_e$ obtained from the rotation of particles in shear flow alone by means of the equation in Table I-1 and [2]. All theoretical calculations were made using $\bar{r}_e$ and $P(q,r_e)$ obtained experimentally as described in the next section. For convenience the conditions of the various experiments, which are subsequently identified by Roman numerals, are listed in Table II.

3. RESULTS

(a) Sub-critical Field: $f^2 < 1$

The tracings of one end of the axis of revolution of a rod and a disc on the x_2x_3-plane in a sub-critical field

FIGURE 3

Projections of ends of unit length of axis of revolution of particles on the x_2x_3-plane in sub-critical fields.

(a) Elliptical spiral for a rod $r_e = 4.43$ with initial $C = 0.19$, indicated by the large closed circle, at $G = 0.4$ sec^{-1} and $E_o = 0.98$ statvolts/cm (corresponding to $f = 0.23$), the locus being drawn to fit the experimental points. The rotational orbit drifts to the predicted $C = \infty$.

(b) A disc $r_e = 0.155$ with initial $C = 38.0$ at $G = 0.4$ sec^{-1} and $E_o = 1.07$ statvolts/cm (corresponding to $f = 0.24$), drifting in the direction of diminishing C and (not shown) eventually reaching the predicted value $C = 0$.

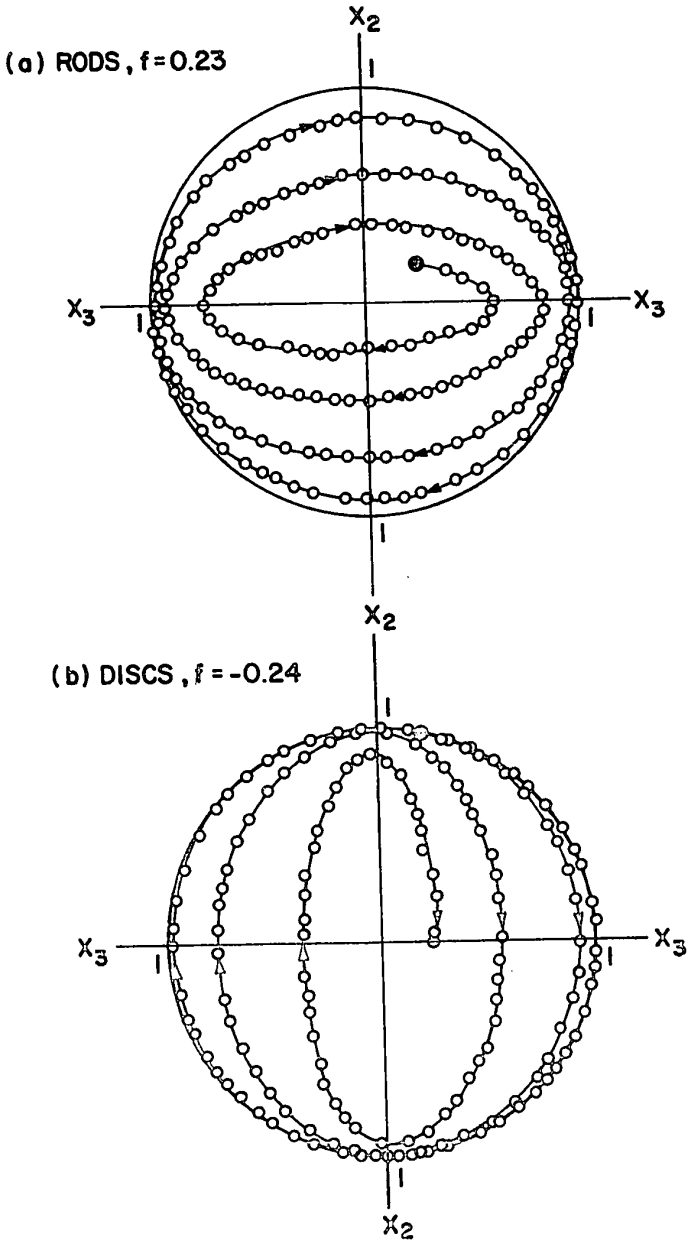
(a) RODS, f=0.23
X2
1
X3
1
X3
1
1
(b) DISCS, f = -0.24
X2
1
X3
1
X3
1
1
X2

are shown in Fig. 3. Starting at the points shown by the large solid circles, the locus of a particle end was an elliptic spiral as predicted by the theory[1]. The rod drifted to $C = \infty$ ($\phi_{2m} = \phi_{3m} = 90°$), finally rotating in the x_2x_3-plane so that the locus was a circle of diameter equal to the length of the rod. For the disc it moved toward $C = 0$ ($\phi_{2m} = \phi_{3m} = 0°$) and eventually lay with its face parallel to the x_2x_3-plane and spinning about its axis with constant angular velocity $G/2$. This predicted behavior was also observed with single rods by Allan and Mason[4], and for single discs by Chaffey and Mason[5]. The factor f was calculated from the measured period of rotation T_1 between $\phi_1 = 0°$ and 360° by means of [29]-1 and the parameter $P(q,r_e)$ by means of [30]-1; values are listed in Table II. Reasonably good agreement with the value of $P(q,r_e)$ calculated from [27b]-1 was obtained. As expected from the rotation of single particles (Fig. 3), progressive drifts in the distribution of orbits were observed in Expts I and IV as illustrated in Table III and Fig. 4. Reasonably good agreement with the values calculated by numerical integration of [7] using [5], shown by the solid lines in Fig. 4, was obtained. The initial distributions $P_o(\phi_{im})$ were close to $P_E(\phi_{im})$ corresponding to random orientation. It is clearly seen in Fig. 4 that the orbits of rods shifted toward $\phi_{3m} = 90°$ and those of discs toward $\phi_{2m} = 0°$. At $t/T_1 = 2$, nearly 70% of rods had $\phi_{3m} > 80°$ and 80% of discs had $\phi_{2m} < 20°$.

TABLE III

Measured Orbit Distributions $P_t(\phi_{im})$ for $0 < f^2 < 1$

	ϕ_{im} (deg.)	$P_E(\phi_{im})$ a)	$P_t(\phi_{im})$ t/T_1=0	0.5	1.0	1.5	2.0
	10	0.057	0.022	-	-	-	-
	20	0.167	0.132	0.012	-	-	-
RODS	30	0.287	0.253	0.037	0.011	0.021	-
	40	0.407	0.374	0.171	0.021	0.082	-
Expt.I	50	0.527	0.489	0.232	0.053	0.113	0.022
	60	0.646	0.689	0.439	0.192	0.288	0.089
(i = 3)	70	0.764	0.856	0.646	0.446	0.402	0.178
	75	0.823	0.890	0.786	0.542	0.495	0.222
	80	0.882	0.903	0.866	0.660	0.536	0.322
	85	0.941	0.953	0.933	0.800	0.721	0.500
	90	1.000	1.000	1.000	1.000	1.000	1.000
	5	0.022	0.009	0.037	0.075	0.149	0.226
	10	0.072	0.029	0.157	0.257	0.455	0.603
DISCS	15	0.129	0.071	0.222	0.450	0.619	0.771
	20	0.188	0.139	0.296	0.564	0.762	0.875
Expt.IV	30	0.306	0.263	0.509	0.743	0.891	0.937
	40	0.423	0.402	0.648	0.881	0.940	0.982
(i = 2)	50	0.540	0.559	0.796	0.911	0.950	0.991
	60	0.655	0.716	0.898	0.941	0.970	-
	70	0.770	0.864	0.954	0.950	0.980	-
	80	0.885	0.944	0.963	0.970	0.990	-
	90	1.000	1.000	1.000	1.000	1.000	1.000

a) Calculated from the equations in Table I-2

FIGURE 4

Changes of distributions of orbit parameters $P_t(\phi_{3m})$ for rods (Expt. I, $f = 0.32$) and $P_t(\phi_{2m})$ for discs (Expt. IV, $f = -0.25$) in sub-critical electric fields at various times t/T_1. The solid lines were calculated by numerical integration of [7] for an initially isotropic suspension using the measured f value. The broken lines are drawn to fit experimental points.

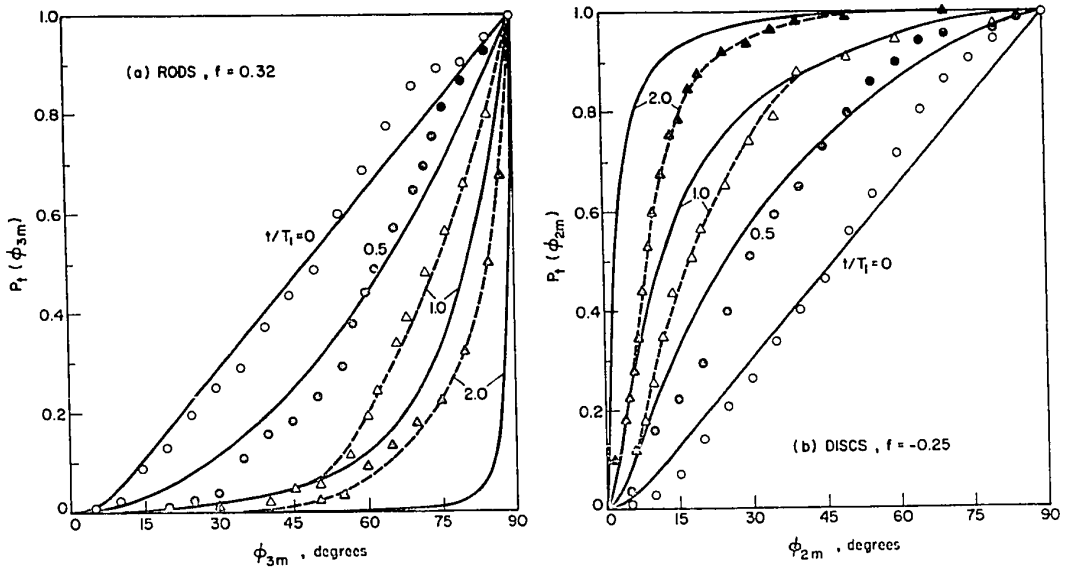
(a) RODS , f = 0.32
t/T1=0
0.5
1.0
2.0
P1 (φ3m)
φ3m , degrees
(b) DISCS , f = -0.25
P1 (φ2m)
φ2m , degrees

The probability distributions $p_t(\phi_1) = dP_t(\phi_1)/d\phi_1$ obtained from the slope of smoothed curve of experimental distributions $P_t(\phi_1)$ versus ϕ_1 are shown in Fig. 5 using polar plots, the radial coordinate being $\sqrt{p_t(\phi_1)}$. Initially the experimental points were close to the circle of radius $1/\sqrt{2\pi}$ corresponding to random orientations. When shear and electric fields were applied the probability $p_t(\phi_1)$ for rods showed a maximum at $\phi_1 = 70°$ and a minimum at $\phi_1 = 160°$ at $t/T_1 = 0.08$ [Fig. 5(ii)] and then the maximum crossed $\phi_1 = 90°$ into the second quadrant [Fig. 5(iii)]. Similar behavior was shown by discs (Expt. III), but the maxima were shifted by 90°. At $t/T_1 = 0.5$, $p_t(\phi_1)$ assumed nearly an initial distribution for rods, but not so for discs for reasons discussed later. Although not shown in Fig. 5, in the second half-rotation $p_t(\phi_1)$ continued to change as in the first half, and thus oscillated with frequency $2/T_1$. However the oscillations of $p_t(\phi_1)$ were damped and the steady (equilibrium) distribution $p_\infty(\phi_1)$ was established after a few particle rotations, as shown for the rods in Fig. 5(v) after 5 rotations. For discs ϕ_1 became indeterminate since all assumed the orbit $C = 0$ (i.e., their faces lay in the x_2x_3-plane). The experimental points for rods are in good agreement with the theoretical values of $p_\infty(\phi_1)$ calculated from [65]-1. It should be noted that at equilibrium the maximum probability occurred at $\phi_1 = 86°$ indicating that the electric torque acting on the rods shifts the position of minimum angular velocity $(d\phi_1/dt)$ below $\phi_1 = 90°$ (the angle

FIGURE 5

Polar diagrams of probability orientation distributions $p_t(\phi_1)$ versus ϕ_1 (the radial coordinate being $\sqrt{p_t(\phi_1)}$ in order to decrease the axis ratio of resultant envelops) for rods (open circles, Expt. I, f = 0.32) and for discs (closed circles, Expt. IV, f = -0.25) in sub-critical fields at various times (i to iv). The solid lines are $\sqrt{p_t(\phi_1)}$ calculated from [54]-1 for an initially isotropic and collision-free suspension using the measured f value. The equilibrium for rods at $t/T_1 = 5$, is shown in (v) where the equilibrium values $\sqrt{p_\infty(\phi_1)}$ calculated from [65]-1 are shown by the solid line.

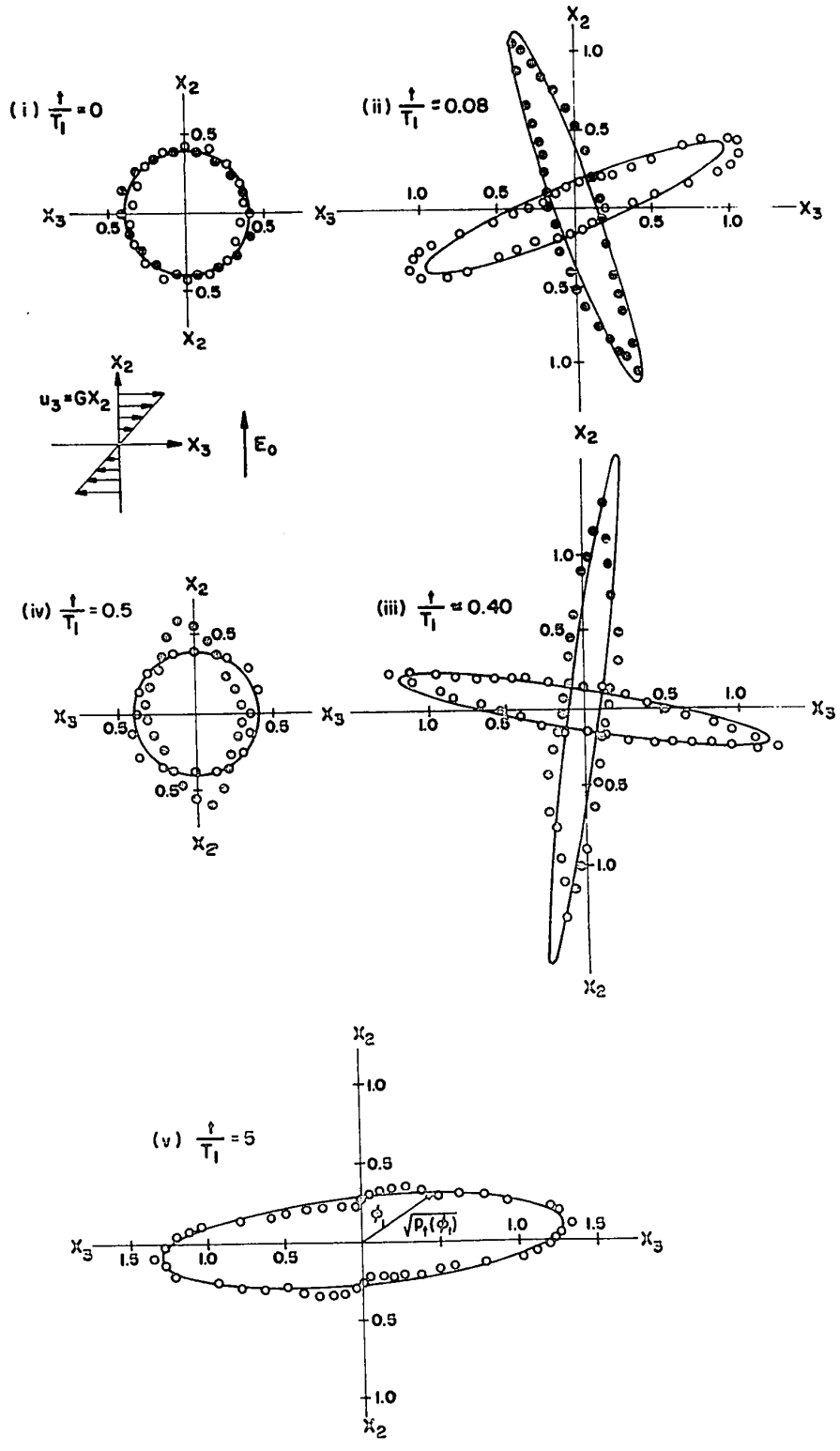
(i) $\frac{t}{T_1}=0$
(ii) $\frac{t}{T_1}=0.08$
(iii) $\frac{t}{T_1}\simeq 0.40$
(iv) $\frac{t}{T_1}=0.5$
(v) $\frac{t}{T_1}=5$
$u_3=GX_2$
E_0
X_2
X_3
0.5
1.0
1.5
ϕ_1
$\sqrt{P_1(\phi_1)}$

of minimum angular velocity at f = 0) as predicted by the theory[1].

As with the case f = 0[2], the oscillatory behavior of the orientation distributions is displayed more clearly by the mean projections $\bar{r}_2$ for rods and $\bar{S}_{12}$ for discs. As shown in Fig. 6, $\bar{r}_2$ (= 0.548 initially) of rods decreased to a minimum (= 0.102) at $t/T_1 = 0.32$, then increased to 0.596 at $t/T_1 = 0.5$, thus showing oscillations with frequency $2/T_1$ which then became damped. The amplitude A(t) of each oscillation was determined for each quarter period of rotation (see [30]-2) and was then compared with the amplitude obtained from the theoretical calculation of $\bar{r}_2$ from [68b]-1 as the ratio:

$$D = \frac{A(t)_{meas.}}{A(t)_{calc.}} \quad . \qquad [8]$$

Values of D for rods obtained in this way are plotted as closed circles in Fig. 6a. The relaxation time τ/T_1 for the damped oscillation of $\bar{r}_2$ was taken as the time at which D decays to 1/e as indicated by the arrow in Fig. 6a, so that for Expt. I

$$\tau/\bar{T}_1 = 1.73 \quad . \qquad [9]$$

Similar damping of oscillations of $\bar{r}_1$ and $\bar{r}_3$ were also observed, and in Expt. I each $\bar{r}_i$ reached equilibrium at $t/T_1 = 5$, at which $\bar{r}_1 = 0.019$, $\bar{r}_2 = 0.314$ and $\bar{r}_3 = 0.880$; these are in good agreement with the theoretical values

FIGURE 6

Mean projection length $\bar{r}_2$ for rods (Expt.I, f = 0.32) and mean projection area $\bar{S}_{12}$ for discs (Expt. IV, f = -0.25) in sub-critical fields. The solid lines are theoretical values calculated by numerical integration of [68]-1 for collision-free suspensions. The closed circles in (a) are the relative amplitudes D obtained from the measured and calculated amplitudes of oscillations of $\bar{r}_2$ and the broken lines are drawn to fit these points. The relaxation time τ/T_1 (= 1.73) at which D is reduced to 1/e is indicated by the arrow.

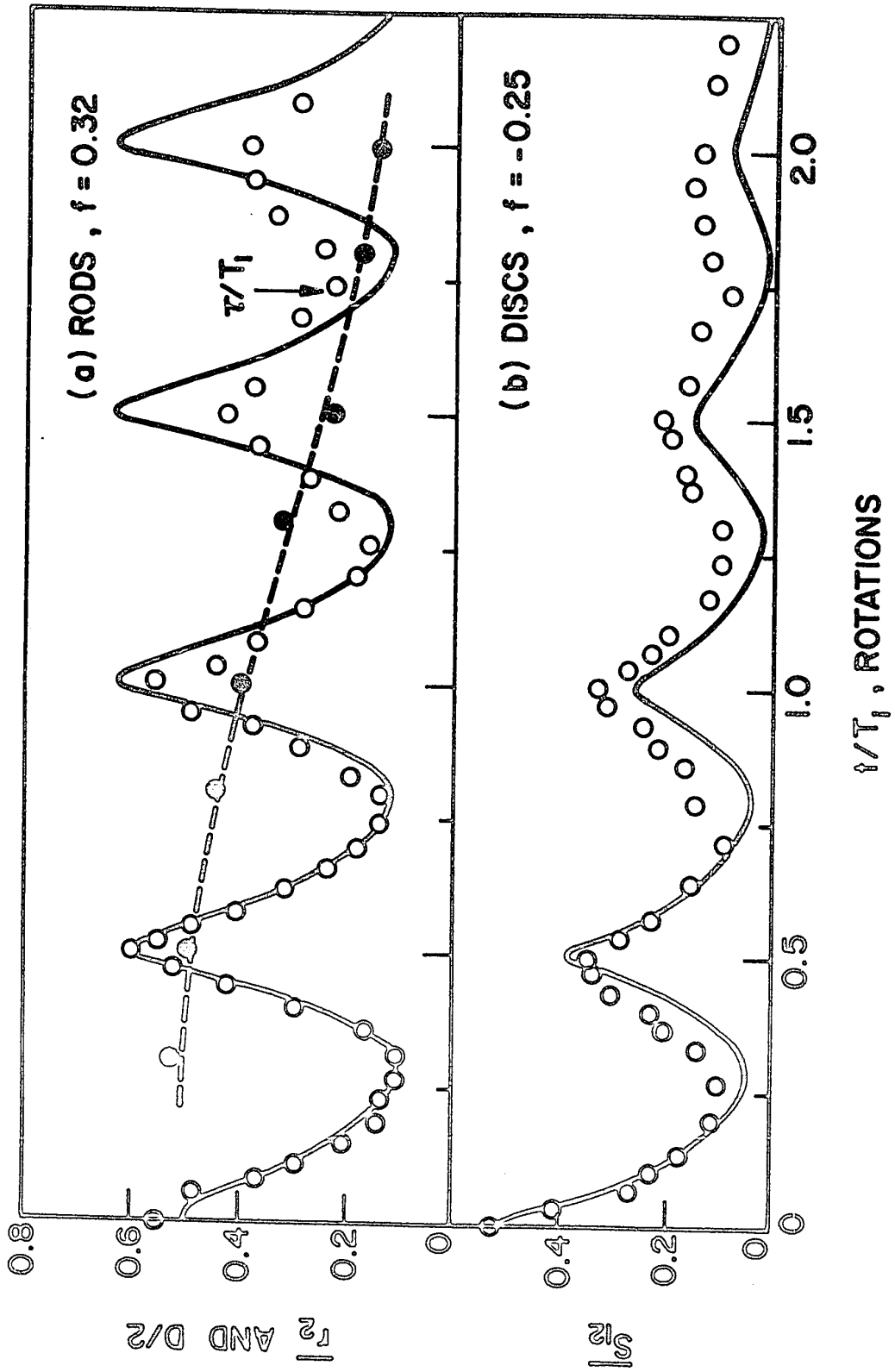
(a) RODS , f = 0.32
(b) DISCS , f = -0.25
τ/T1
0.8
0.6
0.4
0.2
0
0.4
0.2
0
0.5
1.0
1.5
2.0
t/T1 , ROTATIONS
r2 AND D/2
S12

($\bar{r}_{1\infty} = 0$, $\bar{r}_{2\infty} = 0.325$, $\bar{r}_{3\infty} = 0.895$) calculated from [71]-1.

Damped oscillations of frequency $2/T_1$ were also exhibited by $\bar{S}_{ij}$ of discs, as illustrated by $\bar{S}_{12}$ in Fig. 6b. $\bar{S}_{23}$ approached an equilibrium value of unity, and $\bar{S}_{12}$ and $\bar{S}_{13}$ equilibrium values of zero, indicating that all discs drifted toward the lower orbits and eventually lay in the x_2x_3-plane. Since the calculated $\bar{S}_{12}$ (shown by the solid line in Fig. 6b) obtained from [68c]-1 also shows a damped oscillation (i.e., $A(t)_{calc.}$ decreased asymptotically to zero), it is impractical to estimate the relaxation time for this case.

(b) Super-critical Field: $f^2 > 1$

In super critical fields the particles no longer executed complete rotation about the x_1-axis; instead they gradually assumed the steady orientation $\phi'_{1\infty}$ at which the hydrodynamic and electric torques were balanced[1]. Progressive changes in $P_t(\phi_1)$ for rods (Expt.II, f = 1.22) and discs (Expt.V, f = -1.21) obtained from the measurement from the x_2x_3-projection are shown in Fig. 7, where from symmetry considerations, the range of ϕ_1 was taken between 0° and 180°. In both cases the initial distribution $P_o(\phi_1)$ was nearly a straight line corresponding to random orientation; $P_t(\phi_1)$ then changed gradually toward the steady orientation $\phi'_{1\infty}$ indicated by the vertical solid lines $\phi'_{1\infty} = 67°$ for rods and 164° for discs. The values $P(q,r_e)_{meas.}$ calculated from the measured $\phi'_{1\infty}$ using [33a]-1 and [30]-1 are listed in Table II,

FIGURE 7

Cumulative orientation distribution $P_t(\phi_1)$ versus ϕ_1 in super-critical fields for (a) rods (Expt. II, f = 1.22) and (b) discs (Expt. V, f = -1.21) at various time intervals. The solid lines are calculated from [56b]-1 using the measured f values. The solid vertical lines indicate the measured steady orientations $\phi'_{1\infty} = 67°$ for the rods and 164° for the discs; the unstable steady orientations $\phi''_{1\infty} = 83°$ (rods), 175° (discs) calculated from the measured $\phi'_{1\infty}$ are indicated by the vertical broken lines.

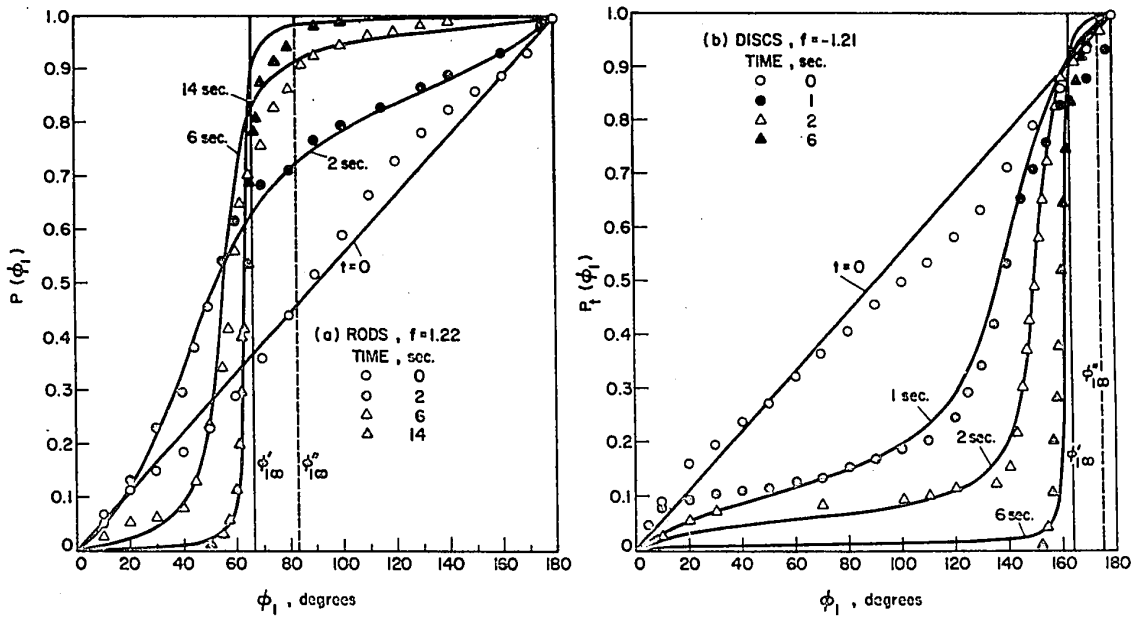
(a) RODS , f=1.22
TIME , sec.
0
2
6
14
14 sec.
6 sec.
2 sec.
t=0
P (φ1)
φ1 , degrees
(b) DISCS , f=-1.21
TIME , sec.
0
1
2
6
t=0
1 sec.
2 sec.
6 sec.
P1 (φ1)
φ1 , degrees

showing reasonably good agreement with the theoretical values calculated from [27b]-1 for $q = \infty$. The unstable steady orientations $\phi''_{1\infty}$ were calculated from [33b]-1 using f obtained from measured $\phi'_{1\infty}$ and are indicated by the vertical broken lines in Fig. 7. Good agreement of $P_t(\phi_1)$ with the theoretical calculation from [56b]-1 using f values obtained above were observed for both experiments, showing that as predicted the probability distribution $p_\infty(\phi_1)$ became the delta function $\delta(\phi_1 - \phi'_{1\infty})$.

The corresponding changes in mean projections $\bar{r}_i$ and $\bar{S}_{ij}$ obtained from the measured orientations are summarized in Table IV and are shown in Fig. 8. With rods $\bar{r}_2$ passed through a maximum and $\bar{r}_3$ a minimum in the early stages and then asymptotically approached the equilibrium values $\bar{r}_{2\infty} = \cos\phi'_{1\infty} = 0.397$ and $\bar{r}_{3\infty} = \sin\phi'_{1\infty} = 0.918$; $\bar{r}_1$ decreased monotonically to 0.082 at t = 30 sec. indicating that nearly all rods lay in the x_2x_3-plane. The experimental points are in generally good agreement with the theoretical values obtained from [68]-1 except for $\bar{r}_1$ at high t. With the discs $\bar{S}_{13}$ passed through a maximum and $\bar{S}_{23}$ a minimum in the early stages and asymptotically approached the equilibrium values $\bar{S}_{13\infty} = 0$ and $\bar{S}_{23\infty} = 1$; $\bar{S}_{12}$ gradually decreased from 0.542 initially to 0.028 at t = 60 sec., indicating that all the discs approached the predicted value $\theta_1 = 0$. Good agreement with values of $\bar{S}_{ij}$ calculated from [68]-1 were found except for $\bar{S}_{13}$ and $\bar{S}_{23}$ at large t.

TABLE IV

Measured Mean Projections, Calculated Intrinsic Viscosity and Normal Stress Difference for $f^2 > 1$

t (sec)	RODS (Expt. II, f = 1.22)					DISCS (Expt. V, f = -1.21)				
	$\bar{r}_1$	$\bar{r}_2$	$\bar{r}_3$	$[\eta]^{b)}$ calc.	$[\xi_{23}]^{c)}$ calc.	$\bar{s}_{12}$	$\bar{s}_{23}$	$\bar{s}_{13}$	$[\eta]^{b)}$ calc.	$[\xi_{23}]^{c)}$ calc.
0	0.469	0.471	0.574	3.32	-2.49	0.542	0.453	0.536	3.86	-1.12
1						0.477	0.439	0.615	4.95	-2.05
2	0.406	0.557	0.386	4.70	-2.82	0.388	0.439	0.691	4.95	-3.12
4	0.331	0.524	0.700	5.54	-4.18	0.307	0.446	0.735	4.51	-3.44
6	0.283	0.769	0.523	5.43	-4.85	0.277	0.471	0.740	4.34	-3.29
8	0.233	0.468	0.810	5.57	-5.58	0.255	0.474	0.732	4.11	-3.25
10	0.168	0.437	0.847	5.28	-5.88	0.227	0.566	0.678	4.58	-2.75
12						0.233	0.526	0.701	4.41	-2.89
14	0.163	0.407	0.876	5.18	-6.10	0.218	0.579	0.667	4.62	-2.68
16						0.205	0.582	0.653	4.61	-2.57
18	0.157	0.416	0.867	5.22	-6.29	0.197	0.629	0.613	4.81	-2.37
20						0.185	0.640	0.612	4.72	-2.39
22	0.155	0.391	0.897	5.01	-6.35					
25						0.140	0.725	0.515	5.11	-1.96
26	0.078	0.395	0.900	5.05	-6.37					
30	0.082	0.385	0.904	4.96	-6.28	0.103	0.806	0.412	5.46	-1.53
35						0.077	0.856	0.338	5.71	-1.30
40						0.060	0.877	0.300	5.82	-1.11
45						0.041	0.898	0.266	5.91	-0.92
50						0.043	0.901	0.266	6.03	-0.90
55						0.025	0.938	0.204	6.18	-0.71
60						0.028	0.940	0.203	6.22	-0.71
$\infty^{a)}$	0.000	0.397	0.918	5.17	-6.84	0.000	1.000	0.000	6.96	0.00

a) Equilibrium values are calculated from $\phi'_{1\infty}$ and θ_1 (= $\pi/2$ for rods and = 0 for discs).

b) Calculated from [80a]-I

c) Calculated from [81b]-I

FIGURE 8

Changes of mean projection lengths $\bar{r}_i$ for rods (Expt. II, f = 1.22) and mean projection areas $\bar{S}_{ij}$ for discs (Expt. V, f = -1.21) in super-critical fields calculated from the measured orientations of particles. The solid lines are theoretical values from numerical integration of [68]-1 for an initially isotropic and collision-free suspension. The steady state values $\bar{r}_{2\infty} = \cos\phi'_{1\infty} = 0.397$ and $\bar{r}_{3\infty} = \sin\phi'_{1\infty} = 0.918$ for rods are indicated by the broken lines.

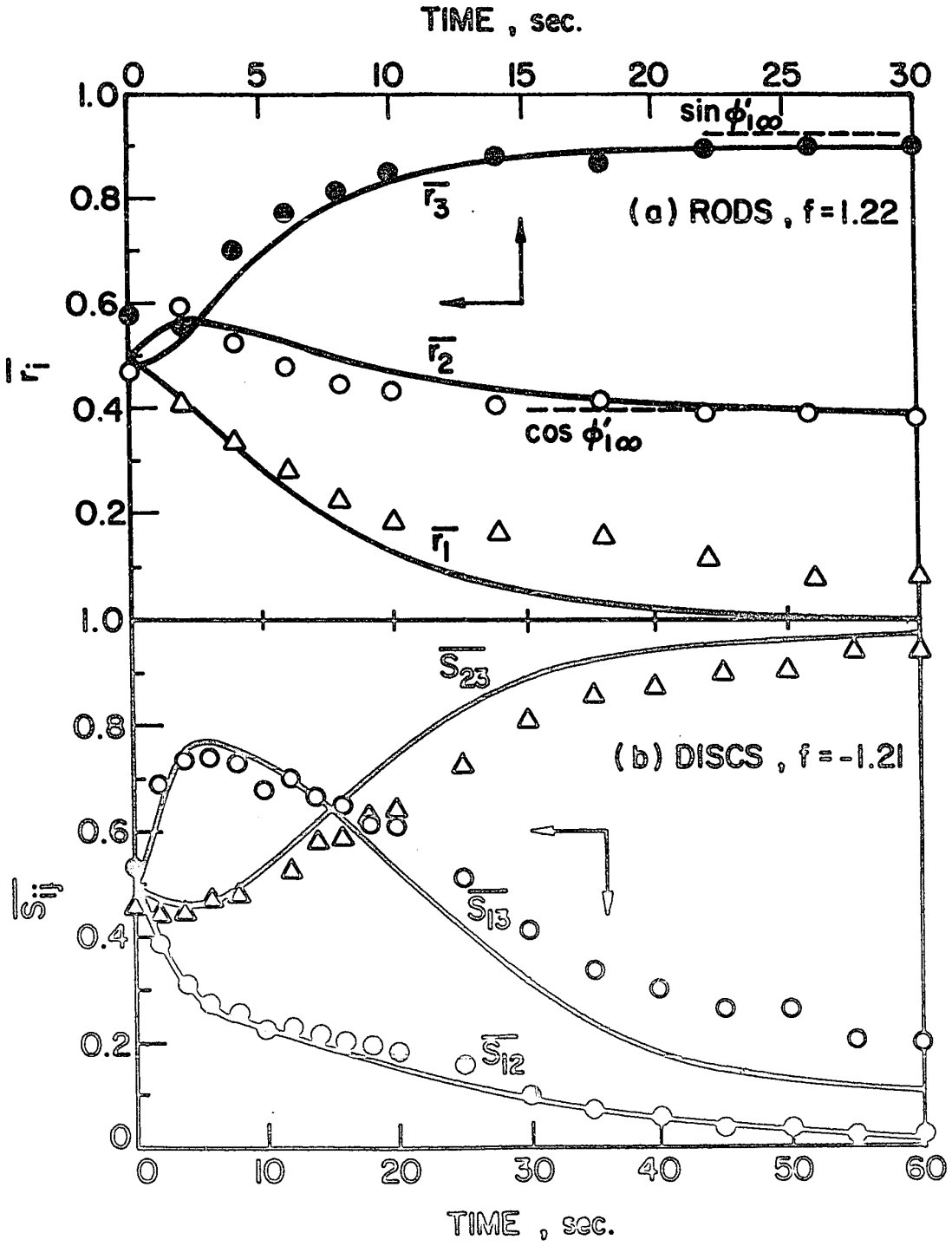
TIME , sec.
0
5
10
15
20
25
30
1.0
0.8
0.6
0.4
0.2
$\sin\phi'_{1\infty}$
$\overline{r_3}$
(a) RODS , f = 1.22
$\overline{r_2}$
$\cos\phi'_{1\infty}$
$\overline{r_1}$
$|\overline{r_i}|$
1.0
0.8
0.6
0.4
0.2
0
$\overline{S_{23}}$
(b) DISCS , f = -1.21
$\overline{S_{13}}$
$\overline{S_{12}}$
$|\overline{S_{ij}}|$
0
10
20
30
40
50
60
TIME , sec.

(c) Electric Field Alone (G = 0)

Upon applying an electric field alone, an isolated rod and disc rotated until ϕ_1 = 0° and 90° respectively. As predicted from the theory[1] and previously observed with single rods[4] and discs[5] $\log_{10}\tan\phi_1$ was linear with time t as shown in Fig. 9, where the time axis is arbitrarily chosen so that ϕ_1 = 45° when t = 0. The slope of this line yields the period T_3 and in turn the parameter $P(q,r_e)$ by use of the equation listed in Table I-1. Each line shown in Fig. 9 is calculated using the mean value of $P(q,r_e)$ from measurement on 10 different particles. The measured (algebraic) values of $P(q,r_e)$ are greater than the theoretical values for spheroids calculated from [27b]-1, and the discrepancies are greater than for finite f (Table II). These discrepancies, which were also noted by Allan and Mason[4] and Chaffey and Mason[5], may be attributed to a particle shape effect; this will be discussed later.

Monotonic changes in $P_t(\phi_1)$ of suspensions were observed as illustrated in Fig. 10, where $P_t(\phi_1)$ is plotted only in the range of ϕ_1 = 0° to 90°, since the rotation of particles is symmetrical with respect to the direction of field (the x_2-axis). Initially the particles were oriented nearly randomly with respect to ϕ_1 as shown by the diagonal line in Fig. 10. Then, to be expected from the rotation of isolated particles, all the rods moved toward ϕ_1 = 0° and the discs toward ϕ_1 = 90°. At t = 60 sec., 80% of rods had ϕ_1 = ± 10°, whereas less than 55% of discs had ϕ_1 = 90 ± 10°.

FIGURE 9

Rotations of single rods and discs in an electric field E_o = 2.14 statvolts/cm and 1.11 statvolts/cm respectively. To avoid congestion the experimental points for only 3 of 10 particles are plotted. The solid lines are calculated from the equations listed in Table I-1 using the mean values of $P(q,r_e)$. The time axis is chosen so that $\phi_1 = 45°$ at t = 0. Similar linear plots were obtained from single rods by Allan and Mason[4] and for single discs by Chaffey and Mason[5].

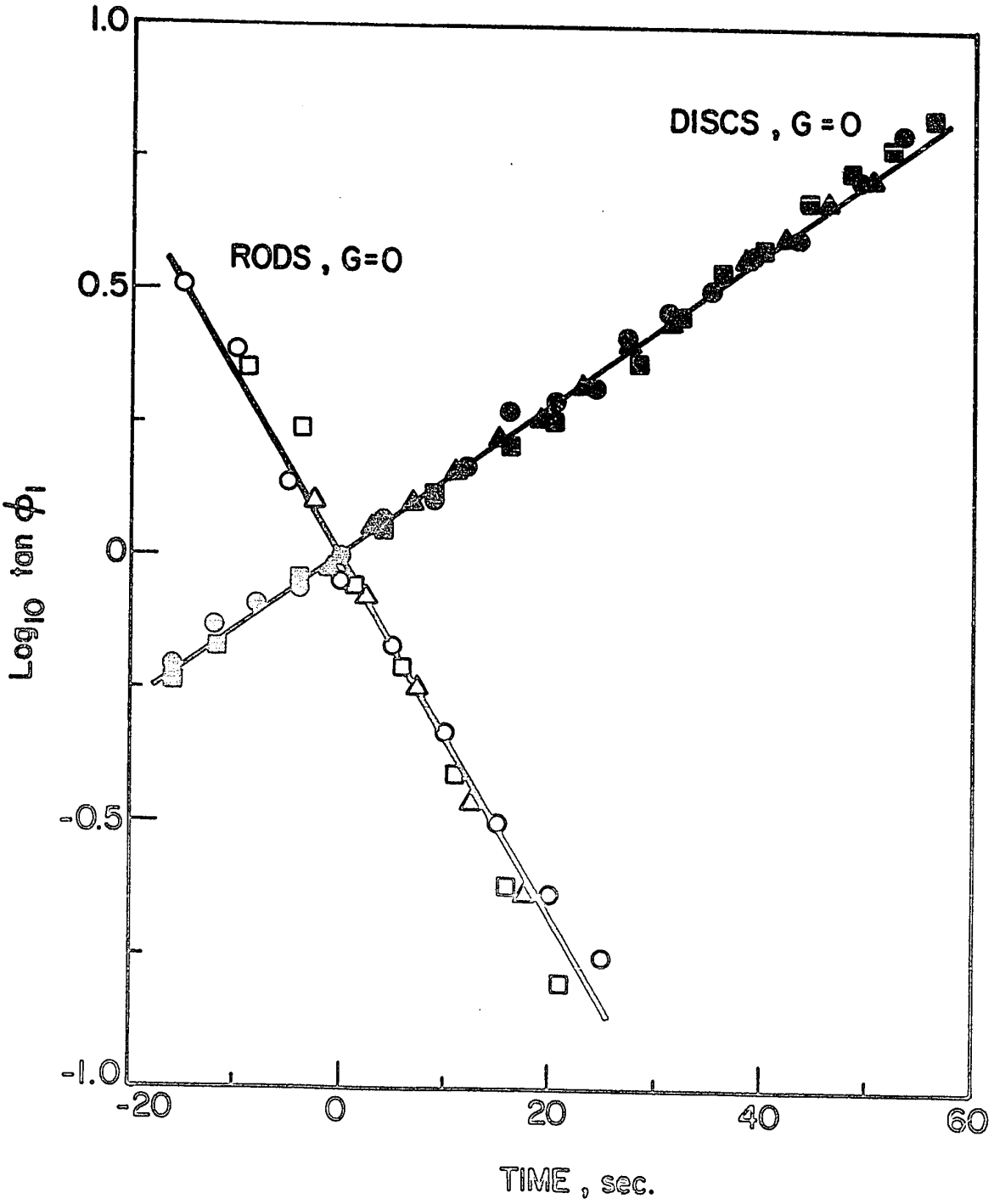
1.0
0.5
0
-0.5
-1.0
-20
0
20
40
60
DISCS , G = 0
RODS , G=0
Log10 tan φ1
TIME , sec.

FIGURE 10

Progressive cumulative orientation distribution $P_t(\phi_1)$ in an electric field alone (G = 0) for (a) rods (Expt. III) and (b) discs (Expt. VI). The solid lines are calculated from [56b]-1 for G = 0 for initially isotropic and collision-free suspensions at the times (sec) indicated.

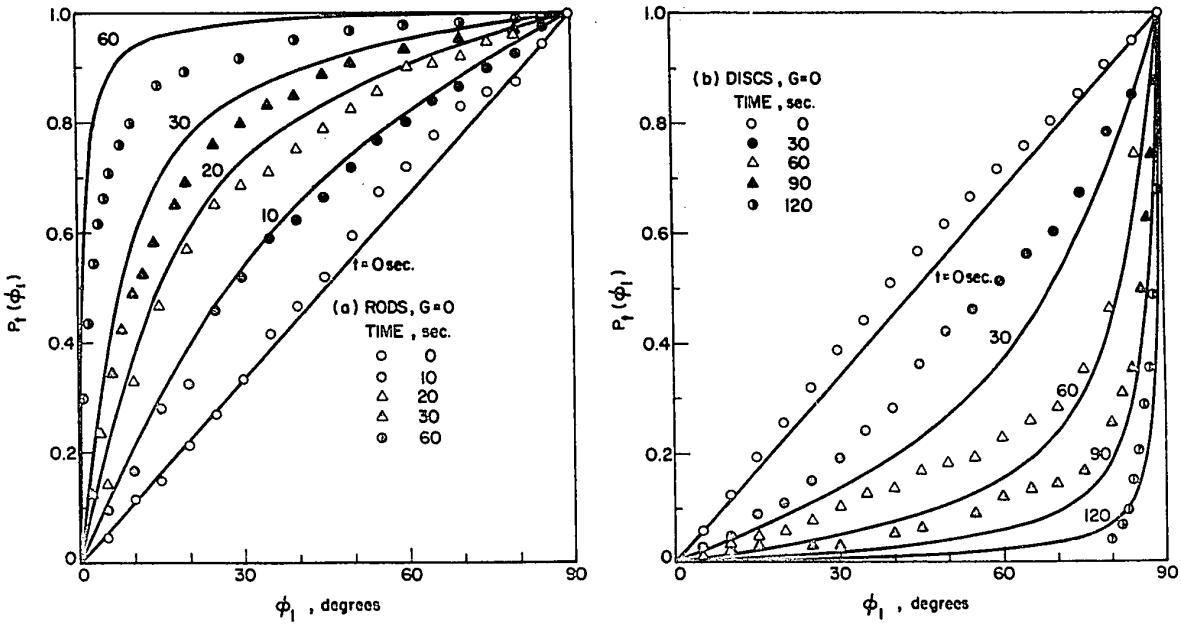
1.0
0.8
0.6
0.4
0.2
0
0
30
60
90
$P_1(\phi_1)$
ϕ_1 , degrees
60
30
20
10
t = 0 sec.
(a) RODS, G=0
TIME , sec.
0
10
20
30
60
(b) DISCS , G=0
TIME , sec.
0
30
60
90
120
t = 0 sec.
30
60
90
120

The calculated $P_t(\phi_1)$ from [56b]-1 using measured $P(q,r_e)$ are not always in close agreement with the experimental points. At equilibrium $p_\infty(\phi_1) = \delta(\phi_1)$ for rods and $= \delta(\phi_1 - \pi/2)$ for discs.

The theory described previously[1] predicts that, at G = 0, particles move along loci of constant ϕ_2 (the azimuthal angle for the particle axis when the x_2-axis is chosen as the polar axis of the spherical coordinate; Fig. 1), and consequently the distribution of ϕ_2 remains constant, independent of time. As predicted, integral distributions $P_t(\phi_2)$ obtained from the measured θ_1 and ϕ_1, summarized in Table V, are effectively constant for 30 sec. The average values of $\overline{P_t(\phi_2)}$ over t = 0 to 30 sec., listed in the last column, are plotted together with the standard deviation σ_2 from the mean at each point in Fig. 11, and fall close to a random orientation of ϕ_2 as expected from the theory ([63b]-1).

The mean projections $\bar{r}_i$ for rods and $\bar{S}_{ij}$ for discs are summarized in Table VI. As shown in Fig. 12, $\bar{r}_1$ and $\bar{r}_3$ of rods decreased gradually to $\bar{r}_1 = \bar{r}_3 = 0$ at $t = \infty$, while $\bar{r}_2$ increased to unity, indicating that all rods became aligned along the x_2-axis. With discs $\bar{S}_{12}$ and $\bar{S}_{23}$ showed small increase to the equilibrium value $2/\pi$ (Table III-1) corresponding to a random orientation of θ_1 at $\phi_1 = 90°$, and $\bar{S}_{13}$ decreased slowly to $\bar{S}_{13} = 0$. Theoretical mean projections $\bar{r}_i$ and $\bar{S}_{ij}$ corresponding to an initially isotropic suspension calculated from [69]-1 using T_3 given in Table II, are shown by the solid lines in Fig. 12; there is generally good

TABLE V

Measured Orientation Distributions $P_t(\phi_2)$ for G = 0

	ϕ_2	$P_o(\phi_2)$ [a]	$P_t(\phi_2)$ t=0 sec	10 sec	20 sec	30 sec	$\overline{P_t(\phi_2)}$ [b]
	10	0.111	0.102	0.108	0.142	0.151	0.126
	20	0.222	0.199	0.178	0.228	0.286	0.223
RODS	30	0.333	0.300	0.270	0.325	0.380	0.319
	40	0.444	0.389	0.340	0.421	0.484	0.409
	50	0.556	0.473	0.459	0.508	0.578	0.505
Expt.III	60	0.667	0.588	0.568	0.604	0.656	0.604
	70	0.778	0.730	0.735	0.700	0.745	0.728
	80	0.889	0.841	0.848	0.838	0.834	0.840
	90	1.000	1.000	1.000	1.000	1.000	1.000
	10	0.111	0.111	0.136	0.089	0.080	0.104
	20	0.222	0.210	0.200	0.161	0.170	0.185
DISCS	30	0.333	0.306	0.288	0.250	0.290	0.284
	40	0.444	0.410	0.384	0.331	0.410	0.384
	50	0.556	0.512	0.488	0.435	0.530	0.491
Expt.IV	60	0.667	0.633	0.608	0.573	0.670	0.621
	70	0.778	0.762	0.752	0.734	0.810	0.765
	80	0.889	0.901	0.936	0.887	0.930	0.914
	90	1.000	1.000	1.000	1.000	1.000	1.000

a) Corresponding to random orientation $P_o(\phi_2) = \phi_2/2\pi$ ([63b]-1).

b) Mean values of $P_t(\phi_2)$ for 4 indicated values of t.

FIGURE 11

Constancy of $P_t(\phi_2)$ for rods (Expt. III, G = 0) and discs (Expt. VI, G = 0) in an electric field alone over t = 0 to 30 sec. Points are the mean values and the vertical bar twice standard deviation σ_2 from the mean. The theoretical distribution corresponding to random orientation of ϕ_2 is indicated by the solid diagonal line (c.f. [63b]-1).

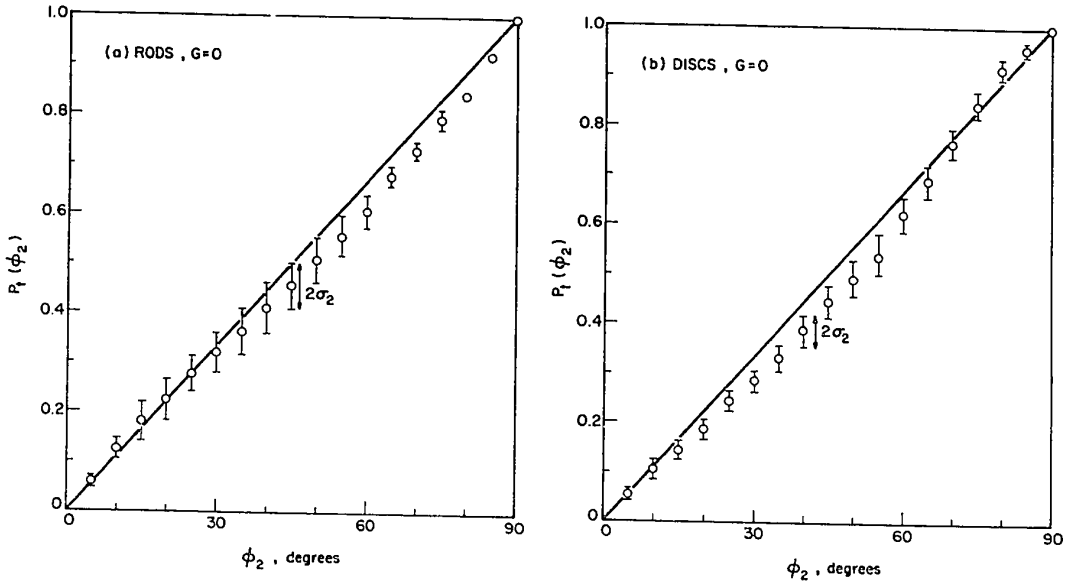
(a) RODS , G=0
(b) DISCS , G=0
$P_1(\phi_2)$
$2\sigma_2$
ϕ_2 , degrees
0
0.2
0.4
0.6
0.8
1.0
30
60
90

TABLE VI

Measured mean projections $\bar{r}_i$ and $\bar{S}_{ij}$, and calculated intrinsic electric normal stress differences $[^E\xi_{ij}]$ for G = 0

		Random[a]	t=0 sec	10	20	30	40	50	60	90	120	∞ [a]
	$\bar{r}_1$	0.500	0.426	0.364	0.322	0.282	0.246	0.208	0.206	0.168	0.151	0.000
RODS	$\bar{r}_2$	0.500	0.545	0.661	0.750	0.828	0.859	0.908	0.917	0.942	0.956	1.000
	$\bar{r}_3$	0.500	0.531	0.445	0.335	0.259	0.198	0.146	0.119	0.083	0.067	0.000
Expt.III	$[^E\xi_{12}]$	-0.113	-0.122	-0.118	-0.105	-0.102	-0.083	-0.075	-0.073	-0.058	-0.053	0.000
	$[^E\xi_{23}]$	0.113	0.139	0.129	0.104	0.092	0.069	0.059	0.053	0.038	0.035	0.000
	$[^E\xi_{31}]$	0.000	-0.017	-0.011	0.001	0.010	0.013	0.016	0.020	0.020	0.018	0.000
	$\bar{S}_{12}$	0.500	0.511	0.514	0.595	0.589	0.642	0.649	0.622	0.605	0.636	0.637
DISCS	$\bar{S}_{23}$	0.500	0.473	0.519	0.543	0.614	0.589	0.602	0.603	0.630	0.680	0.637
	$\bar{S}_{13}$	0.500	0.559	0.487	0.407	0.345	0.225	0.186	0.149	0.066	0.035	0.000
Expt.VI	$[^E\xi_{12}]$	0.196	0.218	0.206	0.195	0.182	0.117	0.102	0.083	0.046	0.037	0.000
	$[^E\xi_{23}]$	-0.196	-0.217	-0.191	-0.187	-0.162	-0.112	-0.094	-0.073	-0.034	-0.021	0.000
	$[^E\xi_{31}]$	0.000	-0.002	-0.015	-0.008	-0.020	-0.005	-0.008	-0.010	-0.013	-0.016	0.000

a) Calculated from theoretical equations in Ref.(1) for $\bar{r}_i$ and $\bar{S}_{ij}$ and from [22] for $[^E\xi_{ij}]$.

FIGURE 12

Monotonic changes in mean projection lengths $\bar{r}_i$ for rods (Expt. III, G = 0) and mean projection areas $\bar{S}_{ij}$ for discs (Expt. VI, G = 0) in an electric field alone calculated from the measured particle orientations. The experimental values are given in Table VI. Theoretical values, shown as the solid lines, are calculated from [69]-1 for initially isotropic and collision-free suspensions, using the measured values of T_3 listed in Table II.

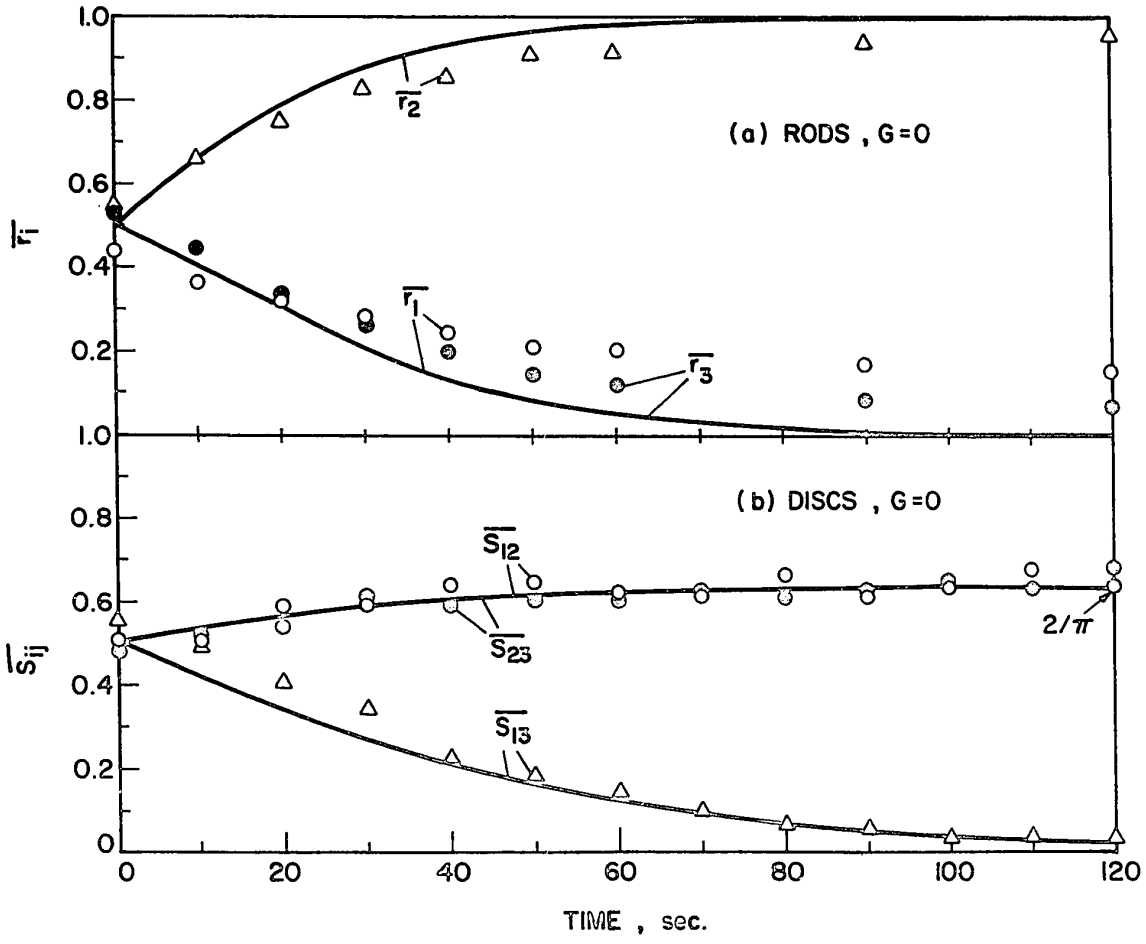
(a) RODS , G=0
(b) DISCS , G=0
$\overline{r_1}$
$\overline{r_2}$
$\overline{r_3}$
$\overline{S_{12}}$
$\overline{S_{23}}$
$\overline{S_{13}}$
2/π
$\overline{r_i}$
$\overline{S_{ij}}$
TIME , sec.
0
20
40
60
80
100
120
0.2
0.4
0.6
0.8
1.0

agreement with the experimental points found for discs, but less so for rods particularly at large t.

4. DISCUSSION

(a) General

The experimental results described above for various combinations of shear and electric fields showed generally good agreement with the theory for monodisperse and collision-free suspensions. As previously considered in detail for $f = 0$[2,6], deviations from the theory can be attributed to heterodispersity, interactions and the shape of the particles. These effects, in addition to rotary Brownian motion of the particles, which we show to be of negligible importance in our experiments, are discussed below.

Finally we consider the rheological properties which are predicted from the measured orientation distributions. Before discussing the effects of heterodispersity and interactions, we remark that the method used for arriving at the relaxation time τ from the experimental data differs from that used at $f = 0$. In the latter case $A(t)_{calc.}$ for a monodisperse and collision-free suspension is constant[2,6], whereas with $0 < f^2 < 1$ it varies with time (approaching asymptotically to zero for $r_e < 1$ and a finite value for $r_e > 1$), so that it is not practical to use $A(t)_{meas.}$ alone.

For this reason we have introduced the relative amplitude D (whose relaxation time is defined as that for which D = 1/e) in the preceding section; D is always unity for a monodisperse and collision-free suspension.

(b) Spread in r_e

When $f^2 < 1$, initially all particles rotate about the vorticity axis in phase with one another, but because of the variations in r_e among the particles they move out of phase as time progresses. It has been shown theoretically[6] that the spread in r_e can lead to a steady orientation $p_\infty(\phi_1)$ in a collision-free suspension at f = 0. A similar (but much less rigorous) analysis can be used to calculate the effect of a spread in r_e on the damping of the oscillations of $\bar{r}_i$ and $\bar{S}_{ij}$ when $0 < f^2 < 1$. Assuming a Gaussian distribution of r_e (with standard deviation σ from the mean $\bar{r}_e$) and expanding the oscillation of $\bar{r}_i$ and $\bar{S}_{ij}$ into a Fourier series, the relaxation time τ_{11} for damping of the oscillations of the first term in Fourier expansion is readily shown to be

$$\frac{\tau_{11}}{\bar{T}_1} = \frac{\bar{r}_e(\bar{r}_e^{\,2} + 1)}{2\sqrt{2}\,\pi\sigma\,|\bar{r}_e^{\,2} - 1|} \qquad [10]$$

which is identical to [95]-6 but with $\bar{T}$ (the mean period of rotation at f = 0) replaced by $\bar{T}_1$. Equation [10] is valid only when f is very small so that the oscillations of $\bar{r}_i$ do

not differ greatly from those at f = 0; there is doubt about its validity for $r_e < 1$ since $\bar{S}_{ij}$ for a monodisperse suspension ($\sigma = 0$) itself undergoes a damped oscillation (Fig. 6) whereas it is undamped when f = 0 [6]. For rods used in Expt. I ($\bar{r}_e = 4.43$, $\sigma = 4.2\%$) [10] yields $\tau_{11}/\bar{T}_1 = 3.0$.

(c) Particle interactions

The rotations of individual particles will be disturbed by hydrodynamic and electrostatic interaction between the particles, the most important at low concentrations being two-body interactions[6]. For hydrodynamic interactions the arguments used at f = 0 apply when $0 < f^2 < 1$, so that we may use the approximate equations previously derived[6] and experimentally confirmed[2] for the relaxation time τ_2 for the damping of $\bar{r}_2$ of slender rods ($r_e >> 1$)

$$\tau_2 = \ell n\, r_e/8GNa^3 \qquad [11]$$

which for Expt. I corresponds to 15 particle rotations so that the suspensions were effectively collision-free on the time scale of most of our experiments. The effect of electric interactions is very much more complicated, and an analysis is not attempted. There are two separate aspects to such interactions, the first being the short-lived perturbations of angular velocities of each of a pair of particles as they

pass by under the action of shear which cause changes in phase angle and (less marked) particle orbits as a result of the electric torque developed on one induced dipole by the action of another[7]. The second, and probably more complicated, is the electric attraction induced by the electric field which causes particles to move together and under certain conditions to form chains[8]; this is a process which can continue to grow with time of application of the electric field.

As an approximation the three separate effects can be combined to give a net relaxation time τ given by

$$\frac{1}{\tau} = \frac{1}{\tau_{11}} + \frac{1}{\tau_2} + \frac{1}{\tau_5} \qquad [12]$$

where τ_{11} and τ_2 are given by [10] and [11]; τ_5, due to the electric field, is unknown. Inserting the numerical values for Expt. I calculated from [10] and [11], we obtain $\tau/\overline{T}_1 < 2.5$ which is compatible with the measured value 1.73 given by [9].

Rotary Brownian motion of the particle can also cause the oscillations of orientation distribution to decay with a relaxation time[2]

$$\tau_4 = 1/6D_r \qquad [13]$$

where D_r is the rotary diffusion constant; τ_4, calculated from [13], is of the order 10^{10} sec. for the particles used[2]

and is thus not a factor in our experiments.

We conclude therefore that the deviations in the observed orientation distributions from those calculated theoretically for monodisperse and collision-free suspensions were due to the small unavoidable spreads in particle dimensions and to hydrodynamic and electric interactions between the particles at the concentrations employed. We also believe that the deviations in measured $\overline{r}_i$ and $\overline{S}_{ij}$ for $f^2 > 1$ and $G = 0$ (Figs. 8 and 12) at large t were mainly due to electrostatic interactions, which act especially to prevent particles from lying flat in the x_2x_3-plane.

(d) Particle Shape

The equations of particle rotation derived in the previous Chapter are for spheroidal particles. The equations for shear flow ($f = 0$) have been shown experimentally[9,10] to hold for cylindrical particles when the hydrodynamically equivalent axis ratio r_{eH} (< 1 for discs and oblate spheroids and > 1 for rods and prolate spheroids) is used, determined experimentally from the measured period of rotation T using the relation $T = 2\pi\ (r_{eH} + r_{eH}^{-1})/G$ (Table I-1). Bretherton[11] has shown theoretically that the rotation of a rigid axisymmetric particle in a simple shear flow is mathematically equivalent to that of a spheroid.

Cox[12] has shown that for long slender particles the equivalent axis ratio r_{eH} is related to the actual axis

ratio r_p by r_{eH} = const. r_p for sharp-ended bodies, and r_{eH} = const. $r_p/\sqrt{\ell n\, r_p}$ for blunt-ended bodies. An empirical relationship[2,13,14] between r_p and r_{eH}, consistent with theory[12], is given by

$$\log_{10} r_{eH} = 0.78 \log_{10} r_p + 0.051 \quad , \qquad [14]$$

and is applicable for a wide range of $r_{eH} \lesssim 1$.

We now consider the motion of a cylinder in an electric field (G = 0) for which the induced dipole moment P'_{2i} in an external electric field E'_{oi} is a linear function

$$P'_{2i} = \nu'_{ij} E'_{oj} \qquad [15]$$

where ν_{ij} is the electric polarizability tensor of the particle; the values for spheroids are given previously[1], and for isotropic bodies of revolution (e.g. spheroids and cylinders) $\nu_{ij} = \delta_{ij}\nu_{ij}$. The torque on the dipole inserted into an electric field E'_{oi} is then[1]

$$\Gamma'_{Ei} = \varepsilon_{ijk} \nu'_{j\ell} E'_{o\ell} E'_{ok} \quad . \qquad [16]$$

For short conductive cylinders ($q = \infty$) Taylor[15] has calculated numerically the electric polarizabilities, from which data we list in Table VII the two components ν'_{11} (the polarizability parallel to the axis of revolution) and $\nu'_{22} = \nu'_{33}$ (that normal to it) for several particle axis ratios.

TABLE VII

Calculated Polarizabilities and Equivalent Axis Ratios of Cylinders

r_p	$\frac{4\pi\nu_{11}}{K_2V}$ a)	$\frac{4\pi\nu_{22}}{K_2V}$ a)	$\Lambda(r_{eE})$	r_{eE} b)	r_{eH} c)
0.0	1.000	∞	- ∞	0	0
0.25	1.7507	6.1814	-4.4307	0.201	0.384
0.5	2.4325	4.2173	-1.7848	0.454	0.657
1.0	3.8614	3.1707	0.6907	1.303	1.124
2.0	7.0966	2.6115	4.4851	2.941	1.923
4.0	15.071	2.3151	12.756	5.648	3.290
∞	∞	2.0000	∞	∞	∞

a) From numerical calculations by Taylor[15)]

b) For calculation see text.

c) Calculated from [14].

Introducing the quantity $\Lambda(r_{eE})$ defined by

$$\Lambda(r_{eE}) = \frac{4\pi(\nu_{11} - \nu_{22})}{K_2 V} \quad , \qquad [17]$$

where V is the volume of particle (for a cylinder $V = 2\pi ab^2$) and r_{eE} is electrically equivalent axis ratio, [16] may be written as

$$\Gamma'_{E1} = 0 \quad ,$$

$$\Gamma'_{E2} = -\frac{K_2 V}{4\pi} \Lambda(r_{eE}) E'_{o3} E'_{o1} \quad , \qquad [18]$$

$$\Gamma'_{E3} = \frac{K_2 V}{4\pi} \Lambda(r_{eE}) E'_{o1} E'_{o2} \quad ,$$

which, by comparison with [13b]-1 of electric torque on a spheroid, yields

$$\Lambda(r_{eE}) = \frac{2(3A - 2)}{3A(A - 1)} \quad , \qquad [19]$$

where A is given by [17]-1 for a spheroid of r_e. Values of $\Lambda(r_{eE})$ for a cylinder calculated from Taylor's data[15] are given in Table VII. Values of the electrically equivalent axis ratio r_{eE}, computed to give the same values of $\Lambda(r_{eE})$ (i.e. to give the same torque) using [19], are listed in Table VII for comparison with r_{eH} from [14]. It is of interest to note the following inequalities:

when $r_p \geq 1$

$$r_{eE} > r_p > r_{eH} \qquad [20a]$$

when $r_p < 1$

$$r_{eE} < r_p < r_{eH} \quad . \qquad [20b]$$

These inequalities are valid for $r_p = 0.25$ to 4, and probably for a wider range of r_p. The large difference between the measured $P(q,r_e)$ at $G = 0$ and the calculated values from [27b]-1 may be caused by using r_{eH} instead of r_{eE} in the calculation.

Better agreement between the two was found previously for rods[4] $(P(q,r_e)_{meas.}/P(q,r_e)_{calc.} = 0.89 \pm 0.05$, c.f. our values 0.74 (rods), 1.51 (discs)). A large discrepancy in $P(q,r_e)$ for discs was also noted by Chaffey and Mason[4]. On the other hand, we note that the measured values of $P(q,r_e)$ for $f^2 > 0$ $(G \neq 0)$ were in good agreement with the calculated values (mean $P(q,r_e)_{meas.}/P(q,r_e)_{calc.}$ for Expts I, II, IV and V is 1.18 ± 0.12).

Separating r_{eH} and r_{eE} in [27b]-1 for $q = \infty$ and using [19] we obtain

$$P(q,r_e) = \frac{3\{2r_{eH}^2 + (1 - 2r_{eH}^2)A\}}{64\pi(r_{eH}^2 + 1)} \Lambda(r_{eE}) \quad , \qquad [21]$$

as the basic equation for the effect of shape. However we have not attempted to calculate r_{eE} for the particles used

in our experiments since they were not the perfect conductors assumed in Taylor's calculation[15]. In our experiments, the rods as a result of microtoming had ends which were non-conductive; each disc, as mentioned above, was a thin Aluminium film between two polyester layers of dielectric constant different from that of the medium. With both kinds of particle the electric charge density probably deviated from that assumed in the theory.

(e) Rheological Properties

The orientation distributions described above are important to a number of physical properties of the suspensions, especially the viscosity and normal stresses. These two quantities may be calculated from the distributions using equations derived in the preceding Chapter[1].

When $f^2 < 1$, oscillations in the distribution of orientation distributions are accompanied by parallel damped oscillations in the calculated intrinsic viscosity $[\eta]$ and the intrinsic normal stress difference $[\xi_{23}]$ with frequency $2/T_1$ as shown in Fig. 13, which include theoretical values calculated from [80a]-1 and [81b]-1 for an initially isotropic and collision-free suspension with $p_t(\theta_1,\phi_1)$ given by [52]-1. The displacement between the two curves for $[\eta]$ of discs resulted from measured values of $\bar{S}_{12}$ which were higher than predicted from the theory (Fig. 6b). Equilibrium values calculated from [84]-1 and [86]-1 are also shown in Fig. 13.

FIGURE 13

Calculated intrinsic viscosity $[\eta]$ and normal stress difference $[\xi_{23}]$ for the suspension of rods (Expt. I, f = 0.32) and discs (Expt. IV, f = -0.25) from the measured particle orientation distributions using [80a]-1 and [81b]-1. The solid lines are calculated from [80a]-1 and [81b]-1 in the same way but using the theoretical values of $p_t(\theta_1,\phi_1)$ for a monodisperse and collision-free suspension given by [52]-1. The broken lines are drawn to fit the points calculated from the measured orientations. The theoretical equilibrium values $[\eta]_\infty = 3.45$ and $[\xi_{23}]_\infty = -0.90$ for rods and $[\eta]_\infty = 6.96$ and $[\xi_{23}]_\infty = 0$ for discs are also indicated. The damped oscillations, of frequency $2/T_1$, reflect similar oscillations in $\bar{r}_2$ and $\bar{S}_{12}$ shown in Fig. 6.

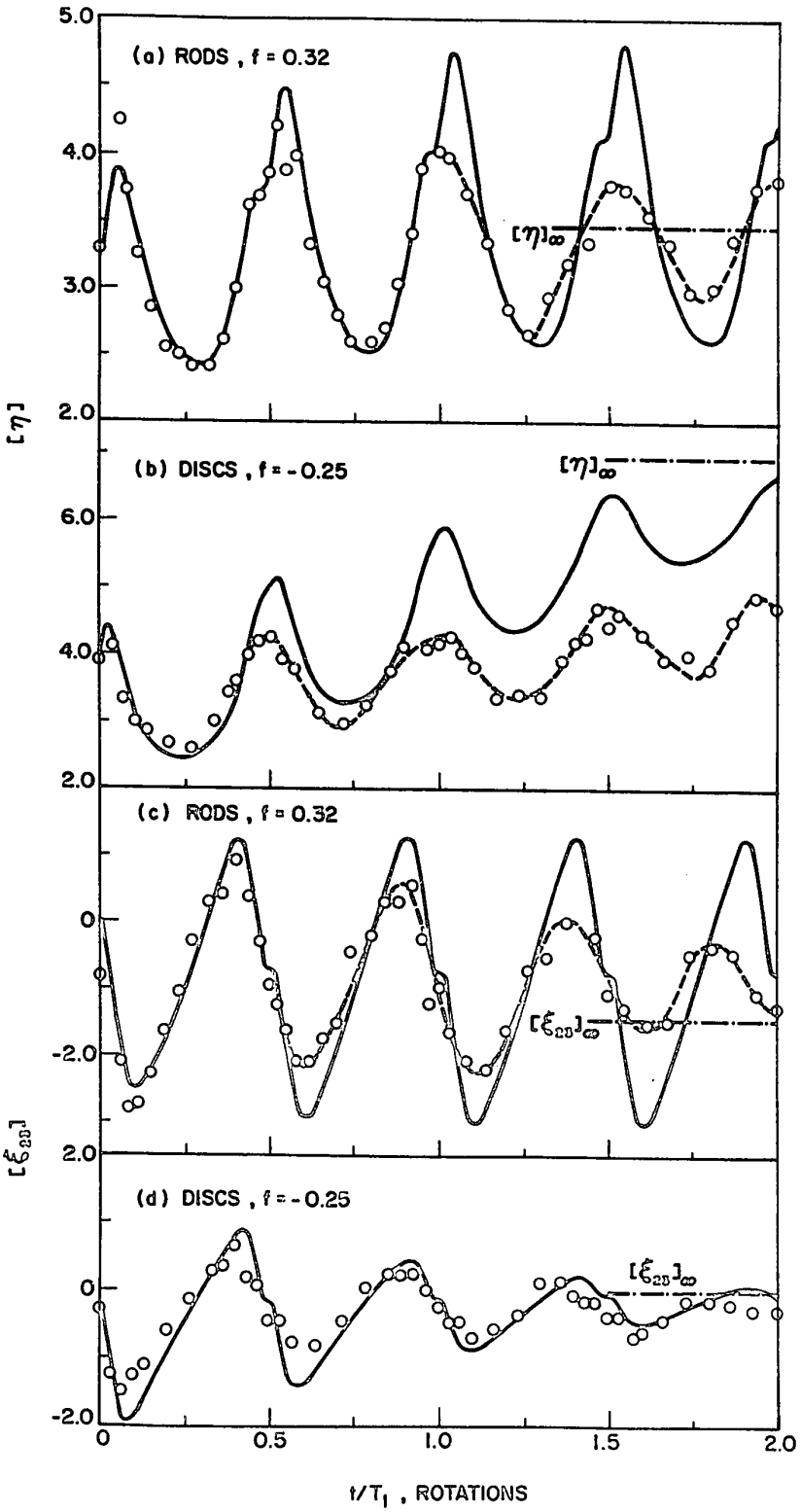
(a) RODS , f = 0.32
(b) DISCS , f = -0.25
(c) RODS , f = 0.32
(d) DISCS , f = -0.25
[η]
[ξ₂₂]
t/T₁ , ROTATIONS

Values of $[\eta]$ and $[\xi_{23}]$ when $f^2 > 1$ calculated from the measured orientation distributions using [80a]-1 and [81b]-1 are summarized in Table IV. With rods $[\eta]$ showed a maximum around 8 sec., and then slowly levelled off to the equilibrium $[\eta]_\infty = 5.17$, and $[\xi_{23}]$ decreased continuously from -2.49 to $[\xi_{23}]_\infty = -6.84$. With discs $[\eta]$ passed through a maximum and minimum and then gradually increased to $[\eta]_\infty = 6.96$; $[\xi_{23}]$ decreased to a minimum (= -3.44) at t = 4 sec., then asymptotically approached $[\xi_{23}]_\infty = 0$.

In an electric field alone (G = 0), the orientation distributions $p_t(\phi_1)$ for initially random orientations were always symmetrical with respect to the x_2-axis, so that the calculated shear stress P_{ij} $(i \neq j)$ was identically zero at all times. However normal stresses P_{ii} are generated by the electric field which we may express most conveniently as electric normal stress differences $[^E\xi_{ij}]$ which we express in intrinsic form from equations derived in the preceding Chapter[1)]

$$[^E\xi_{12}] = [^EP_{11}] - [^EP_{22}] = C_5(2\overline{\sin^2 2\theta_1 \cos^2\phi_1} + \overline{\sin^4\theta_1 \sin^2 2\phi_1}) \quad , \qquad [22a]$$

$$[^E\xi_{23}] = [^EP_{22}] - [^EP_{33}] = -C_5(\overline{\sin^2 2\theta_1 \cos^2\phi_1} + 2\overline{\sin^4\theta_1 \sin^2 2\phi_1}) \quad , \qquad [22b]$$

$$[^E\xi_{31}] = [^EP_{33}] - [^EP_{11}] = -C_5(\overline{\sin^2 2\theta_1 \cos^2\phi_1} - \overline{\sin^4\theta_1 \sin^2 2\phi_1}) \qquad [22c]$$

where

$$C_5 = \frac{2(r_e^2 - 1)P(q,r_e)}{2r_e^2 + (1 - 2r_e^2)A} \quad . \qquad [22d]$$

Numerical values $[^E\xi_{ij}]$ calculated from the measured orientation distributions using [22] are summarized in Table VI, and show gradual changes until $[^E\xi_{ij}]_\infty = 0$. We note that, since the electric field was applied parallel to the x_2-axis and the orientation distribution was assumed to be initially random, the calculated normal stresses P_{11} and P_{33} are equal so that $[^E\xi_{31}] = 0$ from which $[^E\xi_{12}] = -[^E\xi_{23}]$. However, experimentally orientation was not perfectly symmetrical with respect to $\phi_1 = 0°$ and 90° so that $[^E\xi_{31}]$ calculated from the measured orientations did not vanish (Table IV).

It should be emphasized that all of the rheological properties have been calculated from measured and calculated orientation distributions. It would, of course, be of great interest to test the predictions by direct rheological measurements. Several experimental studies of the effect of electric fields on increasing the viscosity of dispersions have been made[16-19] but in no case was the system characterized sufficiently to test the theory[1], although we note nothing in the results at variance with it.

Particle orientations in combined shear and electric fields are also of interest to other phenomena in suspensions such as streaming electrical double refraction[20,21] and

light transmission[22]; these electro-rheo-optical effects would be expected to show damped oscillations when $f^2 < 1$ and monotonic changes when $f^2 > 1$ provided, of course, that there is no appreciable rotary Brownian motion of particles.

REFERENCES

1. This thesis, Chapter IV.
2. This thesis, Chapter III.
3. This thesis, Appendix IV.
4. Allan, R.S. and Mason, S.G., Proc. Roy. Soc. (London), A267, 62 (1962).
5. Chaffey, C.E. and Mason, S.G., J. Colloid Sci., 19, 525 (1964).
6. This thesis, Chapter II.
7. Smyth, W.R., "Static and Dynamic Electricity", McGraw-Hill, New York (1950).
8. Zia, I.Y.Z., Cox, R.G. and Mason, S.G., Proc. Roy. Soc. (London), A300, 421 (1967).
9. Trevelyan, B.J. and Mason, S.G., J. Colloid Sci., 6, 354 (1951).
10. Goldsmith, H.L. and Mason, S.G., J. Fluid Mech., 12, 88 (1962).
11. Bretherton, F.P.,J. Fluid Mech., 14, 284 (1962).
12. Cox, R.G., J. Fluid Mech., 45, 625 (1971).
13. Anczurowski, E. and Mason, S.G., Trans. Soc. Rheol., 12, 209 (1968).
14. Gauthier, F., Goldsmith, H.L. and Mason, S.G., Rheol. Acta, 10, 344 (1972).
15. Taylor, T.T., J. Res. Natl. Bur. Std., 64B, 135, 199 (1960).
16. Bjornstahl, Y. and Snellman, O., Kolloid-Z., 78, 258 (1937).
17. Winslow, W.M., J. Appl. Phys., 20, 1137 (1949).
18. Klass, D.L. and Martinek, T.W., J. Appl. Phys. 38, 67 (1967).
19. El-Tantaway, Y. and Mason, S.G., unpublished results.

20. Demetriades, S.T., J. Chem. Phys., 29, 1054 (1958).

21. Ikeda, S., J. Chem. Phys., 38, 2839 (1963).

22. Sorrentino, M. and Mason, S.G., J. Colloid Interface Sci., 41, 178 (1972).

CHAPTER VI

GENERAL CONCLUSIONS

1. GENERAL SUMMARY

The principal achievements, discoveries and conclusions described in this thesis may be summarized as follows:

(i) The probability distribution functions of particle orientations and particle orbits for monodisperse collision-free suspensions of rods ($r_e > 1$) and discs ($r_e < 1$) subjected to simple shear flow, derived from the equations[1] describing the rotational motion of single spheroids, are oscillating functions of time with frequency 2/T, T being the period of one complete rotation of a particle. These functions have been used to derive relationships for the mean projections of various particle dimensions which are expressed as elliptic integrals and alternate formulas which are convenient for numerical calculations. A complete theoretical description of the macro-rheological properties of dilute suspensions of spheroidal particles and of long slender rods has been obtained by using the method of analysis proposed by Cox and Brenner[2] to calculate all components of the macroscopic stress tensor. There are two possible processes causing the orientation probability distribution to undergo damped oscillations and eventually reach steady values: (1) spread in axis ratio amongst the particles and (2) interactions between particles. Each process has its own characteristic relaxation time.

(ii) Measured transient distributions of particle orientations and orbits for rods and discs with initially random orientation and for rods only with initially parallel alignment made in the early stages of shearing, agreed well with the theory explained in (i). Analysis of the damped oscillations of the mean particle projections (e.g. $\bar{r}_2$ for rods and $\bar{S}_{12}$ for discs) showed that the inverse of the relaxation time varied linearly with particle concentration as predicted by the theory. As expected, particle orientation distributions were reversible with respect to the direction of shear flow in a suspension of initially aligned rods.

(iii) A general theory of the rotational motion of an ellipsoidal particle in combined shear and electric fields was developed as an extension of earlier work[3,4]. Equations for transient and steady state distributions of particle orientations and particle orbits for initially isotropic and collision-free suspensions of spheroids with no permanent dipoles have been derived. When $E_o < E_{crit.}$, the orientation distribution oscillates with frequency $2/T_1$, whereas when $E_o > E_{crit.}$ it changes monotonically. Complete rheological equations for dilute suspensions subjected to shear and electric fields have been evaluated from these orientation distributions. From these equations, some interesting, rheological phenomena in suspensions subjected to electric fields have been predicted.

(iv) Orientation distributions of suspensions of rods and discs measured were in generally good agreement with the theory described in (iii). From the measured orientations, numerical values of several important macro-rheological parameters (which can, in principle, be measured) were calculated from the theory.

2. CLAIMS TO ORIGINAL RESEARCH

(i) Equations were derived for the transient probability distributions of particle orientations and of mean projections of axisymmetric particles in shear flow.

(ii) Complete rheological equations were derived for dilute suspensions of spheroids and long slender rods in shear flow; these equations can be solved numerically when the particle orientations are known.

(iii) A theoretical analysis of the effect of a spread in particle shapes on the orientation distribution has been made from which the characteristic relaxation time for damping of oscillations of mean particle projections can be predicted.

(iv) A theoretical analysis of the orientation probability distribution of spheroids in a suspension was made for the case in which shear and electric fields were applied simultaneously.

(v) Complete rheological equations were derived for a suspension of spheroids subjected to shear and electric fields,

of which (ii) are limiting cases.

(vi) Most of the theoretical calculations and predictions of particle orientations were confirmed experimentally using dilute suspensions of rods and discs suspended in a viscous liquid subjected to various combinations of shear and electric fields.

(vii) For purely shear flow# the inverse of the measured relaxation times was found to be linearly dependent on particle concentration and, for rods, in good quantitative accord with the theory.

(viii) The reversibility of particle orientations in shear flow was demonstrated and shown to be a phenomenon of potential importance.

(ix) The applicability of the electro-rheological theory to magneto-rheological phenomena was suggested.

3. SUGGESTIONS FOR FURTHER WORK

Some of the more interesting lines of future investigation which have come to mind as a result of the research conducted for the preparation of this thesis are given below.

(i) A more extended experimental study of the effect of particle concentration on the transient states, and particularly the changes of orbit distribution over long periods of time.

(ii) Improvements in methods of preparing particles in order to reduce the spread in axis ratios.

(iii) Experiments on the changes in phase angle and orbit constant during interactions in shear flow between pairs of particles in various initial orientations for comparison with the details of Cox's theory[5].

(iv) Experimental and computational studies on the effect of various perturbations on the fading memory of particle orientation when shear flow is cyclically reversed.

(v) Measurements of rheological properties such as shear viscosity and normal stress differences, of suspensions subjected to shear, electric, and combined shear and electric fields in both transient and steady states for comparison with values calculated from the measured particle orientations.

(vi) Theoretical and experimental studies of electro-rheological phenomena when $G = 0$ and $G \to 0$, under which conditions the theory predicts unusual behavior.

(vii) Further theoretical and experimental studies of the relationships between the hydrodynamically and electrically equivalent ellipsoidal axis ratios (r_{eH}, r_{eE}) and of $P(q,r_e)$, and the axis ratios of circular cylinders.

(viii) Extension of the theory of the rotational motion of spheroids in shear and electric fields to cases in which the electric field is arbitrarily oriented with respect to the shear field.

REFERENCES

1. Jeffery, G.B., Proc. Roy. Soc. (London), A102, 161 (1922).

2. Cox, R.G. and Brenner, H., Chem. Eng. Sci., 26, 65 (1971).

3. Demetriades, S.T., J. Chem. Phys., 29, 1054 (1958).

4. Chaffey, C.E. and Mason, S.G., J. Colloid Sci., 19, 525 (1964).

5. Cox, R.G., Forthcoming Publication.

APPENDIX I

DETAILS OF VARIOUS CALCULATIONS

1. Mean projections $\bar{r}_1$ and $\bar{S}_{23}$
2. Mean projections $\bar{r}_2$ and $\bar{S}_{13}$
3. Mean projections $\bar{r}_3$ and $\bar{S}_{12}$
4. Integration of Eq.[83]-II
5. Details of Eq. [109]-II
6. Probability distribution $p_{\sigma,t}(\kappa_1)$
7. Anisotropy of the viscosity of suspensions

1. Mean Projections $\bar{r}_1$ and $\bar{S}_{23}$

The mean projections of unit length of a rod on the X_1-axis or of unit area of the face of a disc on the X_2X_3-plane are expressed[1] as

$$\bar{r}_1 = \bar{S}_{23} = \int_0^{2\pi}\int_0^{\pi} p_t(\theta_1,\phi_1)\cos\theta_1 d\theta_1 d\phi_1 \quad . \qquad [1]$$

If we consider a suspension of initially random orientation, $p_t(\theta_1,\phi_1)$ is given by Eq. [19]-II *, so that

$$\bar{r}_1 = \bar{S}_{23} = \int_0^{2\pi}\int_0^{\pi} \frac{\sin\theta_1\cos\theta_1}{4\pi(\cos^2\theta_1 + \chi^2\sin^2\theta_1)^{3/2}}\, d\theta_1 d\phi_1 \qquad [2]$$

where χ^2 is the known function of ϕ_1 and t given by Eq.[17]-II. The first integration may be made with respect to θ_1;

$$I = 2\int_0^{\pi/2} \frac{\sin\theta_1\cos\theta_1}{(\cos^2\theta_1 + \chi^2\sin^2\theta_1)^{3/2}}\, d\theta_1 \qquad [3a]$$

which, after the substitution of $\sin^2\theta_1 = y$, can be written

$$I = 2\int_0^1 \frac{dy}{\{1 + (\chi^2 - 1)y\}^{3/2}} \quad . \qquad [3b]$$

* According to a convention, this designates Equation [19] of Chapter II of the thesis.

The solution of Eq. [3b] yields[2)]

$$I = 2\left(\frac{1}{\chi} - \frac{1}{\chi + 1}\right) \quad , \qquad [4]$$

so that

$$\bar{r}_1 = \bar{s}_{23} = \frac{1}{2\pi}\left\{\int_o^{2\pi} \frac{d\phi_1}{\chi} - \int_o^{2\pi} \frac{d\phi_1}{\chi + 1}\right\} \quad . \qquad [5]$$

From the expression for χ^2, the first integral of Eq.[5] becomes

$$I_1 = \int_o^{2\pi} (\ell + m \cos 2\phi_1 - n \sin 2\phi_1)^{-\frac{1}{2}} d\phi_1 \qquad [6]$$

where

$$\ell = 1 + \tfrac{1}{4}(r_e - r_e^{-1})^2 (1 - \cos \frac{4\pi t}{T}) \quad ,$$

$$m = \tfrac{1}{4}(r_e^2 - r_e^{-2})(1 - \cos \frac{4\pi t}{T}) \quad ,$$

$$n = \tfrac{1}{2}(r_e - r_e^{-1}) \sin \frac{4\pi t}{T} \quad .$$

By introducing the factor ε defined as

$$\sin \varepsilon = \frac{n}{\sqrt{m^2 + n^2}} \qquad \text{or} \qquad \cos \varepsilon = \frac{m}{\sqrt{m^2 + n^2}} \quad ,$$

then Eq. [6] becomes

$$I_1 = \int_0^{2\pi} \{\ell + \sqrt{m^2 + n^2}\cos(2\phi_1 + \varepsilon)\}^{-\frac{1}{2}} d\phi_1 \quad . \qquad [7]$$

If the substitution of $2\phi_1 + \varepsilon = 2\psi$ is made in Eq. [7], one obtains

$$I_1 = \frac{4}{a}\int_0^{\pi/2} (1 - \frac{b^2}{a^2}\sin^2\psi)^{-\frac{1}{2}} d\psi \qquad [8a]$$

where

$$a^2 = \ell + \sqrt{m^2 + n^2} \quad \text{and} \quad b^2 = 2\sqrt{m^2 + n^2}.$$

This may be written as

$$I_1 = \frac{4}{a} K(k_1) \qquad [8b]$$

where $K(k_1)$ is the complete elliptic integral of the first kind with modulus $k_1 = b/a$.

Following the analysis given above the second part of the integrals in Eq. [5] can be written in the form:

$$I_2 = 4\int_0^{\pi/2} \{(a^2 - b^2\sin^2\psi)^{\frac{1}{2}} + 1\}^{-1} d\phi_1 \quad . \qquad [9]$$

Substituting $(a^2 - b^2\sin^2\psi) = x^2$, one obtains

$$I_2 = 4 \int_c^a \frac{x\,dx}{(x+1)\sqrt{(a^2 - x^2)(x^2 - c^2)}} \qquad [10a]$$

where $c^2 = a^2 - b^2 = \ell - \sqrt{m^2 + n^2}$. Eq. [10a] can be separated into two integrals:

$$I_2 = 4 \left\{ \int_c^a \frac{dx}{\sqrt{(a^2 - x^2)(x^2 - c^2)}} - \int_c^a \frac{dx}{(x+1)\sqrt{(a^2 - x^2)(x^2 - c^2)}} \right\} , \qquad [10b]$$

both of which can be expressed in terms of elliptic integrals[3] as

$$\int_c^a \frac{dx}{\sqrt{(a^2 - x^2)(x^2 - c^2)}} = \frac{1}{a} K(k_1) \qquad [11a]$$

and

$$\int_c^a \frac{dx}{(x+1)\sqrt{(a^2 - x^2)(x^2 - c^2)}} = \frac{2}{(a+c)(1-c)} \left[K(k_2) - 2c\, \Pi(\alpha_1^2, k_2) \right] \qquad [11b]$$

where $\Pi(\alpha^2, k_2)$ is the complete elliptic integral of the third kind with the modulus $k_2 = (a - c)/(a + c)$ and the characteristic $\alpha_1^2 = \frac{(a-c)(1-c)}{(a+c)(1+c)}$. Combining these two results Eq. [10b] becomes

$$I_2 = 4\left[\frac{1}{a}K(k_1) + \frac{2}{(a+c)(1-c)}\{K(k_2) - 2c\,\Pi(\alpha_1^2, k_2)\}\right] \qquad [12]$$

Finally substituting Eqs. [8b] and [12] into [5] yields the mean projection:

$$\bar{r}_1 = \bar{S}_{23} = \frac{4}{\pi(a+c)}\left\{\frac{1}{1-c}K(k_2) - \frac{2c}{1-c^2}\,\Pi(\alpha_1^2, k_2)\right\} . \qquad [13]$$

For convenience in numerical evaluation of $\bar{r}_1$ and $\bar{S}_{23}$, since $0 < \alpha_1^2 < k_2^2$, $\Pi(\alpha_1^2, k_2)$ can be expressed as[3)]

$$\Pi(\alpha_1^2, k_2) = K(k_2) + \frac{\alpha_1^2}{\sqrt{(1-\alpha_1^2)(k_2^2-\alpha_1^2)}}K(k_2)\,Z(\beta, k_2). \qquad [14]$$

where $Z(\beta, k_2)$ is the Jacobi Zeta function with modulus k_2 and amplitude $\beta = \sin^{-1}(\alpha_1/k_2)$.

Hence

$$\bar{r}_1 = \bar{S}_{23} = \frac{4}{\pi}\left[\frac{1}{(a+c)(1+c)}K(k_2) - \frac{1}{\sqrt{(a^2-1)(1-c^2)}}K(k_2)Z(\beta,k_2)\right] .$$

[15]

2. Mean Projections $\bar{r}_2$ and $\bar{S}_{13}$

The other mean projections $\bar{r}_2$ and $\bar{S}_{13}$ are given by

$$\bar{r}_2 = \bar{S}_{13} = \int_0^{2\pi}\int_0^{\pi} \frac{\sin^2\theta_1 \cos\phi_1}{4\pi(\cos^2\theta_1 + \chi^2\sin^2\theta_1)^{3/2}}\, d\theta_1 d\phi_1 \quad . \qquad [16]$$

The first integration with respect to ϕ_1 may be written as

$$I = \int_0^{2\pi} \frac{\cos\phi_1}{(p + q\cos 2\phi_1 + r\sin 2\phi_1)^{3/2}}\, d\phi_1 \qquad [17]$$

where

$$p = 1 + \tfrac{1}{4}\sin^2\theta_1 (r_e - r_e^{-1})^2 (1 - \cos\tfrac{4\pi t}{T}) \quad ,$$

$$q = \tfrac{1}{4}\sin^2\theta\ (r_e^2 - r_e^{-2})(1 - \cos\tfrac{4\pi t}{T}) \quad ,$$

$$r = -\tfrac{1}{2}\sin^2\theta\ (r_e - r_e^{-1})\sin\tfrac{4\pi t}{T} \quad .$$

Since the projection must be always positive, the numerator $\cos\phi_1$ in Eq. [17] must be taken to be positive. Therefore

$$I = 2\int_0^{\pi/2} \frac{\cos\phi_1 d\phi_1}{(p + q\cos 2\phi_1 + r\sin 2\phi_1)^{3/2}}$$

$$- 2\int_{\pi/2}^{\pi} \frac{\cos\phi_1 d\phi_1}{(p + q\cos 2\phi_1 + r\sin 2\phi_1)^{3/2}} \quad . \qquad [18]$$

Substituting $\cot\phi_1 = x$, the first integral of Eq. [18]

becomes

$$I_1 = \frac{2}{(p+q)^{3/2}} \int_o^\infty \frac{x\,dx}{\{(x + \frac{r}{p+q})^2 + \frac{p^2 - q^2 - r^2}{(p+q)^2}\}^{3/2}} \quad . \qquad [19]$$

A further substitution is made by putting $x + \frac{r}{p+q} =$ a sinh z, where $a^2 = \frac{p^2 - q^2 - r^2}{(p+q)^2}$, so that

$$I_1 = \frac{2}{(p+q)^{3/2}} \int_{\sinh \frac{r}{a(p+q)}}^\infty \left[\frac{\sinh z}{a \cosh^2 z} - \frac{r}{a^2(p+q)\cosh^2 z}\right] dz \quad ,$$

[20]

which, on reduction, yields

$$I_1 = \frac{2}{(p+q)^{\frac{1}{2}}(r + \sqrt{p+q})} \quad . \qquad [21a]$$

Similarly, the second integral in Eq. [18] is obtained as

$$I_2 = \frac{2}{(p+q)^{\frac{1}{2}}(r - \sqrt{p+q})} \qquad [21b]$$

Substituting these solutions into Eq. [18] gives the first integration with respect to ϕ_1. Therefore

$$\bar{r}_2 = \bar{s}_{13} = \frac{1}{\pi} \int_o^\pi \frac{\sqrt{p-q}\,\sin^2\theta_1}{p^2 - q^2 - r^2} d\theta_1 \quad . \qquad [22]$$

Substitution of p, q and r and rearranging the equation gives

$$\bar{r}_2 = \bar{S}_{13} = \frac{2}{\pi m\sqrt{m^2+4}} \int_o^{\pi/2} \{\frac{\sin^2\theta_1\sqrt{1-k_1^2\sin^2\theta_1}}{m_1-\sin^2\theta_1} - \frac{\sin^2\theta_1\sqrt{1-k_1^2\sin^2\theta_1}}{m_2-\sin^2\theta_1}\}d\theta_1 \qquad [23]$$

where

$$m = \tfrac{1}{2}(r_e - r_e^{-1})^2(1-\cos\tfrac{4\pi t}{T}) \quad ,$$

$$m_1 = \tfrac{1}{2}\{1+\sqrt{1+4/m^2}\} \quad ,$$

$$m_2 = \tfrac{1}{2}\{1-\sqrt{1+4/m^2}\} \quad ,$$

and

$$k_1^2 = \tfrac{1}{2}(1-r_e^{-2})(1-\cos\tfrac{4\pi t}{T}) \quad ,$$

k_1 being real when $r_e > 1$ and imaginary when $r_e < 1$.
The first integral in Eq. [23] can again be separated into two parts:

$$I_1 = \int_o^{\pi/2} \frac{\sin^2\theta_1\sqrt{1-k_1^2\sin^2\theta_1}}{m_1-\sin^2\theta_1}d\theta_1$$

$$= \frac{1}{m_1}\int_o^{\pi/2} \frac{\sin^2\theta_1 d\theta_1}{(1-\frac{1}{m_1}\sin^2\theta_1)\sqrt{1-k_1^2\sin^2\theta_1}} \qquad [24]$$

$$-\frac{k_1^2}{m_1}\int_o^{\pi/2} \frac{\sin^4\theta_1 d\theta_1}{(1-\frac{1}{m_1}\sin^2\theta_1)\sqrt{1-k_1^2\sin^2\theta_1}}$$

Since k_1^2 is either positive or negative depending on the value r_e, integration thus yields different values for $r_e > 1$ and $r_e < 1$.

(a) Prolate spheroids and rods ($r_e > 1$)

In this case $0 < k_1^2 < 1$, the integrals in Eq. [24] become[3]

$$\int_0^{\pi/2} \frac{\sin^2\theta_1 d\theta_1}{(1 - \frac{1}{m_1}\sin^2\theta_1)\sqrt{1 - k_1^2\sin^2\theta_1}} = m_1\{\Pi(\frac{1}{m_1}, k_1) - K(k_1)\} \quad [25a]$$

and

$$\int_0^{\pi/2} \frac{\sin^4\theta_1 d\theta_1}{(1 - \frac{1}{m_1}\sin^2\theta_1)\sqrt{1 - k_1^2\sin^2\theta_1}} \quad [25b]$$

$$= m_1^2\{\Pi(\frac{1}{m_1}, k_1) + \frac{1}{m_1 k_1^2} E(k_1) - \frac{m_1 + k_1^2}{k_1^2} K(k_1)\} \quad .$$

where $E(k_1)$ is the complete elliptic integral of the second kind with modulus k_1. Hence

$$I_1 = m_1 k_1^2 K(k_1) - E(k_1) + (1 - m_1 k_1^2)\Pi(\frac{1}{m_1}, k_1) \quad . \quad [26a]$$

Similarly, the second part of the integrals in Eq. [23] is

evaluated to give, for $r_e > 1$,

$$I_2 = m_2 k_1^2 K(k_1) - E(k_1) + (1 - m_2 k_1^2) \Pi(\frac{1}{m_2}, k_1) \quad . \qquad [26b]$$

Finally substituting Eq. [26] into [23] yields the mean projection length of rods on the X_2-axis:

$$\bar{r}_2 = \frac{2}{\pi} [\frac{k_1^2}{m^2} K(k_1) + \frac{1 - m_1 k_1^2}{m(m^2 + 4)^{\frac{1}{2}}} \Pi(\frac{1}{m_1}, k_1) - \frac{1 - m_2 k_1^2}{m(m^2 + 4)^{\frac{1}{2}}} \Pi(\frac{1}{m_2}, k_1)] \quad [27]$$

An alternate formula of the complete elliptic integral of the third kind is now given. Since $k_1^2 < \frac{1}{m_1} < 1$,

$$\Pi(\frac{1}{m_1}, k_1) = K(k_1) + \frac{\pi\sqrt{m_1}}{2\sqrt{(1 - m_1 k_1^2)(m_1 - 1)}} [1 - \Lambda_o(\Phi_1, k_1)] \quad , \quad [28a]$$

and since $-\infty < 1/m_2 < 0$,

$$\Pi(\frac{1}{m_2}, k_1) = \frac{m_2 k_1^2}{m_2 k_1^2 - 1} K(k_1) - \frac{\pi\sqrt{m_2}}{2\sqrt{(1 - m_2 k_1^2)(m_2 - 1)}} \Lambda_o(\Phi_2, k_1) \quad [28b]$$

where $\Lambda_o(\Phi, k_1)$ is the Heuman's Lambda function with modulus k_1 and amplitude

$$\Phi_1 = \sin^{-1}\sqrt{\frac{m_1 - 1}{m_1(1 - k_1^2)}} \quad \text{and} \quad \Phi_2 = \sin^{-1}\frac{1}{\sqrt{1 - m_2 k_1^2}} \quad .$$

Therefore $\bar{r}_2$ can be written also as

$$\bar{r}_2 = \frac{1}{m\sqrt{m^2+4}}\left[\frac{2}{\pi}K(k_1) + \sqrt{\frac{m_1(1-m_1k_1^2)}{m_1-1}}\{1-\Lambda_o(\Phi_1,k_1)\}\right.$$

$$\left. - \sqrt{\frac{m_2(1-m_2k_1^2)}{m_2-1}}\Lambda_o(\Phi_2,k_1)\right] \quad . \qquad [29]$$

(b) Oblate spheroids and discs ($r_e < 1$).

Here, k_1 in Eq. [25] is imaginary and the following transformations can be applied:

$$K(ik) = \frac{1}{\sqrt{1+k^2}}K(k')$$

$$E(ik) = \sqrt{1+k^2}\ E(k')$$

$$\Pi(\alpha^2,ik) = \frac{1}{(\alpha^2-k^2)\sqrt{1-k^2}}[k^2K(k') - \alpha^2\Pi(\alpha'^2,k')]$$

where $\quad k' = \dfrac{k^2}{1+k^2}$, $\quad \alpha'^2 = \dfrac{\alpha^2+k^2}{1+k^2}$.

Then I_1 and I_2 given by Eq. [26] can be transformed to

$$I_1 = \frac{1}{\sqrt{1+k_2^2}}\Pi(\alpha_1^2,k_3) - \sqrt{1+k_2^2}\,E(k_3) \qquad [30a]$$

and

$$I_2 = \frac{1}{\sqrt{1 + k_2^2}} \Pi(\alpha_2^2, k_3) - \sqrt{1 + k_2^2}\ E(k_3) \qquad [30b]$$

where

$$k_2^2 = \tfrac{1}{2}(r_e^{-2} - 1)\left(1 - \cos \frac{4\pi t}{T}\right)$$

and

$$\alpha_1^2 = \frac{1 + m_1 k_2^2}{m_1(1 + k_2^2)}\ , \qquad \alpha_2^2 = \frac{1 + m_2 k_2^2}{m_2(1 + k_2^2)}\ .$$

Hence $\bar{S}_{13}$ becomes

$$\bar{S}_{13} = \frac{2}{\pi m \sqrt{(m^2 + 4)(1 + k_2^2)}} [\Pi(\alpha_1^2, k_3) - \Pi(\alpha_2^2, k_3)]. \qquad [31]$$

An alternate formula for $\bar{S}_{13}$ is also obtained by means of the transformation given by Eq. [28]:

$$\bar{S}_{13} = \frac{1}{m\sqrt{m^2 + 4}} \left[\frac{2(1 + m_2 k_2^2)}{\pi\sqrt{1 + k_2^2}} K(k_3) + \sqrt{\frac{m_1(1 + m_1 k_2^2)}{m_1 - 1}} \{1 - \Lambda_o(\Phi_3, k_3)\} \right.$$

$$\left. - \sqrt{\frac{m_1(1 + m_2 k_2^2)}{m_2 - 1}}\ \Lambda_o(\Phi_4, k_3) \right] \qquad [32]$$

where

$$\Phi_3 = \sin^{-1}\sqrt{\frac{m_1 - 1}{m_1}} \quad , \quad \Phi_4 = \sin^{-1}\sqrt{1 - m_2 k_2^2} \quad .$$

3. Mean Projections $\bar{r}_3$ and $\bar{S}_{12}$

The mean projections $\bar{r}_3$ and $\bar{S}_{12}$ given by

$$\bar{r}_3 = \bar{S}_{12} = \int_0^{2\pi}\int_0^{\pi} \frac{\sin^2\theta_1 \sin\phi_1}{4\pi(\cos^2\theta_1 + \chi^2\sin^2\theta_1)^{3/2}}\, d\theta_1 d\phi_1 \qquad [33]$$

can be evaluated by following the analysis given above, the first integration with respect to ϕ_1 being given by

$$\bar{r}_3 = \bar{S}_{12} = \frac{1}{\pi}\int_0^{\pi} \frac{\sqrt{p + q}\ \sin^2\theta_1}{p^2 - q^2 - r^2}\, d\theta_1 \ . \qquad [34]$$

This is equivalent to Eq. [22] except that the numerator for this case is given by $\sqrt{p + q}$. The solution of the integral in Eq. [34] also depends on r_e.

For $r_e > 1$,

$$\bar{r}_3 = \frac{2}{\pi m\sqrt{(m^2 + 4)(1 + k_2^2)^{\frac{1}{2}}}} \{\Pi(\alpha_1^2, k_3) - \Pi(\alpha_2^2, k_3)\} \qquad [35a]$$

and for $r_e < 1$

$$\bar{S}_{12} = \frac{2}{\pi}\left[\frac{k_1^2}{m}K(k_1) - \frac{1 - m_1 k_1^2}{m(m^2+4)^{\frac{1}{2}}}\Pi\left(\frac{1}{m_1}, k_1\right)\right.$$

$$\left. - \frac{1 - m_2 k_2}{m(m^2+4)^{\frac{1}{2}}}\Pi\left(\frac{1}{m_2}, k_1\right)\right] \qquad [35b]$$

where

$$k_1^2 = \tfrac{1}{2}(1 - r_e^2)\left(1 - \cos\frac{4\pi t}{T}\right) \quad ,$$

$$k_2^2 = \tfrac{1}{2}(r_e^2 - 1)\left(1 - \cos\frac{4\pi t}{T}\right) \quad ,$$

and

$$k_3^2 = \frac{k_2^2}{1 + k_2^2} \quad .$$

It is noted from Eqs. [27], [31] and [35], that the mean values of $\bar{r}_2$ and $\bar{r}_3$ for $r_e = R$ $(R > 1)$ give the same values of $\bar{S}_{12}$ and $\bar{S}_{13}$ for $r_e = 1/R$ respectively.

Numerical values of $\bar{r}_i$ and $\bar{S}_{ij}$ for an initially isotropic and collision-free suspension are given in Fig.2 of Chapter II. All are independent of the shear rate G in the creeping flow regime assumed throughout the experiments and the theoretical analysis.

4. Integration of Eq. [83]-II

To perform the integration of the type [83]-II, the more generalized definite integral

$$I = \int_{-\infty}^{+\infty} \exp[-ax^2 + ibx^2 + icx]\, dx \qquad [36]$$

where a, b, c are constants and $i = \sqrt{-1}$, will be evaluated here. Rearrangement of the argument of the exponential gives

$$I = \int_{-\infty}^{\infty} \exp[-(a - ib)\{x^2 - \frac{ic}{a - ib} x\}]\, dx \qquad [37]$$

which, by further rearrangement, yields

$$I = \int_{-\infty}^{\infty} \exp\left[-(a - ib)\{x - \frac{ic}{2(a - ib)}\}^2 + (a - ib)(\frac{ic}{2(a - ib)})^2\right] dx . \qquad [38]$$

The second term in the argument can be taken outside the integral sign, so that

$$I = \exp\left[\frac{-c^2}{4(a - ib)}\right] \int_{-\infty}^{\infty} \exp\left[-(a - ib)\{x - \frac{ic}{2(a - ib)}\}^2\right] dx . \qquad [39]$$

Substituting $y = (a - ib)^{\frac{1}{2}}\{x - \frac{ic}{2(a - ib)}\}$ yields

$$I = \frac{1}{\sqrt{a - ib}} \exp\left[\frac{-c^2}{4(a - ib)}\right] \int_{-\infty}^{\infty} \exp[-y^2]\, dy , \qquad [40]$$

the solution of which is

$$I = \sqrt{\frac{\pi}{a - ib}} \exp\left[\frac{-c^2}{4(a - ib)}\right] \quad . \qquad [41]$$

Consider now the definite integral

$$I_1 = \int_{-\infty}^{\infty} \exp\left[-ax^2 + ibx^2\right] \sin cx \, dx \qquad [42]$$

which may be separated into two parts:

$$I_1 = \frac{1}{2i} \int_{-\infty}^{\infty} \exp\left[-ax^2 + ibx^2 + icx\right] dx$$
$$- \frac{1}{2i} \int_{-\infty}^{\infty} \exp\left[-ax^2 + ibx^2 - icx\right] dx \quad . \qquad [43]$$

The first integral in [43] is identical to [36], the solution thus being given by [41]; the same analysis applied to the second integral is also given by [41]. Therefore the integral [42] is identically zero, and integrals involving the sine in the second term of [83]-II vanish.

Next the integral of type

$$I_2 = \int_{-\infty}^{\infty} \exp\left[-ax^2 + ibx^2\right] \cos cx \, dx \qquad [44]$$

may also be separated into two parts;

$$I_2 = \tfrac{1}{2} \int_{-\infty}^{\infty} \exp[-ax^2 + ibx + icx]\,dx$$

$$+ \tfrac{1}{2} \int_{-\infty}^{\infty} \exp[-ax^2 + ibx - icx]dx \qquad [45]$$

The solutions of these two integrals are identical to [41], so that

$$I_2 = \sqrt{\frac{\pi}{a - ib}}\ \exp\left[\frac{-c^2}{4(a + ib)}\right] \qquad [46]$$

$$= \sqrt{\frac{\pi(a + ib)}{a^2 + b^2}}\ \exp\left[\frac{-ac^2}{4(a^2 + b^2)}\right]\ \exp\left[\frac{-ibc}{4(a^2 + b^2)}\right] .$$

By noting the following relations

$$\sqrt{a + ib} = \left(\frac{\sqrt{a^2 + b^2} + a}{2}\right)^{\frac{1}{2}} + i\left(\frac{\sqrt{a^2 + b^2} - a}{2}\right)^{\frac{1}{2}}$$

$$\exp\left[\frac{-ibc}{4(a^2 + b^2)}\right] = \cos\frac{bc^2}{4(a^2 + b^2)} - i\sin\frac{bc^2}{4(a^2 + b^2)}$$

[46] becomes

$$I_2 = \sqrt{\frac{\pi}{2(a^2 + b^2)}}\ \exp\left[\frac{-ac^2}{4(a^2 + b^2}\right]$$

$$x\ \{(\sqrt{a^2 + b^2} + a)^{\frac{1}{2}} + i(\sqrt{a^2 + b^2} - a)^{\frac{1}{2}}\} \qquad [47]$$

$$x\ \{\cos\frac{bc^2}{4(a^2 + b^2)} - i\sin\frac{bc^2}{4(a^2 + b^2)}\} .$$

(a) The second term in the exponential in [44] may be replaced by either a sine or cosine term; firstly

$$I_3 = \int_{-\infty}^{\infty} \exp[-ax^2] \cos bx^2 \cos cx \, dx \qquad [48]$$

which can be written

$$I_3 = \tfrac{1}{2} \int_{-\infty}^{\infty} \exp[-ax^2 + ibx^2] \cos cx \, dx + \tfrac{1}{2} \int_{-\infty}^{\infty} \exp[-ax^2 - ibx^2] \cos cx \, dx \; . \qquad [49]$$

The first integral in [49] is equivalent to [44] and the second integral has the same solution as [47], i.e.

$$\int_{-\infty}^{\infty} \exp[-ax^2 - ibx^2] \cos cx \, dx = \sqrt{\frac{\pi}{2(a^2+b^2)}} \exp\left[\frac{-ac^2}{4(a^2+b^2)}\right] \qquad [50]$$

$$\times \{(\sqrt{a^2+b^2} + a)^{\frac{1}{2}} - i(\sqrt{a^2+b^2} - a)^{\frac{1}{2}}\}\{\cos \frac{bc^2}{4(a^2+b^2)} + i \sin \frac{bc^2}{4(a^2+b^2)}\}.$$

Hence from [47] and [50]

$$I_3 = \sqrt{\frac{\pi}{2(a^2+b^2)}} \exp\left[\frac{-ac^2}{4(a^2+b^2)}\right] \qquad [51]$$

$$\times \{(\sqrt{a^2+b^2} + a)^{\frac{1}{2}} \cos \frac{bc^2}{4(a^2+b^2)} + (\sqrt{a^2+b^2} - a)^{\frac{1}{2}} \sin \frac{bc^2}{4(a^2+b^2)}\} \; .$$

which is given in Eq. [84a]-II.

(b) Secondly the integral

$$I_4 = \int_{-\infty}^{\infty} \exp\,[-ax^2] \sin bx^2 \cos cx\, dx$$

$$= \frac{1}{2i} \int_{-\infty}^{\infty} \exp\,[-ax^2 + ibx^2] \cos cx\, dx \qquad [52]$$

$$- \frac{1}{2i} \int_{-\infty}^{\infty} \exp\,[-ax^2 - ibx^2] \cos cx\, dx$$

can be obtained from [47] and [50] as

$$I_4 = \sqrt{\frac{\pi}{2(a^2 + b^2}}\ \exp\left[\frac{-ac^2}{4(a^2 + b^2)}\right] \qquad [53]$$

$$x\ \{(\sqrt{a^2+b^2} - a)^{\frac{1}{2}} \cos \frac{bc^2}{4(a^2+b^2)} - (\sqrt{a^2+b^2} + a)^{\frac{1}{2}} \sin \frac{bc^2}{4(a^2 + b^2)}\}$$

which is equal to Eq. [84b]-II.

5. Details of Eq. [109]-II

It follows from Eq. [105]-II that the equilibrium distribution $p_{\sigma,\infty}(\phi_1)$ is

$$p_{\sigma,\infty}(\phi_1) = \int_0^{\infty} p_{\infty}(\phi_1) g(r_e) dr_e \quad . \qquad [54]$$

The integration of [54] is not feasible for general values of ϕ_1, but is tractable for particular values. To estimate

the error in [108]-II, the axis ratio $p_{\sigma,\infty}(\pi/2)/p_{\sigma,\infty}(0)$ of the polar diagram $p_{\sigma,\infty}(\phi_1)$ will be calculated.

Firstly for $\phi_1 = \pi/2$, from [74]-II and [102]-II,

$$p_{\sigma,\infty}(\pi/2) = \frac{1}{(2\pi)^{3/2}\sigma} \int_0^\infty r_e \exp\left[\frac{-(r_e - \bar{r}_e)^2}{2\sigma^2}\right] dr_e \qquad [55]$$

may be evaluated by substituting $\sigma y = r_e - \bar{r}_e$; thus

$$p_{\sigma,\infty}(\pi/2) = \frac{1}{(2\pi)^{3/2}} \int_{-\infty}^\infty (\sigma y + \bar{r}_e) \exp[-\frac{y^2}{2}] dy \qquad [56]$$

where the lower limit of integration $y = -\bar{r}_e/\sigma$ is replaced by $-\infty$, valid if $\sigma << \bar{r}_e$. The first part of the integral in [56]:

$$\int_{-\infty}^\infty \sigma y \exp[-\frac{y^2}{2}] dy = 0 \quad , \qquad [57]$$

and the second part yields

$$\int_{-\infty}^\infty \bar{r}_e \exp[-\frac{y^2}{2}] dy = \bar{r}_e\sqrt{2\pi} \quad , \qquad [58]$$

so that

$$p_{\sigma,\infty}(\pi/2) = \bar{r}_e/2\pi \quad . \qquad [59]$$

For $\phi_1 = 0$, [54] becomes, after the substitution $\sigma y = r_e - \bar{r}_e$,

$$p_{\sigma,\infty}(0) = \frac{1}{(2\pi)^{3/2}} \int_{-\bar{r}_e/\sigma}^\infty \frac{1}{\bar{r}_e + \sigma y} \exp[\frac{-y^2}{2}] dy \qquad [60]$$

where the lower limit $y = -\bar{r}_e/\sigma$ cannot be replaced by $-\infty$, since at this point the function inside the integral becomes singular. However by making a Taylor expansion:

$$\frac{1}{\bar{r}_e + \sigma y} = \frac{1}{\bar{r}_e(1 + \frac{\sigma y}{\bar{r}_e})} = \frac{1}{\bar{r}_e}\left(1 - \frac{\sigma y}{\bar{r}_e} - \frac{\sigma^2 y^2}{\bar{r}_e^2} - \dots\right) \qquad [61]$$

[60] becomes

$$p_{\sigma,\infty}(0) \simeq \frac{1}{(2\pi)^{3/2}} \int_{-\infty}^{\infty} \frac{1}{\bar{r}_e}\left(1 - \frac{\sigma y}{\bar{r}_e} - \frac{\sigma^2 y^2}{\bar{r}_e^2}\right) \exp\left[\frac{-y^2}{2}\right] dy \quad , \qquad [62]$$

with the lower limit now replaced by $-\infty$. The solutions of the three parts of [62] are

$$\int_{-\infty}^{\infty} \frac{1}{\bar{r}_e} \exp\left[\frac{-y^2}{2}\right] dy = \frac{\sqrt{2\pi}}{\bar{r}_e} \qquad [63a]$$

$$\int_{-\infty}^{\infty} \frac{\sigma y}{\bar{r}_e^2} \exp\left[\frac{-y^2}{2}\right] dy = 0 \qquad [63b]$$

$$\int_{-\infty}^{\infty} \frac{\sigma^2 y^2}{\bar{r}_e^3} \exp\left[\frac{-y^2}{2}\right] dy = \frac{\sigma^2}{\bar{r}_e^3}\sqrt{2\pi} \qquad [63c]$$

so that [62] becomes

$$p_{\sigma,\infty}(0) = \frac{1}{2\pi\,\bar{r}_e}\left(1 - \frac{\sigma^2}{\bar{r}_e^2}\right) \quad , \qquad [64]$$

and the axis ratio $p_{\sigma,\infty}(\pi/2)/p_{\sigma,\infty}(0)$ is, from [59] and [64],

$$\frac{p_{\sigma,\infty}(\pi/2)}{p_{\sigma,\infty}(0)} = \frac{\bar{r}_e^2}{1 - \frac{\sigma^2}{\bar{r}_e^2}} \qquad [65]$$

Using the first term of the Taylor expansion [65] may be approximated as

$$\frac{p_{\sigma,\infty}(\pi/2)}{p_{\sigma,\infty}(0)} = \bar{r}_e^{\,2}\left(1 + \frac{\sigma^2}{\bar{r}_e^{\,2}}\right) \qquad [109]\text{-II}$$

6. The Probability Distribution $p_{\sigma,t}(\kappa_1)$

We seek to prove that the function $p_{\sigma,t}(\kappa_1)$ for a collision-free suspension, which was obtained by numerical integration of [18]-III and with the use of [26]-III, and shown in Fig. 7 of Chapter III, changes monotonically with time.

The Probability distribution $p_{\sigma,t}(\kappa_1)$ resulting from the spread in r_e is

$$p_{\sigma,t}(\kappa_1) = p_{\sigma,t}(\phi_1)\left(\frac{\partial\phi_1}{\partial\kappa_1}\right)_t . \qquad [26]\text{-III}$$

Substituting the partial derivative $(\partial\phi_1/\partial\kappa_1)_t$ obtained from [17]-III, and the probability distribution $p_{\sigma,t}(\phi_1)$ given by [18]-III into [26]-III yields

$$p_{\sigma,t}(\kappa_1) = \frac{\bar{r}_e}{\cos^2\left(\frac{2\pi t}{\bar{T}} + \kappa_1\right) + \bar{r}_e^{\,2}\sin^2\left(\frac{2\pi t}{\bar{T}} + \kappa_1\right)} \int_0^\infty p_t(\phi_1)g(r_e)dr_e \; . \qquad [66]$$

It is not feasible to obtain the solution of integral in [66]; an alternate expression for $p_{\sigma,t}(\kappa_1)$ is obtained in the following way.

The phase angle κ is defined by

$$\tan\phi_1 = r_e \tan\left(\frac{2\pi t}{T} + \kappa\right) \quad . \qquad [5]\text{-II}$$

On the other hand κ_1 is defined from [17]-III:

$$\tan\phi_1 = \bar{r}_e \tan\left(\frac{2\pi t}{\bar{T}} + \kappa_1\right) \qquad [67]$$

for the same orientation ϕ_1. Therefore

$$r_e \tan\left(\frac{2\pi t}{T} + \kappa\right) = \bar{r}_e \tan\left(\frac{2\pi t}{\bar{T}} + \kappa_1\right) \quad . \qquad [68]$$

The phase angles κ and κ_1 are related to each other by

$$\kappa = -\frac{2\pi t}{T} + \tan^{-1}\left[\frac{\bar{r}_e}{r_e}\tan\left(\frac{2\pi t}{\bar{T}} + \kappa_1\right)\right] \qquad [69a]$$

or

$$\kappa_1 = -\frac{2\pi t}{\bar{T}} + \tan^{-1}\left[\frac{r_e}{\bar{r}_e}\tan\left(\frac{2\pi t}{T} + \kappa\right)\right] \quad . \qquad [69b]$$

The probability distribution $p_t(\kappa)$ for a fixed r_e is a constant, equal to $p(\kappa)$;

$$p_t(\kappa) = p(\kappa) = \frac{r_e}{2\pi(\cos^2\kappa + r_e^2\sin^2\kappa)} \quad . \qquad [27]\text{-II}$$

The fraction of particles in the interval $d\kappa_1$ at κ_1 is

identical to that in the interval $d\kappa$ at κ, thus

$$p_t(\kappa_1)d\kappa_1 \equiv p_t(\kappa)d\kappa \qquad [70]$$

from which the probability distribution $p_t(\kappa_1)$ for r_e is given by

$$p_t(\kappa_1) = p_t(\kappa)\left(\frac{\partial\kappa}{\partial\kappa_1}\right)_t \quad . \qquad [71]$$

The partial derivative $(\partial\kappa/\partial\kappa_1)_t$ may be obtained from [69a]:

$$\left(\frac{\partial\kappa}{\partial\kappa_1}\right)_t = \frac{\bar{r}_e}{r_e}\left[\cos^2\left(\frac{2\pi t}{\bar{T}} + \kappa_1\right) + \frac{\bar{r}_e^{\,2}}{r_e^{\,2}}\sin^2\left(\frac{2\pi t}{\bar{T}} + \kappa_1\right)\right]^{-1} \quad . \qquad [72]$$

Substituting [27]-II and [72] into [71] and noting κ is given by [69a], one obtains

$$\begin{aligned} p_t(\kappa_1) = \frac{\bar{r}_e}{2\pi}\Bigg[&\cos^2\left\{-\frac{2\pi t}{T} + \tan^{-1}\left[\frac{\bar{r}_e}{r_e}\tan\left(\frac{2\pi t}{\bar{T}} + \kappa_1\right)\right]\right\} \\ &+ r_e^2\sin^2\left\{-\frac{2\pi t}{T} + \tan^{-1}\left[\frac{\bar{r}_e}{r_e}\tan\left(\frac{2\pi t}{\bar{T}} + \kappa_1\right)\right]\right\}\Bigg]^{-1} \quad . \qquad [73] \\ \times\ &\left[\cos^2\left(\frac{2\pi t}{\bar{T}} + \kappa_1\right) + \frac{\bar{r}_e^{\,2}}{r_e^{\,2}}\sin^2\left(\frac{2\pi t}{\bar{T}} + \kappa_1\right)\right]^{-1} \quad . \end{aligned}$$

Rearrangement of [73] yields

$$p_t(\kappa_1) = \frac{\bar{r}_e}{2\pi}\left[(r_e^{-2}-1)\{\tfrac{1}{2}(r_e-\bar{r}_e)\cos(\frac{2\pi t}{\bar{T}}+\frac{2\pi t}{T}+\kappa_1)\right.$$

$$+\tfrac{1}{2}(r_e+\bar{r}_e)\cos(\frac{2\pi t}{\bar{T}}-\frac{2\pi t}{T}+\kappa_1)\}^2 \qquad [74]$$

$$\left.+\bar{r}_e^{\,2}+(r_e^2-\bar{r}_e^{\,2})\cos^2(\frac{2\pi t}{\bar{T}}+\kappa_1)\right]^{-1} .$$

For $\sigma << \bar{r}_e$, the values of r_e are close to $\bar{r}_e$, and thus [74] may be approximated by

$$p_t(\kappa_1) = \frac{\bar{r}_e}{2\pi}\left[(\bar{r}_e^{-2}-1)\bar{r}_e^{\,2}\cos^2(\frac{2\pi t}{\bar{T}}-\frac{2\pi t}{T}+\kappa_1)+\bar{r}_e^{\,2}\right]^{-1} . \qquad [75]$$

The period of rotation T for a given r_e relative to $\bar{T}$ is, from [6]-II,

$$T = \bar{T}\,\frac{r_e + r_e^{-1}}{\bar{r}_e + \bar{r}_e^{-1}} . \qquad [76]$$

Then the difference $(2\pi t/\bar{T} - 2\pi t/T)$ appearing in [75] becomes

$$\frac{2\pi t}{\bar{T}} - \frac{2\pi t}{T} = \frac{2\pi t}{\bar{T}}\cdot\frac{(\bar{r}_e r_e - 1)}{\bar{r}_e(r_e^2+1)}(r_e-\bar{r}_e) \qquad [77]$$

which may be approximated by

$$\frac{2\pi t}{\bar{T}} - \frac{2\pi t}{T} \simeq \frac{2\pi t}{\bar{T}}\,\frac{(\bar{r}_e^{\,2}-1)}{\bar{r}_e(\bar{r}_e^{\,2}+1)}(r_e-\bar{r}_e) . \qquad [78]$$

Substitution of [78] into [75] yields

$$p_t(\kappa_1) = \frac{\bar{r}_e}{2\pi\left[\bar{r}_e^2 + (1-\bar{r}_e^2)\cos^2\left(\frac{2\pi t}{\bar{T}}\frac{(\bar{r}_e^2-1)}{\bar{r}_e(\bar{r}_e^2+1)}(r_e-\bar{r}_e)+\kappa_1\right)\right]} \quad . \qquad [79]$$

This is a periodic function of time for given κ_1. However, the period T_κ for $p_t(\kappa)$ obtained from the equality:

$$\frac{2\pi T_\kappa}{\bar{T}}\frac{(\bar{r}_e^2-1)}{\bar{r}_e(\bar{r}_e^2+1)}(r_e-\bar{r}_e) = 2\pi \quad , \qquad [80]$$

relative to $\bar{T}$ for $\bar{r}_e >> 1$ or $\bar{r}_e << 1$ is

$$\frac{T_\kappa}{\bar{T}} \simeq \frac{\bar{r}_e}{r_e-\bar{r}_e} \simeq \frac{\bar{r}_e}{\sigma} \qquad [27]\text{-III}$$

which is very large compared to the period of one particle rotation.

The probability distribution $p_{\sigma,t}(\kappa_1)$ resulting from the spread in r_e is then given by

$$p_{\sigma,t}(\kappa_1) = \int_0^\infty p_t(\kappa_1)g(r_e)dr_e \qquad [81]$$

where $p_t(\kappa_1)$ is given by [79], and $g(r_e)$ by [74]-II. It is seen from [81] that $p_{\sigma,t}(\kappa_1)$ is the sum of $p_t(\kappa_1)$ for the

various r_e's, and that, if $\sigma << r_e$, the period of $p_{\sigma,t}(\kappa_1)$ is also the same order as given by [27]-III. It therefore appears as almost monotonic change during the time periods of experiments, which were about 5 particle rotations, whereas the period of $p_{\sigma,t}(\kappa)$ is, from [27]-III, of order 20 to 30 particle rotations for the particles employed (Table II of Chapter III).

For the same reasons similarly $\overline{|\sin \kappa_1|}$ and $\overline{|\cos \kappa_1|}$ are periodic functions with period of the same order as [27]-III, and therefore appear as monotonic changes on the line scale employed in Fig. 9 of Chapter III.

7. Anisotropy of the viscosity of suspensions

When the axisymmetric particles in a suspension attain the equilibrium orientation distribution $p_\infty(\phi_1)$, the most probable orientations occur at $\phi_1 = 90°$ for prolate spheroids or their equivalents ($r_e > 1$) and at $\phi_1 = 0°$ for oblate spheroids or equivalents ($r_e < 1$) as shown in Chapter III. The equilibrium distribution $p_\infty(\phi_1)$ is given by

$$p_\infty(\phi_1) = \frac{r_e}{2\pi(r_e^2\cos^2\phi_1 + \sin^2\phi_1)} \qquad [102]\text{-II}$$

thus showing anisotropy in orientation with respect to ϕ_1. This also causes anisotropy in the viscosity which can be

readily demonstrated by changing the direction of shear flow as shown in Fig. 18 of Chapter III. We now give details of the calculations.

The intrinsic viscosity of a suspension of spheroids is

$$[\eta] = C_1 \overline{\sin^4\theta_1 \sin^2 2\phi_1} + C_2 \overline{\cos^2\theta_1} + C_3 \overline{\sin^2\theta_1} \qquad [48]\text{-II}$$

the constants C_1, C_2 and C_3 being only dependent upon the axis ratio r_e. The mean goniometric factors for the steady state in an initial flow system (flow (i) in Fig. 18 of Chapter III) are given by[4)]

$$\overline{\sin^4\theta_1 \sin^2 2\phi_1} = \frac{4r_e^2}{(r_e^2-1)^2} \int_0^\infty \left[\frac{C^2(r_e^2+1)+2}{(C^2r_e^2+1)^{\frac{1}{2}}(C^2+1)^{\frac{1}{2}}} - 2 \right] p_E(C)\,dC \qquad [82]$$

$$\overline{\cos^2\theta_1} = 1 - \overline{\sin^2\theta_1} = 2 \int_0^\infty \frac{p_E(C)}{(C^2r_e^2+1)^{\frac{1}{2}}(C^2+1)^{\frac{1}{2}}}\,dC \qquad [83]$$

assuming that the distribution of orbit constants is given by the Eisenschitz distribution ([26]-II). Numerical integrations of [82] and [83] for $r_e = 10$ and substitution into [48]-II yield $[\eta] = 3.30$ which is shown as line (i) of Fig. 18 in Chapter III.

(a) Flow rotated by 90°

If we stop the flow and rotate the flow field (but not the particles) by 90° about the vorticity axis

(X_1-axis), the orientation angles ϕ_1 change by 90° while the θ_1's remain unchanged. Then the initial orientation with respect to ϕ_1 in the new flow system is, from [102]-II, given by

$$p_o(\phi_{10}) = \frac{r_e}{2\pi(r_e^2\sin^2\phi_{10} + \cos^2\phi_{10})} \quad . \qquad [84]$$

Since we have assumed the Eisenschitz distribution of orbit constants, the distribution $p_t(\theta_1)$ is still given by [21a]-II, therefore the initial distribution $p_o(\theta_{10},\phi_{10})$ is

$$p_o(\theta_{10},\phi_{10}) = \frac{r_e\sin\theta_{10}}{4\pi(r_e^2\sin^2\phi_{10} + \cos^2\phi_{10})} \quad . \qquad [85]$$

Substituting into [16]-II yields

$$p_t(\theta_1,\phi_1) = \frac{\chi_o^2\sin\theta_1}{4\pi\chi_1^2(\cos^2\theta_1 + \chi_o^2\sin^2\theta_1)^{3/2}} \qquad [86]$$

where χ_o^2 and χ_1^2 are given by

$$\chi_o^2 = \chi_{01}\sin^2\phi_1 + \chi_{02}\sin\phi_1\cos\phi_1 + \chi_{03}\cos^2\phi_1 \quad , \qquad [87a]$$

$$\chi_{01} = \tfrac{1}{2}\{1 + r_e^{-2} + (1 - r_e^{-2})\cos\tfrac{4\pi t}{T}\} \quad , \qquad [87b]$$

$$\chi_{02} = (r_e^{-1} - r_e)\sin\tfrac{4\pi t}{T} \quad , \qquad [87c]$$

$$\chi_{03} = \tfrac{1}{2}\{1 + r_e^2 + (1 - r_e^2)\cos\tfrac{4\pi t}{T}\} \quad , \qquad [87d]$$

and

$$\chi_1^2 = \chi_{11} \sin^2\phi_1 + \chi_{12} \sin\phi_1\cos\phi_1 + \chi_{13} \cos^2\phi_1 \quad , \qquad [88a]$$

$$\chi_{11} = \tfrac{1}{2} \{r_e + r_e^{-3} + (r_e - r_e^{-3}) \cos \frac{4\pi t}{T}\} \quad , \qquad [88b]$$

$$\chi_{12} = (r_e^{-2} - r_e^2) \sin \frac{4\pi t}{T} \quad , \qquad [88c]$$

$$\chi_{13} = \tfrac{1}{2} \{r_e^{-1} + r_e^3 + (r_e^{-1} - r_e^3) \cos \frac{4\pi t}{T}\} \quad . \qquad [88d]$$

The goniometric factors in the viscosity equation [48]-II can be evaluated from the integrals

$$\overline{\sin^4\theta_1 \sin^2 2\phi_1} = \int_0^{2\pi}\int_0^{\pi} p_t(\theta_1,\phi_1) \sin^4\theta_1 \sin^2 2\phi_1 d\theta_1 d\phi_1 \qquad [89a]$$

$$\overline{\sin^2\theta_1} = 1 - \overline{\cos^2\theta_1} = \int_0^{2\pi}\int_0^{\pi} p_t(\theta_1,\phi_1) \sin^2\theta_1 d\theta_1 d\phi_1 \quad . \qquad [89b]$$

Substitution of [86] into [89] yields

$$\overline{\sin^4\theta_1 \sin^2 2\phi_1} = \frac{1}{\pi} \int_0^{\pi} \frac{\chi_o^2 \sin^2 2\phi_1}{\chi_1^2} I_1 d\phi_1 \qquad [90a]$$

$$\overline{\sin^2\theta_1} = \frac{1}{\pi} \int_0^{\pi} \frac{\chi_o^2}{\chi_1^2} I_2 d\phi_1 \qquad [90b]$$

where the integrals I_1 and I_2 are

$$I_1 = \int_o^{\pi/2} \frac{\sin^5\theta_1}{(\cos^2\theta_1 + \chi_o^2 \sin^2\theta_1)^{3/2}} \, d\theta_1 \qquad [91a]$$

$$I_2 = \int_o^{\pi/2} \frac{\sin^3\theta_1}{(\cos^2\theta_1 + \chi_o^2 \sin^2\theta_1)^{3/2}} \, d\theta_1 \qquad [91b]$$

Solutions of [91a] and [91b] are given by

<u>for $\chi_o^2 < 1$</u>

$$I_1 = \frac{1}{2(1-\chi_o^2)^2} \left[1 + \frac{2}{\chi_o^2} + \frac{\chi_o^2 - 4}{\sqrt{1-\chi_o^2}} \tanh^{-1}\sqrt{1-\chi_o^2}\right] , \qquad [92a]$$

$$I_2 = \frac{1}{\chi_o^2} + \frac{1}{1-\chi_o^2} - \frac{1}{(1-\chi_o^2)^{3/2}} \tanh^{-1}\sqrt{1-\chi_o^2} . \qquad [92b]$$

<u>For $\chi_o^2 = 1$</u>

$$I_1 = 8/15 \quad , \qquad I_2 = 2/3 \quad . \qquad [93]$$

<u>For $\chi_o^2 > 1$</u>

$$I_1 = \frac{1}{2(\chi_o^2-1)^2} \left[1 + \frac{2}{\chi_o^2} + \frac{\chi_o^2 - 4}{\sqrt{\chi_o^2-1}} \tan^{-1}\sqrt{\chi_o^2-1}\right] , \qquad [94a]$$

$$I_2 = \frac{1}{\chi_o^2} - \frac{1}{\chi_o^2-1} + \frac{1}{(\chi_o^2-1)^{3/2}} \tan^{-1}\sqrt{\chi_o^2-1} . \qquad [94b]$$

The integrals given by [90] are evaluated numerically using I_1 and I_2 given by [92] to [94] for $r_e = 10$ and $[\eta]$ is

obtained from [48]-II with the results shown in Fig. 18 (ii) of Chapter III.

(b) Flow rotated by 45°

When the flow is rotated by 45° about the X_1-axis the initial orientation $p_o(\phi_{10})$ with respect to the new ϕ_1 becomes, from [102]-II,

$$p_o(\phi_{10}) = \frac{r_e}{\pi\{r_e^2 + 1 - (r_e^2 - 1)\ \sin 2\phi_{10}\}} \quad . \qquad [95]$$

Assuming the Eisenschitz distribution of orbits as before, the initial distribution $p_o(\theta_{10},\phi_{10})$ is given by

$$p_o(\theta_{10},\phi_{10}) = \frac{r_e \sin\theta_{10}}{2\pi\{r_e^2 + 1 - (r_e^2 - 1)\ \sin^2\phi_{10}\}} \quad . \qquad [96]$$

Substituting [96] into [16]-II yields the time-dependent distribution $p_t(\theta_1,\phi_1)$ as

$$p_t(\theta_1,\phi_1) = \frac{\chi_o^2 \sin\theta_1}{2\pi\ \chi_2^2(\cos^2\theta_1 + \chi_o^2\sin^2\theta_1)^{3/2}} \quad , \qquad [97]$$

where χ_o^2 is already given by [87] and χ_2^2 is

$$\chi_2^2 = \chi_{21}\ \sin^2\phi_1 + \chi_{22}\ \sin\phi_1\cos\phi_1 + \chi_{23}\ \cos^2\phi_1, \qquad [98a]$$

$$\chi_{21} = \chi_{11} + (r_e^{-2} - 1)\ \sin\frac{4\pi t}{T} + r_e^{-1} \quad , \qquad [98b]$$

$$\chi_{22} = \chi_{12} + 2(r_e^{-1} - r_e) \cos \frac{4\pi t}{T} \quad , \qquad [98c]$$

$$\chi_{23} = \chi_{13} + (r_e^2 - 1) \sin \frac{4\pi t}{T} + r_e \quad . \qquad [98d]$$

The mean goniometric factors $\overline{\sin^4\theta_1 \sin^2 2\phi_1}$ and $\overline{\sin^2\theta_1} = 1 - \overline{\cos^2\theta_1}$ are obtained by numerical integration of [90] using χ_2^2 given by [98] in place of χ_1^2. The intrinsic viscosity $[\eta]$ so obtained for $r_e = 10$ is shown in Fig. 18(iii) of Chapter III.

REFERENCES

1. This thesis, Chapter II.

2. P. Bois, "Tables of Indefinite Integrals", Dover, New York (1961).

3. P.F. Byrd and M.D. Friedman, "Handbook of Elliptic Integrals for Engineers and Physicists". Springer-Verlag, Berlin (1954).

4. E. Anczurowski and S.G. Mason, J. Colloid & Interface Sci., 23, 533 (1967).

APPENDIX II

SOME REVERSIBLE AND IRREVERSIBLE PHENOMENA IN SUSPENSIONS

As shown in Figs. 7 and 14 of Chapter III, the orientation distributions of particles were retraced when the flow was reversed. We now wish to demonstrate, by calculation, some reversible and irreversible phenomena which are not only important in suspension rheology but may also be of wider significance[1].

When a suspension of particles in a fluid undergoes a simple shear flow, each particle translates and rotates, and interacts with others. Under proper conditions the translational and rotational movements are retraced exactly when the direction of the motion of the fluid is reversed so that every pre-existing configuration of the particle assembly is restored: the suspension thus possesses perfect memory. The general requirements for reversibility are that the linearized form of the Navier-Stokes equation applies and that the boundary conditions are identical for forward and reverse flows[2,3]. More specifically, the requirements are that (i) the Reynolds number is so low that particle and fluid inertia are negligible; (ii) the shear flow is geometrically perfect; (iii) the fluid is Newtonian; and (iv) the particles are rigid, non-sedimenting, electrically neutral, and large enough for Brownian motion and van-der-Waals attraction to be negligible. A simple demonstration of the reversibility is shown by the reappearance of dyed letters of fluid on reversing a shear which was first made to disappear by shearing[4,5]. Multi-particle interactions of spheres[6], rods[7] and discs[7,8] have also

been demonstrated to be reversible.

Failing to meet one or more of the requirements listed above causes incomplete reversibility and impairs the memory by measurable amount: for example by increasing Reynolds number so that inertia effects become appreciable, permitting temperature gradients with resulting thermal convection, using small and/or electrically charged particles so that diffusion and/or interparticle attraction can occur, employing non-Newtonian fluids[9,10], etc. As shown in Figs. 7 and 14 of Chapter III, a slight but measurable amount of irreversibility was observed for the orientation distribution of particles in a dilute suspension of rods. This was probably due to the imperfect geometry of the shear flow and some uncontrollable thermal convection.

We wish now to demonstrate, by theoretical calculations, how a system which has perfect memory can be perturbed and so impair the memory. Consider a suspension of rods of various lengths having a Gaussian distribution of equivalent axis ratios r_e:

$$g(r_e) = \frac{1}{\sqrt{2\pi}\,\sigma_e} \exp\left[\frac{-(r_e - \bar{r}_e)^2}{2\sigma_e^2}\right] \qquad [1]$$

where $\bar{r}_e$ is the mean value of r_e and σ_e is the standard deviation. The suspension is then subjected to a uniform electric field to allow all rods to align themselves in the direction of the field[11]. If the electric field is parallel to the

X_2-axis (Fig. 1a, inset) the mean projection of unit length of rods on the X_2-axis, denoted by $\bar{r}_2$, is equal to unity. After removal of the electric field, a shear defined by $u_1 = u_2 = 0$, $u_3 = Gx_2$ (Fig. 1a, inset) is applied. In the ideal case in which the suspension is so dilute that no particle interaction takes place (actually even if there are particle interactions the system can be reversible if the boundary conditions are identical for forward and reverse flow), each rod rotates exactly as described by Jeffery's equation[12] in the X_2X_3-plane, the particle motion being given by

$$\tan\phi_1 = r_e \tan\left(\frac{2\pi t}{T} + \kappa\right) \qquad [2]$$

where ϕ_1 is the angle between the X_2-axis and the axis of revolution of rods (Fig. 1a, inset) and κ (= 0 for case under consideration) is the phase angle determined from the orientation at $t = 0$ and T is the period of rotation given by

$$T = \frac{2\pi}{G}\left(r_e + r_e^{-1}\right) \qquad . \qquad [3]$$

The projection r_2 of unit length of each rod on the X_2-axis is

$$r_2 = \cos\phi_1 = \left[1 + r_e^2 \tan^2\left(\frac{2\pi t}{T} + \kappa\right)\right]^{-\frac{1}{2}} \qquad [4]$$

which is an oscillating function with the frequency 2/T. For the suspension the mean projection $\bar{r}_2$ resulting from the spread in r_e is given by

FIGURE 1

(a) Damped oscillation of $\bar{r}_2$ calculated from [5] for $\bar{r}_e = 10$ and $\sigma_e = 0.2$. The broken line indicates the equilibrium value $\bar{r}_{2\infty} = 0.192$. The coordinate system relative to the shear flow is shown in the inset.

(b) The envelope of the maxima and minima of the oscillations in $\bar{r}_2$, shown as solid and broken lines respectively, obtained by numerical integration of [10]. Curve 1 corresponds to the oscillation shown in (a). Curves 2, 3, and 4 are for the 1st, 4th and 16th reversals following perturbations of κ at $t/\bar{T} = \pm 9.0$, and curve 5 is the equilibrium value $\bar{r}_{2\infty}$. The memory of the system M_i versus i (number of reversals) is shown in the inset.

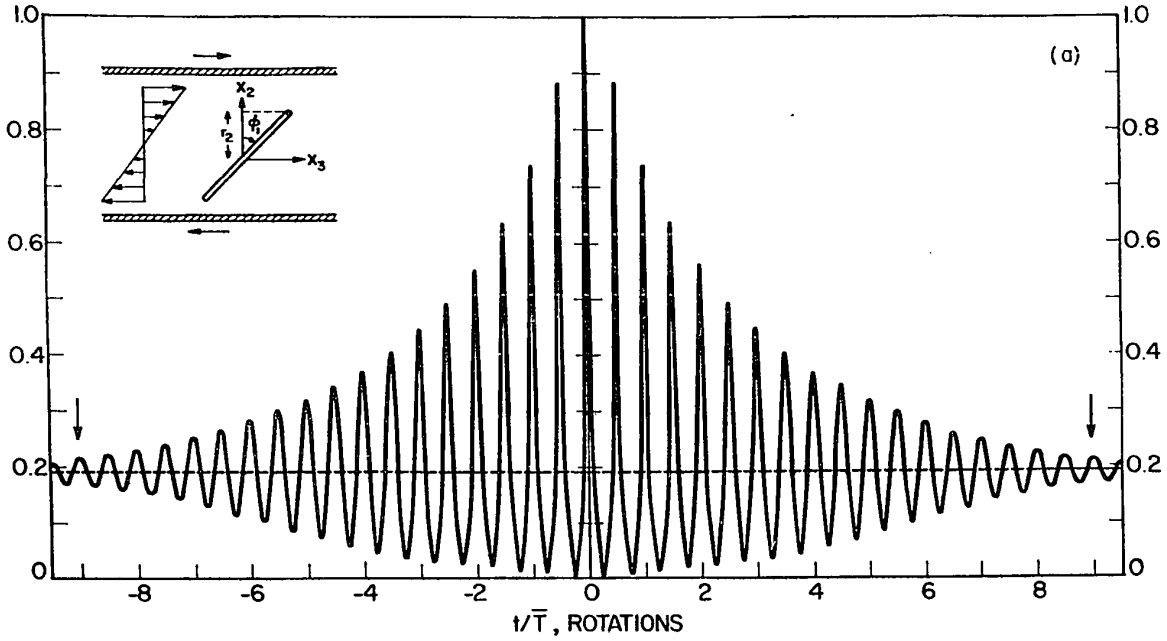
(a)
1.0
0.8
0.6
0.4
0.2
0
-8
-6
-4
-2
0
2
4
6
8
t/T̄, ROTATIONS
X2
X3
φ1
r̄2

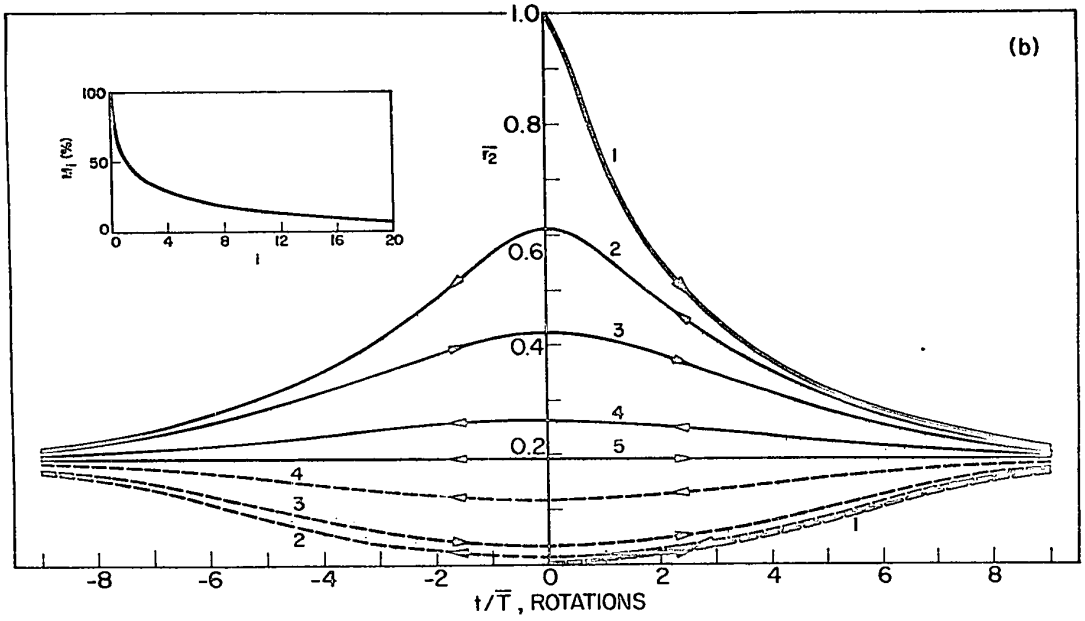
(b)
1.0
0.8
0.6
0.4
0.2
r̄2
1
2
3
4
5
4
3
2
1
100
50
0
0
4
8
12
16
20
I
-8
-6
-4
-2
0
2
4
6
8
t/T̄, ROTATIONS

$$\bar{r}_2 = \frac{1}{\sqrt{2\pi}\,\sigma_e} \int_0^\infty [1 + r_e^2 \tan^2(\frac{2\pi t}{T} + \kappa)]^{-\frac{1}{2}} \exp[\frac{-(r_e - \bar{r}_e)^2}{2\sigma_e^2}]\, dr_e \qquad [5]$$

where the period of rotation T relative to the mean $\bar{T} = 2\pi(\bar{r}_e + \bar{r}_e^{-1})/G$ is

$$T = \bar{T}(r_e + r_e^{-1})/(\bar{r}_e + \bar{r}_e^{-1}) \quad . \qquad [6]$$

Numerical integration of [5] for $\bar{r}_e = 10$ and $\sigma_e = 0.2$ as a function of $t/\bar{T}$ yields the results shown in Fig. 1a, where $\bar{r}_2$ is seen to undergo a damped oscillation whose amplitude becomes vanishingly small as $t \to \infty$ and $\bar{r}_{2\infty} = 0.192$ (indicated by the broken line). On reversing the flow at any time the oscillations can be built up reversibly until $t = 0$ is reached when, in negative time, they decay as mirror images of those in positive time. The envelope of the maxima and minima in $\bar{r}_2$ is shown by curves of Fib. 1b. The pattern can, in principle, be repeated indefinitely by cycling back and forth in time. Thus the system possesses perfect memory. The equilibrium $\bar{r}_{2\infty}$ corresponds to the orientation distribution $p_\infty(\phi_1)$, given by [13]

$$p_\infty(\phi_1) = \frac{\bar{r}_e}{2\pi(\bar{r}_e^2 \cos^2\phi_1 + \sin^2\phi_1)} \qquad [7]$$

where the mean axis ratic $\bar{r}_e$ is used instead of r_e since error involved in [7] is only of order σ_e^2.

We now consider making the system have fading memory. A simple method is to stop the motion at some given time, say $t/\overline{T} = 9$, perturbing the particles in some manner, reversing the motion until $t/\overline{T} = -9$, and then repeating the process. Various kinds of perturbation may be considered. A simple one is to perturb the angular displacement ϕ_1 of all particles having the same values of ϕ_1 in the direction of equilibrium orientation distribution given by [7]. Since the distribution of phase angle κ corresponding to [7] is a random distribution[13]:

$$p_\infty(\kappa) = 1/2\pi \quad , \qquad [8]$$

the perturbation with respect to ϕ_1 mentioned above is equivalent to perturbing the phase angle κ. A simple scheme of perturbation is to employ an identical Gaussian distribution of perturbation for each value of κ. Thus the distribution of κ after the first perturbation becomes

$$g_1(\kappa) = \frac{1}{\sqrt{2\pi}\,\sigma_1} \exp\left[\frac{-\kappa^2}{2\sigma_1^2}\right] \qquad [9]$$

where σ_1 is the standard deviation of κ.

The mean projection $\overline{r}_2$ now becomes from [5] and [9]:

$$\overline{r}_2 = \int_{-\infty}^{\infty}\int_{0}^{\infty} \left[1 + r_e^2 \tan^2\left(\frac{2\pi t}{T} + \kappa\right)\right]^{-\frac{1}{2}} g(r_e) g_1(\kappa)\, dr_e\, d\kappa \quad . \qquad [10]$$

Numerical integration of [10] with $\sigma_1 = 0.2$ radians yields damped oscillations on reversing time similar to those in

in Fig. 1a but with reduced amplitudes. The envelope of the maxima and minima of $\bar{r}_2$ is shown as curve 2 in Fig. 1b. Thus initially $\bar{r}_2$ undergoes damped oscillation along the curve 1 which is now stopped at $t/\bar{T} = 9$, and the system is perturbed according to [9]. On reversing the flow, $\bar{r}_2$ builds up its oscillations along curve 2 until $t = 0$, at which $\bar{r}_2 = 0.610$ indicating that some of the memory of the system has been lost. In negative time $\bar{r}_2$ undergoes the damped oscillations along the curve 2 which is mirror image of those in positive time.

If we next stop the flow again at $t/\bar{T} = -9$, and make identical perturbations as in [9], the memory is impaired further. It is readily seen that, after ith perturbation and time reversal, total perturbation with respect to κ becomes

$$g_i(\kappa) = \frac{1}{\sqrt{2\pi i}\ \sigma_1} \exp\left[\frac{-\kappa^2}{2i\ \sigma_1^2}\right] \quad . \qquad [11]$$

The mean projection $\bar{r}_2$ then is obtained by a numerical integration of the type [10] using [11]. The results for several such cycles for $\sigma_1 = 0.2$ are shown in Fig. 1b. It is seen that the oscillations of $\bar{r}_2$ are no longer exactly restored following each reversal, as indicated by the progressive decrease in $\bar{r}_{2i}$ at zero time after i th reversals. We can express the memory of the system in a number of ways, a simple one being

$$M_i = \frac{\bar{r}_{2i} - \bar{r}_{2\infty}}{\bar{r}_{2o} - \bar{r}_{2\infty}} \quad . \qquad [12]$$

As shown in the inset of Fig. 1b, M_i decreases nearly exponentially with i from 100% initially to zero at $i = \infty$ when $\bar{r}_2$ is flat and the memory of the initial imprint is completely lost (line 5).

We have illustrated as an example of the scheme a system which shows both perfect and imperfect memory. By changing the shape, size, deformability and concentration of the particles, the type of fluid, the duration of each cycle of shear, the number of flow reversals and the type of perturbation, a wide range of memory patterns can doubtless be achieved.

REFERENCES

1. Sachs, R.G., Science, 176, 587 (1972).
2. Bretherton, F.P., J. Fluid Mech., 14, 284 (1962).
3. Slattery, J.C., ibid, 19, 625 (1964).
4. Heller, J.P., Am. J. Phys., 28, 348 (1960).
5. Goldsmith, H.L. and Mason, S.G., "Rheology: Theory and Applications" (Eirich, F.R. ed.) 4, 85 (Academic Press, New York, 1967).
6. Darabaner, C.L. and Mason, S.G., Rheol. Acta, 6, 273 (1967).
7. Anczurowski, E., Cox, R.G. and Mason, S.G., J. Colloid Interface Sci., 23, 547 (1967).
8. Karnis, A., Goldsmith, H.L. and Mason, S.G., J. Colloid Sci., 22, 531 (1966).
9. Karnis, A. and Mason, S.G., Trans. Soc. Rheol., 10, 571 (1966).
10. Gauthier, F., Goldsmith, H.L. and Mason, S.G., Rheol. Acta, 10, 344 (1971).
11. This thesis, Chapter IV.
12. Jeffery, G.B., Proc. Roy. Soc. (London), A102, 161 (1922).
13. This thesis, Chapter II.

APPENDIX III

MAGNETIC TORQUE ON AN ELLIPSOID

Here we consider briefly how the theory described in Chapter IV can be modified when the electric field is replaced by a magnetic field.

A particle suspended in the fluid of magnetic permeability μ_2 and subjected to a uniform and parallel magnetic field of strength $\underset{\sim}{H}_o$ (in e.m.u.) experiences a magnetic torque $\underset{\sim}{\Gamma}'_M$:

$$\underset{\sim}{\Gamma}'_M = \underset{\sim}{M}' \times \underset{\sim}{B}' = \mu_2 \underset{\sim}{M}' \times \underset{\sim}{H}'_o \qquad [1]$$

where $\underset{\sim}{B}'$ is the magnetic induction of the applied field and $\underset{\sim}{M}'$ the magnetic moment which depends upon magnetic properties of the particle. If it is either paramagnetic or diamagnetic (i.e., there is no permanent magnetization), then the induced magnetization per unit volume ξ'_i of the particle with permeability μ'_{ij} which has only diagonal components (i.e., $\mu'_{ij} = \delta_{ij}\mu'_{ij}$) is

$$\xi'_i = \frac{\mu_2}{4\pi} (q'_{ii} - 1) H'_{+i} \qquad [2]$$

where H'_{+i} is the magnetic field created inside the particle, and q'_{ii} is the ratio of the permeability of the particle to that of the medium ($q'_{ii} = \mu'_{ii}/\mu_2$). From the similarity between electric and magnetic field theories, the magnetic field inside the ellipsoid is, by analogy from [10]-IV,

$$H'_{+i} = \frac{H'_{oi}}{1 + \frac{1}{2}a_1a_2a_3(q'_{ii} - 1)\alpha_i} \quad . \qquad [3]$$

Substituting [3] into [2] and eventually into [1], we obtain the magnetic torque acting on the particle due to the induced magnetization as

$$\Gamma'_{Mi} = \frac{1}{3}\, a_1a_2a_3\, \varepsilon_{ijk}\, \frac{\mu_2^2(q'_{jj} - 1)}{1 + \frac{1}{2}a_1a_2a_3(q'_{jj} - 1)\alpha_j}\, H'_{oj}H'_{ok} \quad . \qquad [4]$$

If instead the particle has a permanent magnetization $\underset{\sim}{\xi}'_o$ per unit volume but no induced magnetization (i.e., it is ferro-magnetic), the torque exerted by the external magnetic field is

$$\Gamma'_{Mi} = \frac{4\pi}{3}\, a_1a_2a_3\, \mu_2\, \varepsilon_{ijk}\, \xi'_{oj}\, H'_{ok} \quad . \qquad [5]$$

The angular velocity of a magnetic ellipsoid in shear and magnetic field can be obtained by combining [5]-IV, [4] and [5]. It is clear that, from the comparison between [13b]-IV and [4] for the particles with no permanent magnet, all equations derived in the previous sections hold if $\underset{\sim}{E}_o$ is replaced by $\underset{\sim}{H}_o$ and K_2 by μ_2^2, and that we may expect magneto-rheological phenomena very similar to the electro-rheological phenomena we have described.

Hall and Busenberg [1] calculated viscosity of a suspension of permenently magnetized spheres ($r_e = 1$) in a magnetic field directed arbitrarily in the X_1X_2-plane (Fig. 1-IV).

When H_o is parallel to the X_2-axis, $[\eta]_\infty$ shows similar behavior to that shown in Fig.8a-IV. $[\eta]_\infty$ changes from 2.5 at zero magnetic field to 4 at the critical field where $[\eta]_\infty$ exhibits a sudden change of behavior and above which it is constant (= 4). If H_o is not parallel to the X_2-axis, but in the X_1X_2-plane, then as H_o increases $[\eta]_\infty$ shows a steady increase to an asymptotic value less than 4, and depending upon the orientation of H_o, thus indicating that the spheres rotate no matter how high the field. Similar behavior of the viscosity of a suspension of loaded spheres in a gravitational field has been predicted by Brenner [2].

REFERENCES

1. Hall, W.F. and Busenberg, S.N., J. Chem. Phys., 51, 137 (1969).

2. Brenner, H., J. Colloid Interface Sci., 32, 141 (1970).

APPENDIX IV

THE COUETTE APPARATUS

THE COUETTE APPARATUS

Although the essential features of Couette apparatus in which the hydrodynamic field of laminar shear was produced have been described previously[1], a brief description is given here since several modifications were made.

The principle of the apparatus consisting of two counter-rotating concentric cylinders of radii R_1 and R_2 are rotated in opposite directions with their angular velocities Ω_1 and Ω_2 respectively, is shown in Fig. 1. Solution[2] of the Navier-Stokes equation in the creeping flow regime in the annular gap between the cylinders gives the angular velocity $\Omega(R)$ of the fluid at the distance R as

$$\Omega(R) = \frac{(\Omega_1 R_1^2 + \Omega_2 R_2^2)R^2 - (\Omega_1 + \Omega_2)R_1^2 R_2^2}{(R_2^2 - R_1^2)R^2} \qquad [1]$$

Thus the velocity gradient is

$$G(R) = R\,\frac{d\Omega(R)}{dR} = \frac{2(\Omega_1 + \Omega_2)R_1^2 R_2^2}{(R_2^2 - R_1^2)R^2} \qquad [2]$$

Since the two cylinders rotate in opposite directions

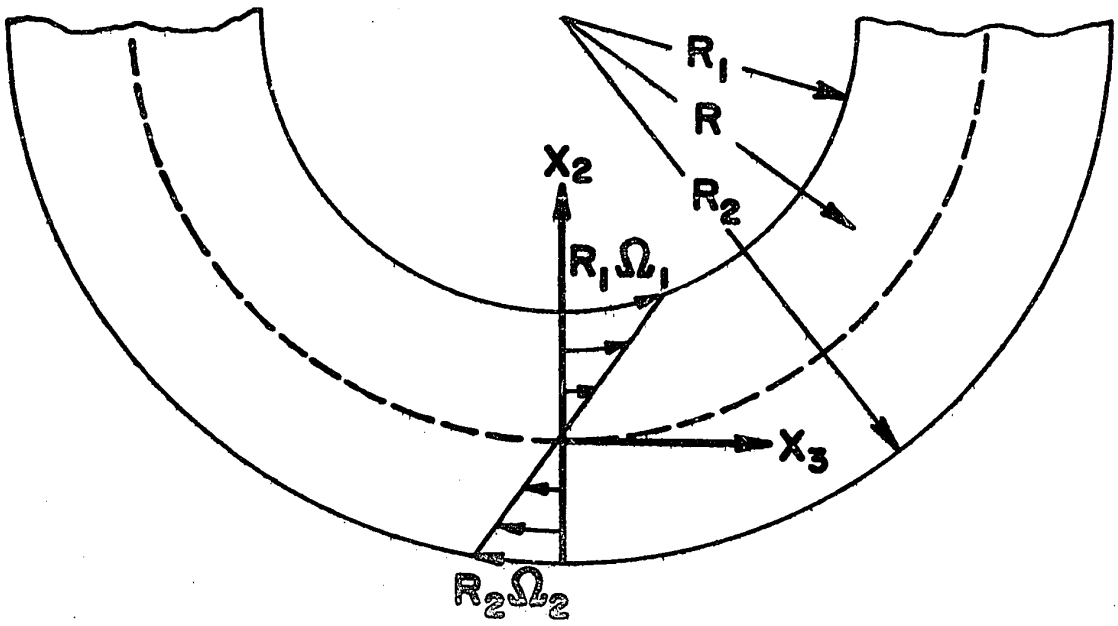

Fig. 1. Principle of the Couette apparatus (After Trevelyan and Mason[2]).

there exsists a cylinder of zero velocity at which Eq. [2] becomes

$$G(R^*) = \frac{2(\Omega_1 R_1^2 + \Omega_2 R_2^2)}{R_2^2 - R_1^2} \qquad [3]$$

where R^* is the radial distance from the center to the stationary layer (i.e. $\Omega(R^*) = 0$).

In most of the experiments an inner cylinder of $R_1 = 13.354$ cm and an outer cylinder of $R_2 = 15.234$ were used, for which Eq. [3] becomes

$$G = 0.6949\ N_1 + 0.9044\ N_2 \quad [\text{sec}^{-1}] \qquad [4]$$

where N_1 and N_2 are the rpm of the inner and outer cylinders respectively. Since the two cylinders are driven by separate continuously variable motors, R^* and $G(R^*)$ can be varied at will.

A Couette Mark II apparatus is shown in Fig. 2. It consists of two stainless steel cylinders (A) and the adjustable common support (C) for microscope and camera. The outer cylinder has a glass bottom plate to permit illumination of the field from below. The individual cylinders are connected through a 4-speed gear box and a set of worm gears to the $\frac{1}{4}$H.P. d.c. motors with magnetic amplifier control (Bepco Canada Ltd.) having a speed range of 150 - 3,000 rpm.

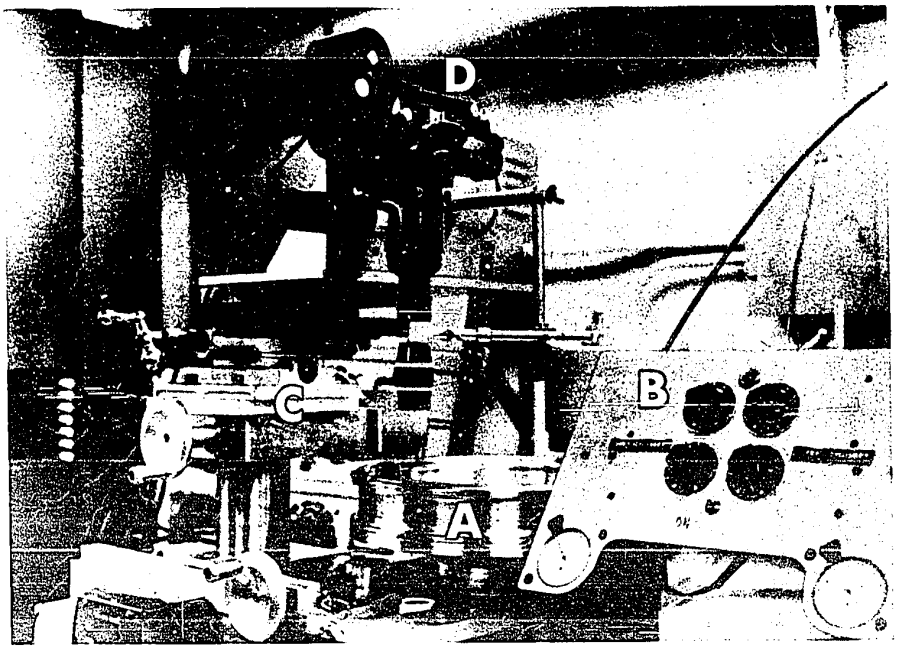

Fig. 2: The Mark II Couette Apparatus. Two stainless steel cylinders (A) are driven by the individual motor with continuous controls (B). A 35mm camera (D) with 70mm sivitar lens and beam splitter are mounted on the support (C) which allows both vertical and radial movements.

By means of three sets of reduction worm gears a wide range of velocity gradients (0 to 40 sec^{-1}) can be obtained. The speed controls and tackometers are mounted on the right-hand panel (B), while the variable a.c. and d.c. voltage supplies and a chopper device for timing are on the left-hand panel (part of it can be seen behind the camera support).

The camera support (C) consists of an aluminium platform capable of concentric rotation with respect to the two cylinders and a column which provides the vertical movement. At the top of the column a compound slide movement supplied the X_2 and X_3 adjustment in order to keep a particle under observation stationary in the field of view of the camera.

In experiments of Chapter III and V an automatic 35mm camera (D) (Robot Motor Recorder 36ME) with a 30 ft film magazine capable of taking 260 frames was used. The magnetic shutter release device attached to the camera is connected to the electronic timer that creates the impulse, intervals of which can vary continuously from $\frac{1}{4}$ sec to 1 min. The camera is also equipped with a small fixed focus lens on the top so that the time can be recorded on the upper right-hand corner of the frame from the image of the electric digital stop watch which is synchronized to the switch of the motor for Couette cylinders. Photographs were generally

taken through 70mm telephoto lens and the beam splitter shown in Fig. 2.

For some experiments the Mark IV device which is similar to the Mark II in principle but is more versatile[3] was also used. Various sets of transparent (Plexiglas) cylinders or discs can be mounted on two concentric counter-rotating spindles to allow observation along both horizontal and vertical directions. By means of a built-in lathe the cyliners can be machined in situ to a tolerance of ± 8 microns. A 16mm cine-camera (Bolex Paillard H16) which is mounted to a similar support assembly as in the Mark II device was used to record the events photographically through a microscope.

In the Couette Mark II device an electric field can be applied by grounding the inner cylinder and connecting the outer cylinder to a 0 to 25 kV stabilized a.c. power supply. The field strength E_o created in an annular gap, from the analogy of a concentric cylindrical condenser, is given by

$$E_o(R) = \frac{V}{R \ \ell n \ R_2/R_1} \qquad [5]$$

where V is the potential difference between cylinders. However if there is a small difference in diameters of inner and outer cylinders as in the case of the Mark II, the variation in E_o across annulus can be ignored[4], and the

electric field becomes simply

$$E_o = V/d \qquad [6]$$

where $d = R_2 - R_1$. Since we have used an a.c. power supply, the root-mean-square value of an applied voltage is calculated from the relationship[5)]

$$V = \frac{V_p}{2\sqrt{2}} \qquad [7]$$

where V_p is the peak-to-peak value which is measured by an oscilloscope (Tektronic Type 564B).

REFERENCES

1. W. Bartok and S.G. Mason, J. Colloid Sci., 12, 243 (1957).

2. B.J. Trevelyan and S.G. Mason, J. Colloid Sci., 6, 354 (1951).

3. C.L. Darabaner, J.K. Raasch and S.G. Mason, Can. J. Chem. Eng. 45, 3 (1967).

4. R.S. Allan and S.G. Mason, Proc. Roy. Soc. (London), A267, 45 (1962).

5. H.V. Malmstadt and C.G. Enke, "Electronics for Scientists", W.A. Benjamin, New York (1963).

APPENDIX V

HISTORICAL SURVEY

The most familiar rheological property of a fluid is its shear viscosity η defined, in effect by Isaac Newton, as the ratio of the shear stress P_{32} to the rate of shear strain G ($\eta = P_{32}/G$, see Chapter II). The first significant development in suspension rheology was made early in this century by Einstein[1] who developed the now classical theory of viscosity of a suspension of rigid spheres by purely hydrodynamic considerations. Assuming the spheres to be suspended in a Newtonian fluid in a neutrally buoyant condition, to be separated from each other by distances much greater than the sphere diameter, and neglecting the inertia term in the Navier-Stokes equation governing motion of the fluid surrounding each sphere which, incidentally, rotates with an angular velocity of one half of the velocity gradient of the fluid, the viscosity η of the suspension was predicted to be

$$\eta = \eta_o \ (1 + 5c/2)$$

where η_o is the viscosity of suspending medium and c is the volume fraction of spheres. The coefficient 5/2 is the intrinsic viscosity $[\eta]$ of the suspension; experimentally $[\eta]$ is obtained from the reduced viscosity $(\eta - \eta_o)/\eta_o c$ at the limit of zero concentration. Einstein's equation was found to hold for very dilute (up to c = 0.01) lyophobic suspensions of spherical particles[2,3]. The viscosity at higher concentrations was investigated theoretically by a number of workers[4-7] by taking into account the interactions between spheres, with the results generally given as a power

series

$$\eta = \eta_o(1 + 2.5c + k_1c^2 + \ldots)$$

where k_1 is the interaction constant whose value has been calculated to vary from 6.25 to 15; there is still no agreement (either theoretically and experimentally) on its correct value.

The first theoretical attempt to predict the viscosity of suspensions of non-spherical particles was made by Jeffery[8] for rigid spheroids. The theory took account of axis ratios and the orientations of the particles in shear flow, assuming negligible Brownian motion of the particles. Several equations were derived later for spheroids under the influence of weak and intense Brownian motion[9-17].

For flexible particles, Taylor[18] extended the Einstein treatment for rigid spheres to the case of spherical liquid drops and obtained $[\eta]$ as a simple function of viscosity ratio of the drops to that of the medium.

Numerous theoretical and experimental studies of the viscosity of polymer solutions have been made since Staudinger's[19] empirical relationship between the intrinsic viscosity and molecular weight of macromolecular solutions was formulated. Huggins[20,21] extended Kuhn's[10] hydrodynamic treatment of a chain of spheres to the case of a randomly-coiled chain of spheres as a model for linear macromolecules. These developments have led to a number of successful theoretical studies of viscosity of polymer

solutions by Flory[22] and others[23,24].

Streaming birefringence (or double refraction) is a rheo-optical effect which can give information regarding the size, shape and flexibility of particles and dissolved macromolecules. Freundlich et al[25] showed that the streaming birefringence in colloidal dispersions of rods and discs was related to the particle orientations. Boeder[26] and Peterlin et al[14,27,28] then developed theories for spheroids in which particle orientation figured prominently. It was suggested that streaming birefringence could be used as a hydrodynamic research tool[29,30]. Excellent reviews of this subject have been given by Edsall[31] and others[32,33]. The optical transmittance of sheared suspensions is another rheo-optical property which depends on the size, shape and orientation of the particles and is especially interesting in dispersions of platelets[34].

Experimental observations of rotations of spheroidal particles suspended in water-glass solutions were first made by Taylor[35] in a simple shear flow produced in an annular gap between two concentric glass cylinders of a Couette apparatus (see Appendix IV). Upon rotating the outer cylinder, periodic motions of particles predicted by Jeffery[8] were qualitatively confirmed. It was also observed that particles were assuming the final orientations of the minimum energy dissipation after about a few hundred rotations as Jeffery[8] speculated; that is prolate spheroids rotated the axis of revolution parallel to the vorticity and oblate spheroids

normal to it. Eirich et al[36] studied the orientations of glass, silk and rayon rods (with axis ratio ranging from 5 to 100) in dilute suspensions in a Couette apparatus at $G = 100$ to 250 sec^{-1}. In the steady state half of the particles were found aligned with the vorticity axis (vertical), and the remainder perpendicular to it (horizontal) for particles of axis ratio 5. With higher axis ratios more particles were aligned with the flow. Similar results were reported by Binder[37]; particles with axis ratio ≤ 15 assumed the vertical position, whereas those with axis ratio > 15 became oriented in the horizontal plane.

Quantitative measurements of particle rotations were first made in this laboratory using a Couette apparatus some 20 years ago. Jeffery's equations for the periodic motion of particles were confirmed for glass rods[38], Orlon rods[39] and polystyrene discs[40]. It was found that an isolated particle remained in the same orbit indefinitely, so that there was no tendency for it to assume a preferred orbit in contrast to earlier findings[35,37]. However in dilute suspensions of rods an equilibrium distribution of orbits was observed at a few hundred particle rotations[41-43]; the observed distribution of orbits lay between that corresponding to minimum dissipation of energy (the so-called Jeffery's hypothesis) and that corresponding to a random distribution of particle orientations (the Eisenschitz distribution, discussed in Chapter II). There are also a number of theoretical considerations to explain this

indeterminacy of particle orbits. Inertial effects, neglected in Jeffery's[8] original calculation, were considered by Saffman[44], who showed that the orbit can change slowly towards that corresponding to Jeffery's hypothesis. However the time required to reach an equilibrium is too large to account for any of the experimental observations. He suggested that non-Newtonian properties of the liquid used might be responsible for Taylor's observations[35]. The drift in orbits of rods and discs at high shear rates (and high Reynolds number) where inertial effects become significant was studied by Karnis et al[45]; formal agreement with Saffman's theory[44] was found. Observations in non-Newtonian liquids[46,47] showed that the orbits of both rods and discs drifted toward the orbits corresponding to the minimum energy dissipation. It has recently been shown in our laboratory[48] that the equilibrium orbits of cylindrical particles in visco-elastic fluids depends both on the axis ratio and applied velocity gradient. Particles of axis ratio greater than 0.9 and less than 0.3 moved to the orbit of least energy dissipation, but those with axis ratio between these two values could assume intermediate equilibrium orbits. It is thus clear from the experimental evidence that the distributions of orbits observed at low velocity gradients in Newtonian fluids[41-43] cannot be explained by the effect observed at high Reynolds numbers and in non-Newtonian fluids.

Recently Brenner[49] pointed out that the long-term effects of Brownian rotation cannot be ignored no matter how

small it may be. When Brownian motion is dominant, the particles become randomly oriented and thus display the Eisenschitz distribution[11] of orbits. The steady state orientation distributions at various rotary Péclet numbers (the ratio of velocity gradient to the rotary diffusion constant) was first obtained by Boeder[26] in his analysis of streaming birefringence of spheroids. The corresponding distribution of particle orbits in case of very weak Brownian motion has recently been obtained by Leal and Hinch[50]. It is striking that the calculated distributions of orbits for large Péclet number were similar to the Eisenschitz distribution and very different from those observed experimentally by Anczurowski and Mason[42]. Therefore Brownian motion cannot account for the experimental observations.

Mason and Manley[41] proposed that the equilibrium distribution of orientations and particle orbits was determined by the interaction between particles in their experiments which, incidentally, are similar to those reported in the present investigation (Chapter II and III). The importance of particle interactions to the viscosity of concentrated suspensions was pointed out by Bingham[51] and others[5,52]. Detailed experiments on collisions of spheres in Couette flow were conducted by Manley and Mason[53]. A doublet formed by a two-body collision rotates as a rigid dumbbell at a constant angular velocity and separates at a point which is a mirror image of the initial contact point.

The measured collision frequency of spherical particles in a suspension showed good agreement with the theoretical calculations based upon simple geometrical considerations. The rotation of fused doublets was found to follow Jeffery's equations for spheroids of axis ratio 2 [39]. Except for that presented in Chapter II, there is no theoretical treatment of two-body interactions between non-spherical particles. A few experimental observations of interactions between rigid rods[41,43] and discs[54] in a simple shear flow showed the sudden jump in particle orbits when they collided with one another; it is, however, clear that such interactions could ultimately determine the steady state distributions of orbits and orientations. The results have been reviewed in detail by Goldsmith and Mason[55].

When a suspension of asymmetric particles is subjected to an electric field it can become anisotropic, as shown for example by the optical birefringence first studied by Kerr[56], and now known as Kerr effect. This electro-optical effect can be observed even when the particles (or molecules) are isotropic. A number of quantitative studies of electrical birefringence in colloidal solutions[57-60] led to the conclusion that, as in streaming birefringence, particle orientation was the principal cause. The effect of permanent dipoles on electric birefringence was first noted in studies of solutions of tobacco mosaic virus[61]. The theory of the Kerr effect for rigid macromolecules was considered by Peterlin and Stuart[28] and several others[62-64]. The electrical torque acting on the particles, which depends upon electrical

properties (such as the permanent dipole moment and dielectric constant) of the particles and of the medium, tends to align the particles, with rods assuming orientations parallel to the electric field, and discs oriented with their axes of revolution perpendicular to it (see Chapter IV). Such alignment is opposed by any Brownian rotation existing, so that the final orientation is determined by the ratio of the electric torque to the Brownian couple. The distribution of particle orientations in an electric field was then calculated by the solution of the rotary diffusion equation[62,63].

The rheological and rheo-optical properties of a solution, dispersion, or suspension can be modified by applying any external field, for example an electric or magnetic field, which generates additional couples on the particles. The changes (generally increases) in the viscosity of liquid and suspensions by applying an electric field were observed as early as 1896 by Duff[65]. This effect is often called an electro-viscous effect, but it should not be confused with the conventional first, second and third electroviscous effects due to the electrical double layer at the surfaces of electrically charged particles (and molecules) and observed without an applied electric field. The first definitive study of the electroviscous effect (as we have defined it) was made by Bjornstahl and Snellman[66,67], who found increase in viscosity in colloidal dispersions of metal and sulfur. Alcock[68] and Andrade and

co-workers[69,70] studied pure liquids in an electric field, and found that the viscosity of certain polar conductive liquids increased, whereas that of non-conductive liquids was not affected. Induced particle aggregation and alignment (termed fibration) and increased viscosity of silica gel suspensions by an electric field were observed by Winslow[71]. The effect was found to be reversible, i.e. the particles could be easily redispersed by mechanical agitation and the original viscosity restored. The measured viscosity of the suspension at a fixed velocity gradient was linear with the square of the electric field strength[71]. Klass and Martinek[72] studied the increase in viscosity of silica and calcium titanate suspensions in electric fields and concluded that induced polarization in the double layer surrounding each particle was the primary cause of the electroviscous effect in their suspensions; they reported that they did not observe any fibration of particles. However direct evidence of fibration into linear chains of spheres in dielectric liquids in an electric field has been presented by Zia et al[73] who also showed that the chains so formed (which would lead to viscosity enhancement) rotated like rigid rods without breaking at low shear. Thus chain formation is almost certainly one cause of the large increase in viscosity observed[66,67,72] when an electric field is applied to a suspension. On the other hand simultaneous application of shear and electric fields to produce rheo-electro-optical effects in suspensions received little

attention until the work of Tolstoi[74]. By generalizing the results of Peterlin and Stuart[28] he obtained expressions for birefringence and extinction angle as the function of electric field strength and velocity gradient for suspensions of electrically isotropic particles with no permanent dipole. His analysis, however, was limited to two-dimensional problems. A relatively complete theory was later given by Demetriades[75] for rigid spheroids having an isotropic dielectric constant but no permanent dipole moment. Upon applying an electric field normal to the vorticity and the direction of shear flow, the angular velocity of the symmetry axis of particles was obtained as the sum of those in shear flow alone and in electric field alone. Demetriades then calculated the steady state orientation distribution by solving the orientation diffusion equation, and obtained the electro-streaming-birefringence and the associated extinction angle of the suspension. This theoretical work was extended by Ikeda[76] to the case where spheroids possess permanent dipoles along the axis of symmetry, and by Chaffey and Mason[77] to the case where the electric field was arbitarrily oriented with respect to the shear flow. Experimental observations of the rotational motion of single rods[78] and single discs[77] (with no appreciable Brownian motion) in combined shear and electric fields showed good agreement with theory (see also Chapter V). Analysis[77] of Demetriades' theory[75] revealed the existence of the critical electric field, below which the particles can

execute a complete rotation, and above which the rotation is impeded by the opposing action of the electric torque on the particle. Chaffey and Mason[79] also calculated the intrinsic viscosity $[\eta]$ of a suspension of spheroids in an electric field; these calculations are extended in Chapter IV.

Since electric and magnetic phenomena are analogous in many ways, the effect of magnetic field on rheology of suspensions may be expected to be similar to that of electric field. Pryce-Jones[80] and Harvey[81] observed the increase in viscosity of suspensions of magnetic iron oxide upon application of a magnetic field. Osipov[82] noted that the viscosity of clay suspensions in a magnetic field varied with time. The theory of the viscosity in a magnetic field was considered by Hall and Busenberg[83] for suspensions of spheres with fixed magnetic moments. McTague[84] studied the effect with ferromagnetic particles of cobalt in a capillary viscometer and reported good agreement with theory of Hall and Busenberg[83]. Simple dimensional analysis of the effects of a magnetic field was made by Rosensweig et al[85]. Results similar to those of Hall and Busenberg were recently obtained by Brenner and Weissman[86] and by Hinch and Leal[87], when Brownian rotation of particles was taken into account. Brenner[88] also calculated viscosity of a suspension of spheres whose gravity and geometrical centers are displaced in a gravitational field and obtained results effectively the same as those of Hall and Busenberg[83].

REFERENCES

1. Einstein, A., Ann. Phys., 19, 289 (1906); 34, 591 (1911). English translation is available in "Investigations on the Theory of the Brownian Movement", Dover, New York (1954).
2. Kraemer, E.O., Treatise on Physical Chemistry, D. van Nostrand, New York (1931).
3. Eirich, F.R., Bunzl, M. and Margaretha, H., Kolloid-Z., 74, 278 (1936).
4. Guth, E. and Simha, R., Kolloid-Z., 74, 266 (1936).
5. Vand, V., J. Phys. Colloid Chem., 52, 277 (1948).
6. Simha, R., J. Appl. Phys., 23, 1020 (1952).
7. Kynch, G.J., Proc. Roy. Soc. (London), A237, 90 (1956).
8. Jeffery, G.B., ibid, A102, 161 (1922).
9. Onsager, L., Phys. Rev., 40, 1028 (1932).
10. Kuhn, W., Kolloid-Z., 62, 269 (1933).
11. Eisenschitz, R., Z. Phys. Chem., A158, 85 (1932); A163, 133 (1933).
12. Guth, E., Kolloid-Z., 74, 147 (1936).
13. Burgers, J.M., Second Report on Viscosity and Plasticity, Chapter III, North Holland, Amsterdam (1938).
14. Peterlin, A., Kolloid-Z., 86, 230 (1939).
15. Simha, R., J. Phys. Chem., 44, 25 (1940).
16. Saito, N., J. Phys. Soc. Japan, 6, 297 (1951).
17. Scheraga, H.A., J. Chem. Phys., 23, 1526 (1955).
18. Taylor, G.I., Proc. Roy. Soc. (London), A138, 41 (1932).
19. Staudinger, H., Die hochmolekularen organishen Verbindungen, Springer, Berlin (1932).
20. Huggins, M.L., J. Phys. Chem., 42, 911 (1938); 43, 439 (1939).

21. Huggins, M.L., J. Appl. Phys., 10, 700 (1939).

22. Flory, P.J., Principles of Polymer Chemistry, Cornell University Press, New York (1953).

23. Kirkwood, J.G. and Riseman, J., J. Chem. Phys., 16, 565 (1948).

24. Debye, P. and Bueche, A.M., ibid, 16, 573 (1948).

25. Freundlich, H., Stapelfeldt, F. and Zocher, H., Z. Phys. Chem., 114, 161, 190 (1924).

26. Boeder, P., Z. Phys., 75, 258 (1932).

27. Peterlin, A., ibid, 111, 232 (1938).

28. Peterlin, A. and Stuart, H.A., ibid, 112, 1, 129 (1939).

29. Humphry, R.H., Proc. Roy. Soc. (London), 35, 217 (1923).

30. Wayland, J.H., J. Appl. Phys., 26, 1197 (1955).

31. Edsall, J.T., Advances in Colloid Science, Vol. 1, 269 (1942).

32. Cerf, R. and Scheraga, H.A., Chem. Rev., 51, 185 (1952).

33. Jerrard, H.G., ibid, 59, 345 (1959).

34. Sorrentino, M. and Mason, S.G., J. Colloid Interface Sci., 41, 178 (1972).

35. Taylor, G.I., Proc. Roy. Soc. (London), A103, 58 (1923).

36. Eirich, F.R., Margaretha, H. and Bunzl, M., Kolloid-Z., 75, 20 (1936).

37. Binder, R.C., J. Appl. Phys., 10, 711 (1939).

38. Trevelyan, B.J. and Mason, S.G., J. Colloid Sci., 6, 354 (1951).

39. Bartok, W. and Mason, S.G., J. Colloid Sci., 12, 243 (1957).

40. Goldsmith, H.L. and Mason, S.G., J. Fluid Mech., 12, 88 (1962).

41. Mason, S.G. and Manley, R.St.J., Proc. Roy. Soc., (London), A238, 117 (1956).

42. Anczurowski, E. and Mason, S.G., J. Colloid Interface Sci., 23, 533 (1967).

43. Anczurowski, E., Cox, R.G. and Mason, S.G., ibid, 23, 547 (1967).

44. Saffman, P.G., J. Fluid Mech., 1, 540 (1957).

45. Karnis, A., Goldsmith, H.L. and Mason, S.G., Can. J. Chem. Eng., 44, 181 (1966).

46. Karnis, A. and Mason, S.G., Trans. Soc. Rheology, 10, 571 (1966).

47. Gauthier, F., Goldsmith, H.L. and Mason, S.G., Rheol. Acta, 10, 344 (1971).

48. Bartram, E. and Mason, S.G., Forthcoming Publication.

49. Brenner, H., J. Colloid Interface Sci., 34, 103 (1970).

50. Leal, L.G. and Hinch, E.J., J. Fluid Mech., 46, 685 (1971).

51. Bingham, E.C., Fluidity and Plasticity, McGraw-Hill, New York (1922).

52. Mooney, M., J. Colloid Sci., 6, 162 (1951).

53. Manley, R.St.J. and Mason, S.G., J. Colloid Sci., 7, 354 (1952); Can. J. Chem., 33, 763 (1955).

54. Karnis, A., Goldsmith, H.L. and Mason, S.G., J. Colloid Interface Sci., 22, 531 (1966).

55. Goldsmith, H.L. and Mason, S.G., Rheology: Theory and Applications (F.R. Eirich, ed.) Vol. 4, Chapter 2, Academic Press, New York (1967).

56. Kerr, J., Phil. Mag., 50, 337 (1875).

57. Bergholm, C. and Bjornstahl, Y., Phys. Z., 21, 137 (1920).

58. Procopin, S., Ann. Phys., 1, 213 (1924).

59. Errera, J., Overbeek, J.Th.G. and Sack, H., J. Chem. Phys., 32, 681 (1935).

60. Marshall, C.E., Trans. Farady Soc., 26, 273 (1930).

61. Lauffer, M.A., J. Phys. Chem., 42, 935 (1938).

62. Benoit, H., Ann. Phys., 6, 561 (1951).

63. Tinoco, I., J. Am. Chem. Soc., 77, 4486 (1955).

64. O'Konski, C.T., Yoshioka, H. and Orttung, W.H., J. Phys. Chem., 63, 1558 (1959).

65. Duff, A.W., Phys. Rev., 4, 23 (1896).

66. Bjornstahl, Y., Physics, 6, 257 (1935).

67. Bjornstahl, Y. and Snellman, K.O., Kolloid-Z., 78, 258 (1937); 86, 223 (1939).

68. Alcock, E.D., Physics, 7, 126 (1936).

69. Andrade, E.N.da C. and Dodd, C., Proc. Roy. Soc. (London), A187, 296 (1946); A204, 449 (1951).

70. Andrade, E.N. da C. and Hart, J., ibid, A225, 463 (1954).

71. Winslow, W.M., J. Appl. Phys., 20, 1137 (1949).

72. Klass, D.L. and Martinek, T.W., ibid, 38, 67, 75 (1967).

73. Zia, I.Y.Z., Cox, R.G. and Mason, S.G., Proc. Roy. Soc. (London) A300, 421 (1967).

74. Tolstoi, N.A., Doklady Akad. Nank. S.S.S.R., 59, 1563 (1948).

75. Demetriades, S.T., J. Chem. Phys., 29, 1054 (1958).

76. Ikeda, S., ibid, 38, 2839 (1963).

77. Chaffey, C.E. and Mason, S.G., J. Colloid Sci., 19, 525 (1964).

78. Allan, R.S. and Mason, S.G., Proc. Roy. Soc. (London) A267, 62 (1962).

79. Chaffey, C.E. and Mason, S.G., J. Colloid Sci., 20, 330 (1965); 27, 115 (1968).

80. Pryce-Jones, J., Kolloid-Z., 129, 96 (1952).

81. Harvey, E.N., J. Colloid Sci., 8, 543 (1953).

82. Osipov, Yu.B., Kolloiduyi Z., 28, 713 (1965).

83. Hall, W.F. and Busenberg, S.N., J. Chem. Phys., 51, 137 (1969).

84. McTague, J.P., ibid, 51, 133 (1969).

85. Rosensweig, R.E., Kaiser, R. and Miskolczy; J. Colloid Interface Sci., 29, 680 (1969).

86. Brenner, H. and Weissman, M.H., J. Colloid Interface Sci., to appear (1973).

87. Hinch, E.J. and Leal, L.G., J. Fluid Mech., 56, 803 (1972).

88. Brenner, H., J. Colloid Interface Sci., 32, 141 (1970).